UNIVERSITY OF SOUTHAMPTON

FACULTY OF ENGINEERING, SCIENCE AND MATHEMATICS

Institute of Sound and Vibration Research

Vibration Control Using an Adaptive Tuned Magneto-Rheological Fluid Vibration Absorber

by

Chompoonoot Hirunyapruk

Thesis for the degree of Doctor of Philosophy

January 2009

UNIVERSITY OF SOUTHAMPTON

ABSTRACT

FACULTY OF ENGINEERING, SCIENCE AND MATHEMATICS
INSTITUTE OF SOUND AND VIBRATION RESEARCH

Doctor of Philosophy

VIBRATION CONTROL USING AN ADAPTIVE TUNED MAGNETO-RHEOLOGICAL FLUID VIBRATION ABSORBER

by Chompoonoot Hirunyapruk

An adaptive tuned vibration absorber (ATVA) can be used to suppress unwanted vibrations. If the excitation frequency is time harmonic but the frequency changes with time, it is desirable to retune the ATVA so that the natural frequency of the ATVA always coincides with the excitation frequency. One way of achieving this is to adjust the stiffness of the ATVA. The key challenge is to change the stiffness in real-time. Tunable fluids such as Magneto-Rheological (MR) fluids, whose properties can be controlled by a magnetic field, may be used to address this challenge.

The subject of this thesis is an ATVA exploiting the changeable properties of MR fluids in the pre-yield state. The ATVA is designed as a three-layer beam with elastic face plates and MR fluid in the core. Electromagnets are attached to the top and the bottom layers to generate a magnetic field. By varying the current supplied to the electromagnets, the shear stiffness of the MR fluid and hence the stiffness of the ATVA can be varied. The vibration characteristics of the ATVA as a function of the magnetic field strength are predicted by a finite element model together with an empirical model for the shear modulus of the MR fluid and a model for the magnetic field applied to the fluid. An MR fluid-filled ATVA was manufactured and tested to validate the predictions. This ATVA design allows the natural frequency to be changed by 40.6%.

The self-tuning of the MR fluid-filled ATVA can be achieved by integrating an adaptive-passive controller with the ATVA so that its stiffness can be continuously adjusted in real-time. The control aims to drive the cosine of phase angle between the velocities of the host structure and the ATVA to zero. Various control algorithms, i.e. non-linear proportional, derivative, and proportional-plus-derivative controls, are investigated. Computer simulations and experimental results demonstrate that the MR fluid-filled ATVA is able to retune itself in the order of 0.2 seconds. The ATVA can also maintain the tuned condition within a reasonably wide frequency range between 110 and 146 Hz in the face of changes in the forcing frequency. The MR fluid-filled ATVA has the potential to substantially reduce vibration of a host structure. The proportional-plus-derivative control was found to be the best control approach for the ATVA.

Contents

List of Tables

List of Figures

DECLARATION OF AUTHORSHIP

I, Chompoonoot Hirunyapruk, declare that the thesis entitled VIBRATION CONTROL USING AN ADAPTIVE TUNED MAGNETO-RHEOLOGICAL FLUID VIBRATION ABSORBER and the work presented in the thesis are both my own, and have been generated by me as the result of my own original research.

I confirm that this work was done wholly or mainly while in candidature for a research degree at this University; where I have consulted the published work of others, this is always clearly attributed; I have acknowledged all main sources of help.

Signed: .....

Date: .....

Acknowledgements

I would like to thank my supervisors Brian Mace and Michael Brennan, who endured this long process with me, for their instructive guidance and assistance at every stage of the thesis process. Their gentle support has been most appreciated. Next I wish to thank the members of my internal review panel: Tim Waters, Paolo Gardonio and Neil Ferguson. They provided insights that guided and challenged my thinking.

I am also grateful to the Royal Thai Government for the scholarship to complete this thesis. Many thanks to all those, especially at the ISVR and the house no. 27, who I have met along the way. Their friendship and support are valuable and unforgettable.

This thesis would not have been possible without my family. Thanks to my brother and his family for the on-going aid. Words alone cannot express the thanks I owe to my mother for her encouragement and assistance during this long period. Finally, I wish to dedicate this thesis to my father who is always in my heart.

Abbreviations

ATVA	Adaptive tuned vibration absorber
CSD	Control shear deformation
D	Derivative
DOF	Degree-of-freedom
ER	Electro-Rheological
FE	Finite element
FRF	Frequency response function
MR	Magneto-Rheological
MRD	Magneto-Rheological Device
P	Proportional
PC	Personal computer
PD	Proportional-plus-derivative
SDOF	Single degree-of-freedom
SMA	Shape memory alloy
TVA	Tuned vibration absorber

List of Symbols

$a_0 - a_1$	Constant
$A_1 - A_6$	Constant
A	Area
A^*	Constant
A_0	Amplitude
A_1	Cross-sectional area of the beam, $A_1 = bh_1$
A_p	Cross-sectional area of the outer layers
A_{s1}	Cross-sectional area of steel path 1
A_{s2}	Cross-sectional area of steel path 2
A_m	Cross-sectional area of MR gap
$A_t^{90^\circ}$	Attenuation when the TVA is tuned such that $\cos\phi = 0$
A_t^o	Optimum attenuation
b	Width of the beam
$b_0 - b_3$	Constant
$b_1' - b_5'$	Constant
B	Magnetic flux density
B_{s1}	Magnetic flux density corresponding to steel path 1
B_{s2}	Magnetic flux density corresponding to steel path 2
B_m	Magnetic flux density corresponding to MR gap
B_f	Magnetic flux density across the free gap of the parallel plate rheometer
c_a	Viscous damping coefficient
$C_1 - C_6$	Constant
d	Distance between the top and bottom plates of rheometer
d_n	Derivative of the error
D	Controller gain

e	Element number
e_n	Error signal
e_{n-2}	Error signal at the time step $n-2$
E	Young's modulus of elasticity
E_1	Young's modulus of elasticity of layer 1
E_3	Young's modulus of elasticity of layer 3
E'	Storage modulus of perspex
f	Excitation force
$\mathbf{f}$	Nodal force vector
G	Complex shear modulus
G'	Storage modulus
G_0	Effective shear modulus of the core without magnetic field applied
G_a	Complex shear modulus of air
G_e	Effective shear modulus of the core with magnetic field applied
G_f	Complex shear modulus of the off-state MR fluid
G'_f	Storage modulus of the off-state MR fluid
G_n	Complex shear modulus of the on-state MR fluid
G'_n	Storage modulus of the on-state MR fluid
G_p	Complex shear modulus of perspex
G'_p	Storage modulus of perspex
G_t	Effective shear modulus due to the tape
G'_t	Storage shear modulus due to the tape
G'_z	Zero magnetic field storage modulus
G'_∞	Saturated magnetic field storage modulus
G'_s	Saturated storage modulus
G''	Loss modulus
h_1	Thickness of layer 1
h_2	Thickness of layer 2
h_3	Thickness of layer 3
h_g	Gap between the particles in a chain in MR fluid
H	Magnetic field strength

H_{s1}	Magnetic field strength corresponding to steel path 1
H_{s2}	Magnetic field strength corresponding to steel path 2
H_m	Magnetic field strength corresponding to MR gap
i	Mode number
I	Current
I_1	Second moment of area of the beam, $I_1 = bh_1^3/12$
I_m	Motor current
I_n	Current at the n time step
I_{n+1}	Current at the $n+1$ time step
I_p	Second moment of area of the outer layers
I_r	MRD current
J_p	Average particle polarization density
k	Wavenumber
k_1	Stiffness of the host structure
k_a	Stiffness of the TVA
k_i	Wavenumber of mode i
k^b	Stiffness of the three-layer beam
k_0^b	Stiffness of the beam with zero shear stiffness in the core
k_∞^b	Stiffness of the beam with infinitely stiff shear core
$\mathbf{K}$	Total stiffness matrix
$\mathbf{K_e}$	Element stiffness matrix
l	Length of element
l_{s1}	Length of steel path 1
l_{s2}	Length of steel path 2
l_m	Length of steel MR gap
L	Length of the beam
L_i	Length of integration path
m_1	Mass of the mass-like structure
m_a	Mass of the TVA
m_T	Total mass
M	Bending moment

M_1	Bending moment of layer 1
M_2	Bending moment of layer 2
M_3	Bending moment of layer 3
M_m	Mass of electromagnet
$\mathbf{M}$	Total mass matrix
$\mathbf{M_e}$	Element mass matrix
M_s	Saturate magnetization
n	The number of element
N	The number of turns of wire
p	Parameter to be updated
p_0	Total transverse loading
p^*	Order of the derivative
p_i	The value of parameter p at the i step of the updating process
p_{i+1}	The value of parameter p at the $i+1$ step of the updating process
P	Controller gain
P_1	Longitudinal force in layer 1
P_3	Longitudinal force in layer 3
q	Force per unite length
$\mathbf{q_0}$	Nodal displacement vector for the entire beam
$\mathbf{q_i}$	Nodal DOFs vector for a single element of the beam
Q	External force
r	Radius displacement
R	Resistance
R_0	Outer radius of the top plate of rheometer
S	Shear force
S_1	Shear force of layer 1
S_2	Shear force of layer 2
S_3	Shear force of layer 3
T	Kinetic energy
T_0	Torque
T_c	Control period

T_p	Period of sinusoid
T_s	Settling time
T_1	Kinetic energy of layer 1
T_2	Kinetic energy of layer 2
T_3	Kinetic energy of layer 3
T_e	Element kinetic energy
u	Longitudinal displacement
u_1	Longitudinal displacement within layer 1
u_2	Longitudinal displacement within layer 2
u_3	Longitudinal displacement within layer 3
u_{10}	Longitudinal extension of the mid-surface of layer 1
u_{30}	Longitudinal extension of the mid-surface of layer 3
U	Strain energy
U_1	Strain energy of layer 1
U_2	Strain energy of layer 2
U_3	Strain energy of layer 3
U_e	Element strain energy
v	Volume
V	Voltage
w	Transverse displacement
z_1	Distance measured from the mid-plane axis of layer 1
z_2	Distance measured from the mid-plane axis of layer 2
z_3	Distance measured from the mid-plane axis of layer 3
$\alpha_1 - \alpha_4$	Empirical constant
δ	Phase difference between stress and strain
η	Loss factor of MR fluid
η_a	Loss factor of the TVA
η_f	Loss factor of the off-state MR fluid
η_m	Viscosity
η_n	Loss factor of the on-state MR fluid
η_p	Loss factor of perspex

η_t	Loss factor of tape
η_z	Zero magnetic field loss factor
η_T^F	Predicted total loss factor of the ATVA
η_T^m	Measured total loss factor of the ATVA
η_∞	Saturated magnetic field loss factor
γ	Shear strain
$\dot{\gamma}$	Shear strain rate
γ_0	Shear strain amplitude
γ_2	Shear strain in layer 2
γ_y	Yield strain
κ	Radius of gyration of electromagnet
λ	Eigenvalues
λ_j	Mass normalised eigenvalue of mode j
μ	Mass ratio, $\mu = m_a/m_1$
μ^*	Permeability of material
μ_0	Permeability of free space
μ_1	Relative permeability of medium
μ_m	Relative permeability of MR fluid
μ_r	Relative permeability of material, $\mu_r = \mu^*/\mu_0$
μ_s	Relative permeability of steel
ν_p	Poisson's ratio of perspex
ω_0	Angular frequency of the top plate of rheometer
ω	Frequency, rad/sec
ω_1	Natural frequency of the host structure
ω_1^*	Initial forcing frequency
ω_2^*	Final forcing frequency
ω_a	Anti-resonance frequency or natural frequency of the TVA
ω_a^F	Predicted anti-resonance frequency
ω_a^m	Measured anti-resonance frequency
ω_f	Off-state tuned frequency

ω_i	Natural frequency of mode i
ω_n	On-state tuned frequency
ω_r	Resonance frequency
ϕ	Phase difference
ϕ_0	Volume fraction of particles in the composite
ϕ_j	Mass normalised eigenvactor of mode j
ρ	Density
ρ_1	Density of layer 1
ρ_2	Density of layer 2
ρ_3	Density of layer 3
ρ_m	Density of layer 2
ρ_p	Density of layers 1 and 3
σ	Normal stress
τ	Shear stress
τ_0	Shear stress amplitude
τ_y	Yield stress
τ_{ys}	Saturated yield stress
θ_0	Angular displacement or deflection angle
θ_m	Measured deflection angle
ζ	damping ratio, $\zeta = c_a/2m_a\omega_a$
ε	Normal strain
ε_1	Normal strain within layer 1
ε_3	Normal strain within layer 3
Ω_1	Frequency ratio, $\Omega_1 = \omega/\omega_1$
Ω_a	Frequency ratio, $\Omega_a = \omega/\omega_a$
Φ	Magnetic flux
Ψ	Eigenvectors
$\mathcal{H}$	Magnetic field strength in Oersted

Chapter 1

Introduction

1.1 Background

Despite the increased awareness of vibration control, vibrations still cause many problems. Vibrations are involved in many aspects of human life and have a wide variety of effects on people, for example discomfort [1]. Vibrations can also degrade the performance of equipment and cause damage to structures. For example, the transfer rate of a hard disk drive can be reduced by the vibration of the cooling fan and the spindle motor of the hard disk can affect its read-write accuracy [2]. Damage to buildings can be caused by, for example, road and rail vehicles and the severe vibrations induced by earthquakes [3]. Vibrations in machines can be caused by, for example, misalignment, loose mountings, changes in temperature and pressure, unbalanced rotating parts, and fluctuation in magnetic force due to the alternating current in transformers and magnetically actuated devices [4, 5].

Efforts have been made for many years to prevent and control vibrations. Preventative measure can be taken in the early stages of design. However, in-situ operating conditions might change. Hence the methods for vibration treatment and control of structures are often required [6]. Structural vibrations can be suppressed by several means such as adding damping to specific locations in the structures using damping materials and adding additional devices, such as a vibration isolator or a vibration absorber, to the structure [6].

Damping treatment aims to absorb the energy present in a vibrating structure by adding damping to the structure. Structures such as plates and beams can be damped

by a damping layer, which can be either added to the surface of the structure or sandwiched between layers of the structure [7]. An alternative way of adding damping to a structure is using damping devices such as a dashpot damper, a friction damper, an air damper or a magnetic damper [5]. Dampers can be used in many applications such as vehicle suspensions, seats and cable bridges [8, 9].

Vibration isolators are used to reduce the transmission of vibration from a vibrating source to a receiver [5]. This is achieved by mounting the structure on a flexible isolator which is a spring-damper system. There are a variety of isolators in the marketplace, for example metal coil springs commonly used under foundations [5], the air spring isolator often used for very low frequency isolation systems and the spring-in-series hanger used for the isolation of pipes in buildings [10]. An isolator made of rubber is one of the most common isolators and can be used for a wide range of applications such as machine mounts and large concrete blocks [5].

The tuned vibration absorber (TVA) was developed early in the 20th century [11]. It is an additional system attached to a vibrating structure to suppress its vibration. It must be properly tuned to be effective. There are two general forms of TVA, i.e. mass-spring and mass-spring-damper systems. The damped TVA aims to add damping to the host structure [12]. It is effective at reducing vibrations over a wide range of frequencies, and hence is often used for random excitation and broadband applications. The damped TVA is used, for example, to reduce the torsional vibration produced during the start-up of the compressor driven by synchronous motors [13], to suppress vibration caused by the voice coil motor and the head actuator in a hard disk drive [14] and to attenuate vibration due to the rotational motion of a paper machine roll [15]. The TVA can also be attached to buildings to control the vibration due to the wind or earthquake excitations [16, 17] and can be used to reduce railway noise caused by vibration propagating in the wheel and rail [18, 19].

The undamped TVA, which is the subject of this thesis, attempts to add a large impedance to structure at the point of attachment [12]. It can completely suppress vibration of the structure at a particular forcing frequency when its natural frequency is tuned to the disturbance frequency. However some damping in the TVA is always present in reality and degrades the effectiveness of the device. The dynamics of the

TVA, the equation of motion and the effect of damping in the TVA are discussed in the next chapter. The undamped TVA is effective for discrete frequency applications such as the electric hair clipper [11] and printed circuit boards [20]. The aircraft industry uses undamped TVAs to suppress the fuselage vibration due to engines and propellers [21].

Many designs of the TVA have been developed, for example the TVA consisting of a tuning mass, which is a tungsten block, and elastomeric pads [21], a beam-like TVA with a mass at one end [14] or two ends [22], a mass-spring-pendulum TVA [23] and an electromechanical TVA [24], which is a coil connected to an electrical circuit. The TVA described by Thompson *et al.* [19] consists of steel masses having elastomeric material layers between the masses and the rail. The sloshing absorber used in the work of Truong and Semerciqil [25] and Sakamota *et al.* [26] comprised a tank containing ER fluid and several sets of electrodes. Although vibration absorbers are commercially available, the developments of new technology are still needed, for example the new technology required for making absorbers tunable.

1.2 Adaptive Tuned Vibration Absorber

The classic passive TVA has fixed characteristics, which are designed for a particular operating condition. The performance of a TVA is sensitive to mass, stiffness and so on and hence accurate tuning is required. The passive TVA is not effective for applications in which the excitation frequency might change with time nor is it able to accommodate mistune, either when installed or if its environmental conditions change with time. Consequently, there have been attempts to make the TVA tunable [21]. There are several methods of tuning the TVA. One of them is by changing its stiffness. A TVA used in the work of La Malfa *et al.* [20] is a mass attached to a rod. Its natural frequency can be tuned by adjusting the position of the mass along the threaded rod. The coil spring TVA is proposed by Ryan *et al.* [27] and Buhr *et al.* [28]. It is a mass connected to a helical spring, which was fixed to a gear train through a collar. The mass was supported by a linear bearing and moved horizontally along the guide rod. The stiffness of the absorber was changed by adjusting the number of active coils of

the spring. This can be achieved by rotating the spring through the collar using a motor attached to the end of the gear train. The TVA studied by Long *et al.* [29] consists of a mass placed between two rubber bellows. The stiffness of the TVA can be changed by adjusting the air pressure in the bellows. Nagaya *et al.* [30] developed a tunable absorber as a cantilever beam with a lumped mass attached to the free end of the beam. The beam was also held by a support at its centre. A motor was used to change the position of the support, resulting in a change in the stiffness.

The change in stiffness can be achieved by adjusting the shape of the absorber, for example by varying the distance between the two parallel beams of the TVA [31, 32]. The TVA proposed by Walsh and Lamancusa [31] consists of two masses and two leaf springs made of sheet metal. The two ends of the leaf springs were fixed to the two masses. Varying the gap between the two springs by using a motor results in a change in the stiffness of the TVA. Bonello *et al.* [33] used piezoelectric actuators to change the shape of the TVA. The stiffness elements of the TVA were two curved beams made of piezo-ceramic layer sandwiched between a thick aluminium layer and a thick steel plate. Two parallel curved beams were placed between the absorber mass and the base. The shape of the two beams can be altered by adjusting the voltage applied to the piezoelectric material fitted to the beams. However, the methods involving actuating mechanisms often show slow tuning times.

Adjusting the properties of the TVA without any mechanical movement is another strategy for stiffness change. Baz *et al.* [34], Williams *et al.* [35] and Rustighi *et al.* [36] used shape memory alloy (SMA) as a stiffness element. The elastic modulus depends on temperature so the stiffness can be changed by adjusting its temperature. The shape memory alloy TVA proposed in [36] was an aluminium beam to which a set of SMA wires is fitted. Varying the current applied to the SMA wire could heat up and cool down the SMA and hence vary its stiffness. However a long response time, at least 50 s in the TVA designed by Rustighi *et al.* [36], is a major limitation of using an SMA element.

Smart materials, e.g. electro-rheological (ER) and magneto-rheological (MR) fluids, might overcome this limitation because their properties have a fast response time, of the order of milliseconds, to a change in an external field [37]. The adjustable

properties of ER fluids have been the subject of many studies. For example ER fluids were used to incorporate a variable stiffness element in a boring tool, which is a cantilever bar, in the work of Min and Renyuan [38]. The ER fluid was sandwiched between two electrodes fixed to the bar. The electrodes were used to generate the electric field applied to the ER fluid and hence to change the stiffness of the bar.

More recently, adaptive TVAs (ATVAs) exploiting the changeable pre-yield properties of MR fluids have been developed. Ginder *et al.* [39] and Deng *et al.* [40] designed an ATVA using an MR elastomer. In [39] the TVA was a mass-spring system placed in the air gap of a U-shaped steel base. The mass was connected to the base through an MR elastomer, which behaves as a spring. The stiffness was changed by altering the magnetic field generated by a coil wound around one arm of the steel base. The ATVA showed a variation of the natural frequency of about 22%. The ATVA in [40] had a similar shape to that in [39], but its relative natural frequency could be changed up to 147%. Instead of using an MR elastomer, Albanese and Cunefare [41] employed MR silicon gel as a variable stiffness spring placed in the small air gap of a steel toroid. By changing the current flowing through the coil placed around the toroid, the stiffness and hence the natural frequency was changed. However, the steel base configuration was usually large and heavy; as a result, its application might be limited to only large host structures. A sandwich beam configuration was studied by Yalcintas and Dai [42]. The two outer elastic layers of length 381 mm and width 25.4 mm were made of aluminium strips. The middle layer contained MR fluid. The magnetic field was generated by permanent magnets and adjusting the distance between these magnets by using a simple screw mechanism resulted in the change in the stiffness of the TVA. However it is difficult to change the magnetic field strengths of permanent magnets continuously.

Although ways of changing the stiffness have been studied widely, the challenge is to change stiffness in real-time. This can be achieved by the inclusion of a control system. The ATVA with adaptive-passive control, like the passive TVA, requires no external energy at the excitation frequency unlike an active system. Instead of producing a control signal to drive an actuator, an ATVA generates a control signal to change the properties such as the stiffness of the ATVA.

The adaptive-passive control of the ATVA has been discussed in a number of studies. One of the control algorithms involves utilizing the phase between the accelerations or velocities of the absorber mass and the host structure. As the tuned condition of the undamped ATVA occurs when this relative phase is 90°, the controller employs the cosine of this relative phase ($\cos\phi$) as an error signal and aims to drive this signal to zero. Various control laws, i.e. proportional (P), proportional-plus-derivative (PD) and fuzzy control, have been studied using this technique. Kidner and Brennan [32] applied simple P control and fuzzy control to a beam-like neutralizer, whose stiffness can be varied by changing the beam geometry. The performances of two controllers were reported and compared. Although both controllers worked effectively, the fuzzy control gave better performance, i.e. smaller steady state error. Later, Rustighi *et al.* [43] investigated the performance of four different controllers, i.e. non-linear P, non-linear PD, fuzzy and continuous controllers. These controllers were implemented on a shape memory alloy ATVA and the PD controller showed the best performance. One of the reasons for this is the presence of the derivative term. This term improves the stability of the system by adding damping to the controller. This PD controller was also successfully applied to the variable shape ATVA presented in [33].

1.3 Motivation of the Thesis

This thesis concerns ATVAs, in particular ATVAs utilising MR fluid in the pre-yield state. The motivation is to develop a self-tuning TVA, which can rapidly re-tune to accommodate change in the excitation.

MR fluids have received increasing attention in many applications due to their ability to respond rapidly to a change in magnetic field and their reversible properties. There has been a significant amount of research on the applications of MR fluid in mechanical devices, for example dampers [44–46], brakes [47, 48], clutches [49, 50], and isolators [51, 52]. However, few devices, especially ATVAs in the pre-yield state, have exploited the controllable properties of MR fluids. A review of such ATVAs has been given previously [39–42] and it was shown that the designs of TVAs with

MR fluid to date have been limited to a large and heavy steel base configuration. This is due to the strong magnetic field requirement for changing properties of MR fluid. In this thesis, an alternative design, which is a sandwich beam ATVA made of lightweight material and with an MR fluid core, is presented to address this limitation. However, the challenge for the beam-like ATVA is to achieve a wide effective tunable frequency range and to be able to self-tune.

1.4 Objectives and Scope of the Thesis

The objectives of this thesis are:

- To design and construct a narrow-band ATVA which exploits the changeable pre-yield properties of MR fluids. This ATVA is called the MR fluid-filled ATVA.
- To model the dynamic vibrations of the MR fluid-filled ATVA, which is a non-uniform three-layer beam with electromagnets attached to the outer layers, using the finite element (FE) method.
- To model the pre-yield shear modulus for MR fluid used in the thesis as a function of magnetic field.
- To model the strength of magnetic field by the electromagnets.
- To verify the models for vibrational characteristics of the MR fluid-filled ATVA for various magnetic field strengths experimentally.
- To implement an adaptive-passive control system and the MR fluid-filled ATVA.
- To investigate the MR fluid-filled ATVA and its control numerically and experimentally.

1.5 Contributions of the Thesis

This thesis makes the following contributions:

- Designs of a sandwich beam ATVA using MR fluids and its electromagnets.
- Application of the FE method to predict the dynamic vibration of an MR fluid-filled ATVA for various magnetic field strengths.
- Development of empirical models for the shear modulus of MR fluid used in the thesis.
- Numerical investigation of dynamic vibration and tunable performance of the MR fluid-filled ATVA.
- Experimental verification of theoretical models for the characteristics of the MR fluid-filled ATVA.
- Numerical and experimental investigation of the self-tuning ability of the MR fluid-filled ATVA.

1.6 Contents of the Thesis

The next chapter describes the theoretical aspects of the dynamics of the TVA and develops a model for the TVA using a two degree-of-freedom model. Also the tuning strategy of the TVA is introduced. Preliminary investigations of the performance of the beam-like configuration of the TVA using the Mead and Markus model are described.

Chapter 3 introduces MR fluids and describes their behaviour in response to an applied magnetic field. The method used for measuring the pre-yield shear modulus of MR fluid is described and measured results as a function of magnetic field are reported. Also empirical models for the fluid used later are proposed.

Chapter 4 presents a numerical method, i.e. the FE method, to model the vibration of the three-layer beam for various magnetic field strengths. The FE model for a uniform sandwich beam is also validated by the analytical Mead and Markus model.

Chapter 5 describes the designs of the MR fluid-filled ATVA and the electromagnets used to apply a magnetic field to the ATVA. Parametric studies are conducted

using the FE model proposed in Chapter 4 to investigate the influence of various geometric parameters on the performance of the MR fluid-filled ATVA.

In Chapter 6, the FE model for the MR fluid-filled ATVA together, with the empirical model for the shear modulus of MR fluid and the simple model for the magnetic field, are verified and the characteristics of the MR fluid-filled ATVA are investigated experimentally. The experimental procedures are described and the measured point frequency response functions are reported and compared with the predictions.

In Chapter 7, the MR fluid-filled ATVA is integrated with adaptive-passive control to investigate the self-tuning behaviour of the ATVA numerically and experimentally. The control algorithm developed in [29, 43] is implemented.

Chapter 8 concludes the main findings and presents recommendations for further study.

Chapter 2

Tuned Vibration Absorber

2.1 Introduction

In chapter 1 it was seen that the tuned vibration absorber (TVA) has been a widely used method for vibration control. TVAs with variable stiffness are tunable. In this chapter the vibrations of the TVA are reviewed and issues concerning tuning are considered. First the simple mass-spring system is considered, then attention is focused on a three-layer beam TVA described by the Mead and Markus model.

2.2 Tuned Vibration Absorber

The conventional approach to investigate the characteristics of the TVA concerns the vibration analysis of the host structure with the TVA attached. For a simple analysis, this combined system is often considered as a 2 degree-of-freedom (DOF) system, whose vibrations can be obtained by solving the equations of motion. The equations are derived and discussed in this section.

2.2.1 Undamped Tuned Vibration Absorber

The undamped TVA is simply a mass-spring system attached to the host structure as shown in Fig. 2.1. In the case considered the host structure alone is modelled as a single degree-of-freedom (SDOF) system whose equation of motion is given by

$$m_1\ddot{x}_1 + k_1 x_1 = f \tag{2.1}$$

where m_1, k_1 and f are the mass and the stiffness of the host structure and the excitation force respectively. Assuming harmonic motion, i.e. $x_1 = X_1 e^{\mathrm{i}\omega t}$ and $f = Fe^{\mathrm{i}\omega t}$, the receptance of the host structure is

$$\frac{X_1}{F} = \frac{1}{k_1} \frac{1}{1-\Omega_1^2} \tag{2.2}$$

where $\Omega_1 = \frac{\omega}{\omega_1}$ and $\omega_1 = \sqrt{\frac{k_1}{m_1}}$, which is the natural frequency of the host structure. With the absorber attached to the host structure, the equations of motion of the host structure and undamped absorber are given respectively by

$$m_1\ddot{x_1} + (k_1 + k_a)x_1 - k_a x_a = f \tag{2.3}$$

$$m_a\ddot{x_a} - k_a x_1 + k_a x_a = 0 \tag{2.4}$$

where m_a and k_a are the mass and the stiffness of the absorber. Assuming harmonic motion, the receptances of the host structure and the absorber respectively are

$$\frac{X_1}{F} = \frac{1}{k_1} \frac{1-\Omega_a^2}{1-\Omega_a^2+\Omega_1^2\left[\Omega_a^2-(1+\mu)\right]} \tag{2.5}$$

$$\frac{X_a}{F} = \frac{1}{k_1} \frac{1}{1-\Omega_a^2+\Omega_1^2\left[\Omega_a^2-(1+\mu)\right]} \tag{2.6}$$

where $\Omega_a = \frac{\omega}{\omega_a}$, $\omega_a = \sqrt{\frac{k_a}{m_a}}$ is the natural frequency of the absorber and $\mu = \frac{m_a}{m_1}$ is the mass ratio. Note that the receptance of the host structure is zero at the frequency $\omega = \omega_a$, the tuned frequency of the absorber. This frequency can be tuned by varying either the mass or the stiffness of the TVA. The tuned frequency increases with increasing the stiffness or decreasing the mass of the TVA.

The frequency response functions (FRFs) of the host structure with and without absorber attached are shown in Fig. 2.2 for the case where $\omega_a = \omega_1$. They are simulated using parameters shown in Tab. 2.1. It can be seen from the dashed line that the original structure experiences excessive vibration when the excitation frequency ω is coincident with the natural frequency of the structure, ω_1. The vibration at this frequency can be reduced to zero when the undamped TVA, whose natural frequency

is tuned to the resonance frequency of the structure, is attached as shown in Fig. 2.2. However, this introduces a resonance peak below and above the tuned frequency of the TVA. As a result the undamped TVA is not effective at reducing vibration over a wide range of frequencies.

2.2.2 Damped Tuned Vibration Absorber

In broadband applications, the TVA is generally damped with an appropriate damping level. If the structural damping is incorporated in the TVA, the equations of motion of the host structure and the damped TVA can be obtained by replacing k_a in Eqs. (2.3-2.4) by $k_a(1+\mathrm{i}\eta_a)$, i.e.

$$m_1\ddot{x_1} + [k_1 + k_a(1+\mathrm{i}\eta_a)]x_1 - k_a(1+\mathrm{i}\eta_a)x_a = f \tag{2.7}$$

$$m_a\ddot{x_a} - k_a(1+\mathrm{i}\eta_a)x_1 + k_a(1+\mathrm{i}\eta_a)x_a = 0 \tag{2.8}$$

where η_a is the loss factor of the TVA. Assuming harmonic motion, the receptance of the host structure and the damped TVA are given respectively by

$$\frac{X_1}{F} = \frac{1}{k_1}\,\frac{1-\Omega_a^2+\mathrm{i}\eta_a}{1-\Omega_a^2+\mathrm{i}\eta_a+\Omega_1^2\left[\Omega_a^2-(1+\mu)-\mathrm{i}\eta_a(1+\mu)\right]} \tag{2.9}$$

$$\frac{X_a}{F} = \frac{1}{k_1}\,\frac{1+\mathrm{i}\eta_a}{1-\Omega_a^2+\mathrm{i}\eta_a+\Omega_1^2\left[\Omega_a^2-(1+\mu)-\mathrm{i}\eta_a(1+\mu)\right]}. \tag{2.10}$$

If the TVA has viscous damping, the equations of motion can be written by replacing $\mathrm{i}\eta_a k_a$ with $\mathrm{i}2\zeta\omega m_a\omega_a$ where $\zeta = \frac{c_a}{2m_a\omega_a}$ is the damping ratio and c_a is the damping coefficient of the TVA.

The effect of adding damping to the TVA for the case where $\omega_a = \omega_1$ is shown in Fig. 2.3, which is simulated using parameters shown in Tab. 2.1. It can be seen that with the presence of finite damping in the TVA (i.e. $\zeta = 0.2$), the response of the host structure can be reduced over a wide range of frequencies, but the receptance of the host structure is not zero at $\omega = \omega_a$. Also if the damping of the TVA is too high, for example the infinitely damped system as shown in Fig. 2.3 (dotted line), the combined 2DOF system is reduced to a SDOF system because the masses of the

host structure and TVA are in essence fixed together, and hence one resonance peak is introduced [11]. Therefore, it can be inferred that the level of damping affects the effectiveness of the TVA.

The effective bandwidth of the TVA can be increased if the damped TVA is optimally tuned. One way of tuning the TVA is using the equal-peak method [11]. It can be seen from Fig. 2.3 that all three curves intersect at two points A and B, which are independent of damping. The equal-peak method aims to set the magnitudes at these two points being equal and this occurs when [11]

$$\omega_a = \frac{\omega_1}{1+\mu}. \tag{2.11}$$

The optimum damping in the TVA is selected such that the curve of the FRF passes horizontally through either A or B. For the case of Eq. (2.11), the optimum damping is found to be [11]

$$\zeta^2 = \frac{3\mu}{8(1+\mu)} \tag{2.12}$$

and hence the magnitude at the two points A and B is [11]

$$\left|\frac{X_1}{F}\right| = \frac{1}{k_1}\sqrt{1+\frac{2}{\mu}}. \tag{2.13}$$

The receptance of the host structure with the optimally damped TVA simulated using parameters shown in Tab. 2.2 is shown in Fig. 2.4 (solid line). It can be seen that the performance improves when the TVA is optimally tuned.

2.2.3 Tuning of the Narrow-Band TVA

The TVA considered in this thesis is used for narrow-band applications. It must be precisely tuned to the disturbance frequency to be effective at reducing vibration at this frequency. However small damping is always present in the TVA and degrades its effectiveness. In this subsection, the tuning of the narrow-band TVA concerning the phases of the host structure and the TVA is described and the effect of damping on its performance is investigated.

For simplicity the host structure is assumed to behave as a simple mass, and hence the receptances of the mass-like host structure and the absorber in Eqs. (2.9-2.10) reduce to

$$\frac{X_1}{F} = \frac{1}{\omega^2 m_1} \frac{1 - \Omega_a^2 + \mathrm{i}\eta_a}{\Omega_a^2 - (1+\mu) - \mathrm{i}\eta_a(1+\mu)} \tag{2.14}$$

$$\frac{X_a}{F} = \frac{1}{\omega^2 m_1} \frac{1 + \mathrm{i}\eta_a}{\Omega_a^2 - (1+\mu) - \mathrm{i}\eta_a(1+\mu)}. \tag{2.15}$$

Note that when the TVA is tuned such that $\omega = \omega_a$, the receptance of the host structure is not zero due to damping in the TVA. The effects of damping on the receptances of the host structure and the absorber are also shown in Figs. 2.5(a) and 2.6(a) respectively. They are simulated using parameters shown in Tab. 2.1, but $k_1 = 0$. It can be seen from both figures that the damping has influence mainly around the resonance and anti-resonance frequencies. Increasing damping decreases the amplitude around resonance, but increases that around anti-resonance.

For the receptance of the host structure with the undamped TVA shown in Figs. 2.5 (solid line), the resonance frequency at which the receptance tends to infinity is the natural frequency of the combined 2DOF system. It is given by

$$\omega_r = \omega_a \sqrt{1+\mu}. \tag{2.16}$$

It can be seen from Eq. (2.14) that at low frequencies, i.e. when $\Omega_a << 1$, the receptance of the host structure reduces to

$$\frac{X_1}{F} = \frac{1}{-\omega^2(m_1 + m_a)} \tag{2.17}$$

i.e. that of the sum of the two masses. At high frequencies, i.e. when $\Omega_a >> 1$, the receptance in Eq. (2.14) can be expressed as

$$\frac{X_1}{F} = \frac{1}{-\omega^2 m_1} \tag{2.18}$$

i.e. that of the host mass, the absorber stiffness acting as an isolator. By Eqs. (2.14) and (2.15), the phases of the host structure and the absorber are given respectively

by

$$\angle\frac{X_1}{F} = tan^{-1}\left(\frac{\eta_a}{1-\Omega_a^2}\right) - tan^{-1}\left(\frac{-\eta_a(1+\mu)}{\Omega_a^2-(1+\mu)}\right) \tag{2.19}$$

$$\angle\frac{X_a}{F} = tan^{-1}(\eta_a) - tan^{1}\left(\frac{-\eta_a(1+\mu)}{\Omega_a^2-(1+\mu)}\right). \tag{2.20}$$

Hence the phase difference between receptance of the host structure and the absorber is given by

$$\phi = \angle\frac{X_1}{F} - \angle\frac{X_a}{F} = tan^{-1}\left(\frac{\eta_a}{1-\Omega_a^2}\right) - tan^{-1}(\eta_a). \tag{2.21}$$

Eq. (2.21) can be rewritten in the form

$$\tan(\phi) = \frac{\Omega_a^2\eta_a}{(1+\eta_a^2)-\Omega_a^2}. \tag{2.22}$$

It can be seen from Figs. 2.5(b) and 2.6(b) that the phases of the host structure and absorber masses change rapidly at the anti-resonance and resonance frequencies. However increasing damping decreases the rate of the phase change at both frequencies. It also can be seen that at low frequencies, these two masses move in-phase with each other, however, at high frequencies they move 180 degrees out of phase.

The cosine of the phase difference between the displacements of the host structure and the TVA simulated using parameters shown in Tab. 2.1 with $k_1 = 0$ is shown in Fig. 2.7(b). One way of tuning the natural frequency of the TVA to the disturbance frequency is to tune $\cos\phi$ to zero. As for the undamped TVA, $\omega = \omega_a$ and the receptance of the host structure is minimum when $\cos\phi = 0$ as shown in Fig. 2.7(a) and (b) (solid line). However tuning $\cos\phi$ to zero is not an optimal tuning when the damping of the TVA is considered because the receptance of the host structure is not minimum, but is equal to

$$\left|\frac{X_1}{F}\right|_{90^\circ} = \frac{1}{\omega^2 m_1}\ \frac{1}{\sqrt{1+\mu^2/\eta_a^2}}. \tag{2.23}$$

Eq. (2.23) can be obtained by substituting the frequency when $\cos\phi = 0$ or when $\phi = 90^\circ$, i.e.

$$\Omega_{90^\circ}^2 = (1+\eta_a^2) \tag{2.24}$$

derived from Eq. (2.22) into Eq. (2.14). Hence the attenuation that can be attained using the TVA tuned such that $\cos\phi = 0$ can be determined as

$$A_t^{90^\circ} = \frac{1/\omega^2 m_1}{1/(\omega^2 m_1\sqrt{1+\mu^2/\eta_a^2})} = \sqrt{1+\mu^2/\eta_a^2}. \tag{2.25}$$

In the case of optimum tuning, the minimum receptance of the host structure occurs when

$$\frac{d\left(\left|\frac{X_1}{F}\right|^2\right)}{d(\Omega_a^2)} = 0. \tag{2.26}$$

Solving Eq. (2.26) for the frequency ratio Ω_a when the receptance of the host structure is minimum gives

$$\Omega_a^2 = \left(1+\frac{\mu}{2}\right)\left(1+\eta_a^2\right) \pm \frac{1}{2}[\mu+(2+\mu)\eta_a^2]\left[1+\frac{4\eta_a^2}{\left[\mu+(2+\mu)\eta_a^2\right]^2}\right]^{1/2}. \tag{2.27}$$

By applying a first-order Taylor series expansion in η_a to Eq. (2.27), the minimum and maximum receptances occur approximately at

$$\Omega_{min}^2 \approx 1 - \frac{\eta_a^2}{\mu+(2+\mu)\eta_a^2} \tag{2.28}$$

$$\Omega_{max}^2 \approx 1+\mu+(2+\mu)\eta_a^2 + \frac{\eta_a^2}{\mu+(2+\mu)\eta_a^2}. \tag{2.29}$$

Substituting the frequency ratio Ω_a from Eq. (2.28) into Eq. (2.14) gives the amplitude of the receptance when the TVA is optimally tuned as

$$\left|\frac{X_1}{F}\right|_o = \frac{1}{\omega^2 m_1}\left[\frac{\eta_a^2+[\mu+(2+\mu)\eta_a^2]^2}{\eta_a^2+[(\mu+1)^2+\mu^2/\eta_a^2][\mu+(2+\mu)\eta_a^2]^2+2\mu[\mu+(2+\mu)\eta_a^2]}\right]^{1/2}. \tag{2.30}$$

Hence, the optimum attenuation is given by

$$A_t^o = \left[\frac{\eta_a^2+[(\mu+1)^2+\mu^2/\eta_a^2][\mu+(2+\mu)\eta_a^2]^2+2\mu[\mu+(2+\mu)\eta_a^2]}{\eta_a^2+[\mu+(2+\mu)\eta_a^2]^2}\right]^{1/2}. \tag{2.31}$$

The optimum attenuation of the host structure as a function of loss factor for various mass ratios is shown in Fig. 2.8. It can be seen that the attenuation decreases

with increasing damping in the TVA. However increasing the mass ratio increases the attenuation. Fig. 2.9 shows the ratio of the attenuation when the TVA is tuned such that $\phi = 90^\circ$ shown in Eq. (2.25) to the attenuation when optimally tuning shown in Eq. (2.31). Note that the differences are generally small. Also it can be seen that as the damping in the TVA increases, the effect of mistuning increases, i.e. the attenuation ratio decreases. However increasing the mass ratio reduces the effect of mistuning.

2.3 Three-Layer Beam TVA

As an alternative to the spring-mass system of Fig. 2.1, a TVA is often implemented as a beam in bending with the first bending mode acting as the spring mass system. The TVA implemented in this thesis is a three-layer beam attached at its centre to the host structure as shown in Fig. 2.10. It consists of elastic outer layers and a linear viscoelastic core. The outer layers are assumed to undergo bending and longitudinal extension, while the middle layer experiences shear deformation. In this thesis the middle layer of the TVA contains magneto-rheological (MR) fluid. The three-layer TVA is a narrow-band device, but can be tuned over a range of frequencies to increase the usable frequency range. The tuning can be done by changing the shear stiffness of the device, by varying the shear properties of the MR fluid in the core. Hence the shear properties of the fluid before it yields are of interest. Detailed analysis is presented in Chapter 4 and Appendix A using finite element and Mead and Markus models. Here a simple static analysis is presented to explore the change in stiffness that might potentially be achieved, so as to indicate the order of magnitude of the tunable range.

The analysis of the three-layer TVA is based on the sandwich beam theory of Mead and Markus [53]. In this theory a static analysis is preformed to estimate the stiffness of the beam and hence how the stiffness can be changed by changing the shear modulus of the core. Also for simplicity, it is assumed that half of the free-free beam shown in Fig. 2.10 behaves as a cantilever beam excited by external force Q at its end as shown in Fig. 2.11. The equation of motion for the transverse displacement

W of the three-layer beam is derived in Appendix A and is given by [53]

$$\frac{d^6W}{dx^6} - g(1+Y)\frac{d^4W}{dx^4} = 0 \tag{2.32}$$

where the shear parameter g and the geometric parameter Y are given by

$$g = \frac{G}{h_2}\left(\frac{E_1h_1 + E_3h_3}{E_1h_1E_3h_3}\right) \tag{2.33}$$

$$Y = \frac{H^2}{D_t}\left(\frac{E_1h_1E_3h_3}{E_1h_1 + E_3h_3}\right) \tag{2.34}$$

and D_t and H are

$$D_t = \frac{E_1h_1^3}{12} + \frac{E_3h_3^3}{12} \tag{2.35}$$

$$H = h_2 + \frac{1}{2}(h_1 + h_3). \tag{2.36}$$

Here G, E, and h are the shear modulus in the middle layer, the Young's modulus and the thickness respectively. The subscripts $_{1,2,3}$ represent the top, the middle and the bottom layers respectively.

Eq.(2.32) has solution in the form of

$$W(x) = C_1 + C_2x + C_3x^2 + C_4x^3 + C_5e^{sx} + C_6e^{-sx} \tag{2.37}$$

where $C_1 - C_6$ are constants, and where

$$s = \sqrt{g(1+Y)}. \tag{2.38}$$

The constants $C_1 - C_6$ can be determined from the six boundary conditions (Eqs. (A.40-A.42) and Eqs. (A.45-A.47) in Appendix A). However in this case, the shear force at the free end is $S(L) = -Q$, where L is the length of the beam. Substituting the six constants into Eq. (2.37) gives the solutions for the tip displacement as

$$W(L) = \frac{L^3Q}{3bD_t(1+Y)}\left\{1 + 3Y\left[\frac{sL - \tanh(sL)}{(sL)^3}\right]\right\}. \tag{2.39}$$

Hence, the stiffness of the beam is given by

$$k^b = \frac{Q}{W(L)} = \frac{3bD_t(1+Y)}{L^3\left\{1+3Y\left[\frac{sL-\tanh(sL)}{(sL)^3}\right]\right\}}. \tag{2.40}$$

It can be seen from Eq. (2.40) that when the shear parameter s is changed, only the term in the square brackets, i.e. $\left[\frac{sL-\tanh(sL)}{(sL)^3}\right]$, changes. This term becomes zero if the beam has an infinitely stiff shear core, and hence the maximum stiffness of the beam is given by

$$k^b_\infty = \frac{3bD_t(1+Y)}{L^3}. \tag{2.41}$$

The beam with an infinitely stiff core behaves as a single beam, i.e. the top and bottom layers will move as if they are connected together and bend about the neutral axis of the whole beam. Assuming that the top and bottom layers are made of the same material, i.e. $E_1 = E_3$, and have the same dimensions, i.e. $h_1 = h_3$, Eq. (2.41) reduces to

$$k^b_\infty = \frac{3E_1}{L^3}\left[2I_1 + 2A_1\left(\frac{H}{2}\right)^2\right] \tag{2.42}$$

where $I_1 = \frac{bh_1^3}{12}$ and $A_1 = bh_1$.

Consider the three-layer beam with zero shear stiffness in the middle layer, i.e. $s = 0$. The top and bottom beams will vibrate as if they are unconnected and they each bend about their own axis. The shear term in Eq. (2.40) becomes $\left[\frac{sL-\tanh(sL)}{(sL)^3}\right] = \frac{0}{0}$. To obtain the limit of this term, the l'Hopital's rule [54] is applied. The limit is found to be 1/3. Hence the stiffness of the beam becomes

$$k^b_0 = \frac{3bD_t}{L^3}. \tag{2.43}$$

If the outer layers are identical, Eq. (2.43) reduces to

$$k^b_0 = 6\frac{E_1I_1}{L^3}. \tag{2.44}$$

The effect of changing the shear modulus of the core on the stiffness of the three-layer TVA is shown in Fig. 2.12. Parameters used in the simulation are shown in

Tab. 2.3. It can be seen from Fig. 2.12 that if the shear modulus in the core can be changed from zero to a very high value, e.g. 10 GPa, the stiffness of the beam can be varied up to the order of 47 kN/m. However the shear modulus of the fluid used in the thesis can only be varied within a smaller range, i.e. between 2470 Pa and 4.33 MPa (see Chapter 3), which corresponds to a change in stiffness between 0.8 and 9 kN/m. Although in theory this might be the range of stiffness achievable, in practice it is limited by the ability to provide a magnetic field over the whole surface to the beam.

2.4 Conclusions

An undamped TVA is a narrow-band device used for suppressing the vibration of the structure at the specific forcing frequency. However this device can be damped with an appropriate level of damping to increase its effective bandwidth. The TVA considered in this thesis is a TVA with small damping designed for discrete frequency applications, however, its natural frequency is able to be tuned so that it can minimise vibration over a range of frequencies.

Expressions for the response and attenuation of vibration of a structure with a TVA attached have been derived using a 2DOF model. It was seen that damping in the TVA lowers the effectiveness of the device at the tuned frequency, but increasing the mass ratio can improve the performance of the TVA. A method for determining the tuned condition of the TVA was described. The natural frequency of a TVA can be tuned by adjusting the cosine of the relative phase between the host structure and the TVA to zero. Although this is not optimal tuning when the damping is present in the TVA, the performance of the TVA does not significantly deteriorate if the damping is small. This tuning strategy is implemented in real-time in Chapter 7.

In this chapter, the three-layer TVA using MR fluids has been discussed. The TVA can be tuned by changing the shear stiffness of the core. The expression for the stiffness was derived and the limits of changing stiffness of the TVA was investigated using a simple static analysis based on the Mead and Markus model. For the TVA with given dimensions and material properties shown in the simulation, its stiffness

can be potentially varied between 0.8 and 9 kN/m.

In this thesis, the non-uniform three-layer TVA is of interest. Its shear stiffness can be changed by varying the properties of MR fluid in the TVA. The way in which the properties of MR fluid can be altered will be presented in the next chapter and the vibration characteristics of the non-uniform TVA will be studied using the finite element (FE) method in Chapter 4.

Tables

Mass of the host structure	m_1	1 kg
Mass of the absorber	m_a	0.25 kg
Stiffness of the host structure	k_1	25 N/m
Stiffness of the absorber	k_a	6.25 N/m

Tab. 2.1: Properties of the 2DOF system.

Mass of the host structure	m_1	1 kg
Mass of the absorber	m_a	0.25 kg
Stiffness of the host structure	k_1	25 N/m
Stiffness of the absorber	k_a	4 N/m

Tab. 2.2: Properties of the 2DOF system consisting of the host structure and the optimally damped TVA.

Length	L	24.64 mm
Width	b	10.25 mm
Thickness of outer layers	$h_1 = h_3$	0.86 mm
Thickness of core	h_2	2.94 mm
Young's modulus of outer layers	$E_1 = E_3$	3.71×10^9 N/m^2

Tab. 2.3: Geometrical and material properties of the three-layer beam.

Figures

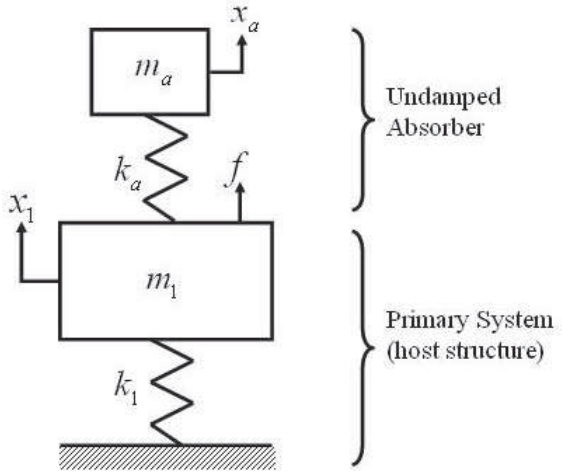

Fig. 2.1: Tuned vibration absorber attached to host structure.

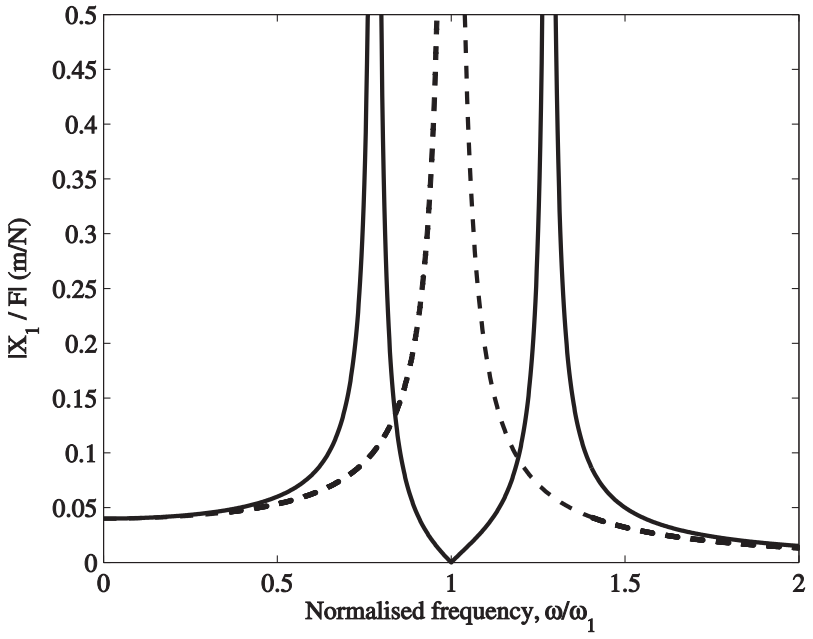

Fig. 2.2: Receptance of the host structure:--- without and — with undamped TVA.

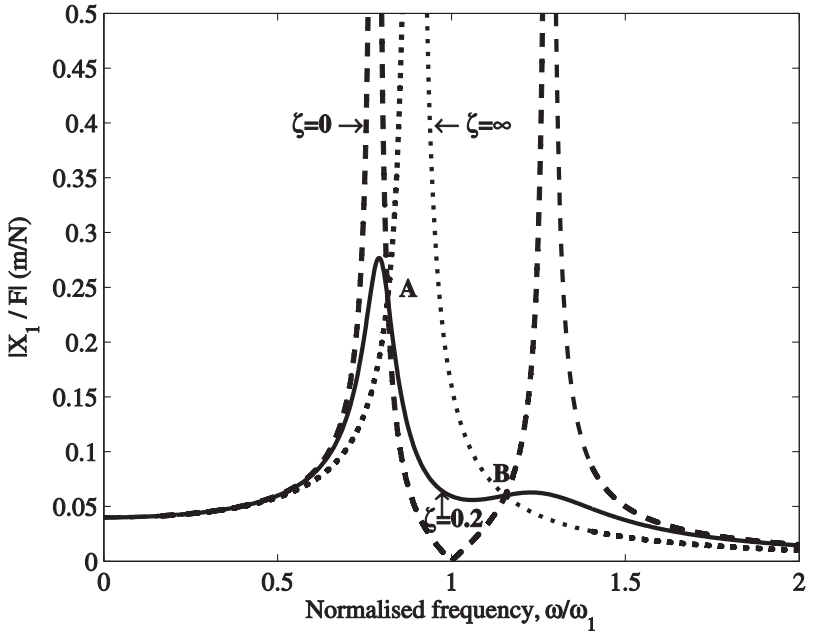

Fig. 2.3: Receptance of the host structure with TVA attached for $\omega_a = \omega_1$ and ζ is equal to:--- 0, — 0.2 and $\cdots$ ∞.

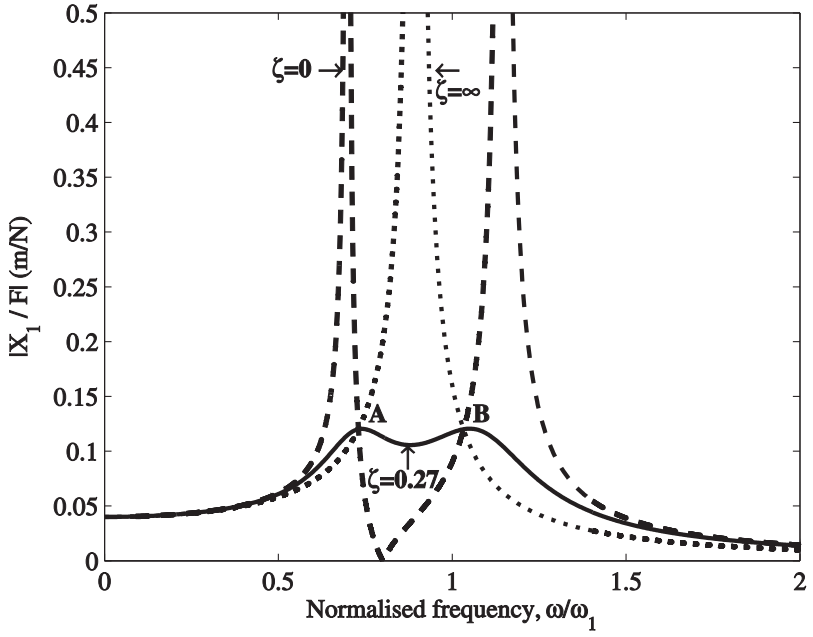

Fig. 2.4: Receptance of the host structure with TVA attached for $\omega_a = \frac{\omega_1}{1+\mu}$ and ζ is equal to:--- 0, — 0.27 and $\cdots$ ∞.

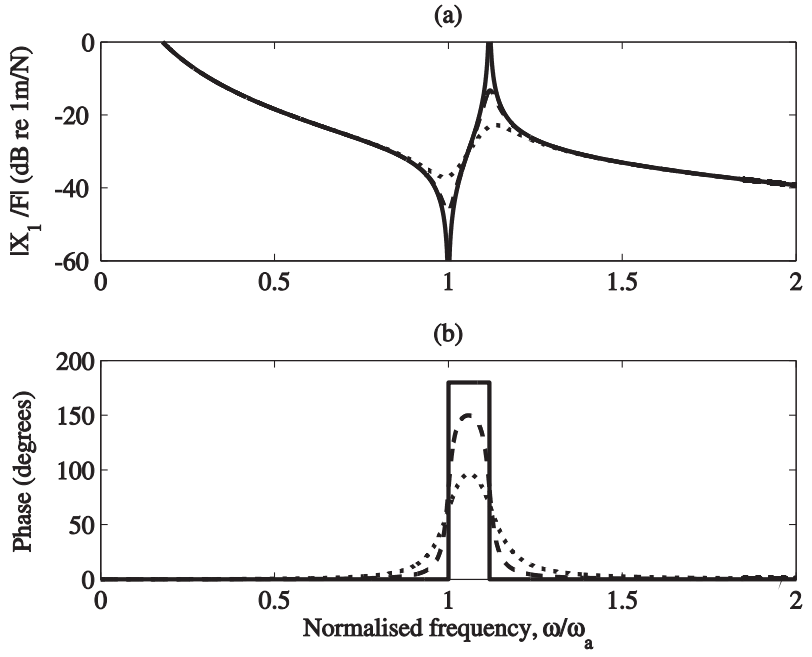

Fig. 2.5: Magnitude and phase of receptance of a mass-like host structure as a function of normalised frequency for η_a equal to:— 0, --- 0.03 and $\cdots$ 0.1.

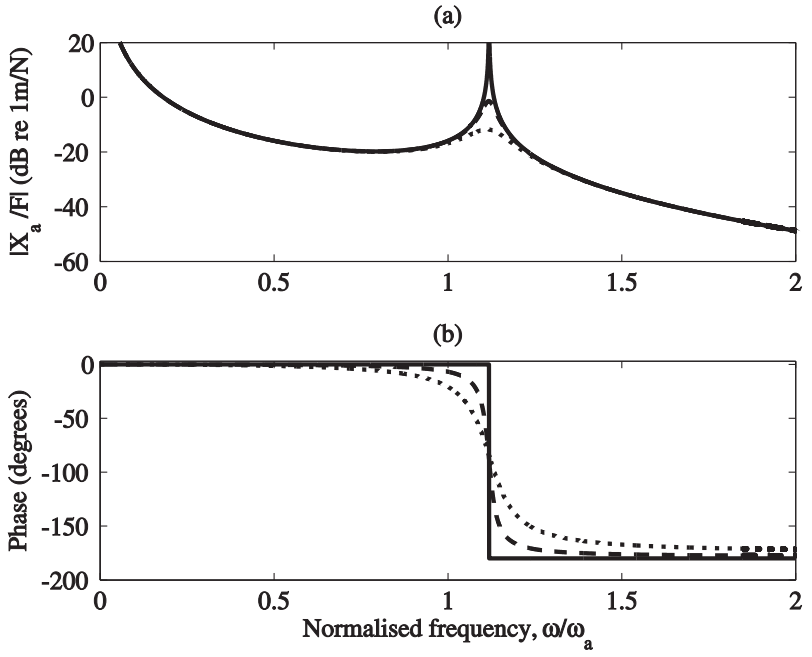

Fig. 2.6: Magnitude and phase of receptance of the TVA as a function of normalised frequency for η_a equal to:— 0, --- 0.03 and $\cdots$ 0.1.

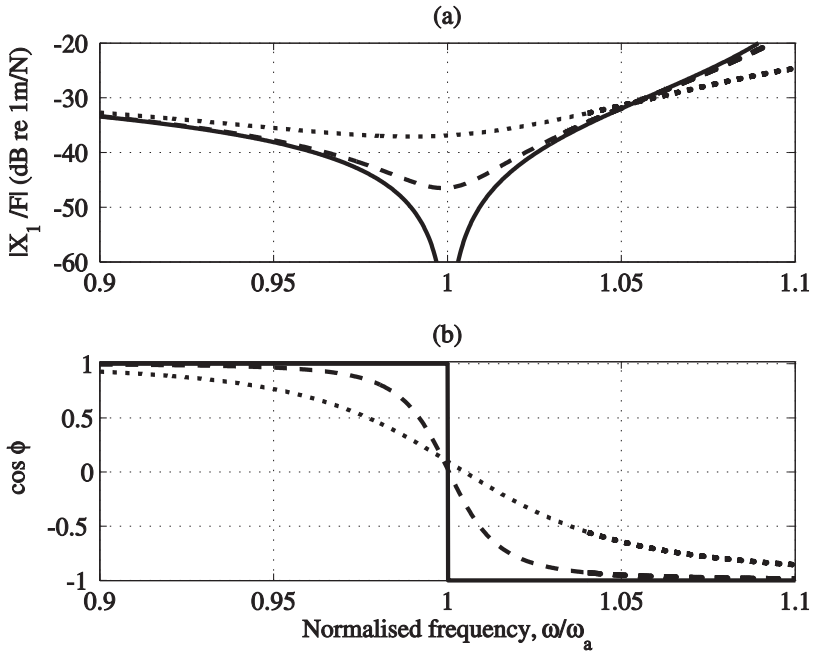

Fig. 2.7: Receptance of a mass-like host structure and the cosine of phase difference as a function of normalised frequency for η_a equal to:— 0, --- 0.03 and $\cdots$ 0.1.

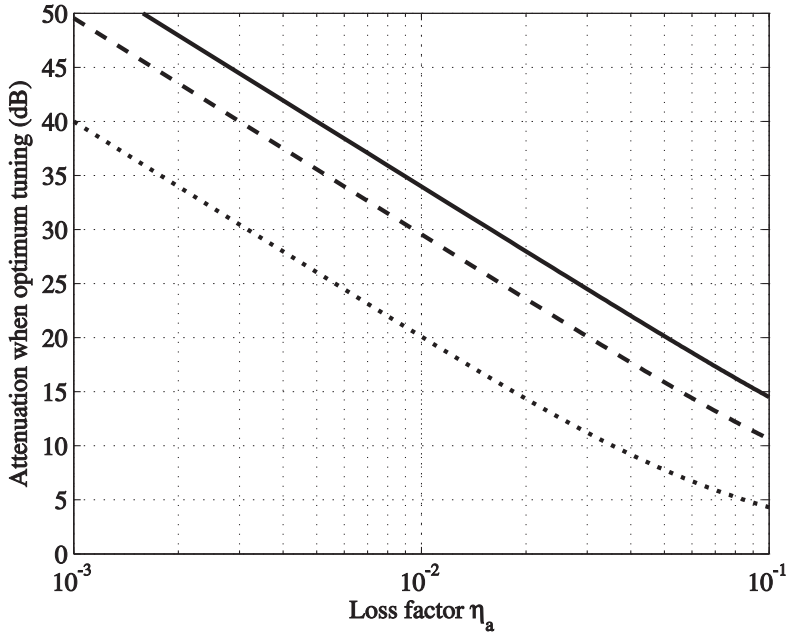

Fig. 2.8: Attenuation when optimum tuning of a mass-like host structure with TVA attached as a function of damping for μ equal to:$\cdots$ 0.1, --- 0.3 and — 0.5.

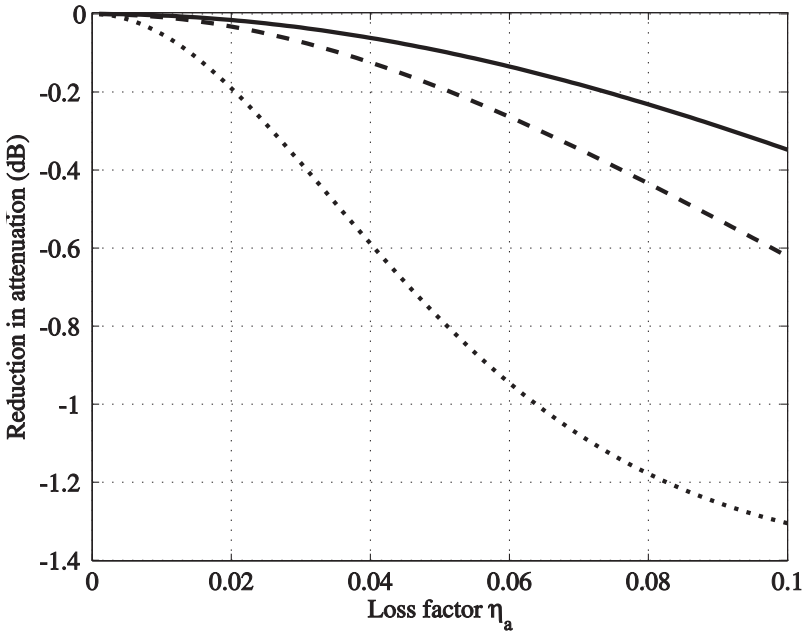

Fig. 2.9: Difference in attenuation between tuning criterion of $\phi = 90°$ and optimum tuning for a mass-like host structure with TVA attached as a function of damping for μ equal to:$\cdots$ 0.1, --- 0.3 and — 0.5.

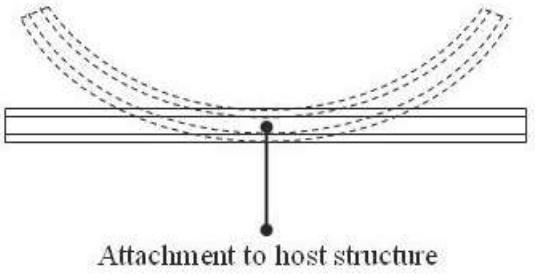

Fig. 2.10: Three-layer beam TVA.

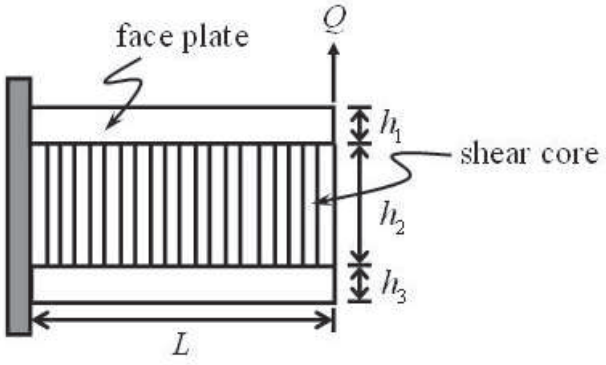

Fig. 2.11: Fixed-free three-layer TVA.

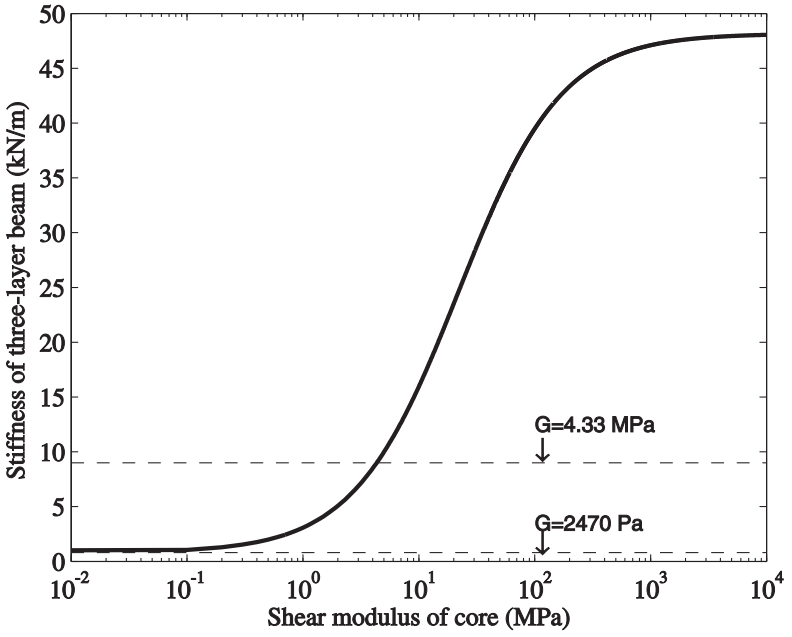

Fig. 2.12: The stiffness of the three-layer beam as a function of shear modulus in the core.

Chapter 3

Magneto-Rheological Fluids

3.1 Introduction

Magneto-Rheological (MR) and Electro-Rheological (ER) fluids are examples of smart materials whose physical properties can be changed by an external field. MR fluids are magnetic-field responsive fluids, while ER fluids respond to an electric field [37]. ER fluids were discovered before MR fluids and have attracted more attention since their discovery. However, the applications of ER fluids to commercial devices are somewhat limited. This is due, at least in the past, to limitations such as low yield stress, the requirement for a high voltage source, and sensitivity to contaminants [55]. Hence, currently attention is turned to MR fluids which might overcome those limitations and are of interest in this thesis.

MR fluids were discovered by Jacob Rabinow in 1948 [56]. For decades, they have been the subject of much research since their properties can be rapidly changed in response to an applied magnetic field and they return to the original state when the magnetic field is removed. Also, they can provide high values of yield stress and pre-yield storage modulus, which are several orders of magnitude greater than those obtained from ER fluids [57].

In this thesis, the MR fluid is integrated to an adaptive tuned vibration absorber (ATVA). The composition of MR fluids for the ATVA is described in Chapters 2 and 5. This ATVA allows the MR fluid to strain below the yield strain, hence only the tunable shear stiffness of the fluid in the pre-yield state is of interest in this thesis. Typically the pre-yield shear stiffness is represented by a complex shear

modulus. The shear modulus of MR fluids has been experimentally investigated by various researchers e.g. [57–60]. However, there is no published data for the pre-yield properties of the MR fluid (MRF-140CG, LORD Corporation) used in this thesis. Consequently, experiments on the fluid were conducted to measure the pre-yield shear modulus of the fluid.

Following this introduction, the structure of MR fluids is described and the pre-yield and post yield behaviour is presented. Section 3.3 reviews pre-yield properties, in particular the shear modulus, of MR fluids. Section 3.4 describes how the pre-yield complex shear modulus was measured and the experimental data is presented. Empirical models are given and compared with the measurements in section 3.5. Finally, section 3.6 contains some conclusions.

3.2 Structure and Properties of MR Fluids

MR fluids are suspensions of particles in an inert carrier liquid. These particles are generally micron-sized magnetic particles such as carbonyl iron powder [56], iron-cobalt alloy, iron-nickel alloys [61], and electrolytic iron powder [62]. The carrier liquid can vary widely, for example hydrocarbon oils, silicone oils, and water.

The formation of magnetic particles in response to an applied magnetic field has been described by Tao [63]. Without a magnetic field, the particles are randomly distributed in the fluid as shown in Figure 3.1(a). The particles in MR fluids form chains in the direction of a magnetic field after its application as shown in Figure 3.1(b). These chains are resistant to shear and the shear properties of MR fluids depend on the magnetic field. When a shear force is applied, the fluids deform with shear strain γ as shown in Figure 3.1(c), and when the fluids experience very large strain, they start to flow.

It is possible that the formation of the chains is not a single-chain structure. Tao [63] and Gulley and Tao [64] studied the structure formation in MR fluid and simulated the motion of particles. Their studies show that the structure of the chains depends on the duration of the application of the magnetic field. At the beginning of the application, the particles form many single chains. But a few seconds afterwards,

several single chains aggregate together and form a thick column structure as shown in Fig. 3.2. However, several analytical models to describe the behaviour of MR fluids have been developed based on a single-chain formulation. The models reported in literature are presented in section 3.3.

MR fluids may be characterised as viscoelastic materials, which exhibit both viscous and elastic behaviour. The viscoelastic properties of MR fluids have been experimentally investigated by Weiss *et al.* [57] and Li *et al.* [58]. It is shown in the work of Weiss *et al.* [57] that MR fluids present elastic behaviour when they experience small shear strain, which is less than the yield strain. The yield strain γ_y is defined as a strain level where the storage modulus of MR fluids has nonlinear behaviour and where the fluid starts to flow. As a result, the elastic behaviour can be called the pre-yield behaviour. The yield strain observed by Weiss *et al.* [57] was less than 1%, while the work of Li *et al.* [58] suggested a smaller value, which was not greater than 0.1%. In the pre-yield or elastic region, MR fluids exhibit linear behaviour as shown in Figure 3.3 and the behaviour in this region follows Hooke's law, i.e. $\tau = \frac{G}{\gamma}$, where τ is the shear stress.

The post-yield behaviour of MR fluids in the absence of a magnetic field can be modelled as a Newtonian fluid, which has zero yield stress and is given by [37, 65]

$$\tau = \eta_m \dot{\gamma} \tag{3.1}$$

where η_m and $\dot{\gamma}$ are the viscosity and strain rate respectively. However a yield stress τ_y is introduced when the magnetic field is applied to MR fluids, and the fluids behave more like a Bingham plastic model, which is [37, 65]

$$\tau = \tau_y + \eta_m \dot{\gamma}. \tag{3.2}$$

The yield stress necessary to break the chains and make the fluid flow is field-dependent. It increases with increasing magnetic field as shown in Figs. 3.3 and 3.4.

3.3 Pre-Yield Properties of MR Fluids

Not very much has been published concerning the linear viscoelastic (pre-yield) properties of MR fluids. Weiss *et al.* [57] experimentally investigated the viscoelastic properties of MR and ER fluids using oscillatory shear techniques. The measured storage modulus as a function of an applied external field was presented. The results showed that with the application of a 2000 Oersted magnetic field, the storage modulus exhibited by the MR fluid (MRX-I, LORD Corporation) was several orders of magnitude higher than that of ER fluid (ERX-III, LORD Corporation) with the application of a 3 kV/mm electric field. The yield stress as a function of strain was also presented. At an electric field of 3 kV/mm, the ER fluid had a static yield stress about 120 Pa, which was several orders of magnitude lower than that of the MR fluid with the application of a 2000 Oersted magnetic field.

Li *et al.* [58] conducted similar experiments to Weiss *et al.* [57] but used a different MR fluid, which was a suspension of reduced iron powders in silicone oil. In [58] the MR fluid with 10% volume fraction was studied by being strained up to 0.1%. It was shown that the measured storage and loss moduli increased with the magnetic field strength, while the measured loss factor decreased. Also the effect of particle concentration was observed. MR fluid with 15% volume fraction provided higher storage modulus, loss modulus and loss factor than that with 10% volume fraction.

Li *et al.* [60] studied the dependence of the dynamic behaviour of MR fluid on the strain amplitude and oscillatory driving frequency using the oscillatory shear method. The fluid used in this work was reduced iron powders in silicone oil with 40% volume fraction. Measurements were conducted on MR fluid with an applied magnetic field of 340 mT. It was observed that at very small strain amplitude of $\gamma \leqslant 0.1\%$, the storage and loss moduli were largely independent of strain amplitude and oscillatory driving frequency.

Several publications have presented analytical models for the pre-yield behaviour of MR fluids. Ginder *et al.* [66] reported an analytical model for the storage modulus G' and yield stress τ_y. With the application of a low magnetic field, the storage modulus and yield stress increase in proportion to the square of the magnetic field. However, with the application of a medium strength magnetic field, the models were

changed to the forms

$$G' = 3\phi_0\mu_0 M_s H \tag{3.3}$$

$$\tau_y = \sqrt{3}\phi_0\mu_0 M_s^{1/2} H^{3/2} \tag{3.4}$$

where ϕ_0, μ_0, H and M_s are the volume fraction of particles in the composite, the permeability of free space (i.e. $4\pi \times 10^{-7}$ H/m), magnetic field strength in A/m and saturate magnetization respectively. For an iron-based MR fluid $\mu_0 M_s$ is approximately equal to 2.1 T. However, by comparing with experimental data presented by Weiss *et al.* [57], the predicted modulus was about 10 times less than that measured experimentally. Also, in [66] the model for MR fluids, whose particles are completely saturated, are presented. In the model the saturated storage modulus G'_s and the saturated yield stress τ_{ys} are independent of magnetic field strength, and are given by

$$G'_s = 0.3\phi_0\mu_0 M_s \tag{3.5}$$

$$\tau_{ys} = 0.086\phi_0\mu_0 M_s^2. \tag{3.6}$$

Jolly *et al.* [67] derived an analytical model from the simple dipole model of particle energy interaction leading to

$$G = \frac{\phi_0 J_p^2}{2\mu_0\mu_1 h_g^3} \tag{3.7}$$

where μ_1, h_g, and J_p are the relative permeability of medium, the gap between the particles in a chain, and the average particle polarization density respectively. However, the model seems to underestimate the shear modulus when compared to the experimental data presented by Li *et al* [68]. The reason for this discrepancy is likely to be that this model assumed MR fluids have single-chain structures.

Later on, Harland [69] developed empirical models for storage modulus G' by fitting the data obtained from Weiss *et al.* [57, 70] giving

$$G' = 7.96 \times 10^5 \mathcal{H}^{1.65} + 4 \times 10^3 \tag{3.8}$$

where $\mathcal{H}$ is magnetic field strength given in Oersted (Oe)/mm.

In brief, as different types of MR fluids exhibit different shear response to the changes in the applied magnetic field, then the published experimental data cannot be applied to MR fluid (MRF-140CG) used in this thesis. Moreover, few analytical models for the pre-yield shear modulus of MR fluids have been published. In most cases, the analytical models have been developed based on the ideal-single-chain structure and these models provide less shear modulus than the measurements, so presumably these models are only suitable for low volume fraction MR fluids. Hence measurements of MR fluid (MRF-140CG) need to be taken and an empirical model for the shear modulus needs to be developed for the use of MR fluid in the ATVA.

3.4 Experimental Investigation into the Pre-Yield Shear Modulus of MR Fluids

The shear properties of materials can be measured by several testing methods, such as rotational shear tests and oscillatory shear tests, depending on the purpose of the tests. However, the oscillatory shear test was used in this chapter to measure the pre-yield complex shear modulus G of MR fluid (MRF-140CG). The test was conducted in the University of Wollongong, Australia by Dr. Weihua Li and Dr. Xianzhou Zhang and the results of which were reported by Hirunyapruk *et al.* [71]. The properties of the MR fluid given by the manufacturer are shown in Tab. 3.1.

3.4.1 Parallel-Plate Rheometer

The oscillatory shear test was performed using a parallel-plate rheometer (Physica rheometer MCR 301, Anton Paar Germany [72]) and employed the controlled shear deformation (CSD) method [65]. The measurement system is shown in Figure 3.5(a). The measurement system consists of three parts, a personal computer (PC), electronic controller and measuring unit. The measuring unit has a parallel plate configuration, which is equipped with a magneto-rheological device (MRD) shown in figure 3.5(b). The MRD is a coil wound around highly permeable material. It is used to generate a magnetic field across the gap where the MR fluid is placed. The magnetic field was generated by connecting the coil of the MRD to a current source. The magnetic

flux density across the gap can be measured by a tesla gauge (HT 100G, Shanghai Hengtong Magnetoelectricity Co., Ltd.). This can be done by placing a tesla probe with dimensions 0.4 mm thick and 2 mm wide in the free gap, which is the gap without MR fluid between the parallel plates. Then the magnetic flux density across the free gap B_f for various MRD currents I_r is measured. Since the relative permeability of air is 1 and that of the MR fluid is μ_m, the magnetic flux density across the gap with MR fluid is estimated to be $\mu_m B_f$. Fig. 3.5(c) shows a sketch of the parallel-plate geometry. The top plate has radius R_0. The distance between the top plate and the stationary bottom plate is d, which is about 0.4 mm.

As can be seen from Figure 3.5(a), the oscillations of the top plate are produced by a drive system. When the motor current I_m is applied to the drive system, a torque T_0 proportional to the motor current is produced and hence the top plate moves side to side at a steady speed by the torque. Since the bottom plate is stationary, the MR fluid placed in the gap between two plates is being sheared. The shear strain that the fluid experiences is constant across the gap, but varies with radial displacement r as [65]

$$\gamma_0(r) = \frac{r\theta_0}{d} \tag{3.9}$$

where γ_0 is the shear strain amplitude and θ_0 is the angular displacement or deflection angle. The deflection angle can be determined from the displacement of the rotor, which is detected by the incremental encoder. The angular resolution of the rheometer is 0.01 μrad. The shear stress exerted on the plate is also a function of radius r, and is given by

$$\tau_0(r) = G\gamma(r) = G\frac{r\theta_0}{d} \tag{3.10}$$

where $\tau_0(r)$ is the stress amplitude at radius r. The shear stress can be measured in terms of the total torque on the top plate, which is

$$T_0 = \int_0^{R_0} 2\pi r^2 \tau_0(r) \mathrm{d}r. \tag{3.11}$$

3.4.2 Control Shear Deformation Method

The control shear deformation (CSD) method is one of the operating modes of the rheometer. Using this method, the strain amplitude is set to the desired value. The top plate is subjected to harmonic torques and consequently it oscillates with an angular frequency ω_0. This causes the MR fluid to be strained. The actual strain is measured in terms of deflection angle θ_m and then the applied load is adjusted until the actual strain is equal to the desired value. It is assumed that the resulting shear strain is measured at the outer radius R_0, and is in the following form

$$\gamma = \gamma_0 \sin(\omega_0 t), \tag{3.12}$$

which corresponds to the applied harmonic shear stress

$$\tau = \tau_0 \sin(\omega_0 t + \delta) \tag{3.13}$$

where δ is the phase difference between stress and strain, and is such that $0^\circ \leqslant \delta \leqslant 90^\circ$. The corresponding stress and strain waveforms are presented in Fig. 3.6. The pre-yield shear modulus of the MR fluid measured at the edge of the top plate can be calculated from the amplitudes of the stress and strain and the phase difference between them, and is given by

$$G = \frac{\tau}{\gamma} = \frac{\tau_0}{\gamma_0}[\cos(\delta) + \mathrm{i}\ \sin(\delta)]. \tag{3.14}$$

The storage modulus G' is the real part and the loss modulus G'' is the imaginary part of the complex shear modulus, which are

$$G' = \frac{\tau_0}{\gamma_0}\cos\delta \tag{3.15}$$

$$G'' = \frac{\tau_0}{\gamma_0}\sin\delta \tag{3.16}$$

and the loss factor is

$$\eta = \tan\delta = \frac{G''}{G'}. \tag{3.17}$$

According to the studies of Li *et al.* [58, 59, 73], the shear modulus in the pre-yield regime does not depend significantly on the strain amplitude and driving frequency. Hence in this experiment, the angular driving frequency was set to 5 rad/sec, and the strain amplitude was fixed to 0.1 % to assure linear viscoelastic properties.

3.4.3 Results and Discussion

In this experiment, the shear modulus of MR fluid (MRF-140CG) was measured as a function of the MRD current I_r, which was varied from 0 to 1.75 A. To obtain the shear modulus as a function of the magnetic field, a Tesla gauge was used to measure the magnetic field across the gap between the two parallel plates and hence an empirical model for the magnetic flux density as a function of the MRD current was determined by a least square fitting method. The measured magnetic flux density and the empirical linear model of

$$B = 0.23 I_r \tag{3.18}$$

are compared in Fig. 3.7, where B is the magnetic flux density. Consequently, the measured storage and loss moduli as a function of magnetic field were obtained as shown in Fig. 3.8. The measured loss factor is shown in Fig. 3.9.

It can be seen from Fig. 3.8 (+) that the measured storage modulus changes gradually when the magnetic flux density is small and rapidly increases at moderate magnetic flux density, and then tends to a constant at very high magnetic flux density because of saturation. Although the measured storage modulus of MR fluid (MRF-140CG) used in this thesis shows the same trend as that presented in the work of Li *et al.* [73], its magnitude can be changed up to 4 MPa approximately, which is about 2 MPa less than that for MRF-132LD used in [73]. It is also shown in Fig. 3.8 that the measured storage modulus (+) is greater than the measured loss modulus (•).

Fig. 3.9 (+) shows that the measured loss factor decreases with increasing magnetic field applied except for only one point at zero magnetic field. This might be because the measurement is in error or the MR fluid might be flowing.

3.5 The Empirical Model for Pre-Yield Shear Modulus

Although analytical models for the storage modulus have been developed and presented by Ginder *et al.* [66] and Jolly *et al.* [67], these models do not agree well with the experimental results shown in Figs. 3.8 and 3.9. Therefore, empirical models for the pre-yield storage modulus and loss factor of the MR fluid used in this thesis will be used.

As shown in Fig. 3.8(+), the measured storage modulus starts from the zero magnetic field storage modulus G'_z and asymptotes to the saturated magnetic field storage modulus G'_∞ at high magnetic flux density B. This behaviour is similar to the inverted exponential of the form

$$G' = G'_z + (G'_\infty - G'_z)(1 - e^{-\alpha_1 B^{\alpha_2}}) \tag{3.19}$$

where α_1, α_2, G'_z and G'_∞ are empirical constants. Also shown in Fig. 3.9, the loss factor decreases with the applied magnetic field until it falls to about 0.02, and then it remains constant. This behaviour can also be characterised as

$$\eta = \eta_\infty + (\eta_z - \eta_\infty)e^{-\alpha_3 B^{\alpha_4}} \tag{3.20}$$

where $\alpha_3, \alpha_4, \eta_z$, and η_∞ are empirical constants. The empirical constants can be determined using the least square fitting method. The resulting empirical constants are shown in Tab. 3.2. The loss modulus is then given by

$$G'' = \eta G'. \tag{3.21}$$

The storage and loss moduli and loss factor obtained from the empirical models are compared with the experimental data in Fig. 3.8 and Fig. 3.9 respectively.

3.6 Conclusions

In this chapter, the characteristics of MR fluids and their response to an applied magnetic field have been presented. The pre-yield and post-yield behaviour has been

described, but attention was focussed on the pre-yield behaviour, in which MR fluids experience strain less than the yield strain.

The pre-yield shear properties of the MR fluid (MRF-140CG) were measured experimentally using a parallel-plate rheometer, which was equipped with a MRD used for generating magnetic field. The measurement method, an oscillatory shear test employing the controlled shear strain technique, was described, and the measured results were presented. The experimental results showed that an increase in the applied magnetic field results in a higher storage modulus, but a lower loss factor. However, the storage modulus and loss factor are independent of magnetic field for very high magnetic fields because of saturation. When the applied magnetic field increased to 347 mT, the MR fluid exhibited a significant change in the storage modulus to about 4.28×10^6 Pa, and the loss factor changed from 0.61 at zero field to 0.02.

Empirical models for the pre-yield storage modulus and loss factor as a function of the applied magnetic field were proposed by fitting functions to the experimental data. These empirical models will be used, together with the finite element model presented in chapter 4 and the model of the magnetic field presented in chapter 5, to predict the dynamics of an ATVA exploiting an MR fluid for various magnetic field strengths.

Tables

Appearance	Viscosity (Pa@40°C)	Density (kg/m^3)	Operating Temperature (°C)
Dark gray liquid	0.280 ± 0.070	$3540 - 3740$	-40 to $+130$

Tab. 3.1: Typical properties of MRF-140CG [74].

α_1	47.3
α_2	2.0
α_3	31.7
α_4	1.5
Zero magnetic field storage modulus, G'_z	2.47×10^3 Pa
Saturated magnetic field storage modulus, G'_∞	4.33×10^6 Pa
Zero magnetic field loss factor, η_z	0.9
Saturated magnetic field loss factor, η_∞	0.02

Tab. 3.2: Empirical constants used in equations (3.19) and (3.20).

Figures

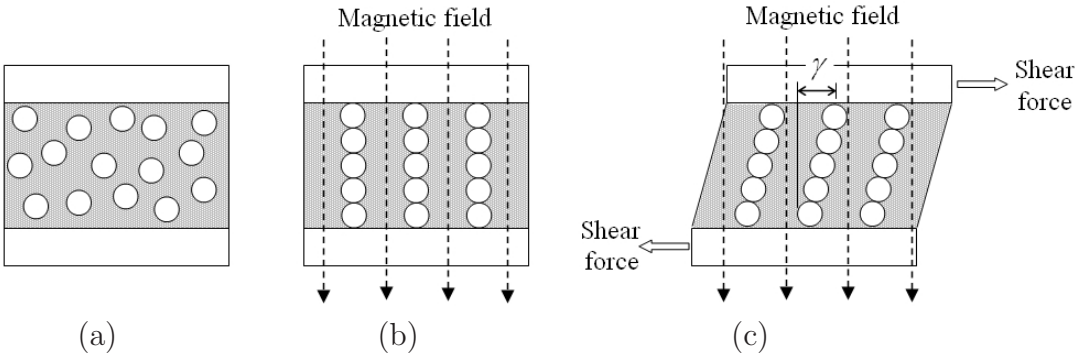

Fig. 3.1: Structure of MR fluids: (a) without a magnetic field; (b) with magnetic field; (c) with magnetic field and shear force.

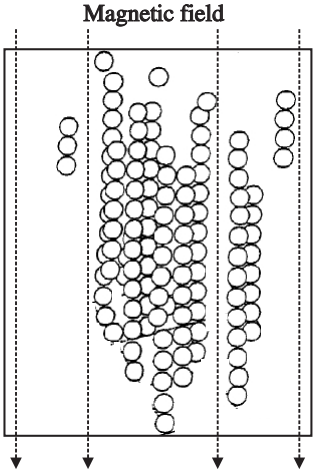

Fig. 3.2: Thick column structure of MR fluids.

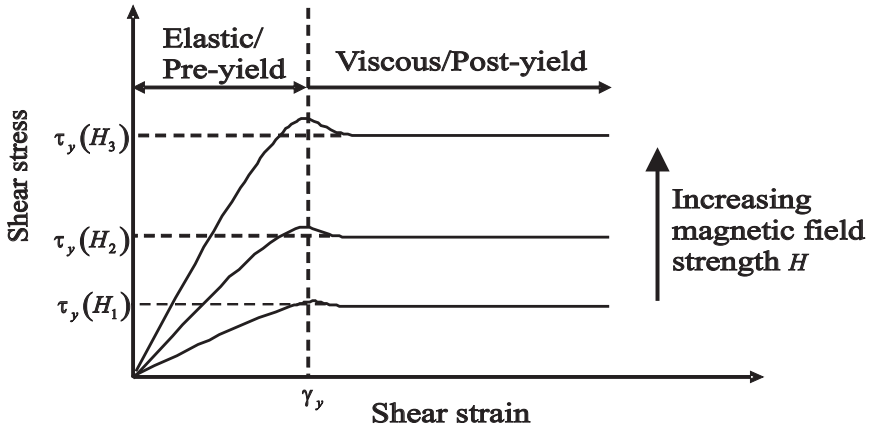

Fig. 3.3: Pre-yield and post-yield characteristics of MR fluids [37]. In the pre-yield region, the stress has a linear relationship with the strain.

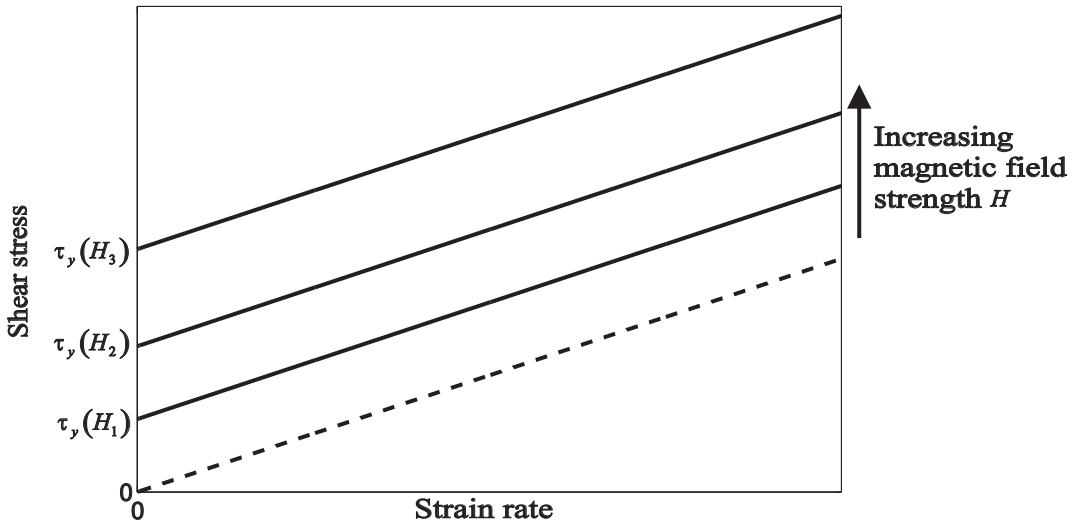

Fig. 3.4: The models for viscous behaviour of MR fluids [37]: --- Newtonian fluid model; — Bingham plastic model.

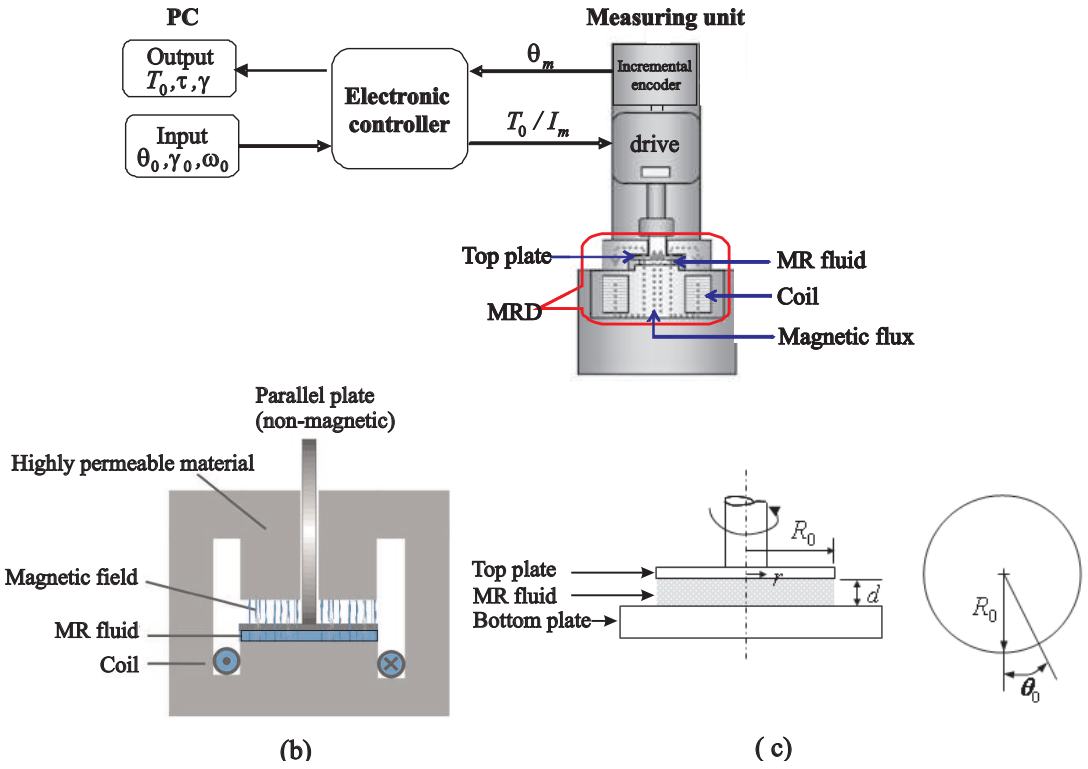

Fig. 3.5: Measurement system to determine the shear properties of an MR fluid: (a) schematic of measuring system using CSD technique [60]; (b) Anton Paar magneto-rheological device (MRD) [75]; (c) sketch of parallel-plate geometry.

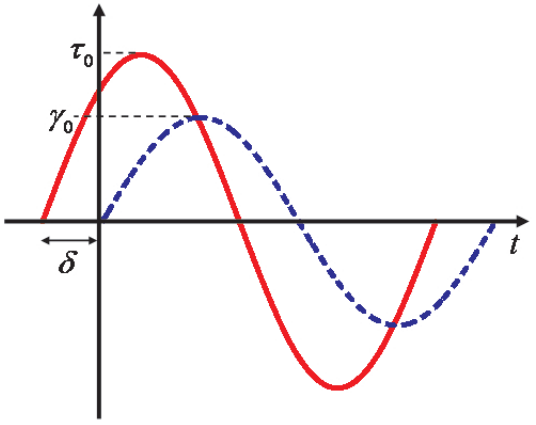

Fig. 3.6: The sinusoidal stress and strain: — shear stress $\tau(t)$; --- shear strain $\gamma(t)$.

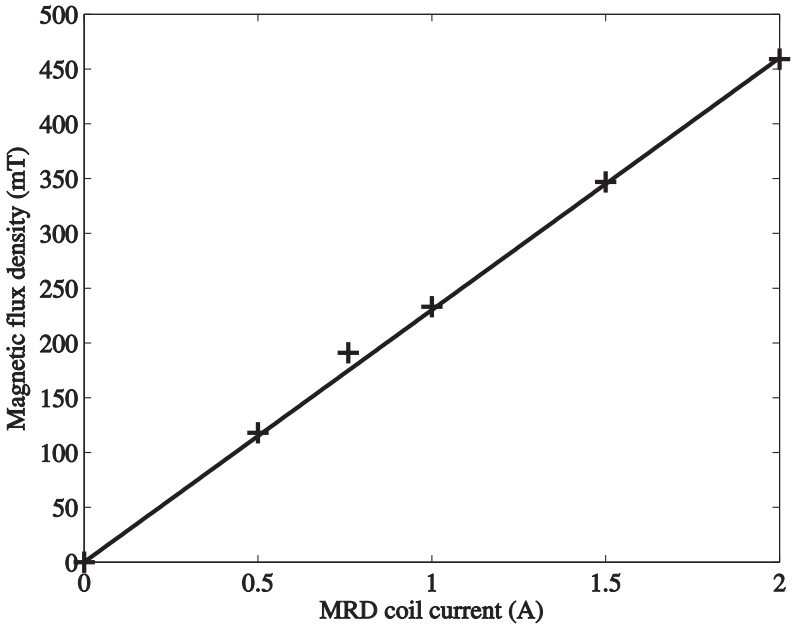

Fig. 3.7: Measured (+) and empirical model (—) of Eq. (3.18) for magnetic flux density as a function of MRD coil current.

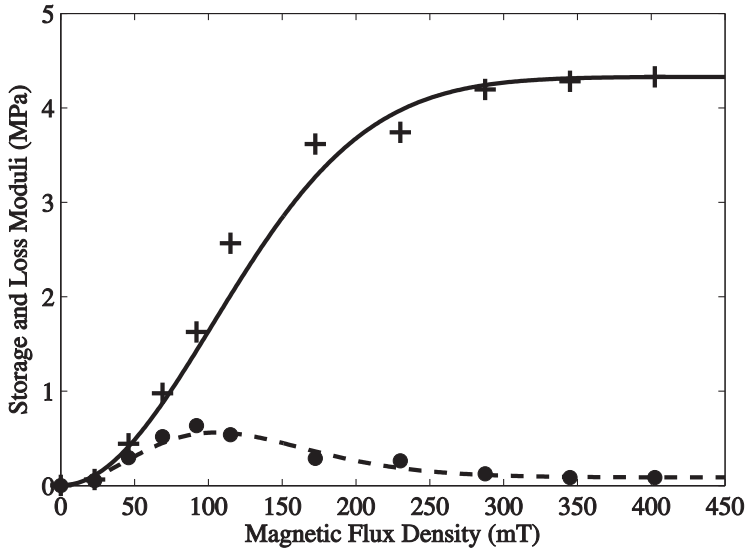

Fig. 3.8: Shear properties of MR fluid (MRF-140CG) as a function of magnetic field: measured (+) and empirical model (—) of Eq. (3.19) for storage modulus; measured (•) and empirical model (---) of Eq. (3.21) for loss modulus.

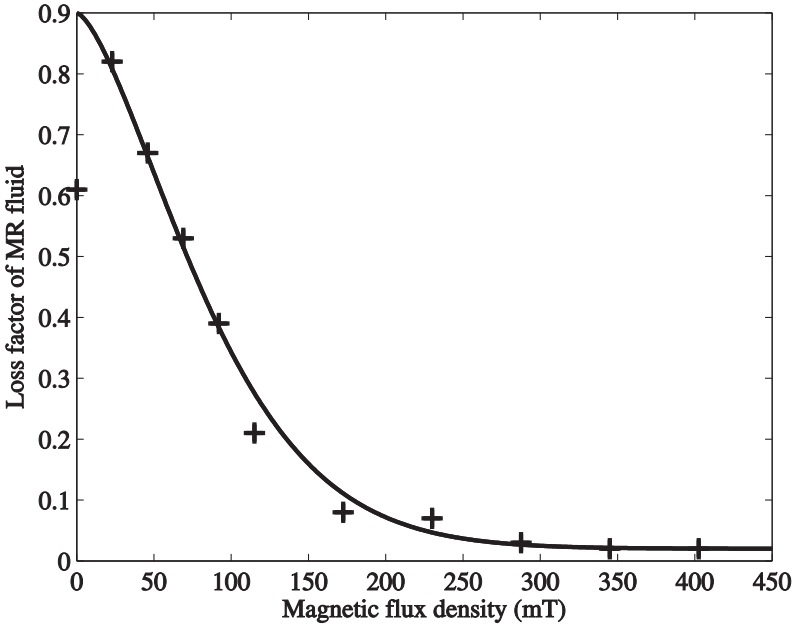

Fig. 3.9: Loss factor of MR fluid (MRF-140CG) as a function of magnetic field: measured (+) and empirical model (—) of Eq. (3.20).

Chapter 4

Finite Element Model of a MR Fluid-Filled ATVA

4.1 Introduction

Vibrations of three-layer sandwich beams have been studied by many researchers and several models have been developed to facilitate understanding of their behaviour. In most studies the shear deformations of the face plates were ignored. The early work involved developing an analytical model for the three-layer beam. DiTaranto [76] derived a sixth-order differential equation of motion for a freely vibrating beam. The solution of this equation leads to the natural frequencies and the loss factor of the beam. Subsequently, the solutions of the sixth-order differential equation obtained from DiTaranto [76] were investigated by DiTaranto and Blasingame [77]. The equation of motion for transverse displacement was derived by Mead and Markus [53], and the solutions to this equation were presented by the same authors in [78]. The models developed by DiTaranto [76] and Mead and Markus [53] were compared by Mead [79]. It is noted that the models in [76] and [53] provide reliable results for beams having flexural wavelengths greater than four times the thickness of the outer layers. Subsequently, He and Rao [80] developed an analytical model for a multi-span sandwich beam using an energy method. The variation of natural frequency and damping loss factor with various structural and geometric parameters were presented. Later, the Green's function was used for analysis of the sandwich beam by Sakiyama *et al.* [81] and the Timoshenko beam equation was adapted for the sandwich

beam in the work of Maheri and Adams [82]. Fasana and Marchesiello [83] studied the dynamic behaviour of sandwich beams by using the Rayleigh-Ritz method.

One major limitation of analytical methods is that it is difficult to obtain analytical solutions for many structures, especially structures with non-uniform properties such as thickness or elastic moludus or with complex boundary conditions. As a result, numerical solutions are often found. The finite element (FE) method is a well-known numerical method which has been used widely since about 1956 [84]. The FE method provides approximate solutions for the response of a continuous system. There is a significant amount of research concerning FE models of a sandwich beam, for example the work on a curved sandwich beam of Ahmed [85]. He studied the effect of the number of degrees-of-freedom (DOFs) on the accuracy of the estimate. The FE model was developed based on the assumptions that the bending stiffness of the middle layer, and the shear deformation and rotary inertia of the outer layers can be ignored. Elements with three, four, and five DOFs were investigated. The author noted that the three DOFs element was a very stiff element, while the five DOFs could improve the accuracy of the estimates at higher frequencies, but not the fundamental frequencies. Subsequently, Ahmed [86] made a further assumption from [85] that the thicknesses of the outer layers were small compared to the total thickness of the sandwich beam. Elements having six DOFs were developed and the displacement functions were approximated as polynomials with four constants. Baber *et al.* [87] developed a twelve DOFs FE for a sandwich beam. He made different assumptions from Ahmed [86], as the two outer layers were allowed to undergo different transverse displacements. A new FE model was presented by Sainsbury and Zhang [88]. In [88] the polynomial shape functions were combined with Galerkin orthogonal functions to improve the accuracy of predictions for higher modes of vibration.

The aim of this chapter is to develop an FE model which can describe the vibration characteristics of the MR fluid-filled ATVA developed in this thesis. The development of the FE model is based on the assumptions that, when the three-layer ATVA is deformed, all layers experience the same transverse displacement. The shear deformation and rotary inertia of the middle layer are taken into account, while those of the outer layers are ignored. Following this introduction, the FE model for

the three-layer beam is described in Section 4.2. The section starts with describing the deformations of a three-layer beam and continues with the derivation of energy functions. Following this the selection of displacement functions and DOFs used in the model is described, then mass and stiffness matrices are established. Lastly, the vibration of the beam is considered. The FE model for a uniform three-layer beam is validated by comparing the results with the Mead and Markus model for a uniform beam in section 4.3. The numerical studies for a non-uniform beam are conducted in section 4.4. Finally, section 4.5 contains some conclusions.

4.2 Finite Element Model of the MR Fluid-Filled ATVA

Vibrations of three-layer beams can be obtained analytically by solving the equations of motion and applying the appropriate boundary conditions. The equations of motion can be determined using Hamilton's principle which concerns the kinetic energy, potential energy, and non-conservative work function [89]. However, it is often difficult to obtain an exact solution using Hamilton's principle. Hence, a numerical solution is often found. Here the FE method is used.

The FE method provides an approximate solution for the behaviour of the structure by dividing the continuous system into several elements, approximating the motion in terms of assumed displacement functions for a single element, and then assembling the elements to represent the original system. An important part of the FE method is the calculation of the mass and stiffness matrices for each element. These matrices are established from the element strain and kinetic energies, which can be expressed in terms of the assumed deformations of the structure.

4.2.1 Deformations of a Three-Layer Beam

The three-layer beam considered for the FE model is shown in Fig. 4.1. The beam has length L and width b. The thicknesses of each layers are h_1, h_2, and h_3. The outer layers are elastic, while the middle layer is viscoelastic. It is assumed that the elastic outer layers behave as Euler-Bernoulli beams, the core carries shear, all the three layers undergo the same transverse displacement w, and there is no slippage

between the layers during deformation. The displacements of the three-layer beam when it deforms are constructed based on the sandwich beam theory of Mead and Markus [53, 79] and the deformation is shown in Fig. 4.2. The left-hand figure represents the beam before deformation and the cross-section XX is the undeformed section. The x-axis coincides with the mid-plane axis of the middle layer, the z-axis is perpendicular and positive upwards. Here z_1, z_2 and z_3 are measured from the mid-plane axis of each layer. It can be estimated from Fig. 4.2 that the longitudinal displacements u at any point within the top and bottom layers are assumed to be of the form [79].

$$u_1 = u_{10} - z_1 \frac{\partial w}{\partial x} \tag{4.1}$$

$$u_3 = u_{30} - z_3 \frac{\partial w}{\partial x} \tag{4.2}$$

where subscripts $_1$ and $_3$ represent the top and bottom layers respectively. Here u_{10} and u_{30} are the longitudinal extensions of the mid-surface of the top and bottom layers respectively. The longitudinal displacement within the middle layer is assumed to be

$$u_2 = u_B + \frac{h_2}{2}\frac{\partial u}{\partial z} + z_2 \frac{\partial u}{\partial z} \tag{4.3}$$

where $\frac{\partial u}{\partial z}$ and u_B are defined in Fig. 4.2, and are given by [79]

$$\frac{\partial u}{\partial z} = \frac{u_A - u_B}{h_2} \tag{4.4}$$

$$u_B = u_{30} - \frac{h_3}{2}\frac{\partial w}{\partial x}. \tag{4.5}$$

Here u_A shown in Fig. 4.2 is [79]

$$u_A = u_{10} + \frac{h_1}{2}\frac{\partial w}{\partial x}. \tag{4.6}$$

Substituting Eqs. (4.4-4.6) into Eq. (4.3) gives

$$u_2 = \left(\frac{1}{2} + \frac{z_2}{h_2}\right)u_{10} + \left(\frac{1}{2} - \frac{z_2}{h_2}\right)u_{30} + \left[\frac{1}{4}(h_1 - h_3) + \frac{z_2}{2h_2}(h_1 + h_3)\right]\frac{\partial w}{\partial x}. \tag{4.7}$$

The shear strain γ_2 in the core is assumed to be constant across the depth of the core and is related to the longitudinal and transverse displacements by [79]

$$\gamma_2 = \frac{\partial u}{\partial z} + \frac{\partial w}{\partial x} = \frac{u_A - u_B}{h_2} + \frac{\partial w}{\partial x}. \tag{4.8}$$

Substituting u_A from Eq. (4.6) and u_B from Eq. (4.5) into Eq. (4.8) gives

$$\gamma_2 = \frac{1}{h_2}(u_{10} - u_{30}) + \frac{H}{h_2}\frac{\partial w}{\partial x} \tag{4.9}$$

where

$$H = h_2 + \frac{h_1 + h_3}{2}. \tag{4.10}$$

4.2.2 Strain Energy

The FE method involves the determination of energy functions, which are kinetic and strain energies, for an element. The element strain energy can be derived by making the following assumptions: the element deflects in the $x - z$ plane only, the plane cross-section in layers 1 and 3 remains plane after bending, all displacements and strains are small so that the linear stress-strain relationship can be applied, the normal stresses in the y and z directions are zero, and the shear stresses in the $x - y$ and $y - z$ planes are zero. The strain energy can be derived from stresses and strains, and is given by [89]

$$U = \frac{1}{2}\int_v \sigma\varepsilon \, \mathrm{d}v + \frac{1}{2}\int_v \tau\gamma \, \mathrm{d}v \tag{4.11}$$

where $\sigma, \varepsilon, \tau$, and γ are normal stress, normal strain, shear stress in the $x - z$ plane and corresponding shear strain respectively. The integrals are evaluated over the volume v occupied by the material. By Hooke's law, the normal stress is given by

$$\sigma = E\varepsilon. \tag{4.12}$$

Assuming that the variation of strain over the cross-section is negligible, the shear stress and the shear strain are related by the shear modulus G of material, such that

$$\tau = G\gamma. \tag{4.13}$$

As the outer layers are assumed to be thin and their behaviour can be described by Euler-Bernoulli beam theory, the plane cross-section is normal to the deformed axis after deformation. Hence, the shear strain in these layers is zero. Combining Eq. (4.11) and Eq. (4.12) gives the strain energies of the top and bottom layers respectively as

$$U_1 = \frac{1}{2}E\int_v \varepsilon_1^2 \mathrm{d}v = \frac{1}{2}E\int_v \left(\frac{\partial u_1}{\partial x}\right)^2 \mathrm{d}v \tag{4.14}$$

$$U_3 = \frac{1}{2}E\int_v \varepsilon_3^2 \mathrm{d}v = \frac{1}{2}E\int_v \left(\frac{\partial u_3}{\partial x}\right)^2 \mathrm{d}v \tag{4.15}$$

where ε_1 and ε_3 are the normal strains within layers 1 and 3 respectively. Substituting Eqs. (4.1) and (4.2) into Eqs. (4.14-4.15) gives the strain functions as

$$U_1 = \frac{1}{2}E\int_v \left(\frac{\partial u_{10}}{\partial x} - z_1\frac{\partial^2 w}{\partial x^2}\right)^2 \mathrm{d}v \tag{4.16}$$

$$U_3 = \frac{1}{2}E\int_v \left(\frac{\partial u_{30}}{\partial x} - z_3\frac{\partial^2 w}{\partial x^2}\right)^2 \mathrm{d}v. \tag{4.17}$$

Since the centre layer is assumed to undergo only shear deformation, the strain energy from Eq. (4.11) becomes

$$U_2 = \frac{1}{2}\int_{z=0}^{H}\int_{y=0}^{b}\int_x \tau\gamma_2 \,\mathrm{d}x\mathrm{d}y\mathrm{d}z. \tag{4.18}$$

Substituting Eq. (4.13) into Eq. (4.18) and carrying out the integration gives

$$U_2 = \frac{1}{2}GbH\int_x \gamma_2^2 \,\mathrm{d}x. \tag{4.19}$$

Combining Eqs (4.9) and (4.19) leads to

$$U_2 = \frac{1}{2}GbH\int_x \left(\frac{1}{h_2}(u_{10} - u_{30}) + \frac{H}{h_2}\frac{\partial w}{\partial x}\right)^2 \mathrm{d}x. \tag{4.20}$$

4.2.3 Kinetic Energy

The kinetic energy consists of the kinetic energy due to axial displacement and that due to transverse displacement, and is given by [89]

$$T = \frac{1}{2}\rho \int_v \left[\left(\frac{\partial u}{\partial t} \right)^2 + \left(\frac{\partial w}{\partial t} \right)^2 \right] \mathrm{d}v \tag{4.21}$$

where ρ is the density. Hence the kinetic energies of layer 1 and layer 3 are given respectively by

$$T_1 = \frac{1}{2}\rho_p \int_v \left[\left(\frac{\partial u_1}{\partial t} \right)^2 + \left(\frac{\partial w}{\partial t} \right)^2 \right] \mathrm{d}v \tag{4.22}$$

$$T_3 = \frac{1}{2}\rho_p \int_v \left[\left(\frac{\partial u_3}{\partial t} \right)^2 + \left(\frac{\partial w}{\partial t} \right)^2 \right] \mathrm{d}v \tag{4.23}$$

where ρ_p is the density of the outer layer. Substituting u_1 and u_3 from Eqs. (4.1) and (4.2) into Eqs. (4.22) and (4.23) results in

$$T_1 = \frac{1}{2}\rho_p \int_v \left[\left(\frac{\partial u_{10}}{\partial t} - z_1 \frac{\partial^2 w}{\partial x \partial t} \right)^2 + \left(\frac{\partial w}{\partial t} \right)^2 \right] \mathrm{d}v \tag{4.24}$$

$$T_3 = \frac{1}{2}\rho_p \int_v \left[\left(\frac{\partial u_{30}}{\partial t} - z_3 \frac{\partial^2 w}{\partial x \partial t} \right)^2 + \left(\frac{\partial w}{\partial t} \right)^2 \right] \mathrm{d}v. \tag{4.25}$$

Neglecting the effect of rotary inertia leads to

$$T_1 = \frac{1}{2}\rho_p \int_v \left[\left(\frac{\partial u_{10}}{\partial t} \right)^2 + \left(\frac{\partial w}{\partial t} \right)^2 \right] \mathrm{d}v \tag{4.26}$$

$$T_3 = \frac{1}{2}\rho_p \int_v \left[\left(\frac{\partial u_{30}}{\partial t} \right)^2 + \left(\frac{\partial w}{\partial t} \right)^2 \right] \mathrm{d}v. \tag{4.27}$$

From Eqs. (4.7) and (4.21) the kinetic energy of the middle layer is given by

$$T_2 = \frac{1}{2}\rho_m \int_v \left[\left(\left[\frac{1}{2} + \frac{z_2}{h_2} \right] \frac{\partial u_{10}}{\partial t} + \left[\frac{1}{2} - \frac{z_2}{h_2} \right] \frac{\partial u_{30}}{\partial t} + \left[\frac{1}{4}(h_1 - h_3) + \frac{z_2}{2h_2}(h_1 + h_3) \right] \frac{\partial^2 w}{\partial x \partial t} \right)^2 + \left(\frac{\partial w}{\partial t} \right)^2 \right] \mathrm{d}v \tag{4.28}$$

where ρ_m is the density of the middle layer. Henceforth it will be assumed that the beam is symmetric, i.e. the top and bottom layers have the same dimensions, $h_1 = h_3$. Also we only have bending motion, so that $u_{30} = -u_{10}$.

4.2.4 Displacement Functions

The FE method provides discrete solutions to the continuous system. These solutions are the displacements at the nodal points. The discrete solutions become closer to the exact solution if there are enough elements. The more elements the model has, the more accurate is the model. The accuracy of the FE model also depends on the assumed displacement function, which is a simple polynomial here. The continuity conditions need to be considered when selecting the DOFs and the displacement functions.

The element considered in this thesis consists of two nodes as shown in Fig 4.3. There are three DOFs at each node. These are u_{10}, w, and $w' = \frac{\mathrm{d}w}{\mathrm{d}x}$. Various assumptions are made in deriving the element matrices and these have been described previously. The choice of DOFs and element shape functions satisfy the conditions of continuity of displacement and slope. This is required because the strain energy functions involve the second derivative of displacement. Also these continuity conditions reflect the choice of the displacement functions.

The displacement functions are assumed to be polynomial functions with an appropriate number of terms. This number is selected such that the continuity condition within the element is satisfied. This condition requires that if the strain energy contains the derivative of the displacement function up to order p^*, the displacement function should contain a polynomial of degree at least p^*. According to this condition, the axial displacement is represented by first order polynomials, and the transverse displacement should be represented by a polynomial of at least order two. Hence, the displacement functions are assumed to be

$$u_{10} = a_0 + xa_1 \tag{4.29}$$

$$w = b_0 + xb_1 + x^2b_2 + x^3b_3 \tag{4.30}$$

$$w' = \frac{\partial w}{\partial x} = b_1 + 2xb_2 + 3x^2 b_3. \tag{4.31}$$

In this case the transverse displacement is a polynomial of order three so that the constants a_0, a_1, b_0, b_1, b_2 and b_3 can be written in terms of the DOFs at two nodes. Details are given in Appendix B.

4.2.5 Mass and Stiffness Matrices

Mass and stiffness matrices are used to express the total element energies in the system in terms of the nodal DOFs. The total element strain and kinetic energies are the summations of the energies for each layer, and are given, respectively, by

$$U_e = U_1 + U_2 + U_3 \tag{4.32}$$

$$T_e = T_1 + T_2 + T_3. \tag{4.33}$$

The element stiffness and mass matrices, $\mathbf{K_e}$ and $\mathbf{M_e}$, follow from the element strain and kinetic energies given in terms of the nodal DOFs $\mathbf{q_i}$ by

$$U_e = \frac{1}{2}\mathbf{q_i}^{\mathrm{T}}\mathbf{K_e}\mathbf{q_i} \tag{4.34}$$

$$T_e = \frac{1}{2}\dot{\mathbf{q}}_\mathbf{i}^{\mathrm{T}}\mathbf{M_e}\dot{\mathbf{q}}_\mathbf{i} \tag{4.35}$$

where $\dot{}$ denotes $\frac{\partial}{\partial t}$ and $^{\mathrm{T}}$ is the transpose. Here $\mathbf{K_e}$ can be obtained by combining Eqs. (4.16, 4.17, 4.20, 4.32) and (4.34). Equations (4.26, 4.27, 4.28, 4.33) and (4.35) are combined to give the element mass matrix $\mathbf{M_e}$. The nodal DOF vector for a single element $\mathbf{q_i}$ and the resulting element mass and stiffness matrices are given in Appendix B.

4.2.6 Vibration of Beams

The forced vibration of the undamped three-layer beam can be obtained by solving the equation of motion [89]

$$\mathbf{M}\ddot{\mathbf{q}}_\mathbf{0} + \mathbf{K}\mathbf{q}_\mathbf{0} = \mathbf{f} \tag{4.36}$$

where the total mass and stiffness matrices, $\mathbf{K}$ and $\mathbf{M}$, are assembled from the element stiffness and mass matrices respectively. The assembly process for the total mass matrix is that the six rows and columns of the matrix $\mathbf{M_e}$ for element number e are added into the rows and columns $3(e-1)+1$ to $3(e-1)+6$ of the total mass $\mathbf{M}$. The same process is used for assembling the total stiffness matrix. Here $\mathbf{q_0}$ and $\mathbf{f}$ are vectors of nodal displacements and nodal forces for the entire beam respectively. For time harmonic motion at frequency ω they are given by

$$\mathbf{q_0} = \left\{ \begin{array}{c} u_{10}^{(1)} \\ w^{(1)} \\ w'^{(1)} \\ \vdots \\ u_{10}^{(n+1)} \\ w^{(n+1)} \\ w'^{(n+1)} \end{array} \right\} e^{\mathrm{i}\omega t} = \widetilde{\mathbf{q}}_\mathbf{0} e^{\mathrm{i}\omega t}, \qquad \mathbf{f} = \widetilde{\mathbf{f}} e^{\mathrm{i}\omega t}, \tag{4.37}$$

where n is the number of elements and $^{()}$ represents node number. Substituting Eq. (4.37) into Eq. (4.36) gives

$$\left[\mathbf{K} - \omega^2 \mathbf{M}\right] \widetilde{\mathbf{q}}_\mathbf{0} = \widetilde{\mathbf{f}}. \tag{4.38}$$

For time harmonic motion, structural damping can be included in the model by replacing Eq. (4.38) by [89]

$$\Big[\left[\mathbf{K} + \mathrm{i}\mathbf{H}\right] - \omega^2 \mathbf{M}\Big] \widetilde{\mathbf{q}}_\mathbf{0} = \widetilde{\mathbf{f}}. \tag{4.39}$$

where the complex matrix $[\mathbf{K} + \mathrm{i}\mathbf{H}]$ is obtained by replacing Young's modulus E and shear modulus G with their complex values.

In the case of free vibration, the undamped natural frequencies ω and mode-shapes $\mathbf{\Psi}$ can be obtained by solving the eigenproblem

$$\left[\mathbf{K} - \lambda \mathbf{M}\right] \mathbf{\Psi} = 0 \tag{4.40}$$

where the eigenvalues $\lambda = \omega^2$. To obtain a non-zero solution, the determinant of $[\mathbf{K} - \lambda\mathbf{M}]$ should vanish, that is

$$\left|\mathbf{K} - \lambda\mathbf{M}\right| = 0. \tag{4.41}$$

Expanding Eq. (4.41) gives the characteristic polynomial whose roots are the eigenvalues. The mode shapes are the eigenvectors that satisfy

$$\left[\mathbf{K} - \lambda\mathbf{M}\right]\boldsymbol{\Psi} = 0. \tag{4.42}$$

In this thesis, the eigenvectors are normalised to have the property that

$$\boldsymbol{\Psi}^{\mathbf{T}}\mathbf{M}\boldsymbol{\Psi} = \mathbf{I}. \tag{4.43}$$

4.3 FE Model Validations

In this section, the FE models are validated against the Mead and Markus model for a uniform beam described in Appendix A. Consider the undamped free-free sandwich beam shown in Fig. 4.1 with dimensions and material properties given in Tab. 4.1. The outer layers of the beam have the same Young's modulus E, density ρ_p, and thickness h_1. The shear modulus of the core is G. The natural frequencies of the beam can be calculated from the FE model by dividing the beam into several elements, calculating the element mass and stiffness matrices using the expressions shown in Appendix B, assembling these element matrices to obtain the mass and stiffness matrices for the complete beam, applying the appropriate boundary conditions, and solving the eigenvalue problem. The results of two simulations, using 6 and 60 elements are shown in Tab. 4.2. Three mode shapes generated from the FE model using 60 elements are shown in Fig. 4.4.

The numerical results from two FE models are compared with those from the Mead and Markus model. It can be seen from Tab. 4.2 that the first two modes are rigid body modes because the natural frequencies are zero. For the third mode, the natural frequencies from the two FE models are slightly higher than the natural

frequency from the Mead and Markus model. It also can be seen that the FE model using 60 elements has less error compared with the Mead and Markus model than that using 6 elements. The error from both FE models increases for higher modes. However, using 60 elements, the maximum error for the first five modes is about 1%, which is still small. Hence, this model is able to predict the natural frequency of the uniform three-layer beam to an acceptable accuracy.

The FE model is also validated for the case where the middle layer of the sandwich beam has zero density and shear modulus. As the top and bottom beams are thin, their behaviour can be described by Euler-Bernoulli beam theory. This model is a well known model in which the effects of rotary inertia and shear deformation are neglected. The natural frequencies obtained from Euler-Bernoulli theory are [90]

$$\omega_i = (k_i L)^2 \sqrt{\frac{EI_1}{\rho A_1 L^4}} \tag{4.44}$$

where i is the mode number, neglecting rigid body modes, $A_1 = bh_1$ is the cross-sectional area, b is the width of the beam, h_1 is the thickness of the beam, $I_1 = \frac{bh_1^3}{12}$ is the second moment of area, k_i is the wavenumber of mode i, and the values of $k_i L$ for free-free conditions are given in Tab. 4.3. The dimensions and material properties shown in Tab. 4.1 are used in this simulation, but the shear modulus G and density ρ_m of the centre layer are set to zero. The natural frequencies obtained from the FE models using 60 elements are compared with those from Euler-Bernoulli theory in Tab. 4.4. As the discrepancies between the results from the two models are very small, i.e. less than 0.1% for the first four modes, the FE model can accurately predict the natural frequencies of the sandwich beam with a core of zero shear stiffness.

4.4 Numerical Studies

Since the Mead and Markus model described in Chapter 2 and Appendix A is difficult to apply to three-layer beams whose properties are non-uniform along the length, numerical FE studies are conducted for such cases. These studies aim to investigate the effect of changing parameters such as the shear stiffness of the middle layer on

the the natural frequency of the beam. The influence of the damping loss factor is also considered. Consider the sandwich beam shown in Fig. 4.5. The top and bottom layers are made of perspex and have the same dimensions and material properties. There is a small piece of perspex in the middle of the centre layer. The complex shear modulus of this perspex is given by

$$G_p = G'_p(1 + \mathrm{i}\eta_p) \tag{4.45}$$

where η_p is the loss factor of perspex and G'_p is the storage modulus of perspex given by

$$G'_p = \frac{E}{2(1+\nu_p)} \tag{4.46}$$

where ν_p is the Poisson's ratio of perspex. Some parts of the centre layer are empty, i.e. the density and shear modulus are zero, while some parts are filled with MR fluid. There are four electromagnets attached to the outer layers. The shear modulus of the MR fluid in the region over which the electromagnets are attached or the shear modulus of the on-state MR fluid is G_n. Outside this area, the shear modulus of the core with the off-state MR fluid is G_f. The shear modulus of the on-state and off-state MR fluids are complex and can be expressed as

$$G_n = G'_n(1 + \mathrm{i}\eta_n). \tag{4.47}$$

$$G_f = G'_f(1 + \mathrm{i}\eta_f). \tag{4.48}$$

where G'_n, η_n, G'_f and η_f are the storage modulus and loss factor of the on-state and off-state MR fluids respectively. All parameters used in the simulation presented in this chapter are given in Tab. 4.5.

The beam has free-free boundary conditions and is excited by a force at its centre. The point frequency response function (FRF) at the centre of the beam is obtained from the FE model. The beam is divided into 100 elements, and hence there are 101 nodes. Each element has length of 1 mm. Following the same procedure as in section 4.3, the mass and stiffness matrices for the entire beam can be determined. As the beam is non-uniform, the mass and stiffness matrices of each element are

different depending on the material properties of the centre layer. There are four values of shear modulus, i.e. G_a, G_p, G_f and G_n, in the middle layer as shown in Fig. 4.5, and hence four values of element stiffness. The element mass matrices are categorised by the density of material in the middle layer of the beam. These materials are perspex, MR fluid, and air. The densities of these materials are given in Tab. 4.5. Moreover, there are electromagnets attached to the beam at node 11 and node 91, two electromagnets at each node. The masses and moments of inertia of these electromagnets are included in the model. An additional mass matrix of the electromagnets is added to the mass matrix of the structure for the DOFs of nodes 11 and 91. As the four electromagnets are identical, the mass matrix added to node 11 is the same as that added to node 91. This matrix is

$$\begin{bmatrix} 2M_m & 0 & 0 \\ 0 & 2M_m & 0 \\ 0 & 0 & 2M_m\kappa^2 \end{bmatrix} \tag{4.49}$$

where M_m and κ are the mass of one electromagnet and its radius of gyration respectively. Substituting the total mass and stiffness matrices into Eq. (4.39) and inverting gives the receptance matrix of the sandwich beam. By multiplying this by $-\omega^2$ the accelerance matrix of the beam is determined to be

$$\mathbf{A_a} = -\omega^2 \Big[\big[\mathbf{K} + \mathrm{i}\mathbf{H}\big] - \omega^2 \mathbf{M} \Big]^{-1}. \tag{4.50}$$

In the case of the beam attached to the mass-like host structure m_1, the accelerance of the combined structure can be found by adding the contribution of m_1 to the mass matrix $\mathbf{M}$ and then inverting as before.

To investigate the effect of the shear modulus of the centre layer, two simulations were carried out. The simulated input accelerances at the centre of the beam for two values of shear modulus G_n are shown in Fig. 4.6. The solid line corresponds to $G_n = 4.15(1 + \mathrm{i}0.04)$ MPa while the dashed line corresponds to $G_n = 0.5(1 + \mathrm{i}0.04)$ MPa. The FRF at low frequency is determined by the mass of the system. The shear modulus of the centre layer affects the FRF. The resonance and anti-resonance

frequencies increase with the shear modulus of the middle layer as shown in Fig. 4.6. Fig. 4.7 shows FRFs for two values of loss factor of the core containing MR fluid, i.e. $\eta_n = 0.04$ and 0.4. The damping loss factor of the middle layer affects the magnitude of FRF at resonance and anti-resonance. It can be seen that when the loss factor increases, the magnitude around resonance decreases but that around anti-resonance increases.

4.5 Conclusions

In this chapter, the FE method was applied to a three-layer beam and used to estimate its vibration behaviour. The assumptions made were that the middle layer experiences shear deformation, while the shear deformation of the outer layers are ignored. The rotary inertia of the outer layers and the bending stiffness of the middle layer were not considered. All the layers undergo the same transverse displacement. In general, the accuracy of the estimates depends on the assumed displacement functions and the number of DOFs in the model. The displacement functions and DOFs were selected such that the conditions of the continuity were satisfied. Elements having three DOFs per node, i.e. axial displacement of the mid-surface of the top layer, transverse displacement, and its first derivative, were used.

The FE model for a uniform sandwich beam was validated by comparing its dynamic behaviour with that of the Mead and Markus model. The numerical results show that the FE model with enough elements can accurately predict the natural frequencies of a three-layer beam. Also, increasing the number of elements improves the accuracy.

The FE method was also used to study the vibration characteristics of a non-uniform beam. The centre layer of the beam considered has four different material properties. Two simulations were conducted for two values of shear modulus of MR fluid in the middle layer. It is clear from the numerical results that the shear modulus of the centre layer affects the FRF of the three-layer beam. Larger values of shear modulus led to higher stiffness, and hence higher resonance and anti-resonance frequencies. The amplitudes at these frequencies were influenced by the damping

loss factor of the centre layer, i.e. the amplitude at resonance decreased and that at anti-resonance increased as damping increases.

The FE model presented here is used in the design of the MR fluid-filled ATVA in Chapter 5. Several simulations using this model are conducted to study the influence of various geometric parameters. In Chapter 6, the FE model for the MR fluid-filled ATVA is validated by a series of experiments.

Tables

Length of the beam	L	1.0 m
Width of the beam	b	10.0 mm
Thickness of layers 1 and 3	h_1	0.5 mm
Thickness of layer 2	h_2	20.0 mm
Density of layers 1 and 3	ρ_p	1169 kg/m^3
Density of layer 2	ρ_m	3860 kg/m^3
Young's modulus of elasticity of layers 1 and 3	E	6.2×10^9 N/m^2
Shear modulus of layer 2	G	1×10^6 Pa

Tab. 4.1: Geometrical and material properties of a free-free beam used in model validations.

Mode number	Natural frequencies (Hz)			% Error compared with Mead and Markus model	
	Mead and Markus model	FE model			
		6 elements	60 elements	6 elements	60 elements
1	0.0000	0.0000	0.0000	–	–
2	0.0000	0.0000	0.0000	–	–
3	8.7197	8.8433	8.7541	1.42	0.39
4	18.1459	18.6259	18.2323	2.65	0.48
5	27.5720	28.5781	27.8480	3.65	1.00

Tab. 4.2: Natural frequencies of the free-free sandwich beam.

Mode Number	Value of k_iL
1	$k_1L = 4.730041$
2	$k_2L = 7.853205$
3	$k_3L = 10.995608$
4	$k_4L = 14.137165$

Tab. 4.3: Value of k_iL for the free-free uniform beam [90].

Mode number	Natural frequencies (Hz)		% Error compared with Euler-Bernoulli theory
	Euler Bernoulli	FE method	
1	1.1836	1.1836	+0.00
2	3.2601	3.2627	+0.08
3	6.4014	6.3963	−0.08
4	10.5776	10.5734	−0.04

Tab. 4.4: Natural frequencies of the free-free sandwich beam with zero shear stiffness in the centre layer excluding rigid body modes.

Length of the beam	L	100 mm
Width of the beam	b	10.0 mm
Thickness of layers 1 and 3	h_1	0.5 mm
Thickness of layer 2	h_2	1.0 mm
Density of layers 1 and 3	ρ_p	1013 kg/m^3
Density of layer 2	ρ_m	4350 kg/m^3
Poisson's ratio of perspex	ν_p	0.4
Young's modulus of elasticity of layers 1 and 3	E	$3.81 \times 10^9(1 + 0.048\text{i})$ N/m^2
Shear modulus of off-state MR fluid	G_f	$2.47 \times 10^3(1 + 0.61\text{i})$ Pa
Shear modulus of air	G_a	0 Pa
Shear modulus of perspex	G_p	$1.36 \times 10^9(1 + 0.048\text{i})$ Pa
Mass of the mass-like structure	m_1	7.5 g
Mass of electromagnet	M_m	0.5 g
Radius of gyration of electromagnet	κ	0.003 m

Tab. 4.5: Geometrical and material properties of a free-free non-uniform beam used in numerical study.

Figures

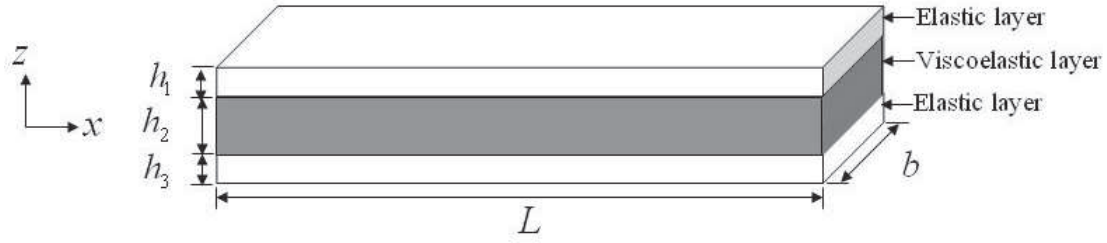

Fig. 4.1: Three-layer beam.

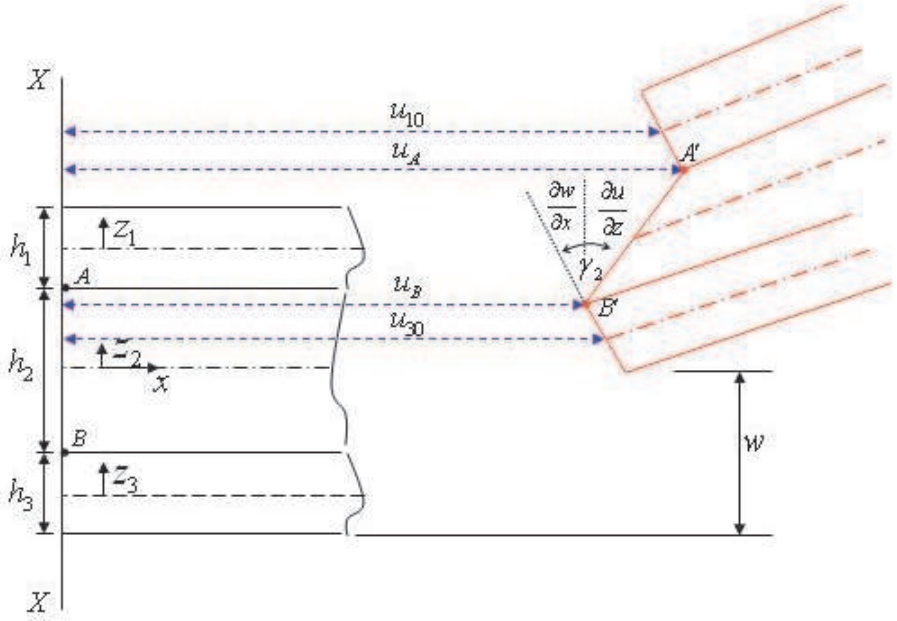

Fig. 4.2: The deformation of the three-layer element.

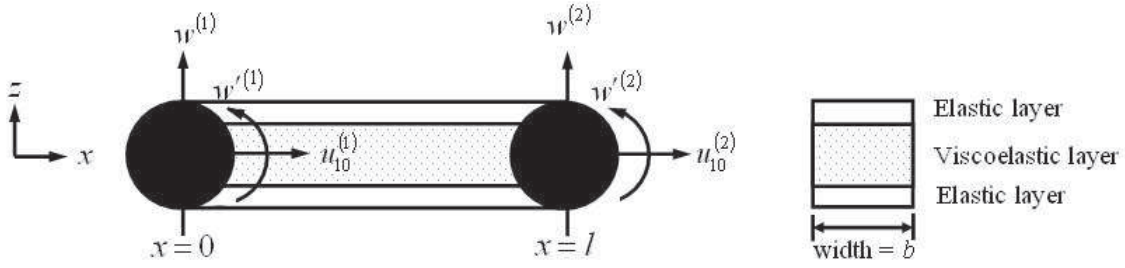

Fig. 4.3: A two-node three-layer beam element with three DOFs at each node.

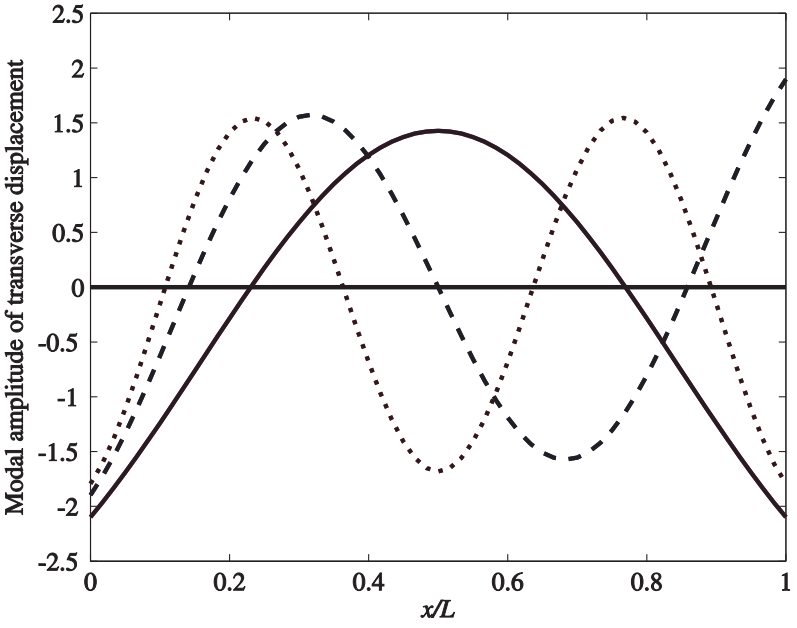

Fig. 4.4: Mode shapes of free-free sandwich beam: — mode 3; --- mode 4; ··· mode 5.

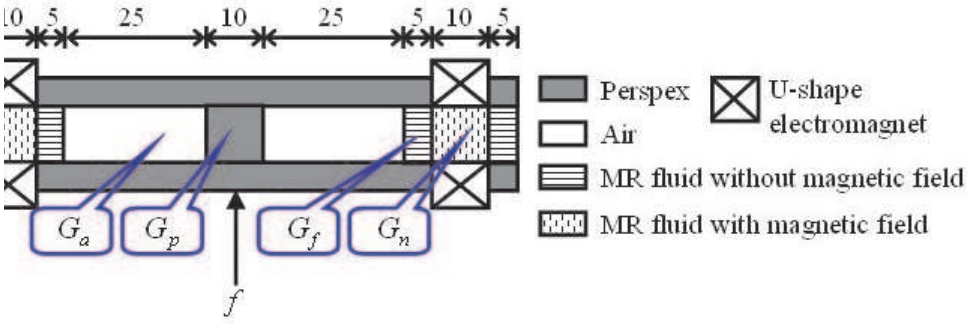

Fig. 4.5: Free-free non-uniform sandwich beam, dimensions are in mm. G_a, G_p, G_f and G_n are the shear modulus of air, perspex, off-state MR fluid and on-state MR fluid respectively.

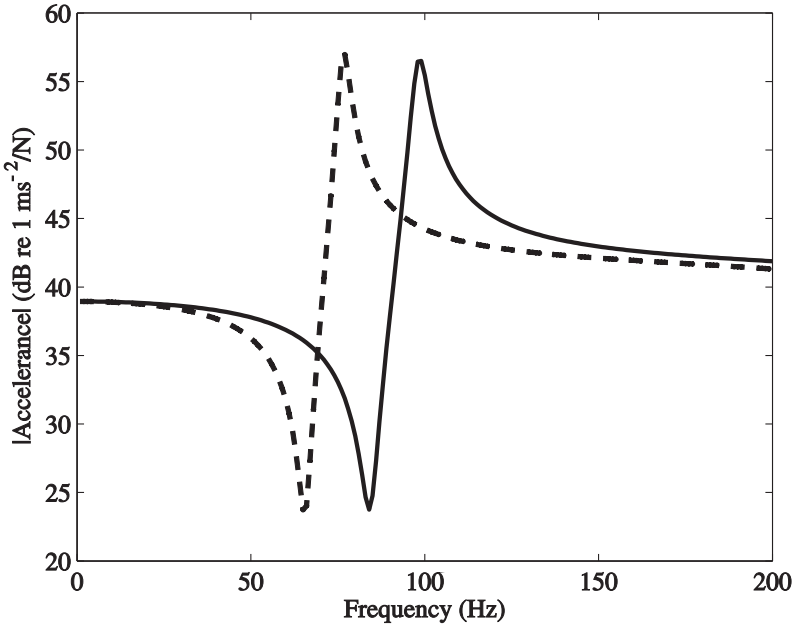

Fig. 4.6: Input accelerance of a free-free non-uniform sandwich beam computed by FE method for — $G'_n = 4.15$ MPa and --- $G'_n = 0.5$ MPa.

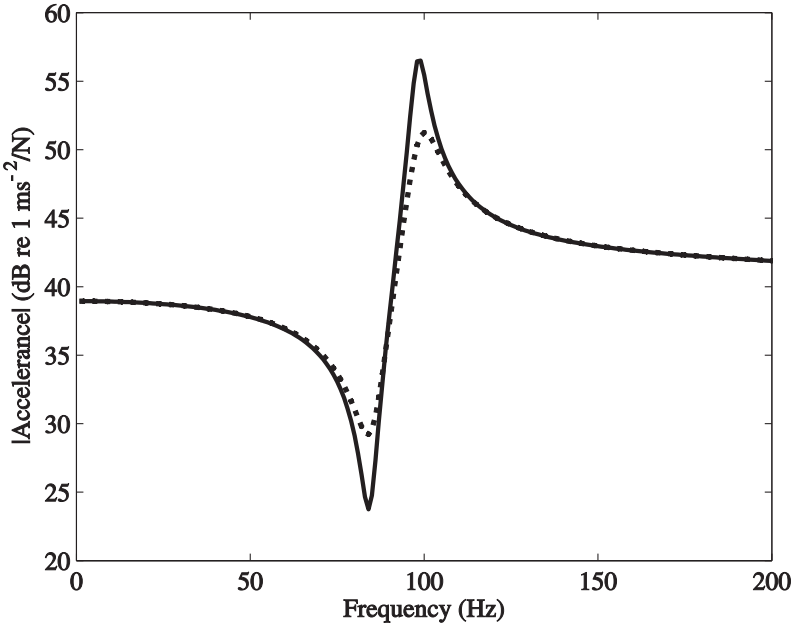

Fig. 4.7: Input accelerance of a free-free non-uniform sandwich beam computed by the FE method for $G'_n = 4.15$ MPa, — $\eta_n = 0.04$ and $\cdots$ $\eta_n = 0.4$.

Chapter 5

Design of the MR Fluid-filled ATVA

5.1 Introduction

In this chapter, the design of the Magneto-Rheological (MR) absorber is described. The MR adaptive tuned vibration absorber (ATVA) is a three-layer beam with MR fluid in the middle layer. It is proposed that the natural frequency of the MR fluid-filled ATVA can be tuned by changing the shear stiffness in the centre layer, by varying the shear modulus of the MR fluid. It was shown in Chapter 3 that the shear modulus of a MR fluid can be changed with the application of a magnetic field.

This chapter describes the design of an ATVA with the aims of changing its natural frequency by 30%. The design of the MR fluid-filled ATVA consists of two phases, i.e. the electromagnet design and the beam design. Electromagnets are used to apply a magnetic field to the MR fluid in the middle layer of the ATVA. They are designed to be small but should be able to provide a strong magnetic field. Their size should be small compared to the ATVA beam so that they can be attached to the beam and not significantly constrain the shear deformation of the beam. The design of the beam is conducted using the finite element (FE) model developed in Chapter 4 to investigate the influence of geometric parameters on the tuned frequency, which is the lowest anti-resonance frequency introduced in section 2.2. Also the number of electromagnets attached to the beam is investigated.

Following this introduction, the design and configuration of the MR fluid-filled ATVA are described in section 5.2. Section 5.3 presents the design of the electromagnets. The section starts with an introduction of the magnetic field and magnetic materials. The section continues with a presentation of the magnetic properties of the MR fluid. Then the calculation of magnetic flux density across the core containing MR fluid is described. Section 5.4 presents some parametric studies conducted using the FE model. The influence of five parameters, i.e. the thickness of the outer layers of the beam, the thickness of the middle layer of the beam, the width of the beam, the length of the beam, and the number of electromagnets attached to the beam, are studied. Hence the dimensions of the MR fluid-filled ATVA are obtained. Finally, section 5.4 contains some conclusions.

5.2 Design of the MR Fluid-Filled ATVA

The MR fluid-filled ATVA is preliminarily designed as a beam shown in Fig. 5.1. The outer layers of the beam are made of perspex, and are designed to support bending and longitudinal extension. The top and bottom layers have the same dimensions and material properties. The middle layer has variable shear stiffness. This layer is filled with a hydrocarbon-based MR fluid (MRF-140CG, LORD Corporation) and is sealed with tape to retain the fluid. The MR fluid-filled ATVA utilizes MR fluid as an adaptive shear stiffness element. The ATVA can be tuned by varying the magnetic field across the centre layer, and hence altering the shear stiffness of the device. The centre of the MR fluid-filled ATVA is designed to be attached to the host structure. Hence there is a piece of perspex in the centre of the device, where there is a threaded hole for a stud that is used to fasten the beam to the host structure.

A magnetic field is generated by electromagnets attached to the beam. One set of electromagnets comprises two small electromagnets, one of which is attached to the top layer and the other to the bottom layer as shown in Fig. 5.2. Electromagnets are attached close to the ends of the beam, where the maximum shear occurs when the beam deforms.

5.3 Design of the Electromagnets

As the shear stiffness of MR fluids are changed by a magnetic field, it is desirable to apply a magnetic field to the MR fluid in the middle layer of the ATVA so that the natural frequency can be altered. There are several ways to generate the magnetic field, for example using permanent magnets, or using electromagnets. Permanent magnets have the advantage of having small size, but being able to provide very strong magnetic field. However, it is difficult to change their magnetic field strength in real-time. To overcome this problem, electromagnets are employed. The design of the electromagnets involves the consideration of the magnetic properties of electromagnets, i.e. mild steel, and those of MR fluid. These properties are described in the following subsections.

5.3.1 Magnetic Fields

Magnetic fields were originally observed from permanent magnets rather than electromagnets. In 1820, the magnetic field produced by a current-carrying conductor was observed by Hans Christian Oersted [91]. Later, in the same year, the French physicist André-Marie Ampére invented the solenoid, which is a coil of N turns of wire carrying a current [91]. The solenoid can also produce a magnetic field but the magnetic field strength from a solenoid is weaker than that from permanent magnets. However, the magnetic field from the solenoid can be increased effectively by placing a magnetic material such as iron within the coil of the solenoid. This device is known as an electromagnet.

A magnetic field can be represented by magnetic flux lines flowing in a continuous loop around the source of the magnetic field. There are several sources of a magnetic field, for example a permanent magnet, current-carrying conductor, and current-carrying coil. For a permanent magnet, the direction of magnetic flux lines is from the north pole to the south pole. The magnetic flux lines per unit area is called the magnetic flux density, which is given by [92]

$$B = \frac{\Phi}{A} \tag{5.1}$$

where Φ is the magnetic flux through the area A. This is based on the assumption that the magnetic flux line is perpendicular to the area A. The magnetic flux density is related to the magnetic field strength H(A m^{-1}), sometimes called the magnetising force, by [92]

$$B = \mu^* H \tag{5.2}$$

where μ^* is the permeability of the material given in Henries per metre (H m^{-1}). Some materials, such as air, show very weak magnetic effects. Hence, they are considered to be non-magnetic materials and their permeability is very low and in practice about the same as that of a vacuum. In contrast to non-magnetic materials, magnetic materials have high permeability because the magnetic flux can be easily established in the materials. The permeability of the material is often presented in terms of the relative permeability, which is given by [92]

$$\mu_r = \frac{\mu^*}{\mu_0} \tag{5.3}$$

where μ_0 is the permeability of a vacuum. The relative permeability of a non-magnetic material is 1 and that of a magnetic material is greater than 1. There are several types of magnetic materials, which are classified by their magnetic properties. For example diamagnetic materials exhibit weak magnetic effects and ferromagnetic materials show very high magnetic effects. The relative permeability of ferromagnetic materials is not constant, and depends, for example, on the applied field [92]. The properties of ferromagnetic materials are normally illustrated by a magnetization curve, which is a graph of B as a function of H. The magnetization curve of mild steel is shown in Fig. 5.3. It can be seen that mild steel exhibits approximate linear magnetic properties for a low magnetic field, i.e. the magnetic flux density B increases linearly with increasing magnetising force H. In this region the relative permeability is approximately 1000 [59]. Beyond the linear region, saturation occurs. When saturation is reached, the B-H curve tends to be flat because B reaches its maximum value.

5.3.2 Magnetic Properties of MR fluid

As an MR fluid consists of magnetizable particles in a non-magnetic medium, the properties of an MR fluid changes in response to the application of a magnetic field. The magnetic properties of the MR fluid (MRF-140CG) are shown in Fig. 5.4. This is a *B-H* curve given by LORD Corporation. For positive B it can be seen that as H increases, the value of B increases rapidly at low magnetic field H and then increases more slowly. The magnetic properties of MR fluids are similar to those of ferromagnetic materials in that they exhibit a linear relationship for a low magnetic field. However, the relative permeability of ferromagnetic materials is much higher than that of MR fluid [67]. Jolly *et al.* [67] studied four commercial MR fluids manufactured by LORD Corporation, MRX-126 PD, MRX-140ND, MRX-242AS, and MRX-336AG. This work suggests that the relative permeability of MR fluid varies between 5 and 9, the linear region is where $H \leqslant 15.9$ kA/m, and little or no hysteresis is found from the *B-H* curves of the MR fluids being studied. However, the work of Li *et al.* [59] suggests the relative permeability of MR fluids to be approximately 5.

5.3.3 Electromagnets

The electromagnet designed for the ATVA is a coil of 160 turns of wire wound around a U-shape piece of mild steel as shown in Fig. 5.2(a). The wire is connected to a current source. A magnetic field can be generated by passing a current through this wire. To obtain a strong magnetic field, each set of electromagnets is designed as a closed loop magnetic circuit consisting of steel paths with the gap containing MR fluid. The magnetic flux across the MR fluid can be calculated using Ampére's law, which is [92]

$$\oint_{L_i} H \, dl = NI \tag{5.4}$$

where N, I, and L_i are the number of turns in the winding, the current in each turn, and the length of integration path respectively. The length L_i is selected to be an average path length, and hence the value of H obtained is an average value. Assuming no fringing, i.e. flux lines spreading outside the gap, Ampére's law in Eq. (5.4) can

be written as

$$2H_{s1}l_{s1} + 4H_{s2}l_{s2} + 2H_m l_m = 2NI \tag{5.5}$$

where l_{s1}, l_{s2}, and l_m are the lengths shown in Fig. 5.2(b). Here H_{s1}, H_{s2}, and H_m are the magnetic field strengths corresponding to lengths l_{s1}, l_{s2}, and l_m respectively. Substituting $H = \frac{B}{\mu^*}$ from Eq. (5.2) and $\mu^* = \mu_0\mu_r$ from Eq. (5.3) into Eq. (5.5) gives

$$\frac{B_{s1}l_{s1}}{\mu_0\mu_s} + 2\frac{B_{s2}l_{s2}}{\mu_0\mu_s} + \frac{B_m l_m}{\mu_0\mu_m} = NI \tag{5.6}$$

where μ_s and μ_m are the relative permeability of mild steel and MR fluid respectively. It is assumed that all of the flux is retained within the circuit. Hence, the flux Φ in the steel element is equal to that in the MR fluid element. Substituting $B = \frac{\Phi}{A}$ from Eq. (5.1) into Eq. (5.6) gives

$$\Phi\left[\frac{l_{s1}}{\mu_0\mu_s A_{s_1}} + 2\frac{l_{s2}}{\mu_0\mu_s A_{s2}} + \frac{l_m}{\mu_0\mu_m A_m}\right] = NI \tag{5.7}$$

where the areas A_{s_1}, A_{s_2} and A_m are given in Fig. 5.2(b). Rearranging Eq. (5.7), the magnetic flux can be written as

$$\Phi = \frac{NI}{\left[\frac{l_{s1}}{\mu_0\mu_s A_{s_1}} + 2\frac{l_{s2}}{\mu_0\mu_s A_{s2}} + \frac{l_m}{\mu_0\mu_m A_m}\right]}. \tag{5.8}$$

Hence, the mean flux density across the MR fluid where electromagnets are attached is given by

$$B = \frac{\Phi}{A_m} = \frac{NI}{A_m\left[\frac{l_{s1}}{\mu_0\mu_s A_{s1}} + 2\frac{l_{s2}}{\mu_0\mu_s A_{s2}} + \frac{l_m}{\mu_0\mu_m A_m}\right]} \tag{5.9}$$

where the values of μ_0, μ_s, μ_m, A_m, A_{s1}, A_{s2}, l_m, l_{s1} and l_{s2} are given in Tab. 5.1.

5.4 Parametric Studies

The aim of parametric studies is to investigate the influence of the geometric parameters of the ATVA on its tuning ability, and to examine the dimensions and

configurations of the ATVA that can provide the largest change in the tuned frequency. Parametric studies are conducted using the FE model described in Chapter 4. The beam shown in Fig. 5.1 to which four electromagnets are attached is considered first. Then various numbers of electromagnets are considered. These are assumed to be designed as described in section 5.3.3 with the current limited to 0.8 A to avoid overheating.

The ATVA is made of perspex, MR fluid, and tape. In the simulations it is assumed to be attached to the mass-like host structure m_1. The total mass of the three-layer beam ATVA considered in the FE model has contributions from the masses of the outer layers, the MR fluid, the perspex in the middle layer, and the electromagnets; the mass of the tape is assumed to be negligible in the model. The total stiffness of the ATVA is the combination of the bending and axial stiffnesses of the outer layers and the shear stiffness of the middle layer. The shear stiffness of the core has contributions from the stiffnesses of tape, MR fluid, and the centre piece of perspex. However, only the stiffness of the MR fluid changes with the application of the magnetic field. To investigate the change in the tuned frequency, the shear stiffness of the centre layer is changed by varying the shear modulus of the MR fluid. This is done by varying the magnetic field applied to the fluid. As the magnetic field is generated from electromagnets, the shear modulus of the MR fluid in the region over which the electromagnets are attached is changeable. However, the shear modulus of the MR fluid outside this area is assumed to be constant and not influenced by the magnetic field generated by the electromagnets.

The FE model used here is for a non-uniform beam shown in Fig. 5.5(a). There are two electromagnets attached to the top and the other two to the bottom of the beam. The cross-section of the beam where electromagnets are attached is shown in Fig. 5.5(b) and the side view of the beam is shown in Fig. 5.5(c). It can be seen from Fig. 5.5(b) that the shear modulus of the core across the width of the beam is not constant. The effective shear modulus of the core in the region over which the electromagnets are attached is G_e, while that outside this area is G_0. The effective shear modulus G_0 is the sum of contributions from the tape and the off-state MR fluid or the MR fluid without magnetic field. The effective shear modulus G_e has

contributions from the tape and the on-state MR fluid.

The shear modulus of the core along the beam is also different as shown in Fig. 5.5(c). The piece of perspex at the centre has shear modulus G_p, which is given in section 4.4. The effective shear modulus G_0 is constant, while G_m is variable. As the FE model developed in this thesis is a one-dimensional model but the property across the width of the beam shown in Fig. 5.5(b) is not fixed, the effective shear modulus G_m of the elements in this region is approximated using a simple law of mixtures as

$$G_m = \frac{(b'_1 + b'_3 + b'_5)G_0 + (b'_2 + b'_4)G_e}{b} \tag{5.10}$$

where $b'_1 - b'_5$ are given in Fig. 5.5(b). The shear modulus of the MR fluid as a function of magnetic field is given in Chapter 3. The effective shear modulus due to the tape G_t is obtained empirically in Chapter 6. All the material properties used in the parametric studies are given in Tab. 5.2.

Following the same procedure as in section 4.4 the mass and stiffness matrices, and hence the point frequency response function (FRF) at the point of attachment can be determined. To investigate the change in tuned frequency, two FRFs are calculated. Those are the FRFs of the ATVA without and with the magnetic field applied. The difference between the FE models for these two cases is due to the value used for G_m. Without the magnetic field $G_m = G_0$, while with the magnetic field from the electromagnets $G_m > G_0$.

The tuned frequencies and the loss factors are estimated from the FRFs using the circle-fit method [93]. The relative change in tuned frequency is defined by

$$\frac{\omega_n - \omega_f}{\omega_f} \times 100 \tag{5.11}$$

where ω_n and ω_f are the on-state and off-state tuned frequencies respectively.

5.4.1 Effects of Changing Thickness

The first parameter studied is the thickness of the outer layers of the beam. In this study, the beam model shown in Fig. 5.5 is used with $L = 60$ mm, $b = 10$ mm, and $h_2 = 2$ mm. The on-state storage modulus and loss factor used in this subsection

are $G'_n = 4.1$ MPa and $\eta_n = 0.04$, which correspond to an electromagnet current of 0.8 A. Five values of outer layer thickness, i.e. 1, 2, 3, 4, and 5 mm are investigated. The three-layer beam is divided into 60 elements and the magnetised regions are at elements 2-5 and at elements 56-59.

The total stiffness of the beam depends on the bending stiffness of the outer layers and the shear stiffness of the core. To achieve a high change in tuned frequency, it is desirable for the total stiffness to be mainly influenced by the core shear stiffness. One way of achieving this is to design the thickness of the outer layers to be small compared to the thickness of the core. Fig. 5.6 shows the relative change in tuned frequency with the thickness of the outer layers for a given core thickness. It can be seen that the relative change decreases with increasing thickness of the outer layers. Increasing the thickness of the outer layers increases the bending stiffness of the skins of the ATVA, and hence decreases the effect of the shear stiffness in the MR core. The maximum relative change, which is about 25%, occurs when $h_1 = h_3 = 1$ mm. Hence, this thickness is used in the rest of the studies.

The thickness of the middle layer h_2 affects the magnetic flux density across the core, and hence the on-state shear modulus of MR fluid. It can be seen from Eq. (5.9) that the magnetic flux density B decreases as the core thickness, l_m in Eq. (5.9), increases. Also it is shown in Eq. (3.19) that decreasing the magnetic field strength results in an decrease in the on-state shear modulus of MR fluid. Hence the on-state storage modulus of the MR fluid in the core decreases as the core thickness increases as shown in Fig. 5.7 (solid line). This curve is calculated from Eqs. (3.19) and (5.9) with a constant current of 0.8 A.

By using the values of on-state storage modulus for each core thickness shown in the solid line, the on-state loss factor from Eq. (3.20) and the beam dimensions of $L = 60$ mm, $b = 10$ mm, and $h_1 = h_3 = 1$ mm, the relative change in tuned frequency obtained from the FE model is shown in Fig. 5.7 (dashed line). It can be seen that for $h_2 \leqslant 3$ mm, the relative change in the tuned frequency increases as h_2 increases. However for $h_2 > 3$ mm, the change shows the opposite trend.

The relative change in tuned frequency depends on the relative change in shear modulus of MR fluid in the core. When the core thickness increases, the relative

change in shear modulus of MR fluid decreases, and hence the relative change in tuned frequency decreases. However this is not the case when the values of the core thickness are small, i.e. when $h_2 \leqslant 3$ mm. Because the core thickness is not large compared to the outer layer thickness, the shear stiffness may not dominate. Hence changing the shear modulus of the MR fluid has less influence on the change in the tuned frequency. When the shear stiffness increases by increasing h_2, the relative change in tuned frequency increases. It can be seen from Fig. 5.7 that the maximum relative change in tuned frequency occurs when $h_2 = 3$ mm and $G'_n = 4.1$ MPa. Hence, these values are used in the rest of the studies.

5.4.2 Effects of Changing Width

In this section, the influence of the width of the ATVA beam on the relative change in tuned frequency is investigated. The beam shown in Fig. 5.5 with $h_1 = h_3 = 1$ mm, $h_2 = 3$ mm, $L = 60$ mm, and $G'_n = 4.1$ MPa is used. It is assumed in the FE model that the mass of the electromagnets is independent of the width b.

Fig. 5.8 shows the relative change in tuned frequency as a function of b, which was calculated from the FE model having 60 elements. It can be seen that the relative change decreases as the width of the beam increases. As shown in Fig. 5.5(b) the shear stiffness of the core has the contributions from the variable stiffness due to MR fluid with magnetic field applied and the constant stiffness due to the off-state MR fluid. When the width of the beam increases, the region over which the magnetic field applied is fixed but the area having constant stiffness increases. Hence, the relative effect of the variable stiffness becomes less, and then the relative change in tuned frequency decreases.

By considering the width of the electromagnets shown in Fig. 5.2, which is about 9 mm, the ATVA is designed subsequently to be only a little wider than the electromagnets. Hence the width $b = 10$ mm is used in the rest of the studies.

5.4.3 Effects of Changing Length

The influence of the length of the beam on the change in tuned frequency is studied in this section. The ATVA beams with the length of 30, 60, 70, and 90 mm are investigated. All the four beams have thicknesses $h_1 = h_3 = 1$ mm, $h_2 = 3$ mm and width $b = 10$ mm. The relative change in tuned frequency of these ATVAs is shown in Fig. 5.9, which is simulated from the FE model with the element length of 1 mm and $G'_n = 4.1$ MPa. It can be seen that for $L \geqslant 60$ mm, the relative change decreases as the length of the beam increases. Since the total stiffness of the ATVA is the combination of the variable stiffness due to MR fluid and the constant stiffness due to the rest of the beam. When the beam is longer but the region over which magnetic field is applied is constant, the relative effect of the variable stiffness due to MR fluid becomes less and that of the constant stiffness increases. Hence the relative change in tuned frequency decreases. However, when $L < 60$ mm, the relative change in tuned frequency increases as the length of the beam increases. The reason for this might be that when the beam is too short, the deformation of the beam is significantly constrained by the electromagnets attached to the beam. As $L = 60$ mm gives the maximum change in tuned frequency, this value is used in the rest of the studies.

5.4.4 Effects of Changing the Number of Electromagnets

In this section, the effects of the number of electromagnets are investigated. The ATVA beams to which 4, 8, and 12 electromagnets are attached are shown in Figs. 5.10 (a-c) respectively. The values of geometric parameters studied before are used in this simulation, i.e. $h_1 = h_3 = 1$ mm, $h_2 = 3$ mm, $b = 10$ mm and $L = 60$ mm, and the on-state storage modulus is $G'_n = 4.1$ MPa. Fig. 5.11 (- • -) shows the relative change in tuned frequency for three numbers of electromagnets corresponding to Figs. 5.10(a-c). It can be seen that the relative change increases with an increase in the number of electromagnets. This is because increasing the number of electromagnets increases the region over which magnetic field is applied, and hence increases the area of changeable shear stiffness of MR fluid.

Although the beam with 12 electromagnets shows the highest change in tuned frequency, the beam with 8 electromagnets is selected. The reason for this is that the outer layers of the beam are thin, and hence they might not be able to support the weight of 12 electromagnets. The MR fluid-filled ATVA to which 8 electromagnets are attached, shown in Fig. 5.10(b), can produce a relative change in tuned frequency of approximately 40.6%.

Another design of the MR fluid-filled ATVA investigated is shown in Fig. 5.10(d). This ATVA has the same dimensions and material properties as the ATVA shown in Fig. 5.10(b), except that there are small air gaps in the middle layer. These air gaps, having a shear modulus of $G_a = 0$ Pa, aim to reduce the contribution of the constant shear stiffness in the core, and hence increase the influence of the variable shear stiffness of the MR fluid. The relative change in tuned frequency of this design is about 43.2% as shown in Fig. 5.11(+). This is higher than that of the beam in Fig. 5.10(b). Hence the MR fluid-filled ATVA investigated in the subsequent chapter is manufactured as the beam shown in Fig. 5.10(d) with $L = 60$ mm, $b = 10$ mm, $h_1 = h_3 = 1$ mm, and $h_2 = 3$ mm. Two frequency response functions ($I = 0$ A and $I = 0.8$ A) for the final design are shown in Fig. 5.12. It can be seen that the tuned frequency can be varied between 120 Hz and 172 Hz approximately.

5.5 Conclusions

The design of an MR fluid-filled ATVA has been presented in this chapter. The MR fluid-filled ATVA is a three-layer beam containing two elastic layers with MR fluid in the central core. Electromagnets are attached to the top and bottom layers to generate a magnetic field. To produce a high magnetic field across the MR core, a set of electromagnets was designed as a closed-loop circuit consisting of two electromagnets and the MR fluid in between. The shear stiffness of the MR fluid-filled ATVA is changed by varying the magnetic field across the core, which changes the shear modulus of MR fluid in the core, and hence the tuned frequency of the device.

Parametric studies were conducted to investigate the influence of geometric parameters on the change in tuned frequency of the MR fluid-filled ATVA. Five parameters

were examined numerically. These parameters are the thicknesses of the outer layers and the middle layer, the width and the length of the ATVA beam, and the number of electromagnets attached to the beam.

It was seen in the simulations that the relative change in tuned frequency decreases with increasing the width of the beam and the thickness of the outer layers. However increasing the number of electromagnets showed the opposite effect. The effects of the thickness of the middle layer and the length of the beam were divided into two regions. When the core thickness and the length of the beam are large, i.e. when $h_2 > 3$ mm and $L \geqslant 60$ mm, the relative change in tuned frequency decreases with increasing core thickness and length. However, this is not the case when $h_2 \leqslant 3$ mm and $L < 60$ mm.

Two configurations of the ATVA to which 8 electromagnets are attached were compared. Those are the ATVA with and without small air gaps in the middle layer. It was shown that the ATVA with air gaps provided a higher change in the tuned frequency. Hence the final design is chosen to be this configuration with the dimensions of $L = 60$ mm, $b = 10$ mm, $h_1 = h_3 = 1$ mm, and $h_2 = 3$ mm. This design would allow the tuned frequency to be changed by 43.2% approximately.

The MR fluid-filled ATVA presented in this chapter is manufactured and tested in Chapter 6. The experiments on the characteristics of the MR fluid-filled ATVA are conducted to verify the FE model presented in Chapter 4 and in this chapter, together with the empirical model for the shear modulus of MR fluid given in Chapter 3, and the simple model for the magnetic field shown in this chapter.

Tables

Permeability of the vacuum	μ_0	$4\pi \times 10^{-7}$ Hm^{-1}
Relative permeability of the mild steel	μ_s	~ 1000 [94]
Relative permeability of the MR fluid	μ_m	~ 5 [59]
Cross-sectional area of the steel path 1	A_{s1}	3.46 mm^2
Cross-sectional area of the steel path 2	A_{s2}	12.6 mm^2
Cross-sectional area of the MR gap	A_m	12.6 mm^2
Length of the steel path 1	l_{s1}	11.7 mm
Length of the steel path 2	l_{s2}	0.86 mm
Length of the MR gap	l_m	2.94 mm

Tab. 5.1: Electromagnet properties.

Density of perspex	ρ_p	1013 kg/m^3
Density of MR fluid	ρ_m	3740 kg/m^3
Young's modulus of elasticity of perspex	E	3.71×10^9 N/m^2
Storage modulus of tape	G'_t	3.12×10^5 Pa
Off-state storage modulus of MR fluid	G'_f	2.47×10^3 Pa
Poisson's ratio of perspex	ν_p	0.4
Loss factor of perspex	η_p	0.048
Loss factor of tape	η_t	0.36
Off-state loss factor of MR fluid	η_f	0.9
Radius of gyration of electromagnet	κ	0.003
Mass of electromagnet	M_m	1.15 g
Mass of mass-like host structure	m_1	7.5 g

Tab. 5.2: Geometrical and material properties of simulated ATVA and electromagnets.

Figures

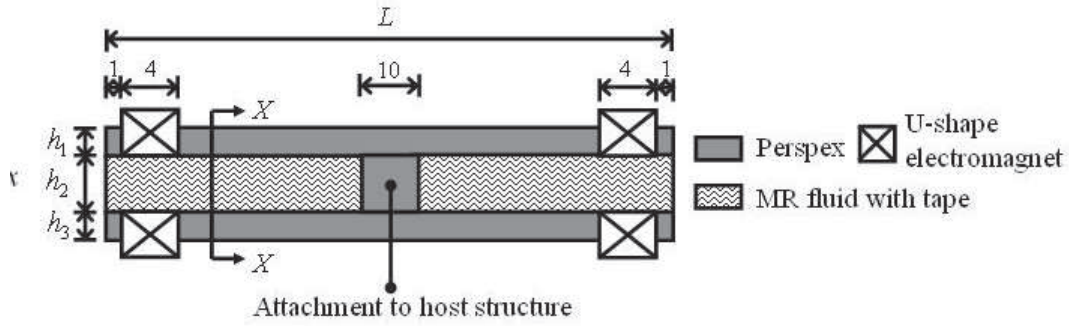

Fig. 5.1: MR fluid-filled ATVA. The ATVA of length L is attached at its centre to the host structure.

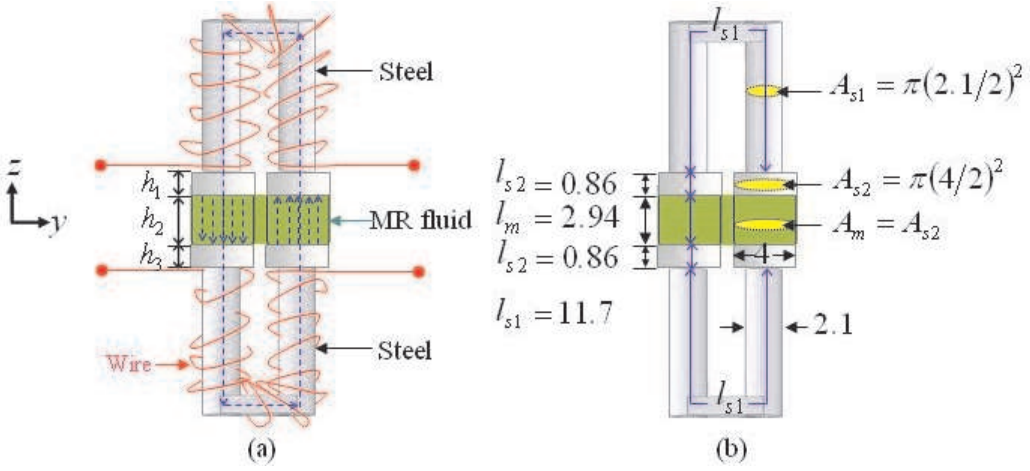

Fig. 5.2: Electromagnets shown in Fig. 5.1 (not to scale): --- magnetic flux generated by current flowing through the wire. (a) Sketch. (b) Dimensions. All dimensions are in mm.

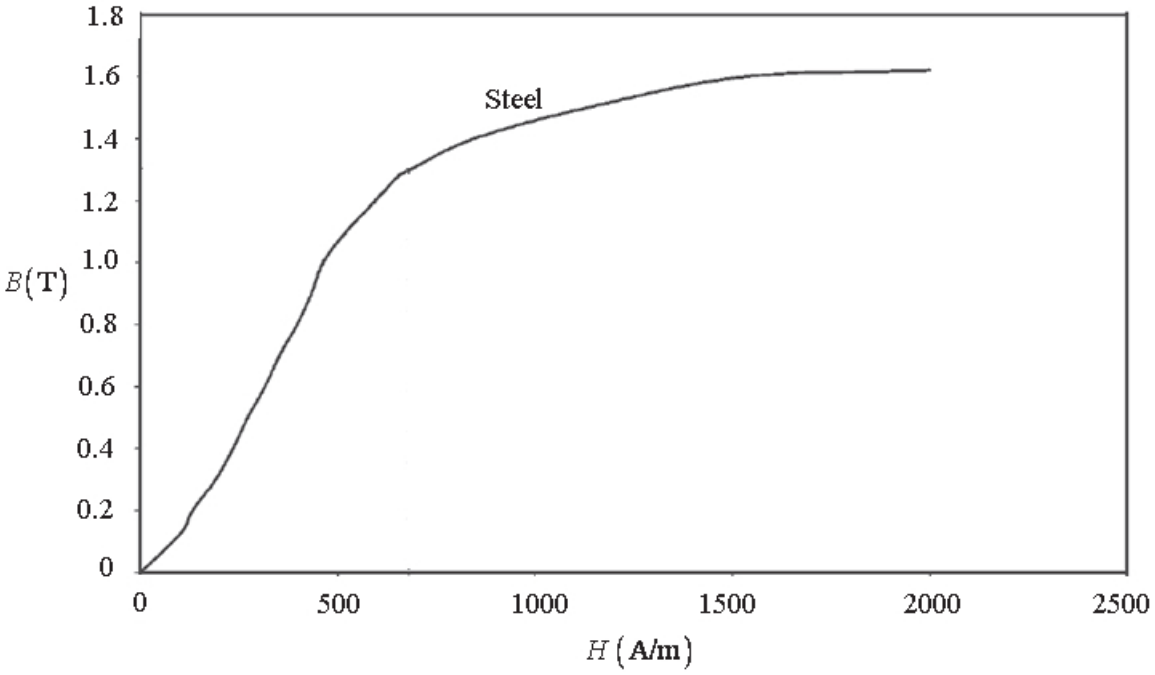

Fig. 5.3: Magnetization curve of mild steel [59].

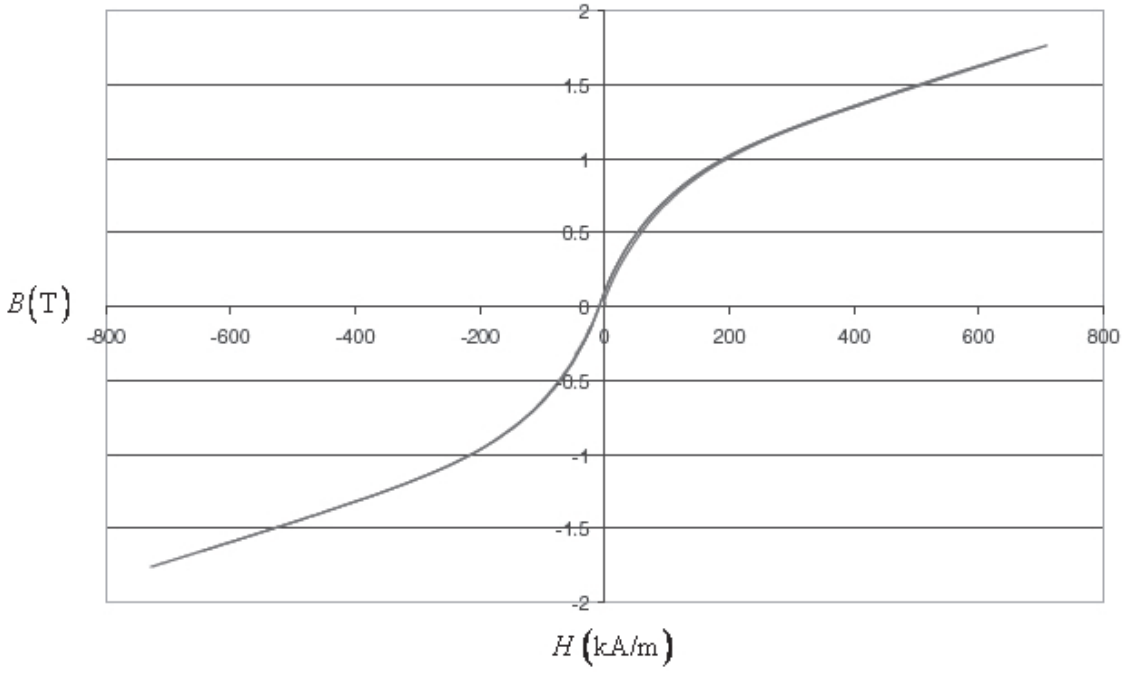

Fig. 5.4: Magnetization curve of MR fluid (MRF-140CG) [74].

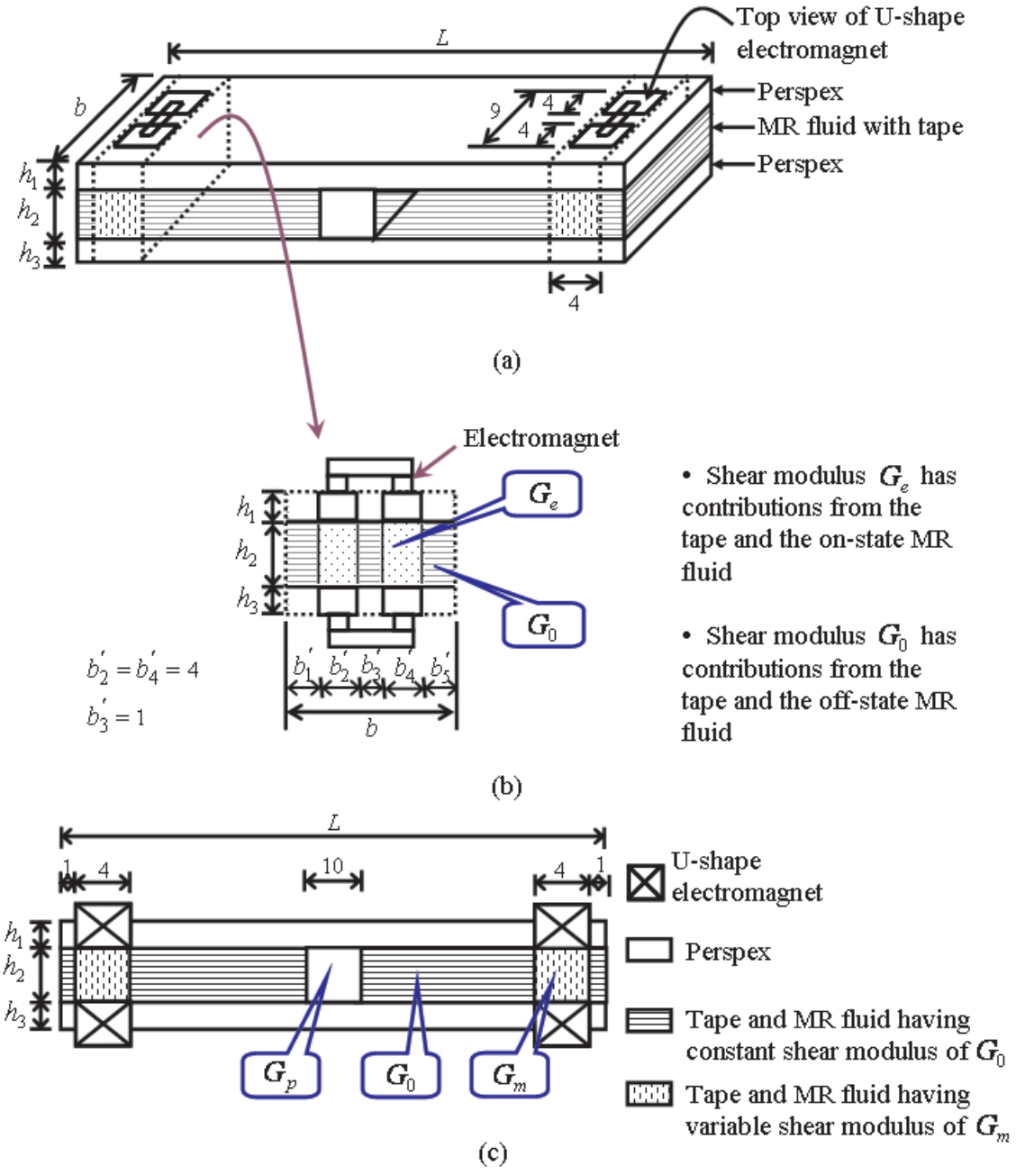

Fig. 5.5: Dimensions and configurations of the free-free non-uniform sandwich beam used in the parametric studies. (a) 3D view of the beam. (b) Cross-section of the beam where electromagnets are attached. (c) Side view of the beam. Dimensions are in mm (not to scale).

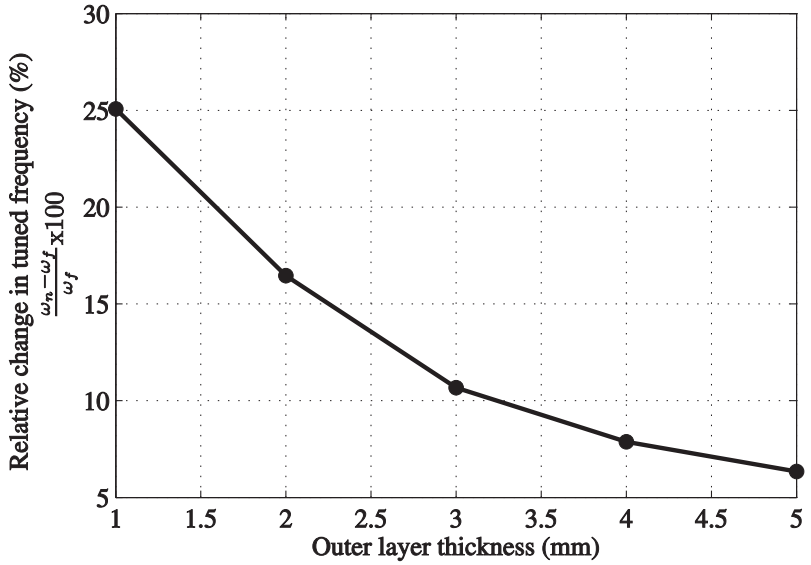

Fig. 5.6: Relative change in tuned frequency for various outer layer thicknesses. $L = 60$ mm, $b = 10$ mm, $h_2 = 3$ mm, and $G_n = 4.1(1 + \mathrm{i}0.04)$ MPa.

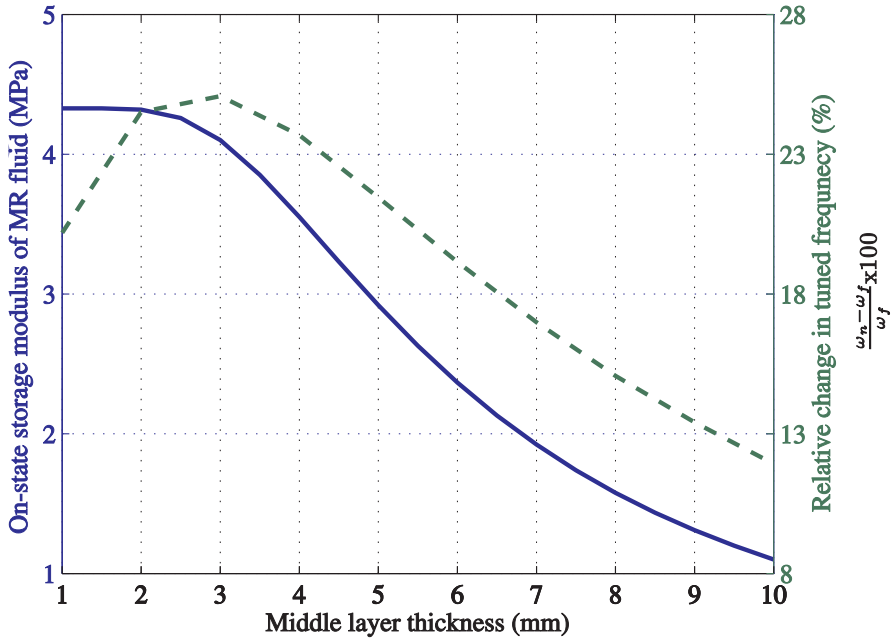

Fig. 5.7: The influence of the middle layer thickness on the on-state storage modulus of MR fluid in the middle layer — and the relative change in tuned frequency ---. $L = 60$ mm, $b = 10$ mm, and $h_1 = h_3 = 1$ mm.

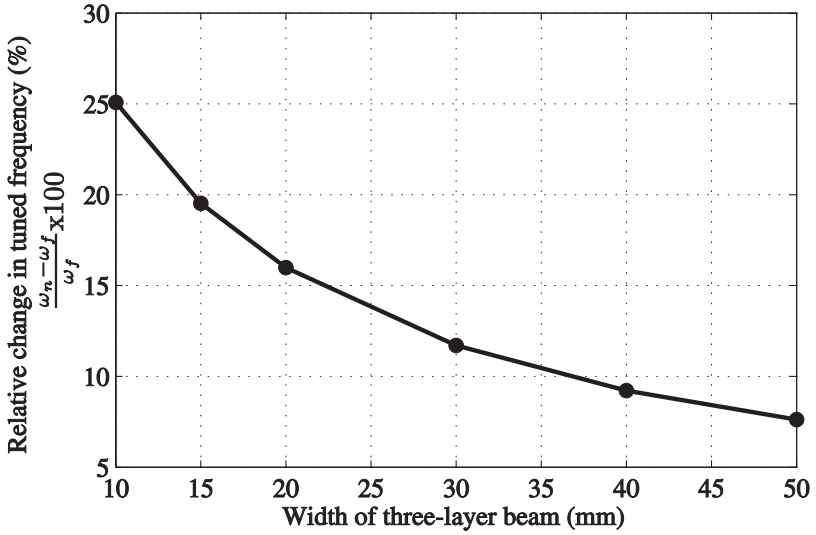

Fig. 5.8: Relative change in tuned frequency for various widths of the three-layer beam. $L = 60$ mm, $h_1 = h_3 = 1$ mm, $h_2 = 3$ mm, and $G_n = 4.1(1 + \text{i}0.04)$ MPa.

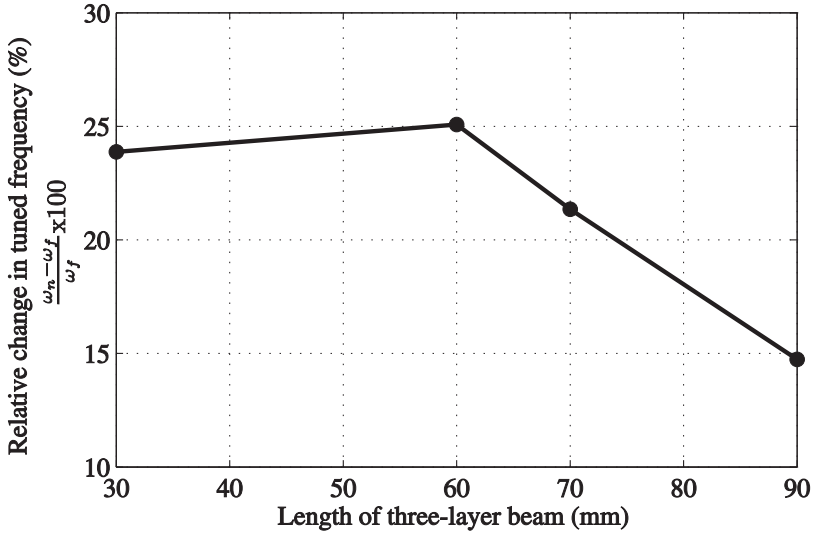

Fig. 5.9: Relative change in tuned frequency for various lengths of the three-layer beam. $b = 10$ mm, $h_1 = h_3 = 1$ mm, $h_2 = 3$ mm, and $G_n = 4.1(1+\text{i}0.04)$ MPa.

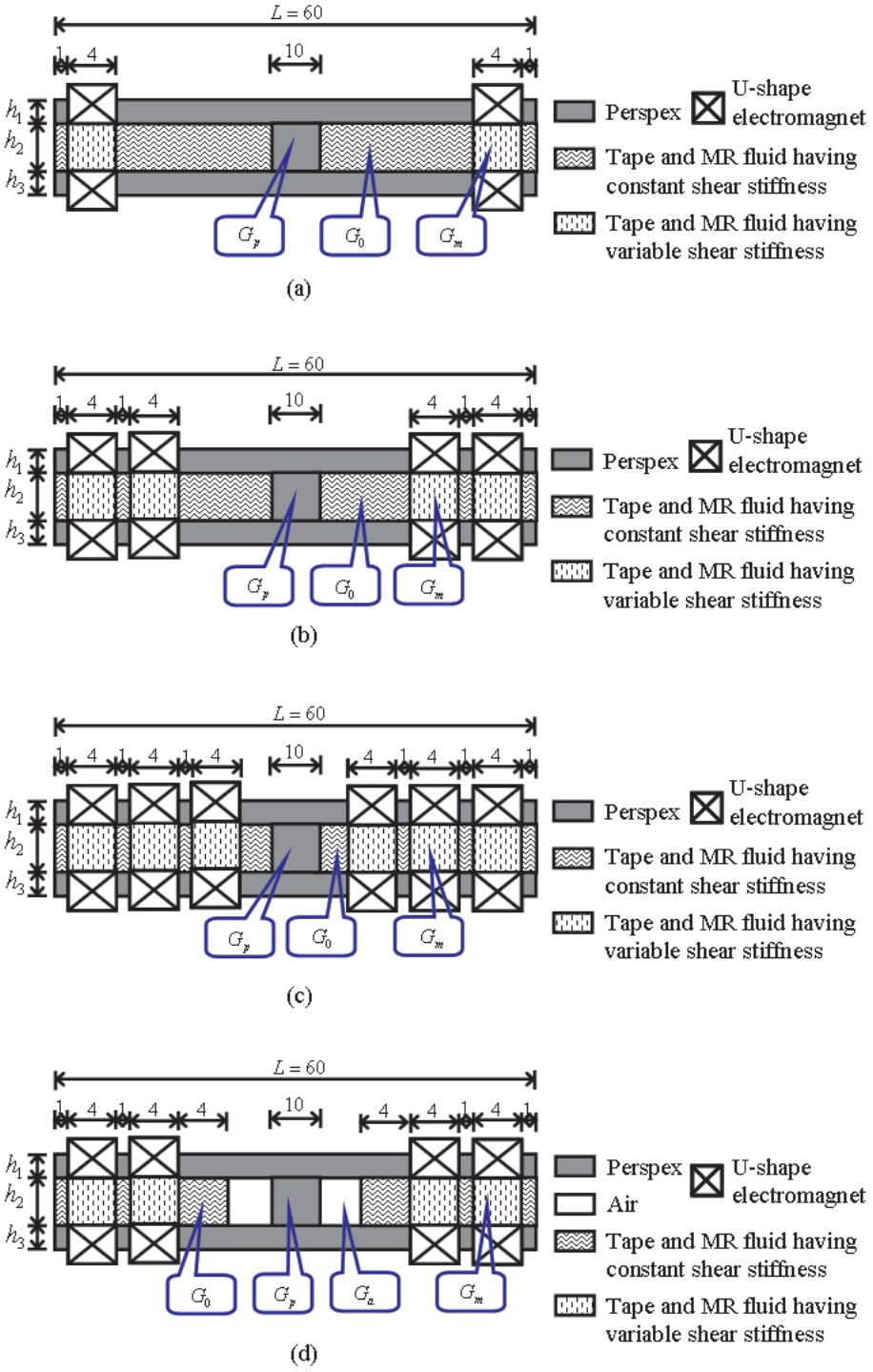

Fig. 5.10: Dimensions and four configurations of the free-free non-uniform sandwich beams used in the parametric studies (not to scale): (a) four electromagnets; (b) eight electromagnets; (c) twelve electromagnets; (d) eight electromagnets with air gaps in the middle layer. Dimensions are in mm.

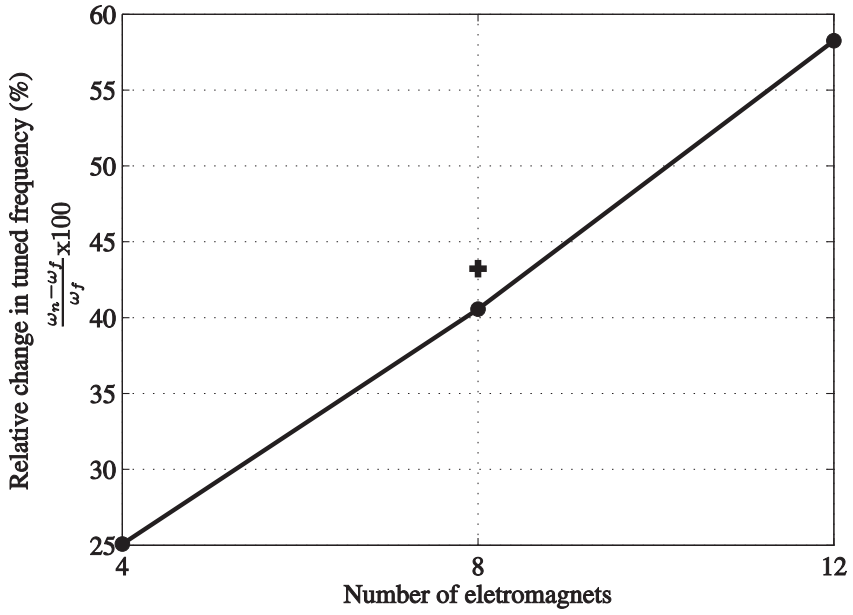

Fig. 5.11: Relative change in tuned frequency for various numbers of electromagnets attached to the three-layer beams in Figs. 5.10(a-d): + with and - • - without air gap. $L = 60$ mm, $b = 10$ mm, $h_1 = h_3 = 1$ mm, $h_2 = 3$ mm, and $G_n = 4.1(1 + \mathrm{i}0.04)$ MPa.

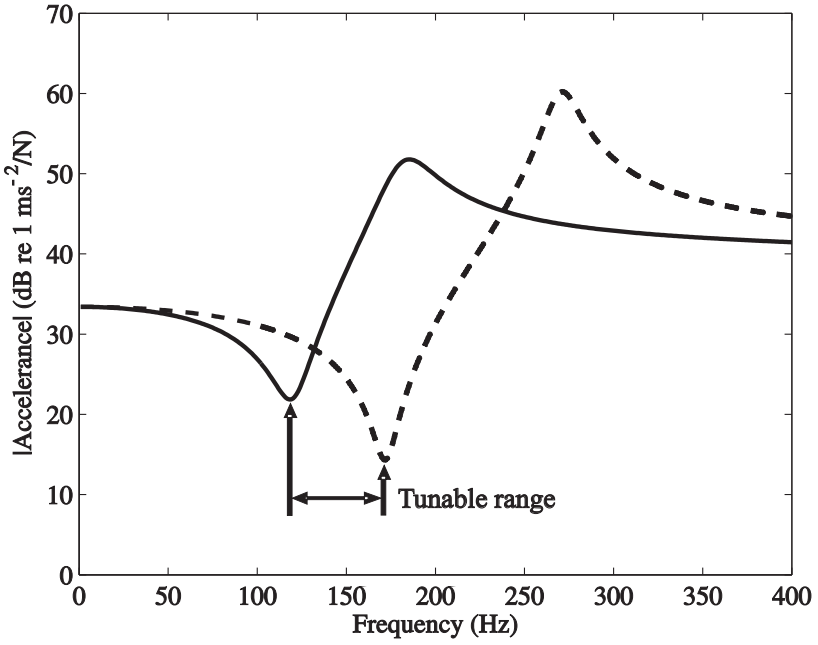

Fig. 5.12: Input accelerance of the three-layer beam shown in Fig. 5.10(d): — $I = 0$ A. and --- $I = 0.8$ A.

Chapter 6

Experimental Verification of the model of the MR Fluid-Filled ATVA

6.1 Introduction

In this chapter, the finite element (FE) model for the Magneto-Rheological (MR) absorber described in Chapter 4 is validated, and the characteristics of the absorber are investigated experimentally. The MR adaptive tuned vibration absorber (ATVA) consists of a three-layer beam with eight electromagnets attached, the design of which was described in Chapter 5. The top and bottom layers are made of perspex, while some sections of the middle layer contain MR fluid and are covered by tape.

The FE model is used to predict the responses of the MR fluid-filled ATVA. However, it is very likely that parameters used in the model, for example material properties of the beam, are not known accurately. Hence, estimates of these parameters are often made. One parameter, i.e. the shear modulus of the MR fluid, was obtained empirically in Chapter 3. In this chapter, two parameters, i.e. the Young's modulus of perspex and the stiffness of the tape, were estimated experimentally. An estimation process aims to fit the predicted anti-resonance frequency to measurements using model updating and sensitivity analysis.

Three experiments were conducted. Experiments on the perspex beam with an empty core and the beam with the tape were carried out to estimate the Young's

modulus of perspex and the shear modulus of the tape respectively. Lastly, the experiment on the MR fluid-filled ATVA subjected to various magnetic field strengths was performed. For the purpose of numerical simulations of the control system described in Chapter 7, the stiffness and damping of the MR fluid-filled ATVA are estimated from the measured data and their empirical models are developed.

Following this introduction, experiments to measure the point FRF of the test beam are described in section 6.2. Two parameters are estimated using the model updating method described in section 6.3 and the estimation process is presented in section 6.4. The experimental results of the MR fluid-filled ATVA are presented in section 6.5. The measured FRFs are also compared with the predictions from the FE model. The empirical models for stiffness and damping of the MR fluid-filled ATVA are developed in section 6.6. Finally, section 6.7 contains some conclusions. Further details can be found in Appendix C.

6.2 Experimental Apparatus and Methods

The MR fluid-filled ATVA manufactured is shown schematically in Fig. 6.1 and a photograph of the device is shown in Fig. 6.2. Some minor changes in the dimensions resulting from parametric studies were made due to manufacturing constraints. The material properties and dimensions of the manufactured beam are shown in Tab. 6.1. The dimensions of the beam, the mass of electromagnets and the density of perspex are obtained from the measurements. The density of the MR fluid is from the manufacture's data sheets and the Poisson's ratio of perspex is taken from [95].

Experiments were conducted to measure the point accelerance of the test beam. The experimental set-up is shown in Fig. 6.3. The centre point of the test beam was attached to an LDS shaker model V201 through an impedance head model PCB 288D01. A Hewlett Packard (HP) 3566A spectrum analyser, which also acted as a signal generator, generated a random input signal to drive the shaker through a Cambridge audio model A1 integrated amplifier, and an ammeter. Hence the test beam was driven at its centre by the shaker, while the two ends of the beam were allowed to move freely. A Lambda power supply model ZUP 10-20 produced the

current in the electromagnets to generate the magnetic field. The impedance head was used to measure force and acceleration at the centre of the beam. The measured signals from the impedance head were input to the spectrum analyser via a PCB Piezotronics model 442B104 4-channel signal conditioner. The input accelerance was subsequently processed in MATLAB using these signals, and hence was scaled by the appropriate calibration factor, which depends on the sensitivities of the force transducer and the signal conditioner gain given in Tab. C.2. Relative calibration of the impedance head was carried out as described in Appendix C. The effective mass on the structure side of the impedance head was estimated to be 6.5 g.

6.3 Model Updating and Sensitivities

The model updating technique aims to improve the FE model and to estimate unknown parameters using the measured data. The model updating can be performed using either the modal data or the frequency domain data. The method employing the modal data can be used to update the parameters in the FE model such that the predicted resonance frequency fits well with the measured value. This method concerns the eigenvalue sensitivity, which is given by [96]

$$\frac{\partial(\omega_r^2)_j}{\partial p} = \phi_j^{\mathrm{T}}\left[\frac{\partial \mathbf{K}}{\partial p} - \lambda_j \frac{\partial \mathbf{M}}{\partial p}\right]\phi_j \tag{6.1}$$

where p, ϕ_j and λ_j are the parameter to be updated and the mass normalised eigenvector and eigenvalue of mode j respectively. However an important part of this thesis is the tuned frequency which is the lowest anti-resonance frequency of the ATVA measured at the centre. Hence the updating method concerning the sensitivity of this frequency is considered here. However the sensitivity of the anti-resonance frequency can be determined in terms of the eigenvalue sensitivity as shown in the following.

The sensitivity of the anti-resonance frequency can be estimated using the 2DOF undamped model of the TVA presented in Chapter 2. It was shown in Eq. (2.16)

that

$$\omega_a^2 = \frac{1}{1+\mu}\,\omega_r^2. \tag{6.2}$$

Assuming that the parameter being updated affects only the stiffness, not the mass, of the ATVA, the sensitivity of the anti-resonance frequency is then given by

$$S_a = \frac{\partial(\omega_a^2)}{\partial p} = \frac{1}{1+\mu}\,\frac{\partial(\omega_r^2)}{\partial p}. \tag{6.3}$$

Rearranging Eq. (6.3) using $\frac{1}{1+\mu} = \left(\frac{\omega_a}{\omega_r}\right)^2$ gives

$$S_a = \left(\frac{\omega_a}{\omega_r}\right)^2 \frac{\partial(\omega_r^2)}{\partial p} \tag{6.4}$$

where the eigenvalue sensitivity $\frac{\partial(\omega_r^2)}{\partial p}$ is given in Eq. (6.1). Since $S_a = \frac{\partial(\omega_a^2)}{\partial p}$, the updated parameter p can be approximated by

$$p_{i+1} = p_i - \frac{1}{S_a}\left[(\omega_a^m)^2 - (\omega_a^F)^2\right] \tag{6.5}$$

where p_i, p_{i+1}, ω_a^m and ω_a^F are the values of the parameter p at the i and at the $i+1$ step of the updating process and the measured and the predicted anti-resonance frequencies respectively. The model updating presented in this section is used to update the Young's modulus of perspex and the stiffness of the tape as described in the following section.

6.4 Estimating Young's Modulus of Perspex and Shear Stiffness of Tape

The perspex three-layer beam without the MR fluid and the tape in the core was used to estimate the Young's modulus of the perspex beam. The point FRF of the beam was measured by the method described in section 6.2. However no current was applied to electromagnets in this test. The measured anti-resonance frequency and total loss factor were determined from the measured FRF using the circle-fit method [93]. These measured values are given in Tab. 6.2.

The FE model for the perspex beam was used to simulate the FRF and the modal properties of the beam. The parameters used in the FE model are shown in Tab. 6.1. Here the contribution of the mass-like host structure m_1 was also considered in the FE model. The mass m_1 was estimated in Appendix C as 6.5 g. However, m_1 was refined here to improve the fit between the measured and predicted FRFs. The refinement was done in an ad-hoc way, i.e. fitting by eye. The value of m_1 after refinement was found to be 7.5 g and this value is used in the rest of the thesis. The loss factor of perspex is 0.048, which is equal to the measured total loss factor of the perspex beam. As for the experimental results, the predicted anti-resonance frequency was obtained from the FRF using the circle-fit method.

By Eq. (6.5) parameter p, i.e. the storage modulus of perspex E', was updated until the squared error in the anti-resonance frequency was less than 0.001. The Young's modulus of perspex was found to be $E' = 3.71 \times 10^9 \mathrm{N/m^2}$. Fig. 6.4 shows the predicted and measured FRFs of the perspex beam. It can be seen that the predicted FRF agrees well with the measured FRF, especially around the anti-resonance.

A similar procedure was used to update the shear stiffness of the tape from the measured accelerance of the perspex beam with tape shown in Fig. 6.2. The effective shear modulus of the tape was estimated as $G'_t = 3.12 \times 10^5$ Pa and the loss factor $\eta_t = 0.36$. The predicted anti-resonance frequency and total loss factor obtained from the FE model are compared to the measured results in Tab. 6.3. Fig. 6.5 shows a good agreement between the predicted and measured FRFs.

6.5 Experimental Results of MR Fluid-Filled ATVA

The MR fluid-filled beam was tested experimentally over the entire tunable range. The point accelerance measurements were taken at different levels of current I and hence various magnetic field strengths. The measured tuned frequencies and loss factors were obtained from the measured FRFs using the circle-fit method and are shown in Tab. C.3. The model for the magnetic field presented in Chapter 5 was used to calculated the magnetic flux density across the MR core. Two measurements ($I = 0$ A and $I = 646$ mA) are shown in Fig. 6.6. It can be seen that as I increases

the tuned frequency, i.e. the frequency when the FRF is minimum, increases because the shear modulus of the MR fluid, and hence the effective stiffness of the ATVA increases. The MR fluid-filled ATVA allows the tuned frequency to be changed by 40.6%. The tunable range of the MR fluid-filled ATVA is between 106 and 149 Hz approximately.

The predicted FRFs for different levels of current obtained from the FE model are compared to the measurements in Fig. 6.7. The FE model used parameters shown in Tab. 6.1, $m_1 = 7.5$ g, the measured storage modulus and loss factor of MR fluid in Chapter 3 (Eqs. (3.19)-(3.20)), and the estimated Young's modulus of perspex and effective shear modulus of tape in section 6.4. Only two parameters, i.e. storage modulus and loss factor of the MR fluid, vary with the current applied to electromagnets. The FE model was computed using 60 elements. It can be seen that the predicted FRFs fit well with the measured FRFs for low currents shown in Figs. 6.7(a)-(d). However, for higher currents, i.e. $I > 182$ mA shown in Figs. 6.7(e)-(i), the predicted amplitudes around resonance are higher and those around anti-resonance are lower than the measured amplitudes. The difference in the amplitudes is due to the difference between the measured and predicted damping of the beam.

Fig. 6.8 shows the measured and predicted total damping loss factors of the beam as a function of electromagnet current. The measured total loss factors (+) were extracted from the measured FRFs using the circle-fit method. Although the total loss factor of the ATVA has contributions from the loss factor of the perspex, the tape, and the MR fluid, only the loss factor of MR fluid varies with the current. As a result, the characteristics of the total loss factor follow the behaviour of the loss factor of the MR fluid shown in Fig. 3.9, i.e. the loss factor decreases with increasing the magnetic field except for the points at very low magnetic fields. Fig. 6.8 (solid line) shows the predicted total loss factors obtained from the FE model using the empirical exponential model for loss factor of MR fluid η shown in Eq. (3.20). It can be seen that the predicted loss factor is much lower than the measured loss factor for high electromagnet currents. To improve the fit between the measurements and the predictions, the loss factor of MR fluid η was obtained from the measured FRFs using the model updating as shown in Fig. 6.9(+), and then an empirical linear model for

η was determined by least square fitting method. The empirical model was found to be

$$\eta = -2.51B + 0.8 \tag{6.6}$$

where B is the magnetic flux density. The model is compared with the measured values in Fig. 6.9. The predicted total loss factors using this model for η are also shown in Fig. 6.8 (dashed line). It can be seen that the dashed line fits to the measured data better than the solid line. The empirical model for η shown in Eq. (6.6) is used in the rest of the thesis. The predicted FRFs for $I = 0$ A and $I = 646$ mA are compared to the measured FRFs in Figs 6.10 and 6.11 respectively. The rest of the FRFs are shown in Appendix C. The dependence of the tuned frequency on I is shown in Fig. 6.12. It can be seen that the predictions reasonably accurate although the predicted tuned frequencies are little higher than the measured tuned frequencies.

6.6 Empirical Models for Stiffness and Damping

The numerical simulations of the control system require the characteristics, such as mass, stiffness, and damping, of the ATVA. The mass of the ATVA can be estimated from the measured FRF. As described in Chapter 2, the FRF asymptotes to the total mass of the system m_T at low frequencies, and to mass m_1 at high frequencies. The total mass m_T and mass m_1 were determined from Fig. 6.10 to be $m_T = 21.6$ g and $m_1 = 7.5$ g. Hence, the mass of the absorber is $m_a = m_T - m_1 = 14.1$ g.

The measured effective stiffness of the MR fluid-filled ATVA as a function of magnetic field can be obtained from

$$k_a^m = (\omega_a^m)^2 m_a, \tag{6.7}$$

because $(\omega_a^m)^2$ varies with the magnetic field, and is shown in Fig. 6.13(+). It can be seen that the stiffness of the ATVA can be changed by about 98% when the electromagnet current is increased to 646 mA. The predicted stiffness obtained from the FE model is also shown in Fig. 6.13 (dashed line). Note that the predictions are slightly higher than the measurements. For simplicity, an empirical model for

stiffness used in the next chapter was determined from the measured data by a least square fitting method, and was found to be

$$k_a = 0.0017G' + 6344. \tag{6.8}$$

The model is compared to the measurement in Fig. 6.13.

The measured effective viscous damping coefficient of the ATVA is given by

$$c_a^m = \eta_T^m m_a \omega_a^m \tag{6.9}$$

and is compared to a quadratic least squares fit

$$c_a = -11.16\eta^2 + 11.5\eta - 0.62 \tag{6.10}$$

in Fig. 6.14. Here η is the loss factor of the MR fluid and η_T^m is the total loss factor of the ATVA corresponding to the loss factor η of Eq. (6.6). It can be seen from Fig. 6.14(+) that the viscous damping coefficient of the ATVA shows the same trend as the total loss factor of the ATVA, i.e. the damping increases as the magnetic field decreases or as the loss factor of MR fluid increases. Still the points at very low magnetic field or at very high loss factor of the MR fluid shows the opposite trend.

6.7 Conclusions

In this chapter, the Young's modulus of perspex and the stiffness of the tape were estimated experimentally. An estimation process has been described that used model updating and sensitivity analysis to fit the predicted anti-resonance frequencies of the perspex beam and the perspex beam with tape to the measured values.

The MR fluid-filled ATVA was manufactured and tested. Experiments on the MR fluid-filled ATVA with various currents were conducted to investigate the characteristics of the ATVA and to verify the FE model developed in Chapter 4, together with the empirical models for the storage modulus and the loss factor of MR fluid presented in Chapter 3 and the simple model for the magnetic field derived in Chapter

5. The experimental results show that the MR fluid-filled ATVA exhibited significant change in the tuned frequency, which was about 40.6%, when the applied current was increased to 646 mA.

Since the loss factor of the MR fluid for high magnetic fields obtained from Chapter 3 was underestimated, the predicted FRFs fit well with the measurements only at low magnetic fields. The loss factor of the MR fluid for various magnetic fields was also estimated using model updating, and hence an empirical linear model for the loss factor was developed to improve the fits between the predictions and the measurements.

Empirical models for the stiffness and viscous damping coefficient of the MR fluid-filled ATVA were proposed by fitting polynomials to the measured values. These models are required for the numerical simulations of the ATVA with a control system conducted in the subsequent chapter.

Tables

Length of the beam	L	59.53 mm
Width of the beam	b	10.25 mm
Thickness of the top layer	h_1	0.86 mm
Thickness of the bottom layer	h_3	0.86 mm
Thickness of the middle layer	h_2	2.94 mm
Density of perspex	ρ_p	1013 kg/m^3
Density of MR fluid	ρ_m	3740 kg/m^3
Poisson's ratio of perspex	ν_p	0.4 [95]
Radius of gyration of an electromagnet	κ	0.003 m
Mass of an electromagnet	M_m	1.15 g

Tab. 6.1: Geometrical and material properties of the MR fluid-filled ATVA and electromagnets.

Anti-resonance frequency (Hz)		Total loss factor		Square Error
Measurement	FE model	Measurement	FE model	
$\omega_a^m/(2\pi)$	$\omega_a^F/(2\pi)$	η_T^m	η_T^F	$\left(\frac{\omega_a^m-\omega_a^F}{2\pi}\right)^2$
88.8481	88.8737	0.0480	0.0480	0.0007

Tab. 6.2: Measured and predicted anti-resonance frequencies and total loss factors of perspex beam. $E' = 3.71 \times 10^9$ N/m^2 and $\eta_p = 0.048$.

Anti-resonance frequency (Hz)		Total loss factor		Square Error
Measurement	FE model	Measurement	FE model	
$\omega_a^m/(2\pi)$	$\omega_a^F/(2\pi)$	η_T^m	η_T^F	$\left(\frac{\omega_a^m-\omega_a^F}{2\pi}\right)^2$
120.3514	120.3347	0.1566	0.1634	0.0003

Tab. 6.3: Measured and predicted anti-resonance frequencies and total loss factors of perspex beam with the tape, but without MR fluid. $G_t' = 3.12 \times 10^5$ Pa and $\eta_t = 0.36$.

Figures

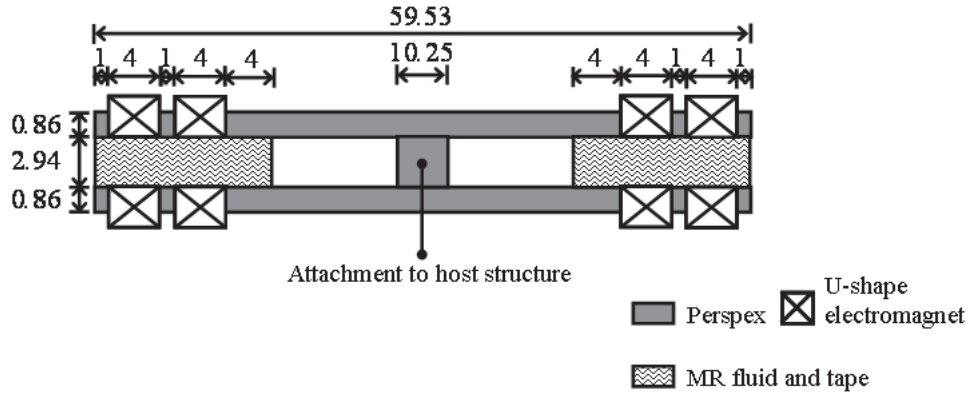

Fig. 6.1: Sketch and dimensions of MR fluid-filled ATVA. Dimensions are in mm.

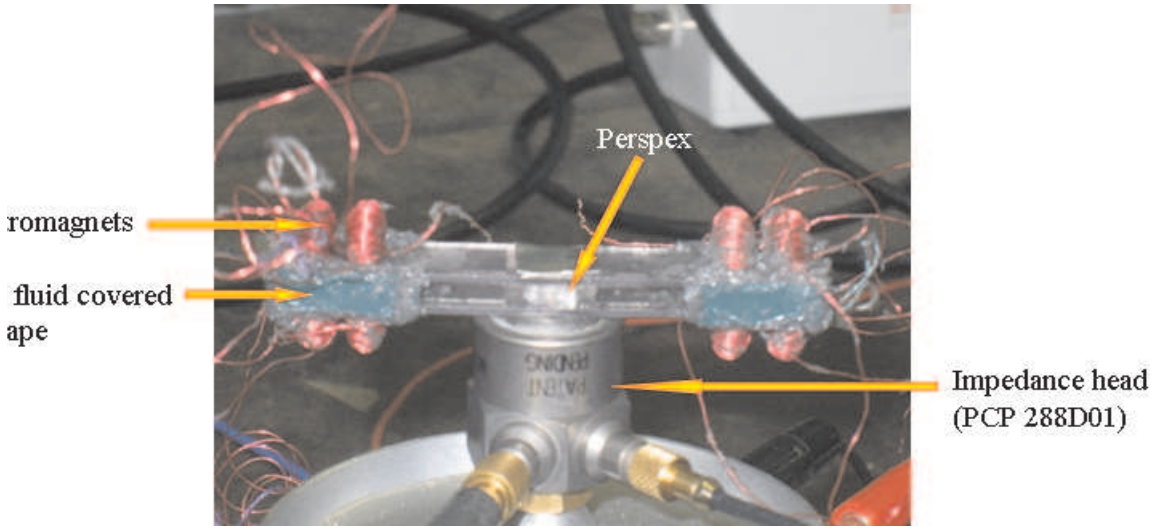

Fig. 6.2: MR ATVA with MR fluid retained by tape in the middle layer.

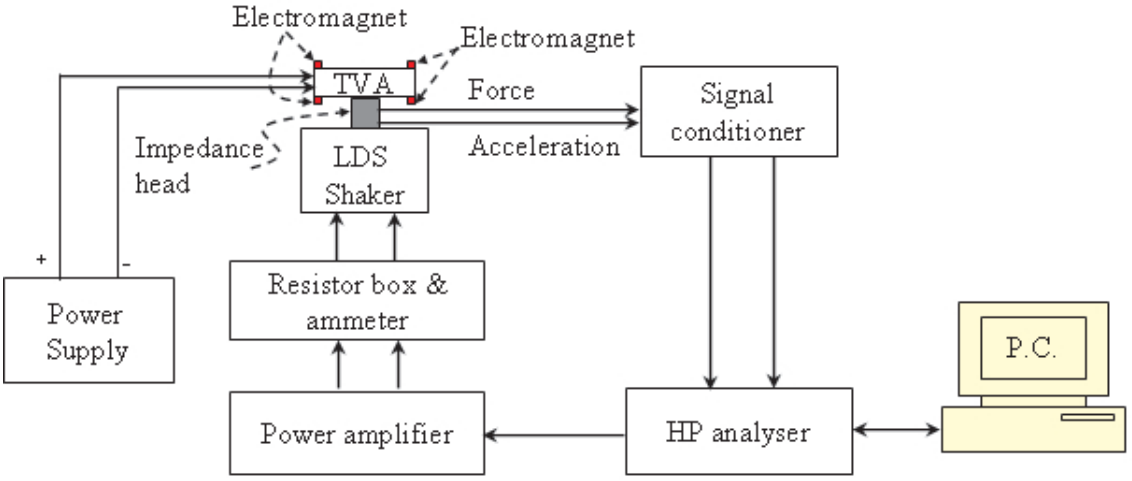

Fig. 6.3: Experimental set-up to measure the accelerance of the MR fluid-filled ATVA.

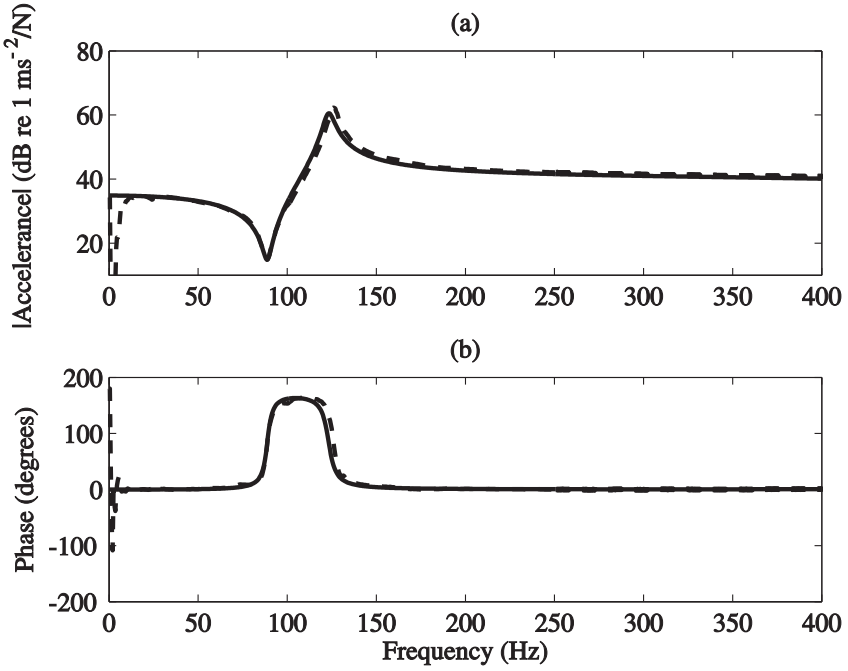

Fig. 6.4: Input accelerance of the perspex beam with empty core:--- measured; — predicted. (a) Magnitude of accelerance. (b) Phase of accelerance.

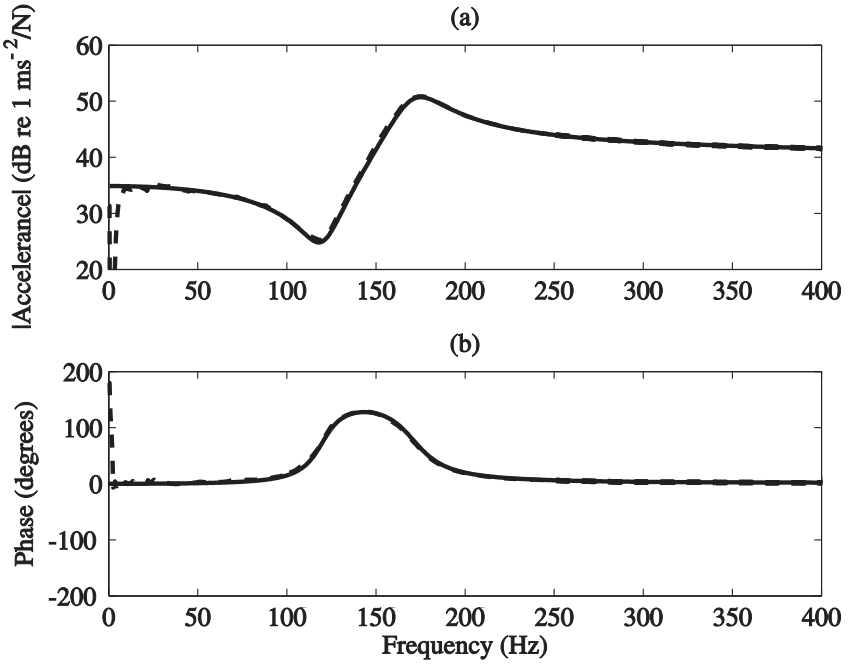

Fig. 6.5: Input accelerance of the perspex beam with tape, but without MR fluid in the core:--- measured; — predicted. (a) Magnitude of accelerance. (b) Phase of accelerance.

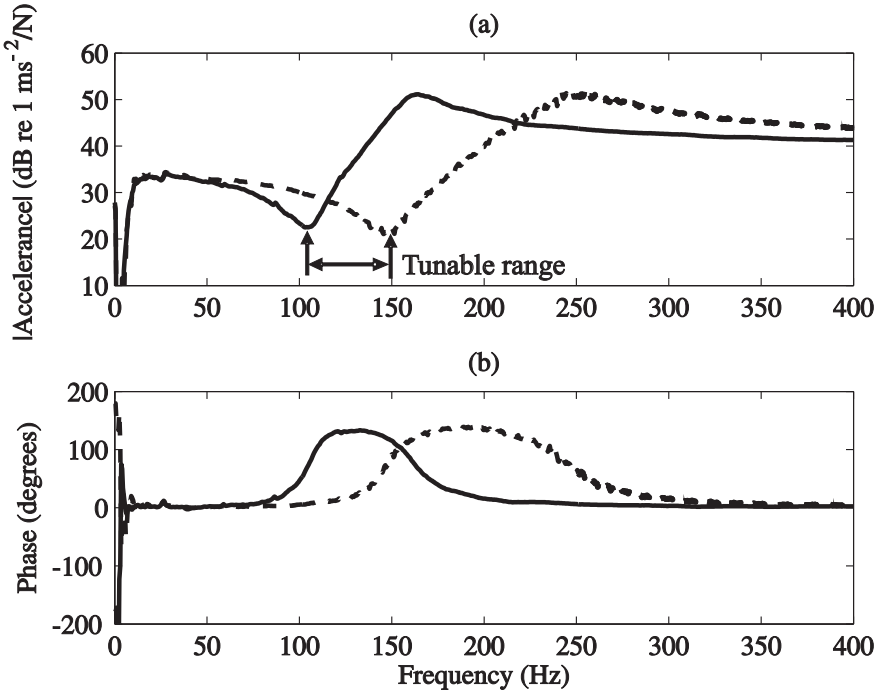

Fig. 6.6: Measured input accelerance of the MR fluid-filled ATVA: — $I = 0$ A and --- $I = 646$ mA. (a) Magnitude of accelerance. (b) Phase of accelerance.

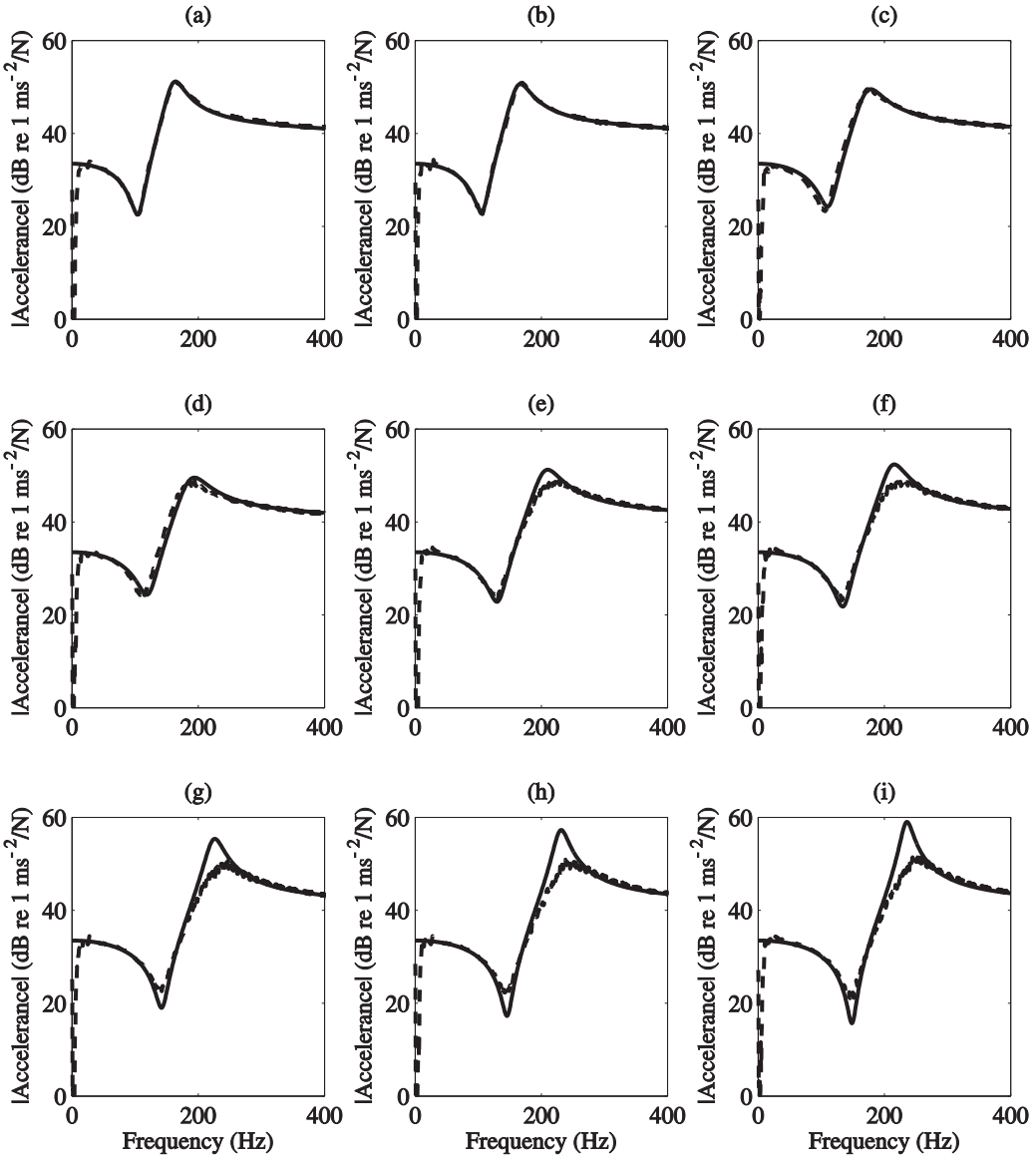

Fig. 6.7: Input accelerance of the MR fluid-filled ATVA with I equal to: (a) 0 A; (b) 46 mA; (c) 109 mA; (d) 182 mA; (e) 280 mA; (f) 327 mA; (g) 446 mA; (h) 534 mA; (i) 646 mA. --- measured and — predicted.

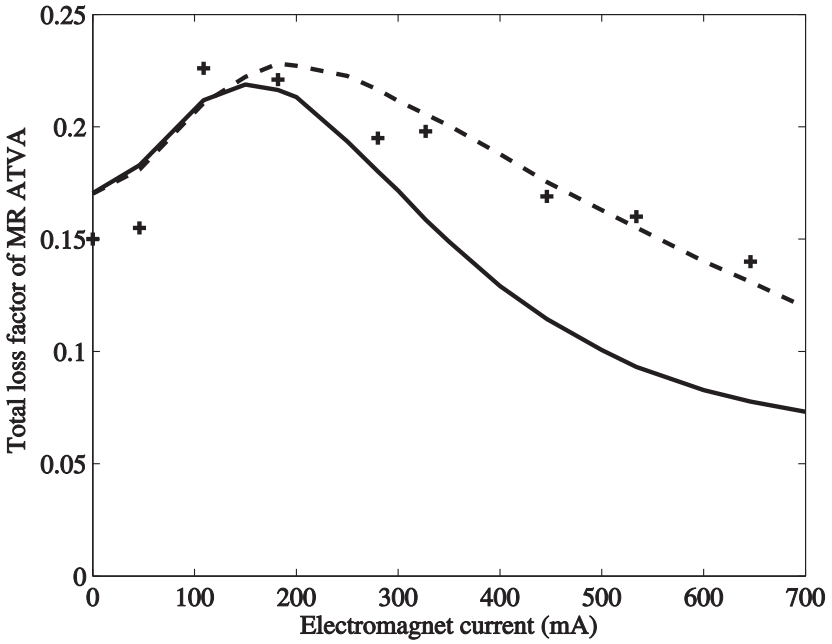

Fig. 6.8: Total loss factor of MR fluid-filled ATVA. +++ measured; — empirical exponential model for η from Eq. (3.20); --- empirical linear model for η from Eq. (6.6).

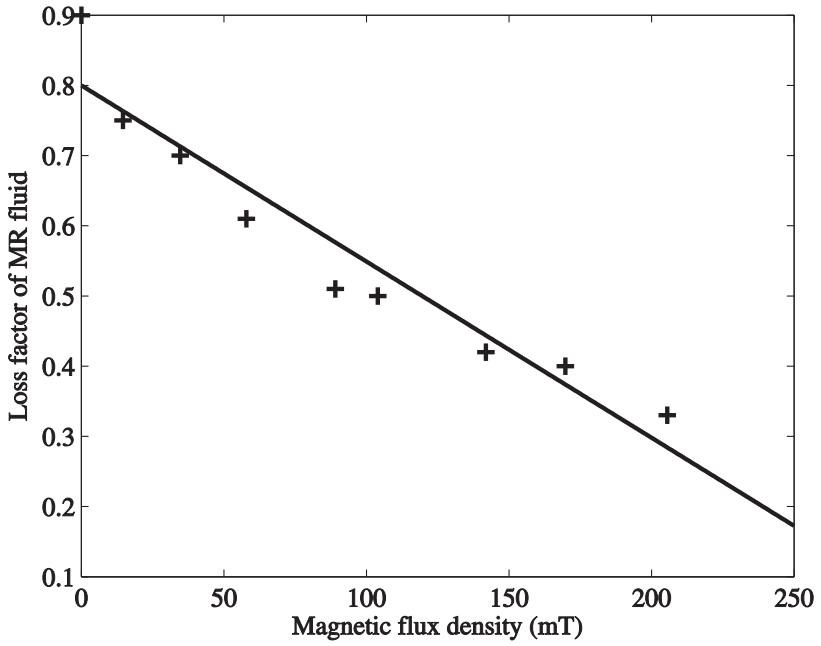

Fig. 6.9: Loss factor of MR fluid:+++ measured; — empirical linear model of Eq. (6.6).

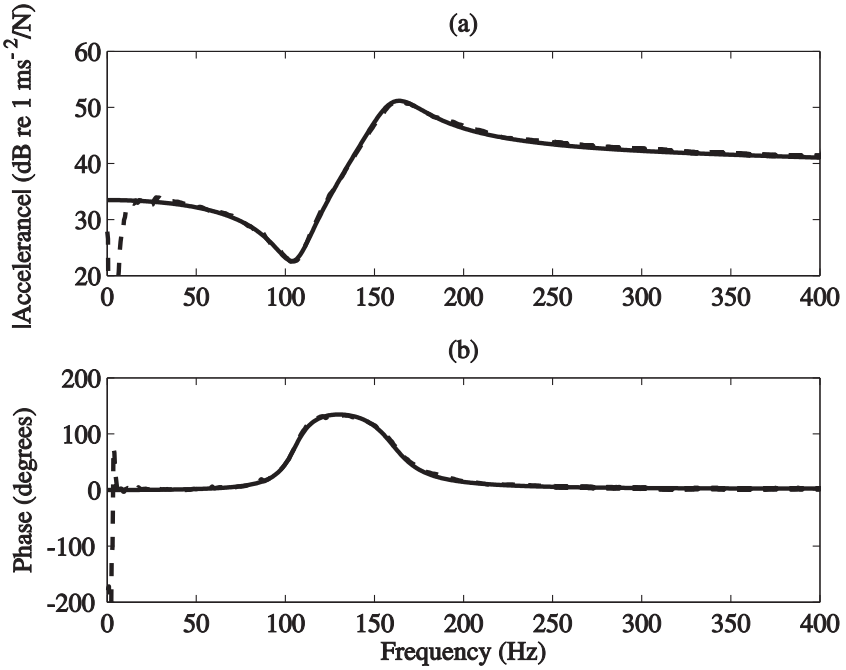

Fig. 6.10: Input accelerance of the MR fluid-filled ATVA without magnetic field:--- measured; — predicted.

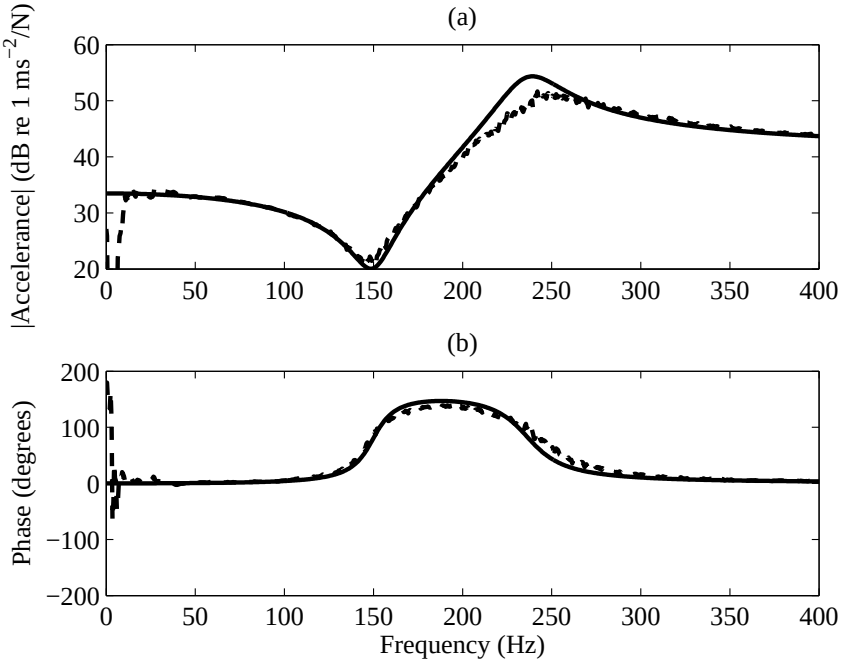

Fig. 6.11: Input accelerance of the MR fluid-filled ATVA with $I = 646$ mA:--- measured; — predicted.

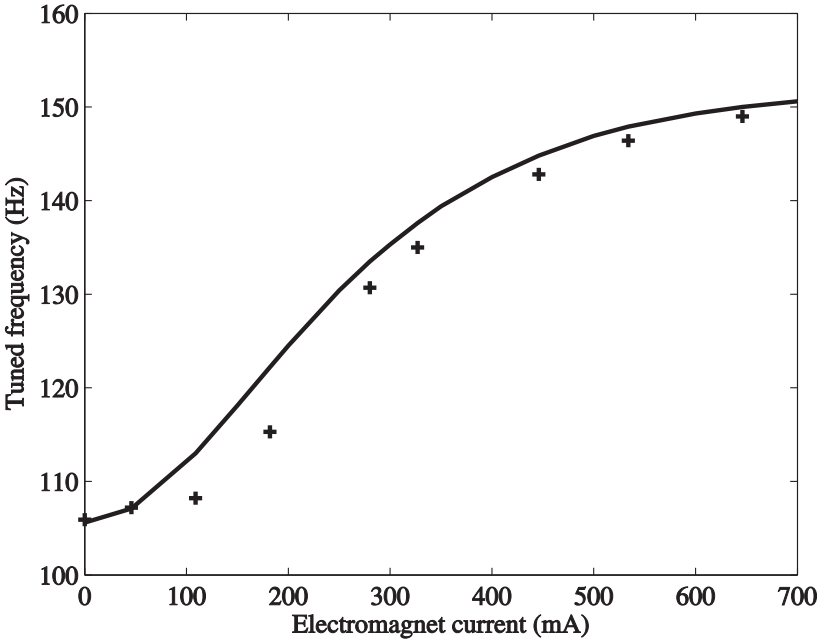

Fig. 6.12: Tuned frequency of the MR fluid-filled ATVA:+++ measured; — predicted.

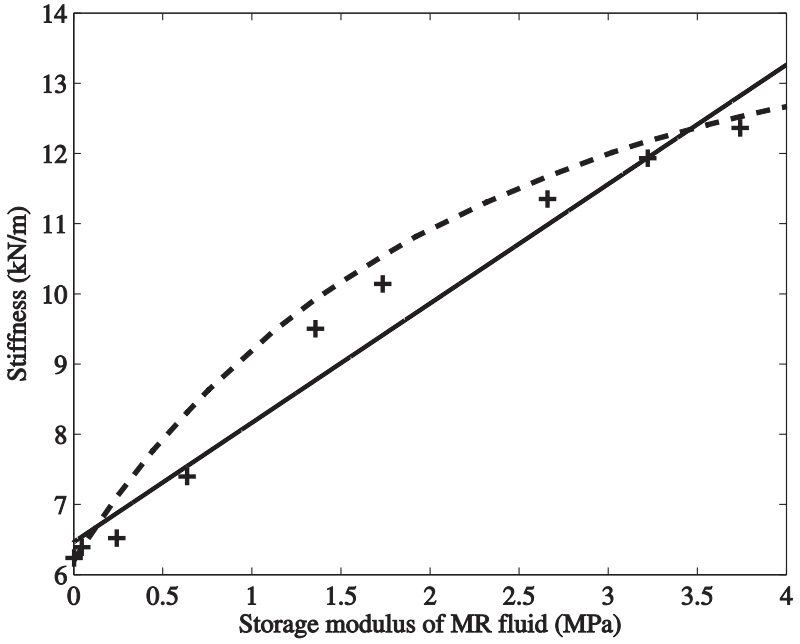

Fig. 6.13: Stiffness of the MR fluid-filled ATVA:+++ measured; --- predicted; — empirical linear model of Eq. (6.8).

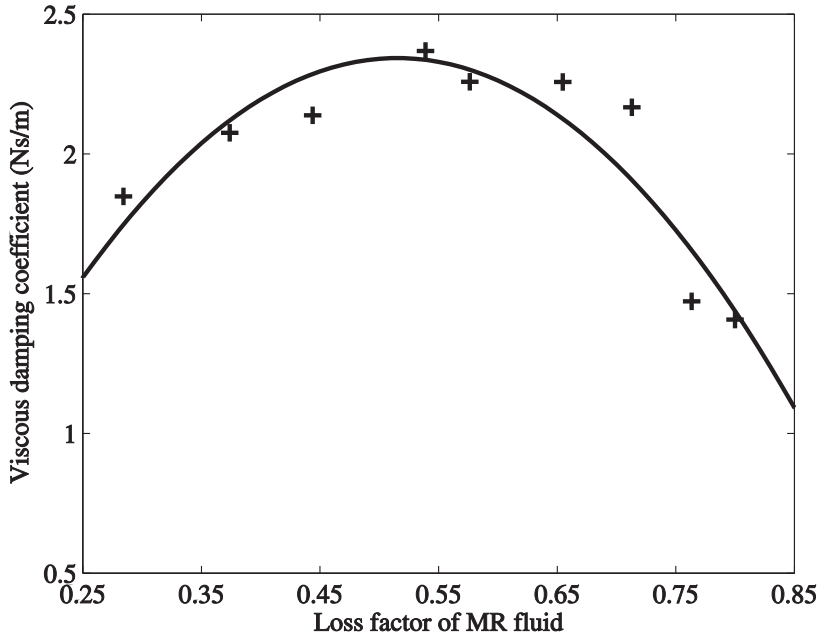

Fig. 6.14: Viscous damping coefficient of the MR fluid-filled ATVA:+++ empirical model for loss factor (Eq. (6.6)) fitted to measured data; — empirical quadratic model of Eq. (6.10).

Chapter 7

Control of the MR fluid-filled ATVA

7.1 Introduction

It is often the case that a passive tuned vibration absorber (TVA) mistunes, i.e. its condition deviates from the tuned condition, if a forcing frequency changes. The mistuning can degrade the performance of the TVA and can possibly increase the vibration of the host structure. To prevent this a control system is required to retune the TVA so that its natural frequency always coincides with the forcing frequency. The combination of the control system and the TVA would make TVA adaptive. The adaptive TVA (ATVA) here involves an adaptive-passive control strategy and the variable properties of Magneto-Rheological (MR) fluid. The control attempts to adjust the shear stiffness of the MR fluid, and hence vary the natural frequency of the ATVA. The ATVA employing MR fluid is called an MR fluid-filled ATVA, which was introduced previously in the thesis.

An important part of the MR fluid-filled ATVA is the ability to retune itself in real-time. Although it was illustrated in Chapter 6 that the MR fluid-filled ATVA is able to be tuned manually within a specific frequency range, automatic real-time tuning is required. In this chapter, real-time control of the MR fluid-filled ATVA is investigated numerically and experimentally.

The numerical studies use the two degrees-of-freedom (DOFs) mass-spring model presented in Chapter 2 together with an empirical model for the storage modulus of

MR fluid developed in Chapter 3, a simple model for the magnetic field in Chapter 5, and stiffness and damping models in Chapter 6 to simulate the behaviour of the MR fluid-filled ATVA. The control algorithm, which aims to drive the cosine of the phase angle between the velocities of the host structure and the ATVA to zero, is implemented. This algorithm can be found in a number of studies, for example [33] and [36].

The experiments were conducted to demonstrate the real behaviour of the MR fluid-filled ATVA and verify the models used in the simulations. As in the numerical simulations, the error signal is determined from the velocities of the ATVA mass and the host structure. These velocities were obtained experimentally from an impedance head and a laser vibrometer. The same controllers as found in the simulations were implemented and investigated experimentally.

Following this introduction, the MR fluid-filled ATVA and its controller are described. Section 7.3 presents the numerical models of the MR fluid-filled ATVA, the control algorithm and the control laws used to maintain the tuned conditions of the MR fluid-filled ATVA. Various numerical simulations are illustrated in section 7.4. Section 7.5 describes the experimental setup to investigate the real-time control of the MR fluid-filled ATVA and the experimental results are given in section 7.6. Finally, section 7.7 contains some conclusions.

7.2 The MR Adaptive Tuned Vibration Absorber

It was shown in Chapter 6 that the MR fluid-filled ATVA can be tuned by changing its shear stiffness, by varying the magnetic field across the core, which changes the tuned frequency of the device. To simplify the analysis of the ATVA, it is assumed that at low frequencies, only rigid body modes and the first bending mode of vibration contribute to the response of the ATVA beam. Hence the three-layer beam ATVA attached to the host structure can be reduced to an equivalent 2DOF system as shown in Fig. 7.1. The self tuning of the ATVA can be achieved by the inclusion of the control system. The control system aims to adjust the control signal automatically to maintain the tuned condition. The control system here is an adaptive-passive

controller, which is similar to the classical feedback or closed-loop controller in that it has sensors to measure the feedback signals as shown in Fig. 7.1. In this work, the measured feedback signals are the velocities of absorber $\dot{x_a}$ and host structure $\dot{x_1}$. The controller utilizes these signals to produce the control signal, which is the current I applied to the electromagnet of the MR fluid-filled ATVA. The control signal is used to change the shear stiffness of the ATVA.

7.3 Numerical Models

The performance of the ATVA and its controller is first studied numerically. The numerical simulations employ the mathematical models to simulate the response of the ATVA and the controller response. The numerical models for ATVA and its controller are developed and implemented in MATLAB® with SIMULINK®. The mass-spring TVA and the controller shown in Fig. 7.1 are modelled by several mathematical models as shown in Fig. 7.2. The block diagrams in Fig. 7.2 represent the relationship among the signals used in the entire control system. The details of each model are presented in the following subsections and the SIMULINK® block diagrams are given in Appendix D.

The simulations used the state-space formulation of the differential equations of motion. The state variables were obtained in real time by performing the time integration using an ode5 solver. However the discrete time control system updated the error signal and changed the response of the ATVA every T_c seconds.

7.3.1 MR fluid-filled ATVA Model

The MR fluid-filled ATVA can be represented by six component mathematical models as shown in Fig. 7.2. The main model is the 2DOF model, which provides the responses, i.e. velocities of TVA and host structure. These velocities can be derived from the equations of motion of the host structure and the TVA, i.e.

$$m_1\ddot{x}_1 + c_a(\dot{x}_1 - \dot{x}_a) + k_a(x_1 - x_a) = f \tag{7.1}$$

$$m_a\ddot{x}_a + c_a(\dot{x}_a - \dot{x}_1) + k_a(x_a - x_1) = 0. \tag{7.2}$$

which can be rewritten as

$$\ddot{x}_1 = \frac{1}{m_1}\left[f - c_a(\dot{x}_1 - \dot{x}_a) - k_a(x_1 - x_a)\right] \tag{7.3}$$

$$\ddot{x}_a = -\frac{1}{m_a}\left[c_a(\dot{x}_a - \dot{x}_1) + k_a(x_a - x_1)\right] \tag{7.4}$$

where masses m_1 and m_a are estimated from the measured FRF shown in Chapter 6 and are presented in Tab 7.1. The inputs to the 2DOF model are the disturbance, the viscous damping and the stiffness of the MR fluid-filled ATVA. The stiffness model was determined from the measured tuned frequency ($\omega_a^2 = k_a/m_a$), which is a function of the storage modulus G' of the MR fluid. It was found in Chapter 6 that k_a increases linearly with G' and was modelled empirically as

$$k_a = 0.0017G' + 6344 \tag{7.5}$$

where G' is given from the storage modulus model. It was shown in Chapter 3 that the storage modulus of MR fluid changes with magnetic field. The relationship was obtained empirically as

$$G' = 2470 + (4.33 \times 10^6 - 2470)(1 - e^{-47.3B^2}). \tag{7.6}$$

The electromagnetic model provides the magnetic flux density B, which is generated by the electromagnets attached to the top and bottom layers of the absorber beam. The mean flux density is a function of the current I passing through the wire of electromagnets, and is given by

$$B = \frac{NI}{A_m\left(\frac{l_{s1}}{\mu_0\mu_s A_{s1}} + 2\frac{l_{s2}}{\mu_0\mu_s A_{s2}} + \frac{l_m}{\mu_0\mu_m A_m}\right)} \tag{7.7}$$

where the values of $N, I, \mu_0, \mu_s, \mu_m, A_m, A_s, l_m, l_{s1}$ and l_{s2} are given in Chapter 5.

It was also shown in Chapter 3 that not only does the storage modulus of MR

fluid change with magnetic field, but also the loss modulus. The loss factor of MR fluid η decreases with increasing magnetic field, and was found empirically in Chapter 6 to be governed by

$$\eta = -2.51B + 0.8. \tag{7.8}$$

Since the hysteretic damping cannot be used in the time domain, viscous damping is employed here. The viscous damping of the ATVA as a function of the loss factor of MR fluid was found empirically in Chapter 6 to be given by

$$c_a = -11.16\eta^2 + 11.5\eta - 0.62. \tag{7.9}$$

7.3.2 Controller Model

The inputs to the controller shown in Fig. 7.2 are the feedback signals from the 2DOF model. These signals are used to produce an error signal e_n, which is an input to the control law. The control law implements the algorithm by which the control output is calculated in order to reduce the error. The output from the controller causes the change in natural frequency of the ATVA. The control laws presented by Rustighi *et al.* [36] are implemented in this work. Three discrete control laws, which are proportional (P) control, derivative (D) control, and proportional-plus-derivative (PD) control, are considered here.

7.3.2.1 Error Signal

The control system presented in this thesis is based on the strategy proposed by Long *et al.* [29] and Rustighi *et al* [36]. This control algorithm involves utilizing the phase ϕ between the velocities of the absorber mass and the host structure. As discussed in Chapter 2 for an undamped ATVA the tuned condition of the ATVA occurs when these velocities are in quadrature, in other words when their relative phase is 90°. The controller employs the cosine of this relative phase ($\cos\phi$) as an error signal input to the control law and aims to drive this signal to zero. For discrete frequency excitation ω, the velocities of the host structure and the absorber masses are given

respectively by

$$\dot{x_1}(t) = |\dot{X}_1| \cos \omega t \tag{7.10}$$

$$\dot{x_a}(t) = |\dot{X}_a| \cos(\omega t - \phi) \tag{7.11}$$

where $|\dot{X}_1|, |\dot{X}_a|$, and ϕ are the amplitudes of the velocities of the host structure and absorber masses, and the phase difference between these velocities respectively. The error signal can be calculated from the time averaged product of the velocities over one cycle of period T_p. This time averaged product can be expressed as [29]

$$\overline{\dot{x_1}\dot{x_a}} = \frac{1}{T_p} \int_0^{T_p} \dot{x_1}\dot{x_a} \, \mathrm{d}t = \frac{|\dot{X}_1||\dot{X}_a|}{2} \cos \phi. \tag{7.12}$$

Long *et al.* [29] thus defined the error signal

$$\cos \phi = 2 \frac{\overline{\dot{x_1}\dot{x_a}}}{|\dot{X}_1||\dot{X}_a|} \tag{7.13}$$

and where $-1 \leqslant \cos \phi \leqslant 1$. For a measured signal of the form $A_0 \sin \omega t$, the amplitude A_0 can be estimated by averaging the absolute value of the signal over one cycle of period T_p. This averaging process can be expressed as

$$\int_0^{T_p} |A_0 \sin \omega t| \, \mathrm{d}t = \frac{2T_p A_0}{\pi}, \tag{7.14}$$

which leads to the estimate of the amplitude

$$A_0 = \frac{\pi}{2T_p} \int_0^{T_p} |A_0 \sin \omega t| \, \mathrm{d}t. \tag{7.15}$$

Hence, the amplitudes $\dot{X}_1$ and $\dot{X}_a$ of the velocities are

$$\dot{X}_1 = \frac{\pi}{2T_p} \int_0^{T_p} |\dot{x_1}(t)| \, \mathrm{d}t, \qquad \dot{X}_a = \frac{\pi}{2T_p} \int_0^{T_p} |\dot{x_a}(t)| \, \mathrm{d}t \tag{7.16}$$

where $T_p = 2\pi/\omega$. As the system used here is a discrete time control system, the response signals are discretised. Furthermore the frequency and period T_p are unknown. As a result, the numerical integration should be done with enough sampled points to calculate the amplitudes of the responses. In this thesis, these amplitudes

were estimated by averaging over a control period T_c rather than a single period T_p of the sinusoid. As the error signal is also discretised, Long *et al.* [29] suggested that the accuracy of the estimate of the product is a function of the integration time T_c used in the control period. The more cycles there are in the time T_c, the better the accuracy of the error signal. The control period T_c should be significantly greater than the period T_p in order to provide accurate estimates. However, if the controller output is updated every T_c seconds then the larger a value of T_c the slower the response of the controller. A suitable value of the control period T_c is investigated later in the numerical simulations and the experiments.

The error signal in the discrete time control system at the n^{th} time step is thus an estimate given by [36]

$$e_n = \cos\hat{\phi}, \tag{7.17}$$

which can be obtained by evaluating Eq. (7.13) every control period T_c.

7.3.2.2 Proportional Control

The error signal e_n is used to update the current I. As defined here, proportional control involves an update proportional to e_n so that

$$I_{n+1} = I_n - Pe_n \tag{7.18}$$

where P, I_n and I_{n+1} are the controller gain, the current at the n^{th} time step, and the current at the $(n+1)^{th}$ time step respectively. Although the simple proportional controller can reduce the error between the natural frequency of ATVA and the forcing frequency, this controller may introduce a steady-state error and a large transient overshoot [97]. Further, it is pointed out in [98] that the linear proportional control is not effective for the adaptive-passive control of the ATVA, for which the error signal $\cos\phi$ has a highly non-linear characteristic. This ATVA requires a control law, which provides a large change in current when the natural frequency of the ATVA is very different from the forcing frequency, and provides a small change in current when the ATVA is close to the tuned state. For this reason, an alternative model,

which involves a non-linear function of the error signal, was suggested as [36]

$$I_{n+1} = I_n - P(e_n + e_n^3 + e_n^5). \tag{7.19}$$

7.3.2.3 Derivative Control

In principle, the derivative controller adds damping into the system to improve the stability of the system [97]. This controller has the form of [36]

$$I_{n+1} = I_n - Dd_n \tag{7.20}$$

where D is the controller gain and the derivative of the error d_n is approximated by [36]

$$d_n = \frac{e_n - e_{n-2}}{2T_c}. \tag{7.21}$$

Here e_{n-2} is the error at the time step $(n-2)$. Generally, derivative control is not implemented alone. It is often combined with proportional control to give proportional-plus-derivative control.

7.3.2.4 Proportional-plus-Derivative Control

Proportional-plus-derivative control is capable of both reducing the error by the proportional term and improving the stability by the derivative term. The general form of the nonlinear PD controller is given by [36]

$$I_{n+1} = I_n - [P(e_n + e_n^3 + e_n^5) + Dd_n]. \tag{7.22}$$

The controller gains P and D are adjustable in the design of the controller. The performance of the controller depends on these gains. If they are properly selected, the performance of the controller could be improved. The performance of the control system employing various values of P and D are presented and compared in simulations and experiments.

7.4 Numerical Simulations

The performance of the system is measured in terms of how quickly and accurately the ATVA tracks a change the excitation frequency. One specific measure is the settling time, which is the time it takes for the system to settle within a given amount of its final value. In general the performance depends on parameters such as controller algorithm and gains and the time increment at which the controller output is updated. Therefore, a number of computer simulations were conducted to investigate the performance, to estimate suitable values of these parameters and to illustrate the self-tuning behaviour of the MR fluid-filled ATVA. All numerical simulations were conducted in MATLAB® with SIMULINK® using an ode5 solver with a fixed time step of 0.5 ms (2kHz sample rate).

Three types of numerical simulations were conducted. The switch-on test was simulated first to examine the convergence ability of the response of the MR fluid-filled ATVA. Then the step responses were studied to investigate the performance, i.e. settling time, for three different controllers. Also the effects of various controller gains and increment time T_c were explored. Lastly, the tracking ability of the controller was investigated.

7.4.1 Switch-On Test

Simulations were conducted using Eqs. (7.1)-(7.9) and the control law shown in Eq. (7.22). The switch-on test was simulated first. The MR fluid-filled ATVA was subjected to a constant forcing frequency of 140 Hz with control effective from $t = 2$ s. The simulated response of the host structure mass and the control activity are shown in Fig. 7.3. It can be seen from Fig. 7.3(b) that without control in the first two seconds, the amplitude of the acceleration $\ddot{x}_1$ is high because the natural frequency of the ATVA, which is about 106 Hz, does not match the forcing frequency. When the controller is switched on at $t = 2$ s, the amplitude reduces rapidly and eventually converges to the steady state value as the ATVA self-tunes. Fig. 7.3(d) shows the magnitude of accelerance, $|\ddot{X}_1/F|$. The magnitudes of acceleration $\ddot{X}_1$ and force F were determined from the envelopes of the acceleration $\ddot{x}_1$ shown in Fig. 7.3(b)

and force f shown in Fig. 7.3(c) respectively. The envelope was found by taking the Hilbert transforms. The complex time domain signal is formed, where the real part is the original data and the imaginary part is the Hilbert transform. As the complex signal from the Hilbert transform contains noise, this signal was low pass filtered with a cut off frequency of 170 Hz. It can be seen from Fig. 7.3(d) that the magnitude $|\ddot{X}_1/F|$ converges within 15% of the steady state value 0.05 s after the the controller is switched on. After the controller is turned on the current applied to the electromagnets shown in Fig. 7.3(f) is updated every 0.05 seconds from zero to an almost steady value, meanwhile $\cos\phi$ shown in Fig. 7.3(e) increases sharply with some oscillations before converging to zero.

7.4.2 Step Responses

The response to a step change in frequency of the MR fluid-filled ATVA without control, i.e. no current applied to the electromagnets was then investigated. The MR fluid-filled ATVA was subjected to the excitation whose frequency varied between 110 and 146 Hz as shown in Fig. 7.4(a). This range was selected such that, when tuned, the control current varies between 0 and 646 mA. The acceleration $\ddot{x}_1$ of the host structure mass is shown in Fig. 7.4(b). It can be seen that the minimum value of $\ddot{x_1}$ occurs at 110 Hz when the excitation frequency is close to the tuned frequency. The magnitude of $\ddot{x}_1$ increases rapidly when the forcing frequency changes at $t = 6$ s. Since the force is constant as shown in Fig. 7.4(c), the magnitude of $|\ddot{X}_1/F|$ shown in Fig. 7.4(d) shows the same trend as $\ddot{x}_1$. It can also be seen that when $\cos\phi$ shown in Fig. 7.4(e) is close to zero (i.e. for $t < 6$) s, $|\ddot{X}_1/F|$ is small, but when $\cos\phi$ is further from zero, $|\ddot{X}_1/F|$ is large. Hence it is the objective of the control system to maintain $\cos\phi$ as close as possible to zero.

The response to a step change in frequency with control implemented is shown in Fig. 7.5. It can be seen from Figs. 7.5(e-f) that at $t = 2$ s, when the controller is switched on, the controller smoothly changes the natural frequency of the ATVA from 106 Hz to 110 Hz, which equals to the forcing frequency shown in Fig. 7.5(a). However the amplitude of the response shown in Fig. 7.5(b) is very slightly changed because the ATVA is almost in the tuned condition. The forcing frequency changes to 146 Hz at

$t = 6$ s. At this time, the amplitude of the accelerance shown in Fig. 7.5(d) increases and $\cos\phi$ shown in Fig. 7.5(e) is far from zero. However, the control attempts to drive $\cos\phi$ to zero by increasing the current applied to electromagnets every 0.05 s as shown in Fig. 7.5(f). As a result, the amplitude of the response decreases and tends to a steady state value, which is about 18 dB less than the level without control as shown in Fig. 7.5(d). There are time delays in reaching the steady state response. The time delays here are indicated by the settling time T_s, which is the time within which the response settles within 15% of the steady state value. These delays are partly due to control algorithm delays, which are caused by the increment time T_c that controller updates the output current. Also the controller gains (P and D) may cause delays. In the simulations the ATVA is assumed to reach the steady state response instantaneously, while in the experiments there are transients. The computational cost of the control is generally very small. All these delays are combined to give a settling time $T_s \approx 0.06$ s when $T_c = 0.05, P = 0.13$ and $D = 0.005$.

To investigate the effect of the increment time T_c, three simulations were carried out. In these simulations T_c is varied, whereas the controller gains (P and D) are fixed. Figs. 7.6(a-c) show the responses $\ddot{x}_1$, which were obtained by updating the current to the MR fluid-filled ATVA every 0.1, 0.05, and 0.01 s respectively. The respective values of accelerance are shown in Figs. 7.6(d-f), the values of $\cos\phi$ are shown in Figs. 7.6(g-i), and the values of current are shown in Figs. 7.6(j-l). These responses and control activity were due to the step change in input frequency shown in Fig 7.5(a). It can be seen that T_c strongly affects the settling time of the MR fluid-filled ATVA. When T_c equals to 0.1 as shown in Fig. 7.6(a), the response converges to a steady state. Decreasing T_c to 0.05 as shown in Fig. 7.6(b) causes the response to converge more rapidly, but becomes more oscillatory. The oscillation also occurs with $\cos\phi$ shown in Fig. 7.6(h) and the control current shown in Fig. 7.6(k). The control system becomes unstable, i.e. the response and control activities oscillate when $T_c = 0.01$ as shown in Figs. 7.6(c, f, i, l). In short, decreasing T_c decreases the settling time but can cause oscillation. If T_c is too small there is an instability of the system. By comparing the performance of the control system using three values of T_c, $T_c = 0.05$ is used in the rest of the simulations.

Various simulations were conducted to investigate the effects of the controller gains (P, D) on the transient step response. The pure derivative controller presented in Eq. (7.20) was investigated first. The MR fluid-filled ATVA was subjected to the same excitation as in the previous simulations, and three different values of D were examined. The responses $\ddot{x}_1$ for $D = 0.001, 0.005$, and 0.05 are presented in Figs. 7.7(a-c) respectively. The respective values of accelerance $|\ddot{X}_1/F|$ are shown in Figs. 7.7(d-f), the values of $\cos\phi$ are shown in Figs. 7.7(g-i), and the values of current are shown in Figs. 7.7(j-l). It can be seen from Figs. 7.7(a-c) that at $t = 6$ s, when the forcing frequency steps up, the amplitude $\ddot{x}_1$ increases and $\cos\phi$ shown in Fig. 7.7(g-i) is further from zero. Meanwhile, the controller attempts to drive $\cos\phi$ to zero by increasing the current shown in Fig. 7.7(j-l). However, after the current is increased by very small amount, $\cos\phi$ becomes constant. As a result, the current being updated is unchanged. The reason for the constant current can be explained from Eq. (7.21). It can be seen that if the error signal e_n is unchanged, the derivative of the error d_n becomes zero. Consequently, the output controlled current shown in Eq. (7.20) is fixed before the error signal is driven to zero. Hence the controller cannot bring the response down to its minimum value as shown in Figs. 7.7(d-f). However, with a larger value of $D(D = 0.005)$ the controller can drive the level of response shown in Fig. 7.7(e) closer to the minimum value than with $D = 0.001$ shown in Fig. 7.7(d). Too large a value of D (e.g. $D = 0.05$) can lead to instability as shown in Fig. 7.7(f). Thus D control on its own can only effect a small amount of control and can lead to instability.

The performance of proportional control alone was then simulated using Eq. (7.19). Figs. 7.8 (a-c) show the responses for proportional gains of $0.04, 0.13$, and 0.4 respectively. Figs. 7.8 (d-f) show the respective values of accelerance. The respective values of $\cos\phi$ are shown in Figs. 7.8(g-i) and the values of current are shown in Figs. 7.8(j-l). It can be seen from Figs. 7.8(a-c) that when the controller makes smaller adjustments, i.e. a smaller gain P, the controller takes a longer time to drive the magnitude $\ddot{x}_1$ to the steady state. Unlike the derivative gain D, the value of P has no effect on the steady state value as shown in Figs. 7.8(d-f). However larger P causes increasingly oscillatory behaviour as shown in Figs. 7.8(g-i). The performance at each value of

the gain is indicated by the settling time shown in Tab. 7.3. It can be seen that $P = 0.13$ gives the settling time in the order of 0.1 s, while too large a value of P (e.g. $P = 0.4$) causes oscillation in the system.

One way of improving the performance of the control is combining two control strategies to proportional-plus-derivative control. With $P = 0.13$, the effect of derivative term is investigated and illustrated in Fig. 7.9. It can be seen that with the presence of derivative term, with $D = 0.005$, the response shown in Fig. 7.9(b) has a shorter settling time than when $D = 0$ shown in Fig. 7.9(a). However when $D = 0.005$, there is some oscillation in $|\ddot{X}_1/F|$ shown in Fig. 7.9(e), $\cos\phi$ shown in Fig. 7.9(h), and current shown in Fig. 7.9(k). For larger D(e.g. $D = 0.05$) the control becomes unstable and there are large oscillation in response and control activities as shown in Figs. 7.9(c, f, i, l).

7.4.3 Tracking Tests

The final investigation concerns the response of the MR fluid-filled ATVA to the frequency ramp input. This indicates the ability of the ATVA to track a changing input. The simulation was conducted with values of $P = 0.13, D = 0.005$, and $T_c = 0.05$ being used. Fig. 7.10(a) shows the forcing frequency, which increases linearly in 1 s from 110 Hz to 146 Hz starting at a time $t = 6$ s. The excitation frequency was generated using equations shown in [12], which are

$$\begin{aligned} f(t) &= F\sin\omega_1^* t, && t \leqslant t_1 \\ f(t) &= F\sin\left[\frac{(\omega_2^* - \omega_1^*)}{2(t_2 - t_1)}(t - t_1)^2 + \omega_1^*(t - t_1)\right], && t_1 < t < t_2 \\ f(t) &= F\sin\omega_2^* t, && t_2 \leqslant t \end{aligned} \tag{7.23}$$

where ω_1^* is the initial circular forcing frequency before the ramp of frequency starts at time t_1 and ω_2^* is the circular forcing frequency when the change of frequency ends at time t_2.

It can be seen from Fig. 7.10(f) that at the start of the forcing frequency ramp at $t = 6$ s, the current increases every 0.05 s as the ATVA self-tunes and reaches constant soon after the forcing frequency reaches 146 Hz. During the ramping period, the

response in Figs. 7.10(b) and (d) can smoothly track the change in forcing frequency and is able to maintain the magnitude of $\ddot{x}_1$ close to the minimum value throughout the tunable range. Also $\cos\phi$ shown in Fig. 7.10(e) is slightly away from zero when the forcing frequency ramps at $t = 6$ s, but it tends to zero again after the forcing frequency is constant.

7.5 Experimental Rig

Experiments were conducted to implement real-time control and to investigate the performance of the the MR fluid-filled ATVA with a range of controller parameters. The ATVA model shown in Fig. 7.2 was replaced with the real MR fluid-filled ATVA. The control system was implemented in MATLAB® with SIMULINK® using the Real Time Workshop and Real Time Windows Target. The controller could communicate with the MR fluid-filled ATVA via an I/O board (NI, PCI-MIO-16E-4). A sampling frequency of 2kHz was used. The experimental set-up is shown in Fig 7.11. The input to the controller are the velocities of the host structure and the ATVA and the output is the desired current to the electromagnets. This output was passed to the MR fluid-filled ATVA through a Lambda power supply model ZUP 10-20 and an 1-ohm resistor. As the 1-ohm resistor and the eight electromagnets were connected in series, the current through each component was equal. Hence, the control current was the current through the resistor, which was determined from the measured voltage V across the resistor R, i.e. $I = V/R$. The acceleration of the host structure mass was measured at the point where the MR fluid-filled ATVA was attached to the shaker and the velocity of the ATVA mass was measured at one end of the ATVA beam.

The centre point of the MR fluid-filled ATVA was attached to a LDS shaker model V201 through an impedance head model PCB 288D01. The PC acted as a signal generator, generating an input signal to drive the shaker through an I/O board, a Kemo analogue low pass filter model VBF 23, a Cambridge audio model A1 Integrated amplifier, and an ammeter. The acceleration and input force at the attachment point were measured by the impedance head. A Polytec laser vibrometer model OFV 3001S was used to measure velocity at one end of the beam. All three

measured signals were input to the PC via Kemo analogue anti-alias low pass filters model VBF 8 and the I/O board. The measured acceleration was integrated using the integrator function in SIMULINK® to obtain the velocity of the mass-like host structure. The SIMULINK® block diagrams are given in Appendix D.

7.6 Experimental Results

In this section, results are presented to illustrate the real time self-tuning behaviour of the MR fluid-filled ATVA and to make comparisons between experimental and simulated results. All the simulations described in section 7.4 were implemented experimentally.

7.6.1 Switch-On Test

Fig. 7.12 shows the response and control activity of the MR fluid-filled ATVA, which is excited at a forcing frequency of 140 Hz. The simulation of the same test is shown in Fig. 7.3. It can be seen from Fig. 7.12 that after the controller was switched on at $t = 2$ s, the current shown in Fig. 7.12(f) was updated every 0.05 s as the ATVA tunes, and hence the acceleration shown in Fig. 7.12(b) reduces. The level of reduction is about 12 dB as shown in Fig. 7.12(d). The measured force shown in Fig. 7.12(c) increases when the controller is turned on. Meanwhile, $\cos\phi$ shown in Fig. 7.12(e) rises fairly quickly with some oscillation and then tends to zero. It can be noticed that there is oscillation in $\ddot{x}_1$ shown in Fig. 7.12(b), $|\ddot{X}_1/F|$ shown in Fig. 7.12(d), and current shown in Fig. 7.12(f) as well. The current shown in Fig. 7.12(f) is the measured current through the 1-ohm resistor.

The measured (Fig. 7.12(b)) and simulated responses (Fig. 7.3(b)) are similar in that the amplitudes of both decrease with time and eventually reach the steady state a few seconds after the controller is switched on, but the settling time of the measured response is 0.04 s longer than that found in the simulation. This might be due to the dynamic delays described in the following subsection. The measured force shown in Fig. 7.12(c) is not constant because of the low mechanical impedance of the shaker

used. The effect of the ATVA becoming tuned is to present a high impedance, thus increasing the force that is applied to the ATVA.

7.6.2 Step Responses

The behaviour of the MR fluid-filled ATVA without control for a step change in excitation frequency is shown in Fig. 7.13 and its simulation is shown in Fig. 7.4. The MR fluid-filled ATVA was subjected to the excitation , i.e. a change from 110 Hz to 146 Hz at $t = 6$ s as shown in Fig. 7.13(a). It can be seen from Fig. 7.13(b) that for $t < 6$ s, the acceleration $\ddot{x}_1$ is small since the ATVA is nearly in the tuned condition. Acceleration increases when the forcing frequency changes to 146 Hz at time $t = 6$ s, but the measured force shown in Fig. 7.13(c) decreases. It also can be seen that when $t < 6$ s, $\cos\phi$ shown in Fig. 7.13(e) is close to zero and the ratio of the amplitude $|\ddot{X}_1/F|$ shown in Fig. 7.13(d) is small. However, when the condition of ATVA is far from the tuned condition (i.e. when $t \geqslant 6$ s), $\cos\phi$ is further from zero and $|\ddot{X}_1/F|$ is large.

By comparing with the simulation in Fig. 7.4, it can be seen that apart from the measured force shown in Fig. 7.13(c) whose amplitude depends on frequency, the measured response shown in Fig. 7.13(b) and $\cos\phi$ shown in Fig. 7.13(e) have the same trends as seen in the simulation. Furthermore, the ratio of $|\ddot{X}_1/F|$ found in both simulation and measurement varies in the same range, but has slightly different amplitudes as shown in Fig. 7.4(d) and Fig. 7.13(d).

The response and control activities of the MR fluid-filled ATVA to the step input with the control effective from $t = 2$ s are shown in Fig. 7.14 and their simulation is shown in Fig. 7.5. It can be seen that the current shown in Fig. 7.14(f) rises slightly after the start of the controller at $t = 2$ s as ATVA tunes and $\cos\phi$ shown in Fig. 7.14(e) tends to zero. Since the natural frequency of the ATVA nearly coincides with the forcing frequency of 110 Hz when $t < 6$ s, there is so little change in $|\ddot{X}_1/F|$ shown in Fig. 7.14(d) when the controller is turned on. A step change in forcing frequency at $t = 6$ s causes a rise in $|\ddot{X}_1/F|$, and then it comes down to the steady state fairly quickly. Meanwhile at $t = 6$ s, the current overshoots and there is a small oscillation before approaching more or less constant.

It can be seen that the measured response shown in Figs. 7.14(b) and (d) takes longer to converge than the simulated response shown in Figs. 7.5(b) and (d) (see also Tab. 7.3). This might be caused by the dynamic delays, which are not included in the simulation. These delays are due to the MR fluid response time, the electric circuit response, and the vibration decay time, which is the time for transient response to decay. For the stable system, this decay time depends on the level of damping, i.e. decay time is smaller as damping increases. The level of damping also has the effect on the overshoot of the response. The response of a low damped system tends to have a large overshoot.

Although the simulated response has shorter settling time, the simulated result shows more oscillation as shown in Figs. 7.5(e) and 7.14(e). However, the level of simulated controlled current is nearly the same as the measured current throughout the tunable range as shown in Figs. 7.5(f) and 7.14(f) respectively. Also, the real ATVA can achieve the vibration reduction of 16 dB as shown in Fig. 7.14(d), which is 2 dB less than that found in the simulation shown in Fig. 7.5(d).

Three experiments were conducted to investigate how the performance depends on the time increment T_c. The experimental results for three values of T_c are shown in Fig. 7.15, the respective simulations are shown in Fig. 7.6 and the settling times are shown in Tab. 7.3. The measured acceleration $\ddot{x}_1$ for $T_c = 0.1, 0.05$, and 0.01 are shown in Figs. 7.15(a-c) respectively. The respective values of accelerance are shown in Figs. 7.15(d-f), the values of $\cos\phi$ are shown in Figs. 7.15(g-i), and the values of current are shown in Figs. 7.15(j-l). It can be seen from Figs. 7.15(a-c) that when the forcing frequency increases at $t = 6$ s, the accelerations increase as well, and then they reduce until converging to the steady state. However $\ddot{x}_1$ shown in Fig. 7.15(c), which correspond to $T_c = 0.01$, converges fastest. It can be seen from the ratio of amplitude $|\ddot{X}_1/F|$ shown in Figs. 7.15(d-f) that the steady state value does not depend on the value of T_c. When $T_c = 0.1$, $\cos\phi$ shown in Fig. 7.15(g) overshoots and then tends to zero. The overshooting of $\cos\phi$ when $T_c = 0.05$ shown in Fig. 7.15(h) is smaller. When $T_c = 0.01$, there is no overshoot in $\cos\phi$; on the other hand, there is oscillation around the steady state value as shown in Fig. 7.15(i). The currents I for three different value of T_c are shown in Figs. 7.15(j-l). Increasing forcing frequency

at $t = 6$ s leads to the increase in current because the ATVA self-tunes. When T_c is equal to 0.1 shown in Fig. 7.15(j) and 0.05 shown in Fig. 7.15(k), I overshoots before approaching more or less constant. But the current when $T_c = 0.01$ shown in Fig. 7.15(l) is unstable. Given this, it can be inferred that smaller value of T_c causes faster response, but too small value of T_c can lead to instability in the control activities. This agrees with the simulation shown in Fig. 7.6. However, the simulated $|\ddot{X}_1/F|$ when $T_c = 0.01$ shown in Fig. 7.6(f) oscillates and is not able to converge to steady state.

The experimental results for the pure derivative control are shown in Fig. 7.16 and the simulated results are shown in Fig. 7.7. As for the previous experiments, the forcing frequency increases from 110 Hz to 146 Hz at $t = 6$ s. The measured currents for three values of D are shown in Figs. 7.16(j-l). When $D = 0.001$, the current shown in Fig. 7.16(j) increases by a very small amount after the increase in forcing frequency at $t = 6$ s and then tends to a constant. The current when $D = 0.005$ shown in Fig. 7.16(k) shows the same behaviour but increases by a larger amount. However when $D = 0.05$, the current shown in Fig. 7.16(l) is unstable. The ratios of measured magnitude $|\ddot{X}_1/F|$ for $D = 0.001, 0.005$, and 0.05 are shown in Figs. 7.16(d-f) respectively. It can be seen that after the levels of $|\ddot{X}_1/F|$ rises at $t = 6$ s due to the increase in forcing frequency, they cannot be brought down to the minimum level. However, the steady state level when $D = 0.005$ shown in Fig. 7.16(e) is lower than that when $D = 0.001$ shown in Fig. 7.16(d). When the gain D increases to 0.05, $|\ddot{X}_1/F|$ shown in Fig. 7.16(f) shows oscillatory behaviour. The measured responses $\ddot{x}_1$ shown in Figs. 7.16(a-c) show the same behaviour as $|\ddot{X}_1/F|$, i.e. cannot converge to the minimum level. Also $\cos\phi$ for three different values of D shown in Figs. 7.16(g-i) cannot reach zero neither. Therefore, with regard to the pure derivative control, the experimental results shown in Figs. 7.16, like the simulation shown in Figs. 7.7, fail to converge to the tuned state. Also a large enough value of D leads to instability of the system.

However, the responses for the pure proportional control shown in Fig. 7.17(a-b) and their simulations shown in Fig. 7.8(a-b) are able to converge to the steady state value. Figs. 7.17(d-f) show $|\ddot{X}_1/F|$ for $P = 0.04, 0.13$, and 0.4 respectively. The

respective values of $\cos\phi$ are shown in Figs. 7.17(g-i) and the values of current are shown in Figs. 7.17(j-l). It can be seen that the measured response for $P = 0.13$ shown in Fig. 7.17(e) can converge quicker than that for $P = 0.04$ shown in Fig. 7.17(d), but too large a value of P (e.g. $P = 0.4$) causes oscillation of the response as shown in Fig. 7.17(f). With $P = 0.4$, both $\cos\phi$ and the control current oscillate as shown in Figs. 7.17(i) and (l) respectively. As the ATVA self-tunes at $t = 6$ s, the currents I for $P = 0.04$ shown in Fig. 7.17(j) and for $P = 0.13$ shown in Fig. 7.17(k) increase and overshoot before approaching more or less constant. Also $\cos\phi$ in Figs. 7.17(g) and (h) show the same trend as the current, i.e. overshooting and then tending to zero. In brief, a larger value of P leads to faster response. Once again, too large a value of P causes instability.

Simulated responses shown in Figs. 7.8(a-c) are the same as the experimental responses in Figs. 7.17(a-c), but when $P = 0.4$ the simulated response shown in Figs. 7.8(c,f), $\cos\phi$ shown in Fig. 7.8(i), and I shown in Fig. 7.8(l) show less oscillation than the experiment shown in Figs. 7.17(c, f, i, l). Also when $P = 0.04$ and 0.13, there is no overshoot in the simulated control activity as shown in Figs. 7.8(g, h, j, k). As shown in Tab. 7.3, the shortest settling time for the pure proportional control is approximately 0.18 s, which is 0.08 s longer than simulation. This settling time, however, can be improved by using PD control. The results for which are shown in Fig. 7.18.

Fig. 7.18 shows the measured results for PD control with $P = 0.13$ and various values of D and their respective simulation is shown in Fig. 7.9. With $D = 0.005$, the measured response shown in Fig. 7.18(b) converges quicker than with $D = 0$ shown in Fig. 7.18(a). However, when D increases to 0.05, the measured response shown in Figs. 7.18(c,f) and control activity shown in Figs. 7.18(i,l) are unstable. Also with $D = 0.05$ overshooting in $\cos\phi$ shown in Fig. 7.18(h) and current shown in Fig. 7.18(k) still exist. Thus, a larger value of D in the PD control shows better performance, but not large a value. The shortest settling time, i.e. $T_s \approx 0.16$ s, is obtained with $P = 0.13, D = 0.005$ and $T_c = 0.05$. This is about 0.1 s longer than simulation.

7.6.3 Tracking Tests

In this test the excitation consists of a ramp in frequency. Figs. 7.19 and 7.20 illustrate the tracking ability of the ATVA. The former shows the response to a ramp change of frequency of 38 Hz/s and the latter for a slower rate, which is 7.6 Hz/s. The simulated response to a change of frequency of 38 Hz/s is shown in Fig. 7.10. Fig. 7.19(a) shows the forcing frequency, which starts ramping from 110 Hz at $t = 6$ s to 146 Hz at $t = 7$ s. As in the step tests in the previous subsection, the controller is switched on at $t = 2$ s. This leads to the small rise in measured current shown in Fig. 7.19(f) and the change in $|\ddot{X}_1/F|$ shown in Fig. 7.19(d). Since the ATVA is almost in the tuned condition, this change is very small. However, during the period when the forcing frequency changes ($6 \leqslant t \leqslant 7$ s), some dynamics of the measured response are clearly evident. However the response is able to return to the steady state after the end of the ramp at $t = 7$ s. During the period $6 \leqslant t \leqslant 7$ s, $\cos\phi$ shown in Fig. 7.19(e) and I shown in Fig. 7.19(f) show oscillations before approaching the steady state. These oscillations are larger than in the simulations shown in Fig. 7.10.

When the frequency changes more slowly, i.e. changing from 110 Hz to 146 Hz in 5 s as shown in Fig. 7.20(a), the tracking ability is much better, the changes in the dynamics of the response shown in Fig. 7.20(d) are smaller and the ATVA remains almost in the tune throughout. Also $\cos\phi$ shown in Fig. 7.20(e) and I shown in Fig. 7.20(f) are updated more smoothly. Therefore, it can be concluded from Figs. 7.19 and 7.20 that the MR fluid-filled ATVA is effectively tuned to track the change in forcing frequency and the tracking ability is even better when the rate of change of frequency is slower.

7.6.4 Responses to Changes in Excitation Frequency from 146 to 110 Hz

In these experiments the MR fluid-filled ATVA was subjected to an excitation whose frequency decreases. The response to an excitation that decreases in a step from 146 Hz to 110 Hz is shown in Fig. 7.21. The control is turned on at $t = 2$ s and the step change in excitation frequency is at $t = 6$ s. At both times tuning of the ATVA can be

seen and the performance is similar to that when the step changes from 110 Hz to 146 Hz. After the start of the control, the current shown in Fig. 7.21(f) rises, overshoots and then tends to a constant. The current decreases when the forcing frequency is stepped down at $t = 6$. There is a large drop in the level of $|\ddot{X}_1/F|$ shown in Fig. 7.21(d) when the controller is switched on, and then $|\ddot{X}_1/F|$ is constant after ATVA reaches its tuned condition. The level of $|\ddot{X}_1/F|$ rises again when the forcing frequency is changed at $t = 6$ s, and then decreases to the steady state tuned value. Since the MR fluid-filled ATVA without control subjected to the forcing frequency of 110 Hz ($t \geqslant 6$ s) is nearly in the tuned condition, there is little difference between the amplitudes $|\ddot{X}_1/F|$ of the ATVA with and without control. After the start of the control and a step change in forcing frequency, there is an overshoot in $\cos\phi$ shown in Fig. 7.21(e).

The responses to ramp changes in frequency from 146 Hz to 110 Hz in times of 1 s and 5 s are shown in Figs 7.22 and 7.23 respectively. As mentioned earlier, when the controller is switched on at $t = 2$ s the current shown in Fig. 7.22(f) rises and overshoots before approaching the steady state. The current decreases when the forcing frequency decreases at $t = 6$ s. It can be seen from Fig 7.22(d) that the reduction of vibration is large when the forcing frequency is 146 Hz and very little when the forcing frequency is 110 Hz. Also when the forcing frequency changes at $t = 6$ s, there is a very small change in $|\ddot{X}_1/F|$ as shown in Fig. 7.22(d). However, there is oscillation in $\cos\phi$ shown in Fig. 7.22(e) and I shown in Fig. 7.22(f) during the tracking period.

The response to a ramp change of frequency with slower rate, i.e. 7.6 Hz/s, is shown in Fig. 7.23. It can be seen from Fig. 7.23(d) that the changes in $|\ddot{X}_1/F|$ during the period when the frequency changes are smaller than that shown in Fig. 7.22(d). Also there is less oscillation in $\cos\phi$ shown in Fig. 7.23(e) and current shown in Fig. 7.23(f). Therefore, it can be concluded that the response time of ATVA is short enough to track the change in forcing frequency, even if the excitation frequency is reversed.

7.7 Conclusions

In this chapter the self-tuning behaviour of the MR fluid-filled ATVA has been investigated by both computer simulations and experiments. Numerical simulations employed a classical two degrees of freedom model for the vibration of the mass-like host structure having ATVA attached together with a simple model for the magnetic field, an empirical model for the storage modulus of MR fluid, and empirical models for the damping coefficient and stiffness of the MR fluid-filled ATVA.

A control algorithm has been implemented. The control aims to tune the stiffness of the MR fluid-filled ATVA in real-time by driving the cosine of the phase difference between velocities of the host structure and the ATVA mass to zero, by changing the current input to the electromagnets of the ATVA. Three control laws, which are non-linear proportional control, derivative control, and proportional-plus-derivative control, have been examined numerically and experimentally.

It was seen in the simulations of the step response that pure derivative control is not effective since it cannot drive $\cos\phi$ to zero. As a result, the response of the host structure cannot reach the minimum steady state value. Besides this, the steady state response depends on the value of D. Larger values leads to a lower steady state response. However, too large a value produces oscillation of the system (instability).

In contrast with pure derivative control, pure proportional control works effectively. The performance of the control system employing three different value of P was studied. It was seen that larger values of P produce better performance in terms of settling time. However, too large a value for P causes instability in the system once again.

Another control algorithm investigated was proportional-plus-derivative control. The proportional term aims to reduce the error and the derivative term attempts to increase the speed of response of the controller. Because of the combination of these two terms, this control law exhibited the best performance, i.e. shortest setting time, with $P = 0.13$ and $D = 0.005$ being used.

The effect of the time increment T_c on the step response and settling time has also been investigated. If T_c is increased, the settling time increases but the amount of oscillatory behaviour decreases. A suitable value for T_c was found to be 0.05 s.

If the forcing frequency is changed linearly with time the simulations showed that by implementing proportional-plus-derivative control, the ATVA is able to retune itself effectively to track the change in forcing frequency.

Experiments on the real MR fluid-filled ATVA subjected to step and ramp excitations were conducted. The experimental results confirmed the effectiveness of the control algorithms employed and verified the models used in simulations. The results of the measurements are similar to those of the simulations. Nearly as much vibration reduction can be achieved experimentally as in the simulations. The experiment showed 16 dB reduction, while 18 dB reduction was achieved in the simulations. The controlled current in the simulations varied over the same range as in the experiments. However, with regard to settling time, the simulated response converges much more quickly than measured response. The reason for this is probably due to the dynamic delays. Dynamic delays, which exist in the real system, are delays due to the MR fluid response time, the electric circuit response, and the time for transient vibration to decay. However these delays were not considered in the simulation because the ATVA was assumed to reach steady state instantaneously. The shortest setting time found in experiments is 0.16 s, when $P = 0.13, D = 0.005$ and $T_c = 0.05$ for the system considered.

Tables

Mass of the host structure	m_1	7.5 g
Mass of the MR ATVA	m_a	14.1 g

Tab. 7.1: Parameters of the 2DOF system of the MR fluid-filled ATVA.

	$T_c = 0.10$	$T_c = 0.05$	$T_c = 0.01$
Simulation	0.1986	0.0611	unstable
Experiment	0.2263	0.1571	unstable

Tab. 7.2: Settling time of the step response of ATVA with different time increment T_c when $P = 0.13$ and $D = 0.005$.

		$D = 0.000$	$D = 0.001$	$D = 0.005$	$D = 0.050$
$P = 0.00$	Simulation Experiment	does not converge to steady state			unstable
$P = 0.13$	Simulation Experiment	0.0994 0.1802	0.0972 0.1618	0.0611 0.1571	unstable
$P = 0.40$	Simulation Experiment	unstable			

Tab. 7.3: Settling time of the step response of ATVA with different controller constant values when $T_c = 0.05$.

Figures

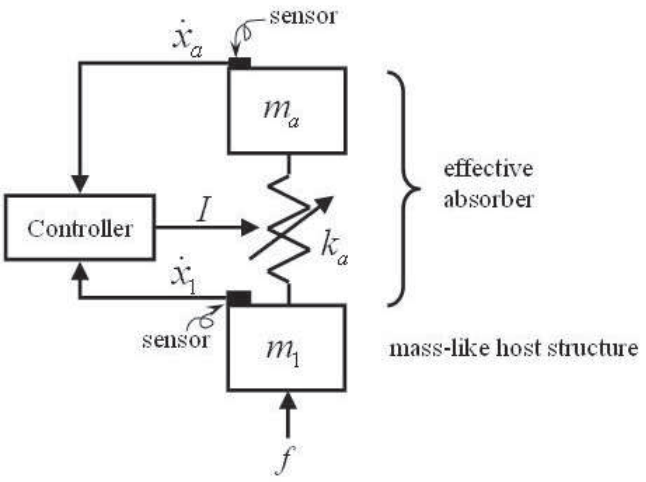

Fig. 7.1: Adaptive-passive vibration absorber.

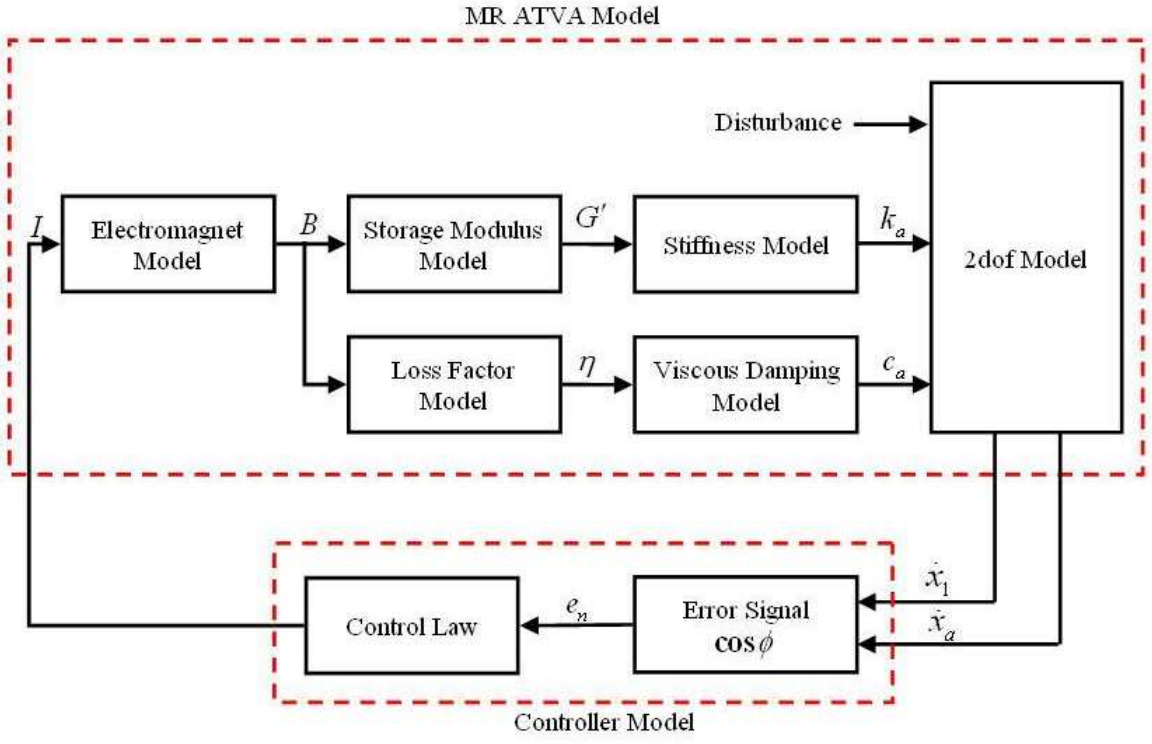

Fig. 7.2: Block diagram of the MR fluid-filled ATVA and its controller.

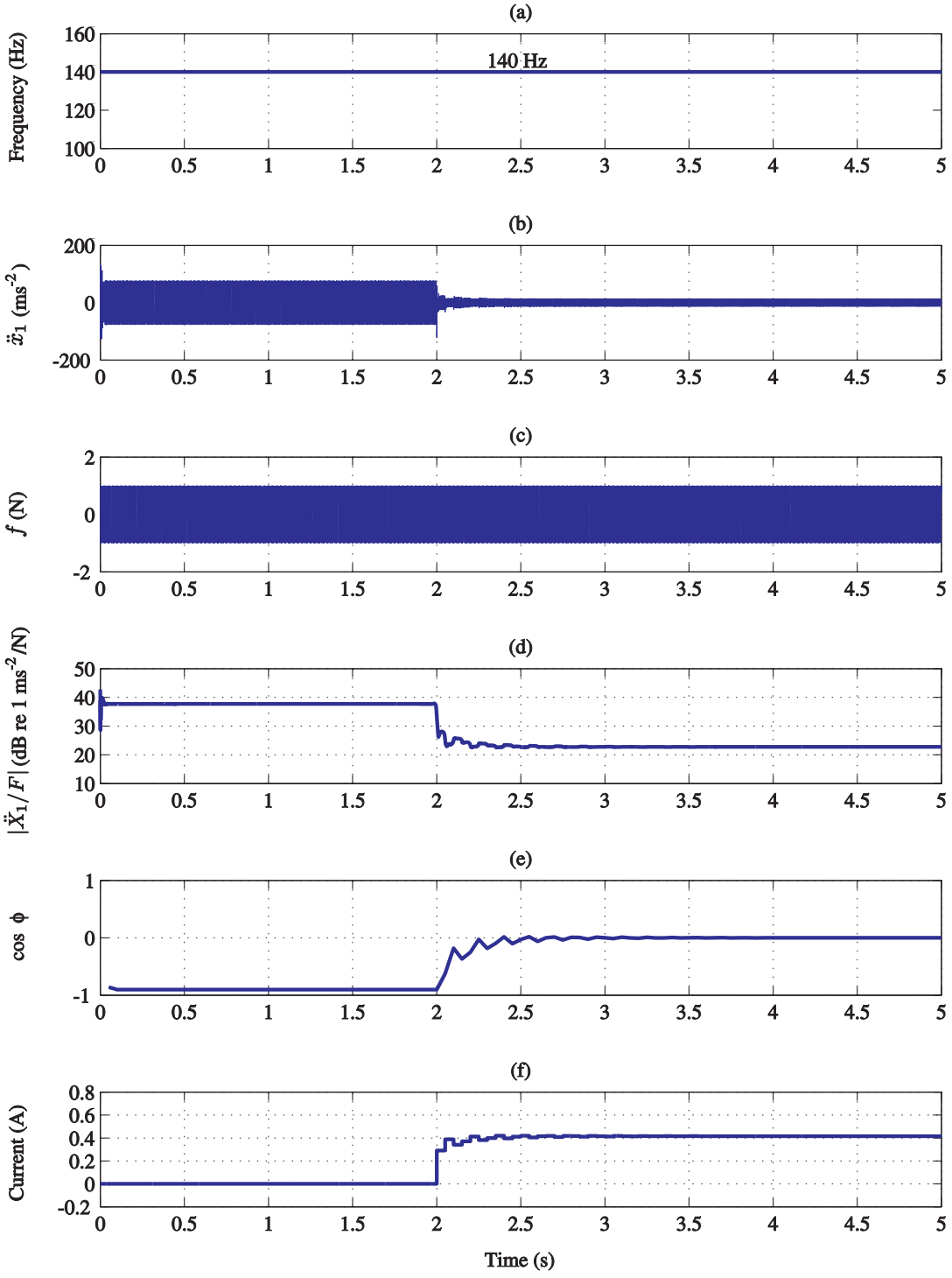

Fig. 7.3: Simulated results of ATVA with the control system for an excitation frequency of 140 Hz: (a) excitation frequency; (b) host structure acceleration; (c) force; (d) host structure accelerance; (e) $\cos\phi$; (f) current I. $P = 0.13, D = 0.005, T_c = 0.05$. The controller is activated at $t = 2$ s.

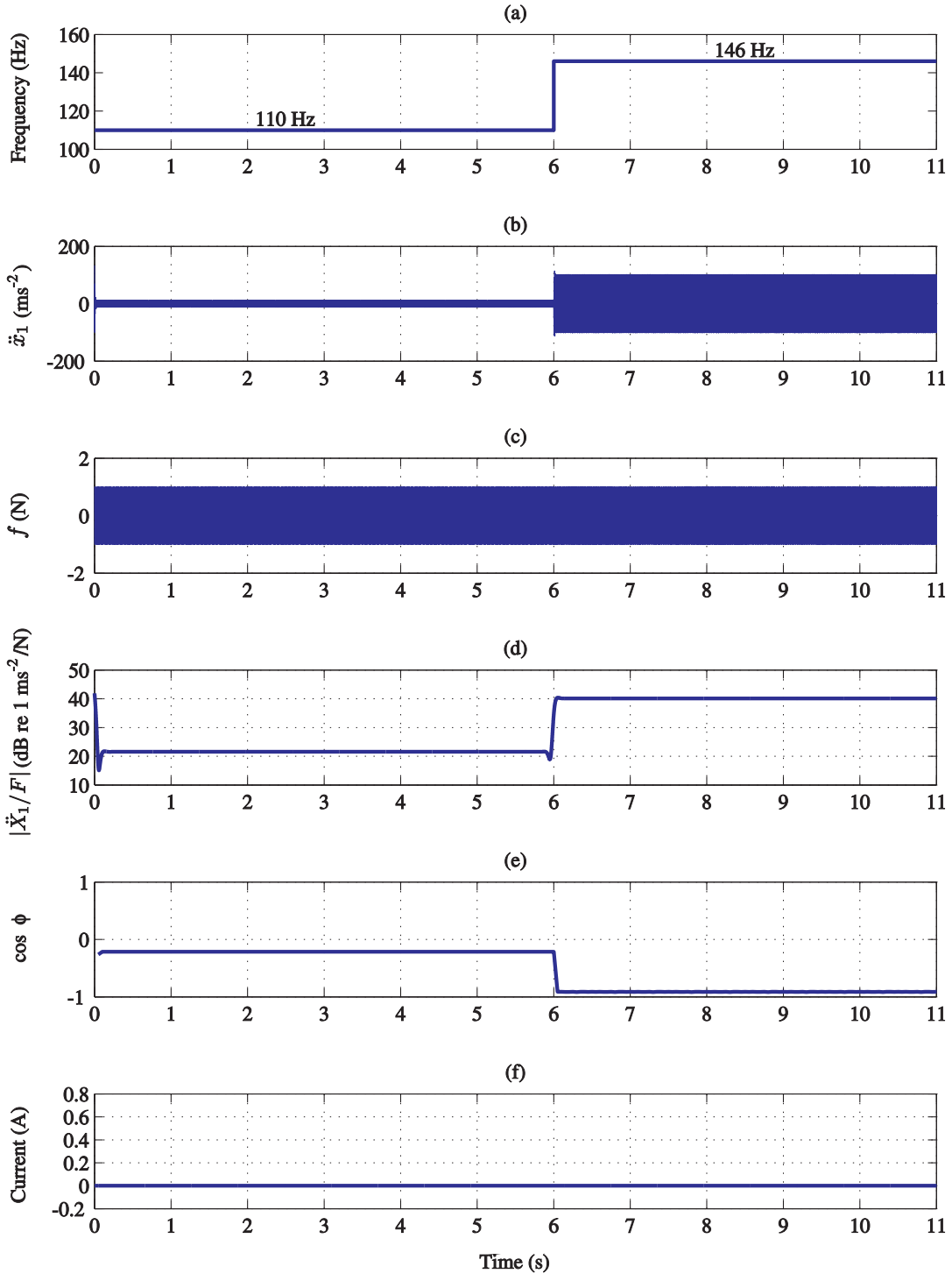

Fig. 7.4: Simulated results of ATVA without the control system for step excitation from 110 to 146 Hz at $t = 6$ s: (a) excitation frequency; (b) host structure acceleration; (c) force; (d) host structure accelerance; (e) $\cos\phi$; (f) current I.

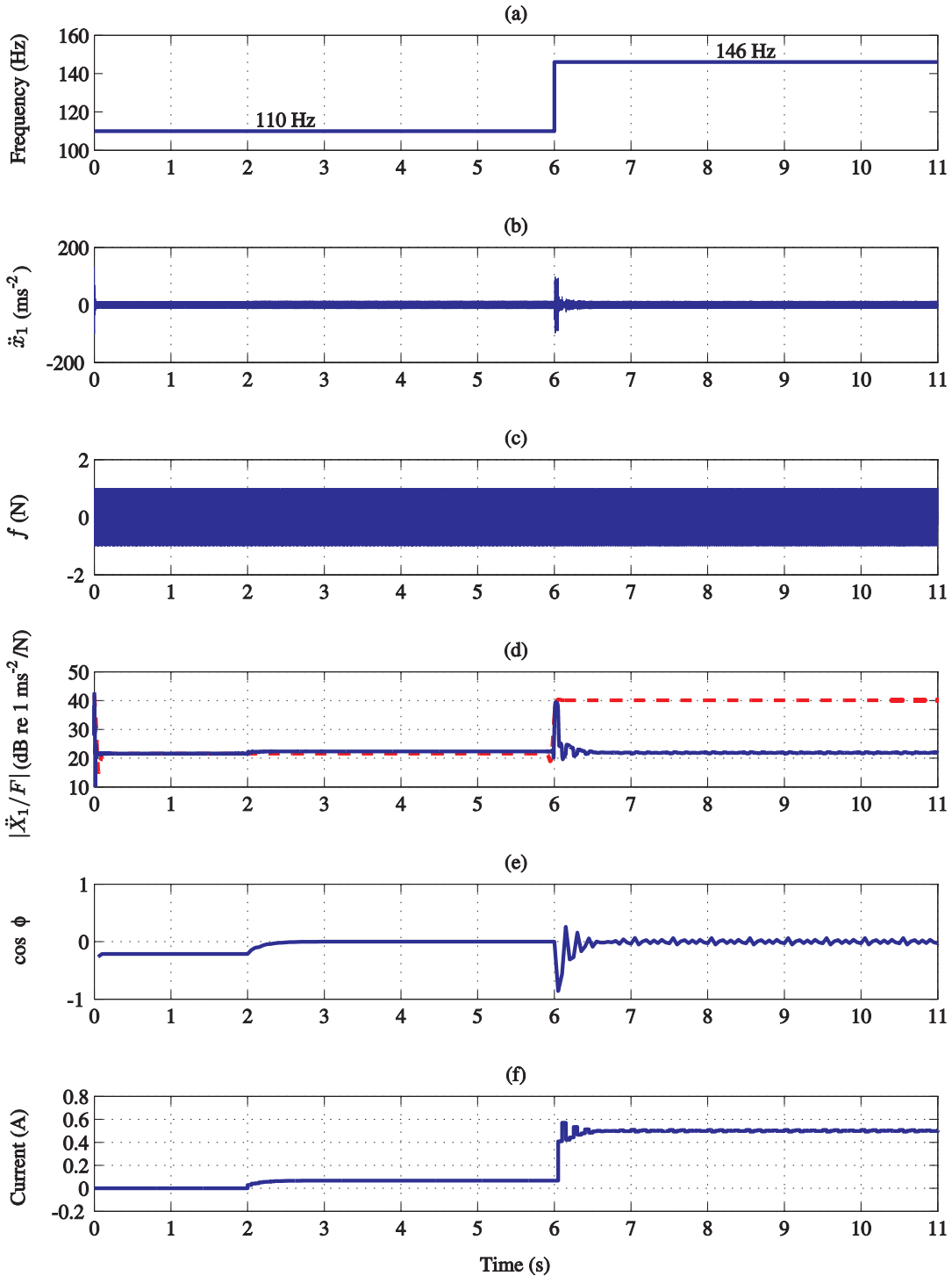

Fig. 7.5: Simulated results of ATVA with the control system for step excitation from 110 to 146 Hz at $t = 6$ s: (a) excitation frequency; (b) host structure acceleration; (c) force; (d) host structure accelerance; (e) $\cos\phi$; (f) current I. $P = 0.13, D = 0.005, T_c = 0.05$; — with and --- without control.

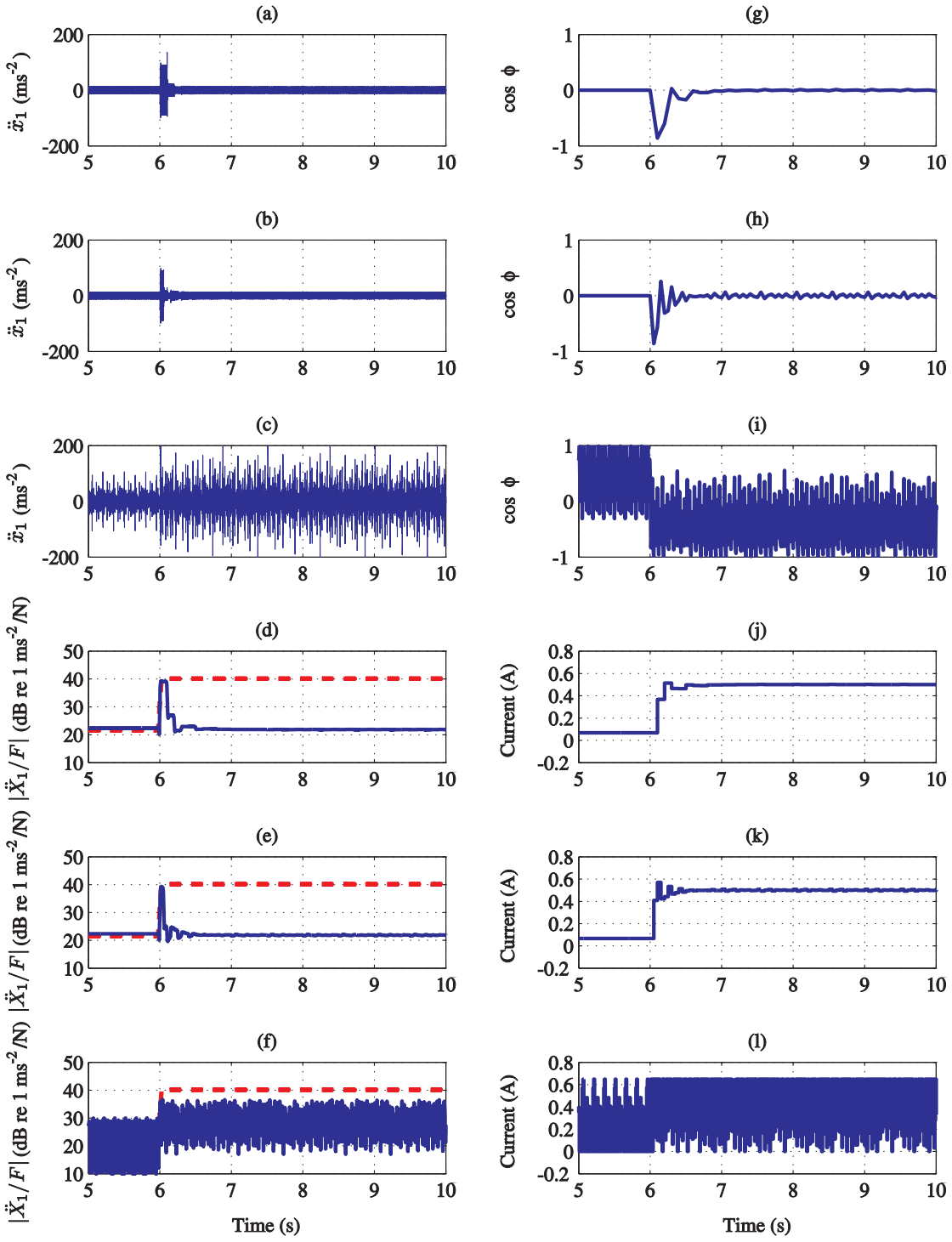

Fig. 7.6: Simulated response of ATVA to the step excitation shown in Fig. 7.5(a) with the control system for variable time increment T_c: (a) $T_c = 0.1$ s; (b) $T_c = 0.05$ s; (c) $T_c = 0.01$ s; $|\ddot{X}_1/F|$ with T_c equal to (d) 0.1 s; (e) 0.05 s; (f) 0.01 s; $\cos\phi$ with T_c equal to (g) 0.1 s; (h) 0.05 s; (i) 0.01 s; and current I with T_c equal to (j) 0.1 s; (k) 0.05 s; (l) 0.01 s. $P = 0.13, D = 0.005$; — with and --- without control.

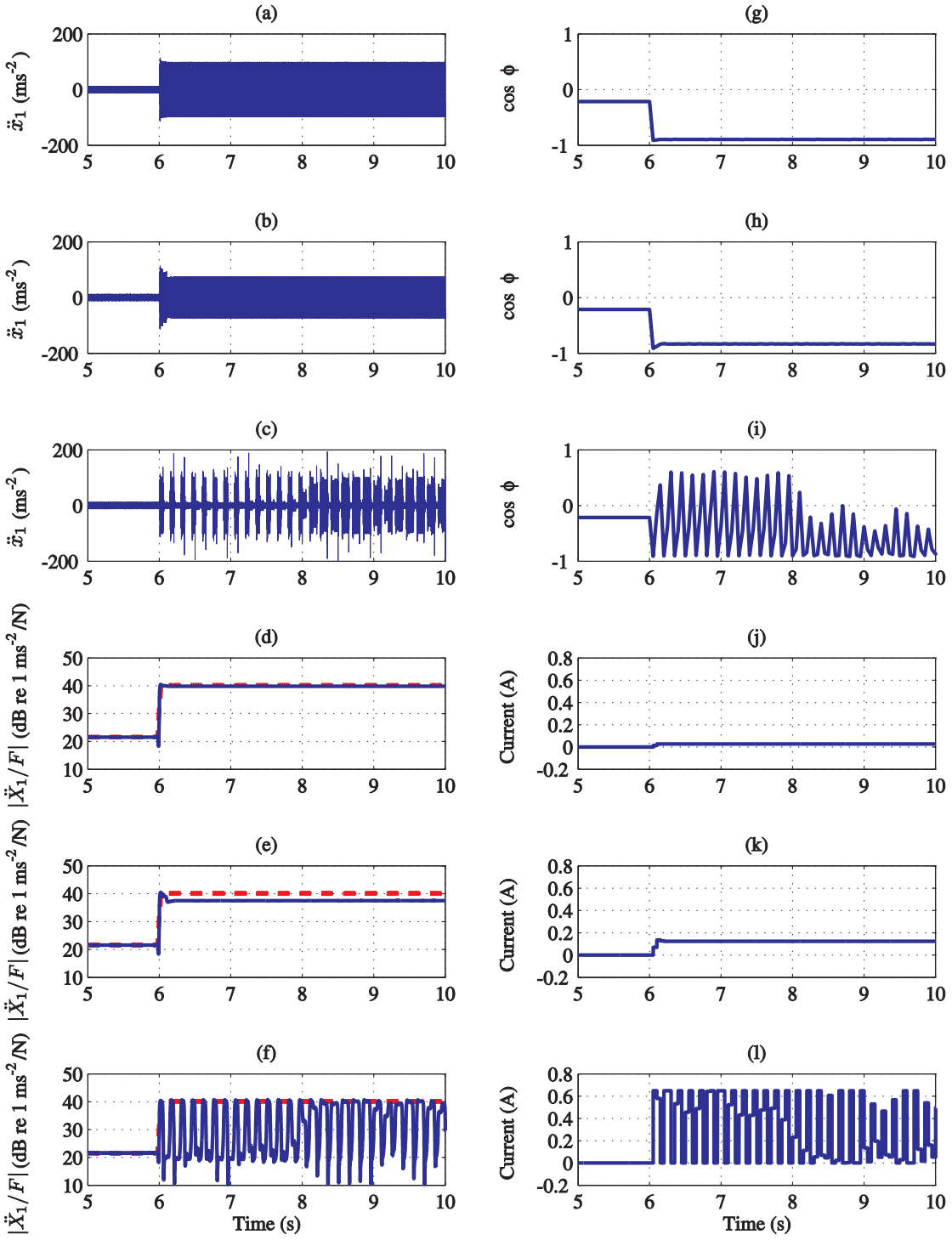

Fig. 7.7: Simulated response of ATVA to the step excitation shown in Fig. 7.5(a) with the derivative control for variable controller constant D: (a) $D = 0.001$; (b) $D = 0.005$; (c) $D = 0.05$; $|\ddot{X}_1/F|$ with D equal to (d) 0.001; (e) 0.005; (f) 0.05; $\cos\phi$ with D equal to (g) 0.001; (h) 0.005; (i) 0.05; and current I with D equal to (j) 0.001; (k) 0.005; (l) 0.05. $P = 0, T_c = 0.05$ s; — with and --- without control.

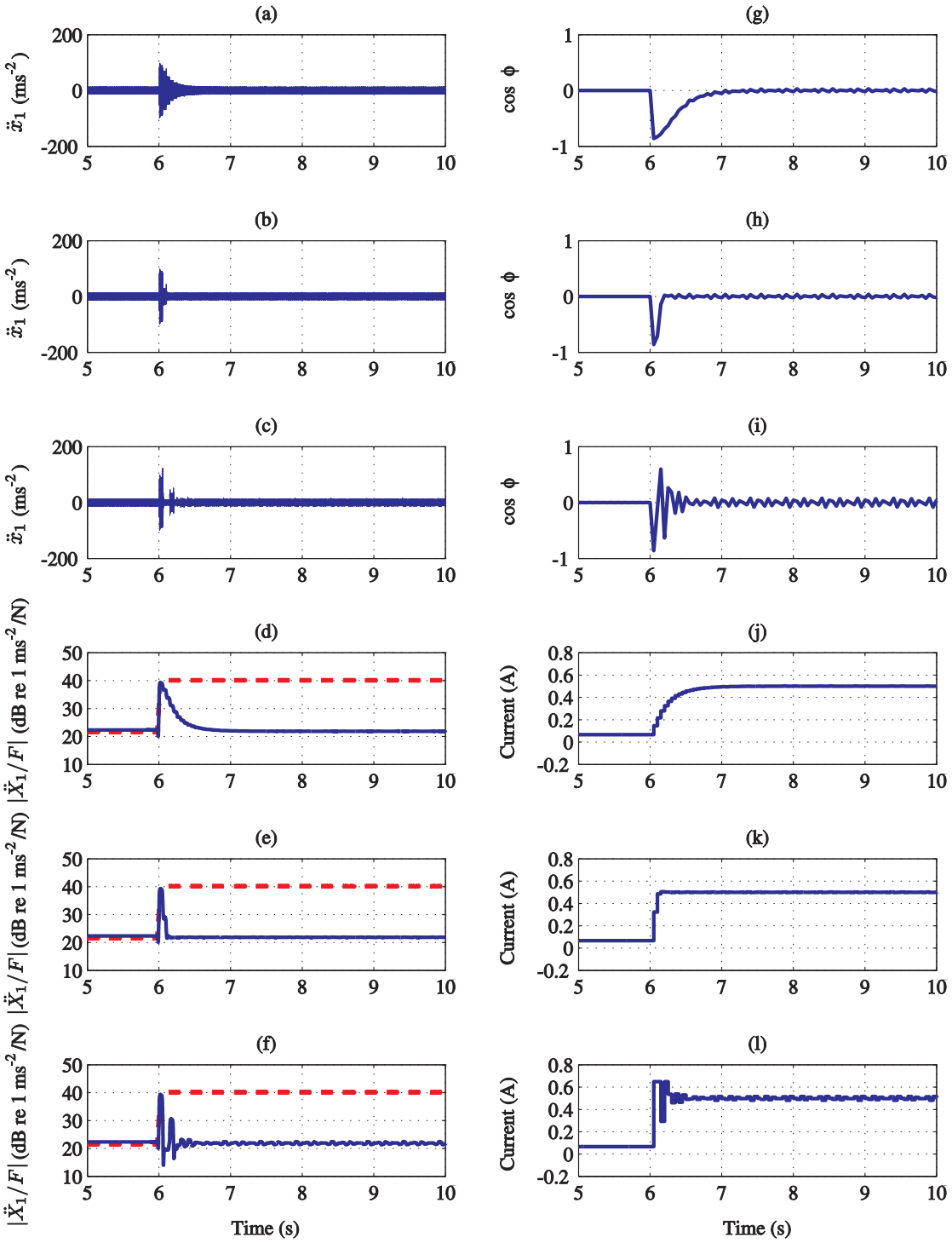

Fig. 7.8: Simulated response of ATVA to the step excitation shown in Fig. 7.5(a) with the proportional control for variable controller constant P: (a) $P = 0.04$; (b) $P = 0.13$; (c) $P = 0.4$; $|\ddot{X}_1/F|$ with P equal to (d) 0.04; (e) 0.13; (f) 0.4; $\cos\phi$ with P equal to (g) 0.04; (h) 0.13; (i) 0.4; and current I with P equal to (j) 0.04; (k) 0.13; (l) 0.4. $D = 0, T_c = 0.05$ s; — with and --- without control.

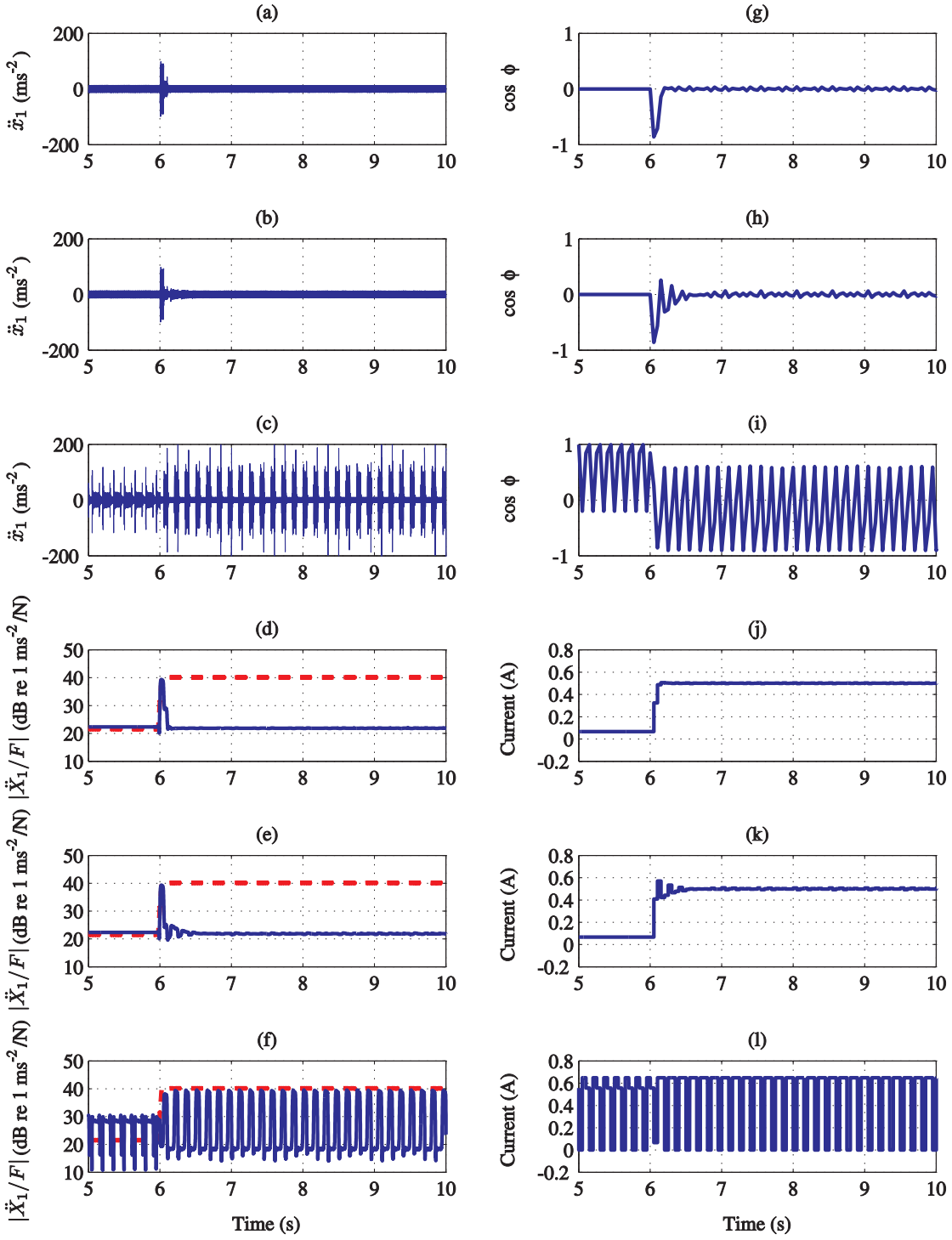

Fig. 7.9: Simulated response of ATVA to the step excitation shown in Fig. 7.5(a) with the proportional-plus-derivative control for variable controller constant D: (a) $D = 0$; (b) $D = 0.005$; (c) $D = 0.05$; $|\ddot{X}_1/F|$ with D equal to (d) 0; (e) 0.005; (f) 0.05; $\cos\phi$ with D equal to (g) 0; (h) 0.005; (i) 0.05; and current I with D equal to (j) 0; (k) 0.005; (l) 0.05. $P = 0.13, T_c = 0.05$ s; — with and --- without control.

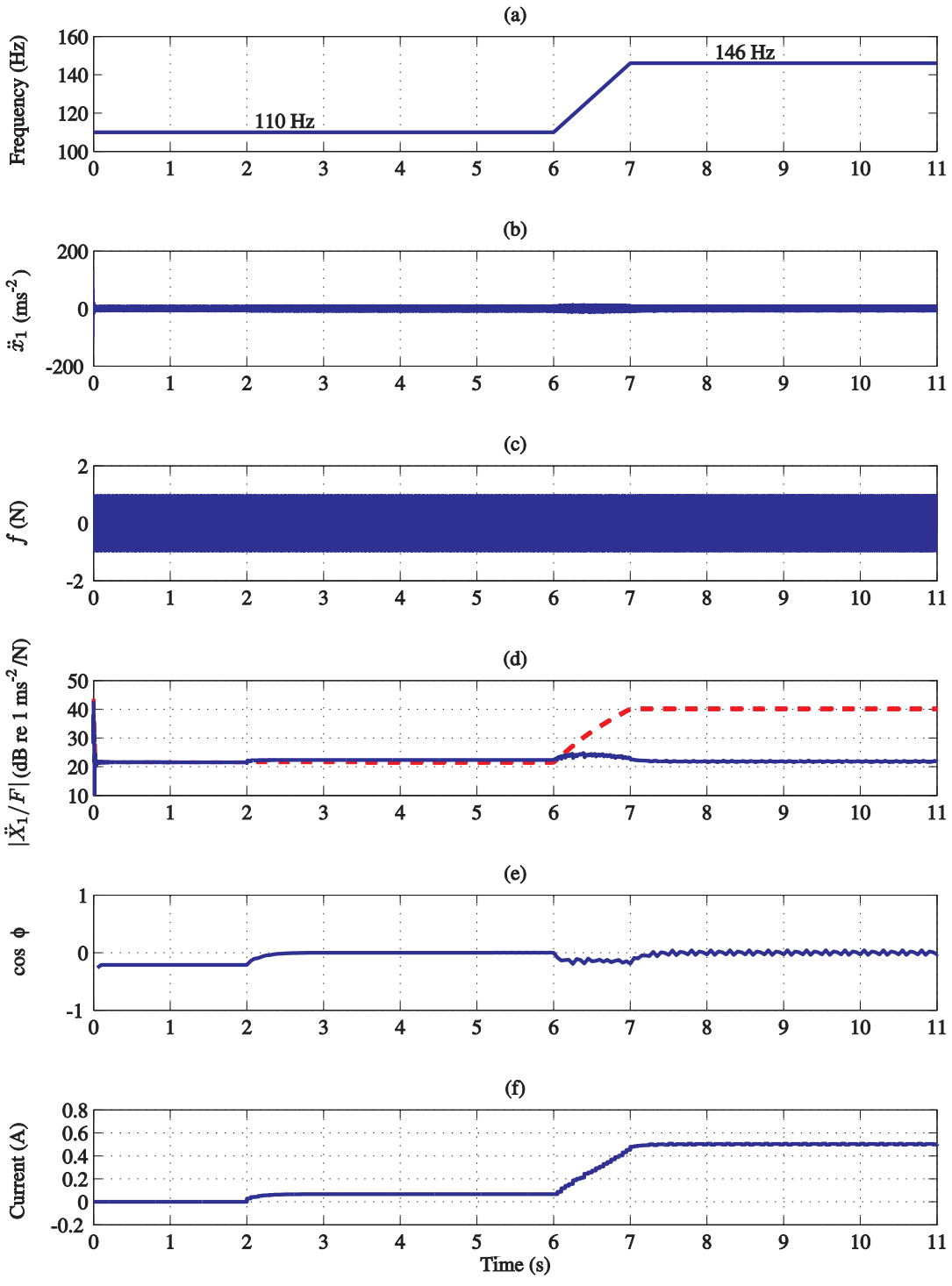

Fig. 7.10: Simulated response of ATVA with the control system for tracking a frequency change of 38 Hz/s (110 Hz to 146 Hz in 1 s starting at $t = 6$ s): (a) excitation frequency; (b) host structure acceleration; (c) force; (d) host structure accelerance; (e) $\cos\phi$; (f) current I. $P = 0.13, D = 0.005, T_c = 0.05$; — with and --- without control.

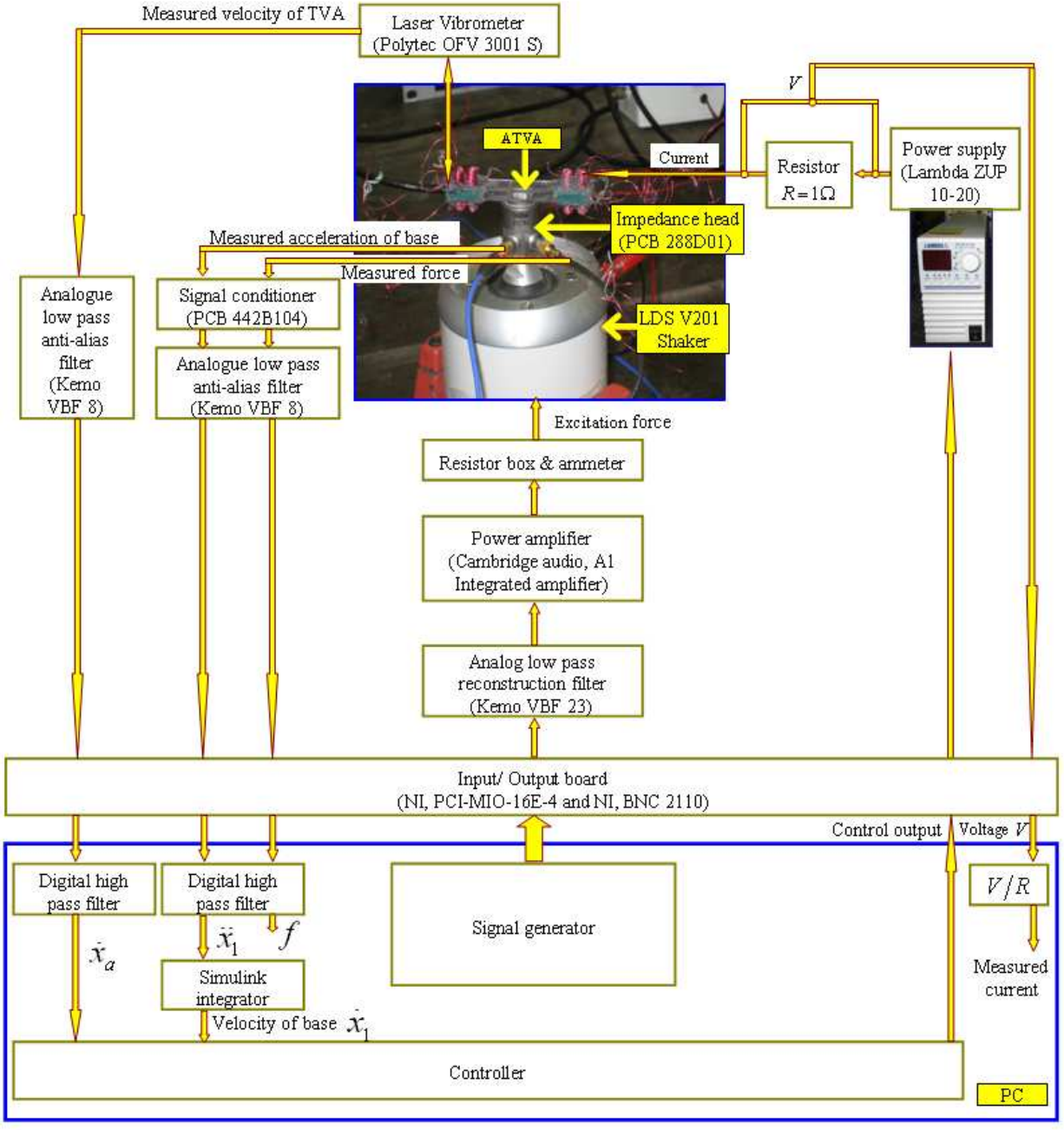

Fig. 7.11: Real-time self-tuning control of MR fluid-filled ATVA.

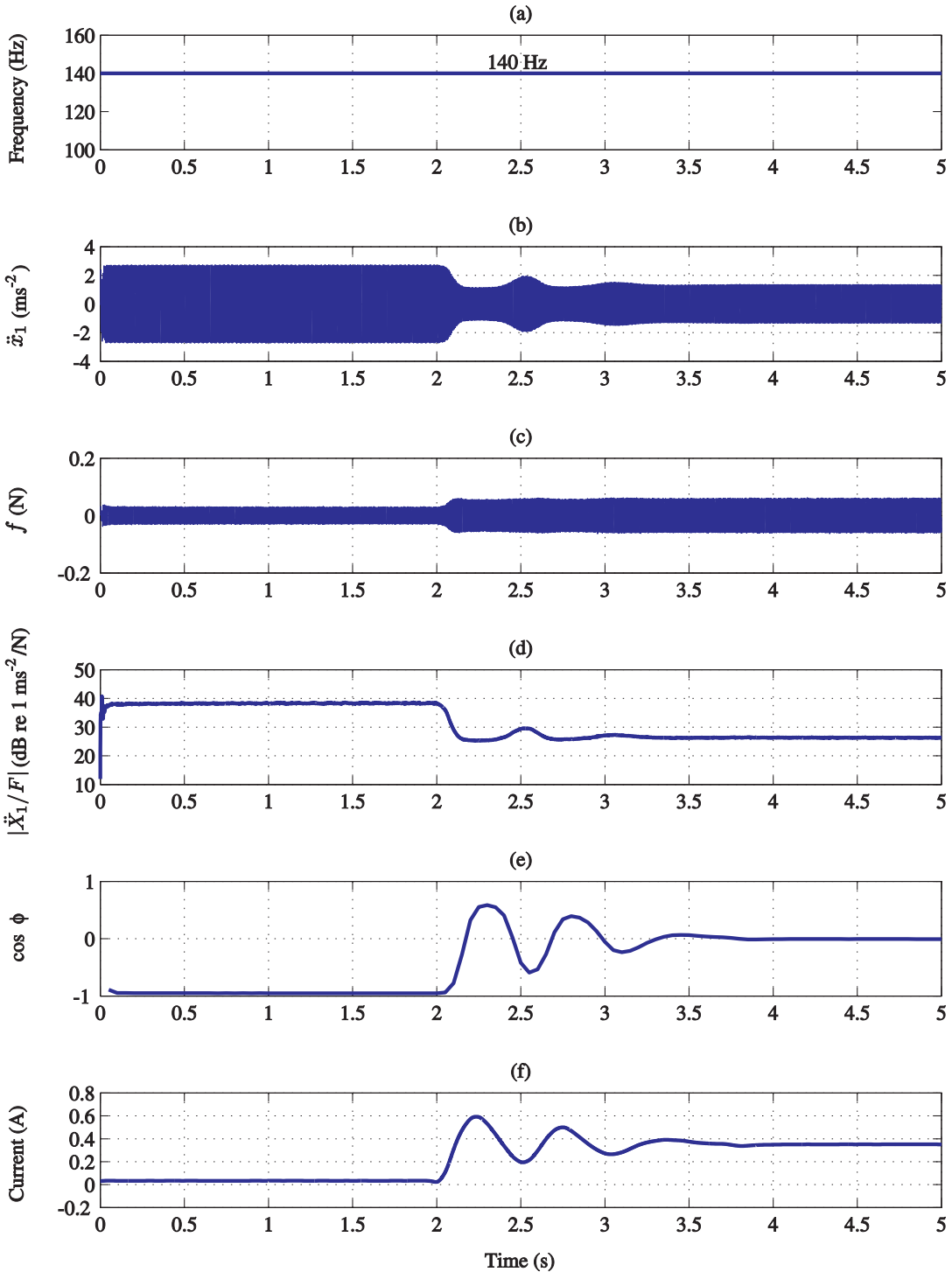

Fig. 7.12: Experimental results of ATVA with the control system for an excitation frequency of 140 Hz: (a) excitation frequency; (b) host structure acceleration; (c) force; (d) host structure accelerance; (e) $\cos\phi$; (f) current I. $P = 0.13, D = 0.005, T_c = 0.05$. The controller is switched on at $t = 2$ s.

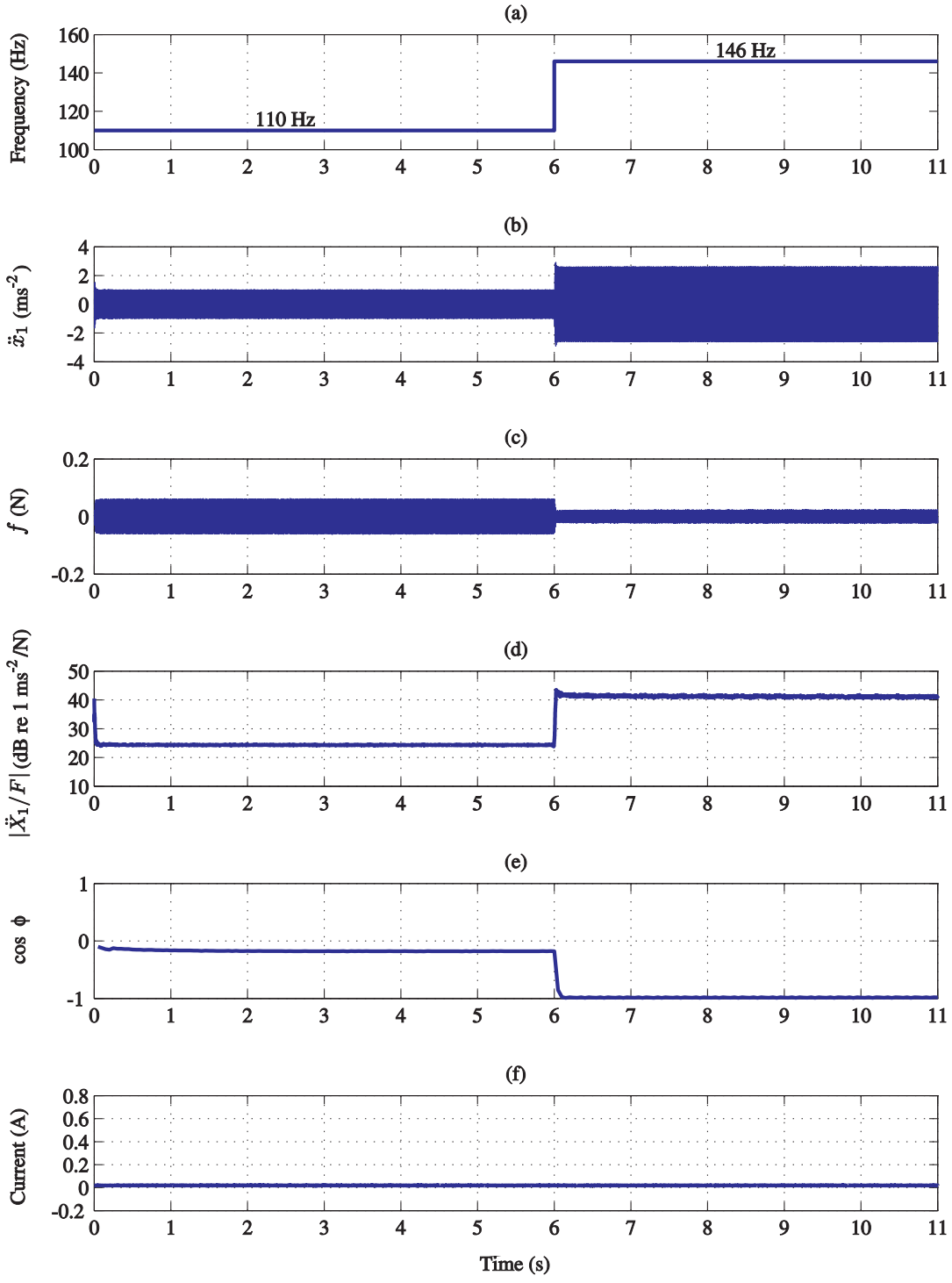

Fig. 7.13: Experimental results of ATVA without the control system for step excitation from 110 to 146 Hz at $t = 6$ s: (a) excitation frequency; (b) host structure acceleration; (c) force; (d) host structure accelerance; (e) $\cos\phi$; (f) current I.

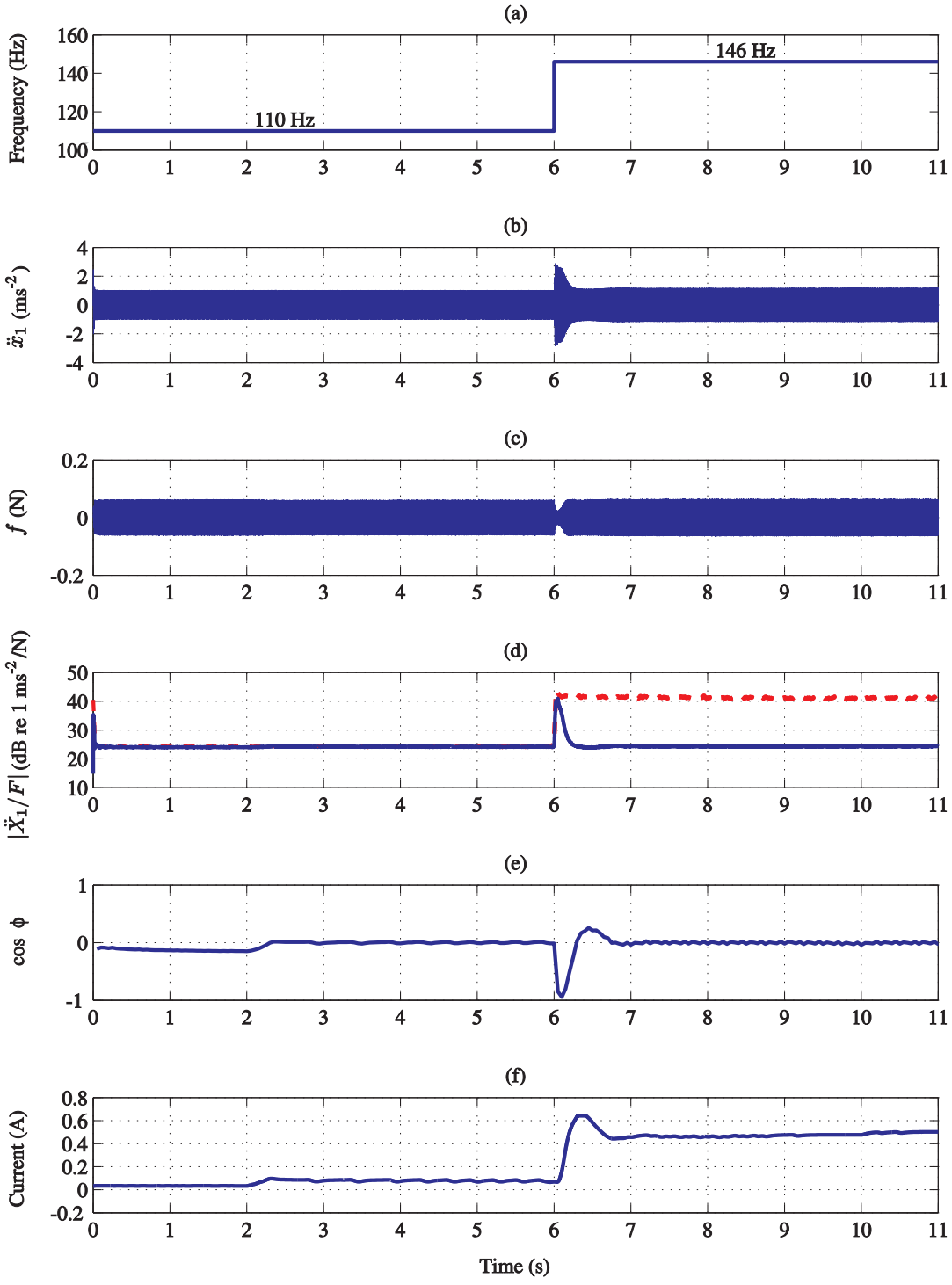

Fig. 7.14: Experimental results of ATVA with the control system for step excitation from 110 to 146 Hz at $t = 6$ s: (a) excitation frequency; (b) host structure acceleration; (c) force; (d) host structure accelerance; (e) $\cos\phi$; (f) current I. $P = 0.13, D = 0.005, T_c = 0.05$; — with and --- without control.

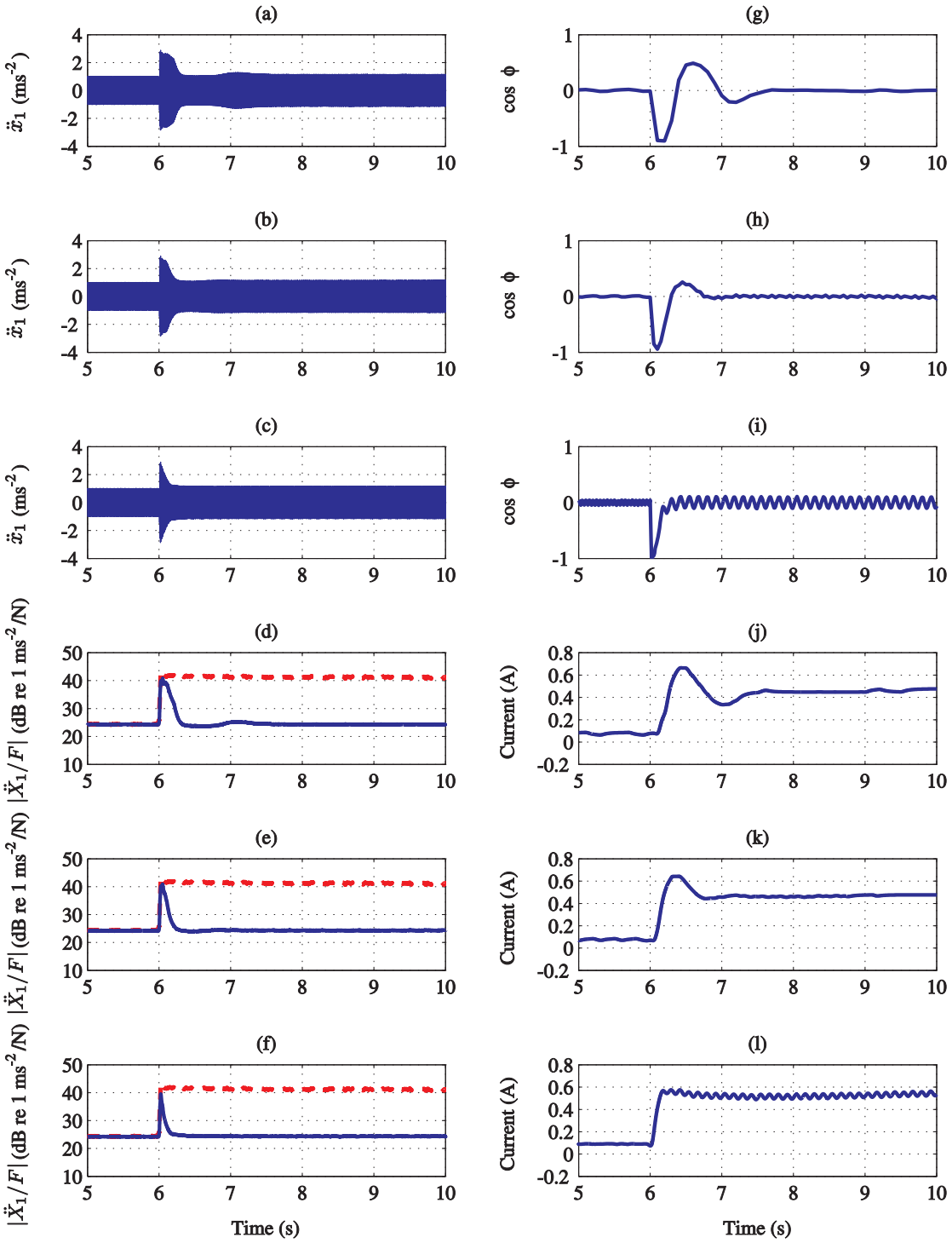

Fig. 7.15: Experimental response of ATVA to the step excitation shown in Fig. 7.14(a) with the control system for variable time increment T_c: (a) $T_c = 0.1$ s; (b) $T_c = 0.05$ s; (c) $T_c = 0.01$ s; $|\ddot{X}_1/F|$ with T_c equal to (d) 0.1 s; (e) 0.05 s; (f) 0.01 s; $\cos\phi$ with T_c equal to (g) 0.1 s; (h) 0.05 s; (i) 0.01 s; and current I with T_c equal to (j) 0.1 s; (k) 0.05 s; (l) 0.01 s. $P = 0.13, D = 0.005$; — with and --- without control.

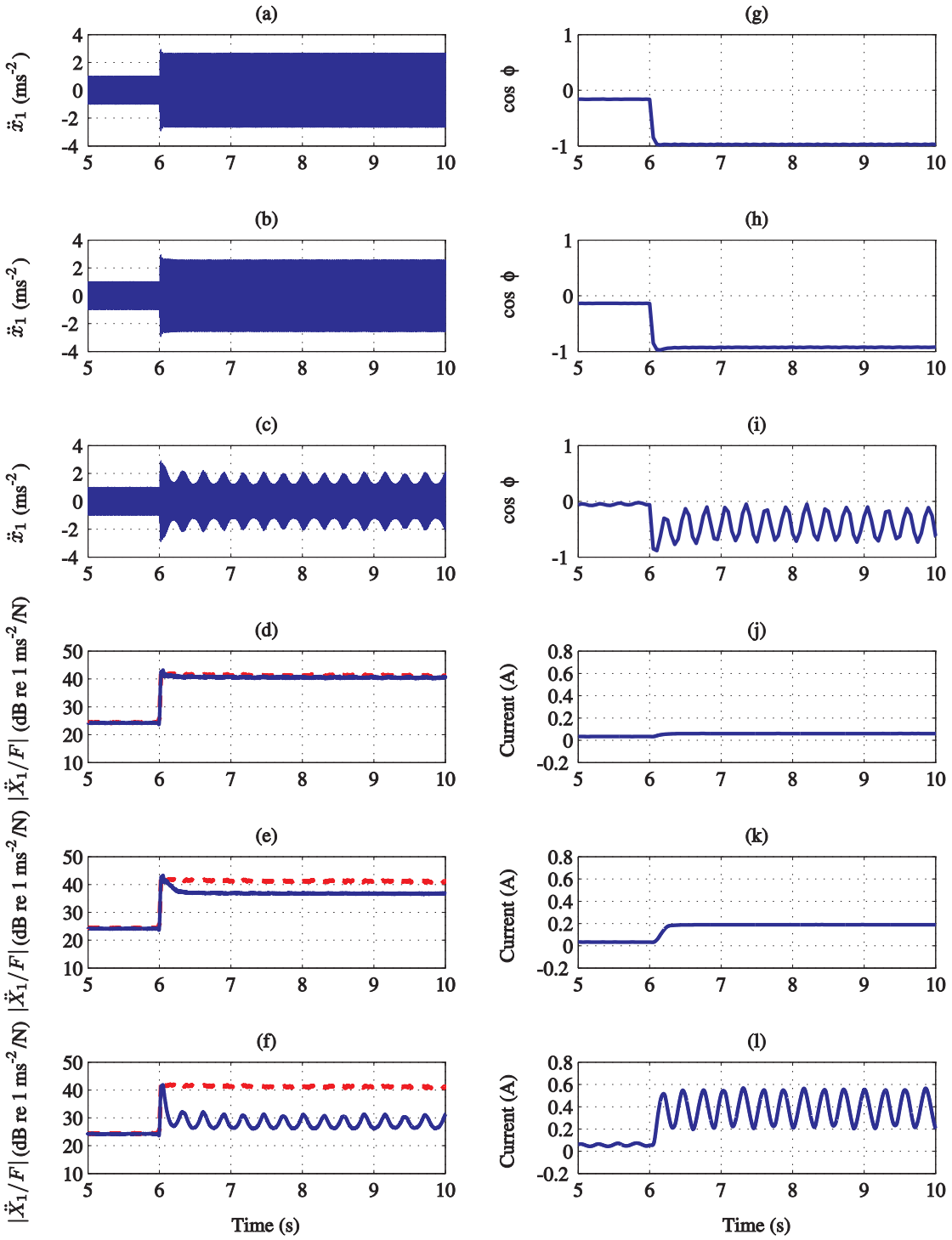

Fig. 7.16: Experimental response of ATVA to the step excitation shown in Fig. 7.14(a) with the derivative control for variable controller constant D: (a) $D = 0.001$; (b) $D = 0.005$; (c) $D = 0.05$; $|\ddot{X}_1/F|$ with D equal to (d) 0.001; (e) 0.005; (f) 0.05; $\cos\phi$ with D equal to (g) 0.001; (h) 0.005; (i) 0.05; and current I with D equal to (j) 0.001; (k) 0.005; (l) 0.05. $P = 0, T_c = 0.05$ s; — with and --- without control.

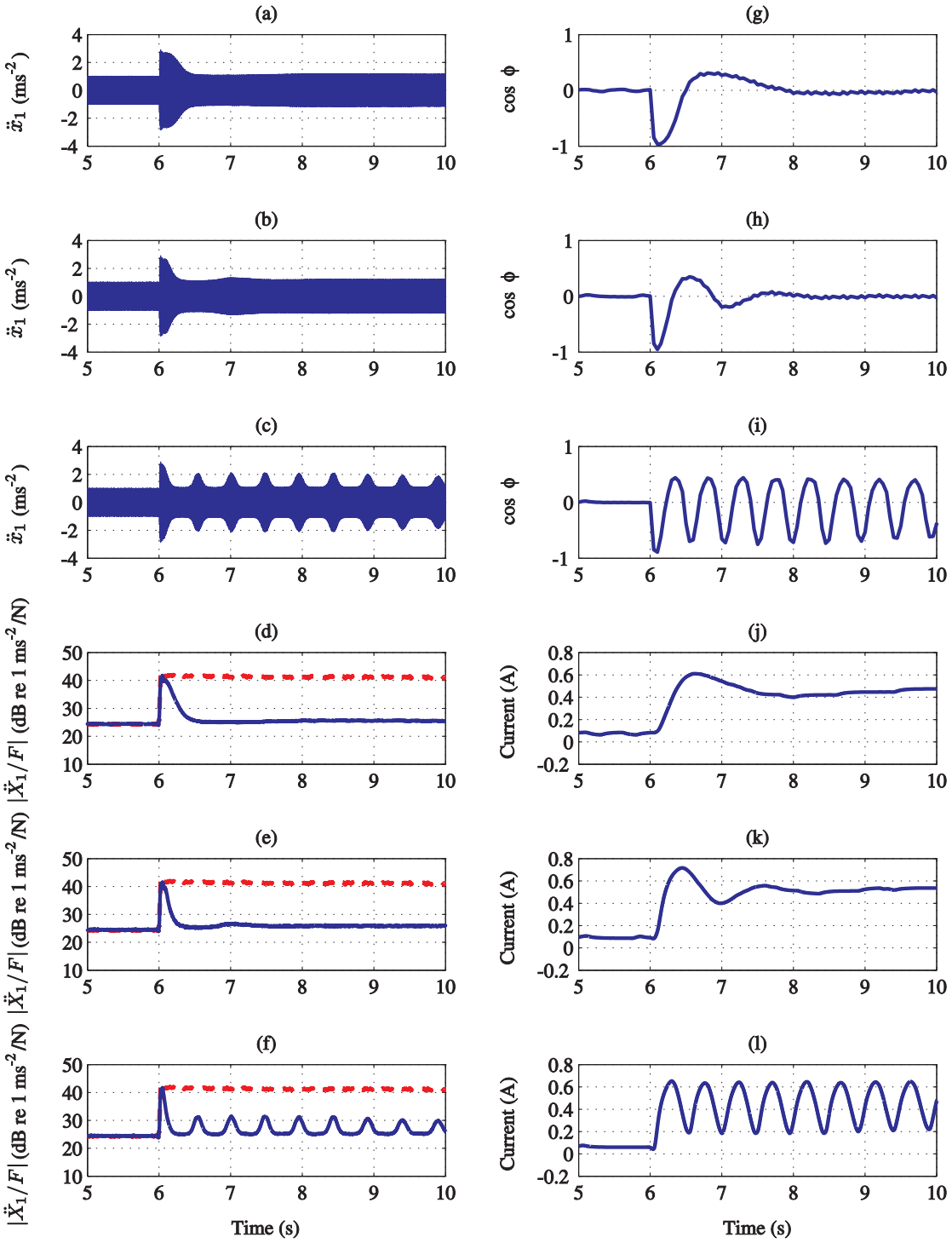

Fig. 7.17: Experimental response of ATVA to the step excitation shown in Fig. 7.14(a) with the proportional control for variable controller constant P: (a) $P = 0.04$; (b) $P = 0.13$; (c) $P = 0.4$; $|\ddot{X}_1/F|$ with P equal to (d) 0.04; (e) 0.13; (f) 0.4; $\cos\phi$ with P equal to (g) 0.04; (h) 0.13; (i) 0.4; and current I with P equal to (j) 0.04; (k) 0.13; (l) 0.4. $D = 0, T_c = 0.05$ s; — with and --- without control.

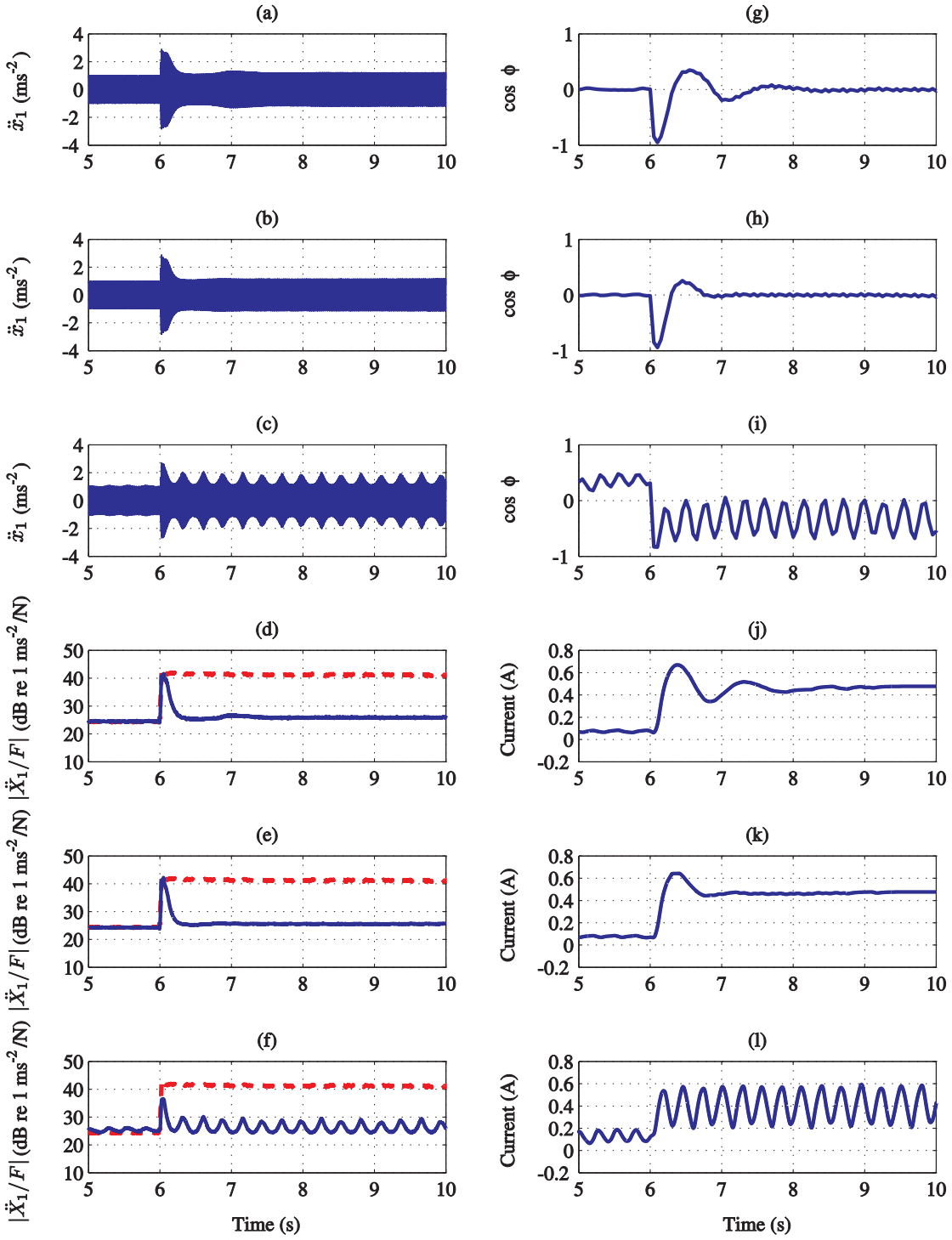

Fig. 7.18: Experimental response of ATVA to the step excitation shown in Fig. 7.14(a) with the proportional-plus-derivative control for variable controller constant D: (a) $D = 0$; (b) $D = 0.005$; (c) $D = 0.05$; $|\ddot{X}_1/F|$ with D equal to (d) 0; (e) 0.005; (f) 0.05; $\cos\phi$ with D equal to (g) 0; (h) 0.005; (i) 0.05; and current I with D equal to (j) 0; (k) 0.005; (l) 0.05. $P = 0.13, T_c = 0.05$ s; — with and --- without control.

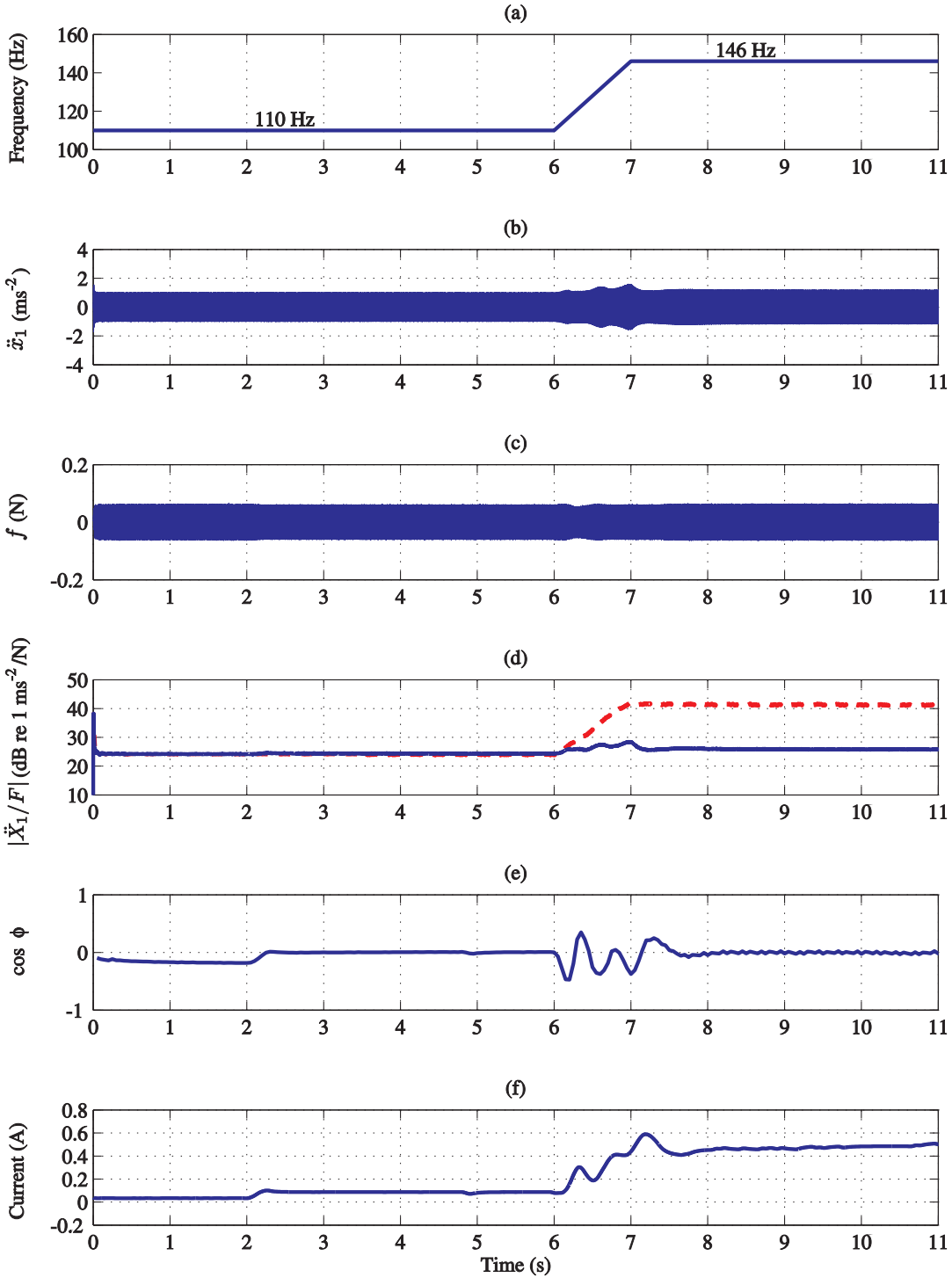

Fig. 7.19: Experimental response of ATVA with the control system for tracking a frequency change of 38 Hz/s (110 Hz to 146 Hz in 1 s starting at $t = 6$ s): (a) excitation frequency; (b) host structure acceleration; (c) force; (d) host structure accelerance; (e) $\cos\phi$; (f) current I. $P = 0.13, D = 0.005, T_c = 0.05$; — with and --- without control.

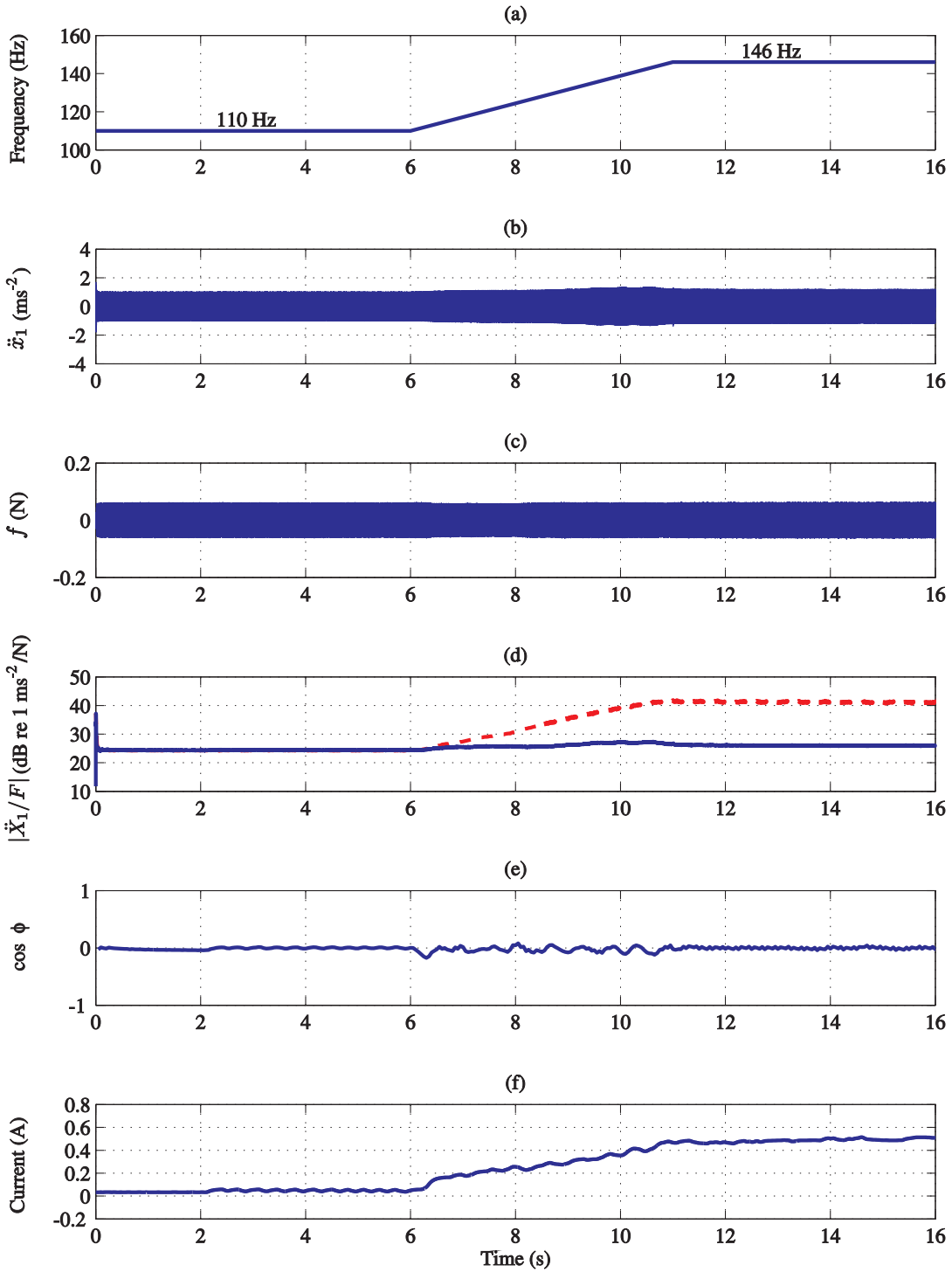

Fig. 7.20: Experimental response of ATVA with the control system for tracking a frequency change of 7.6 Hz/s (110 Hz to 146 Hz in 5 s starting at $t = 6$ s): (a) excitation frequency; (b) host structure acceleration; (c) force; (d) host structure accelerance; (e) $\cos\phi$; (f) current I. $P = 0.13, D = 0.005, T_c = 0.05$; — with and --- without control.

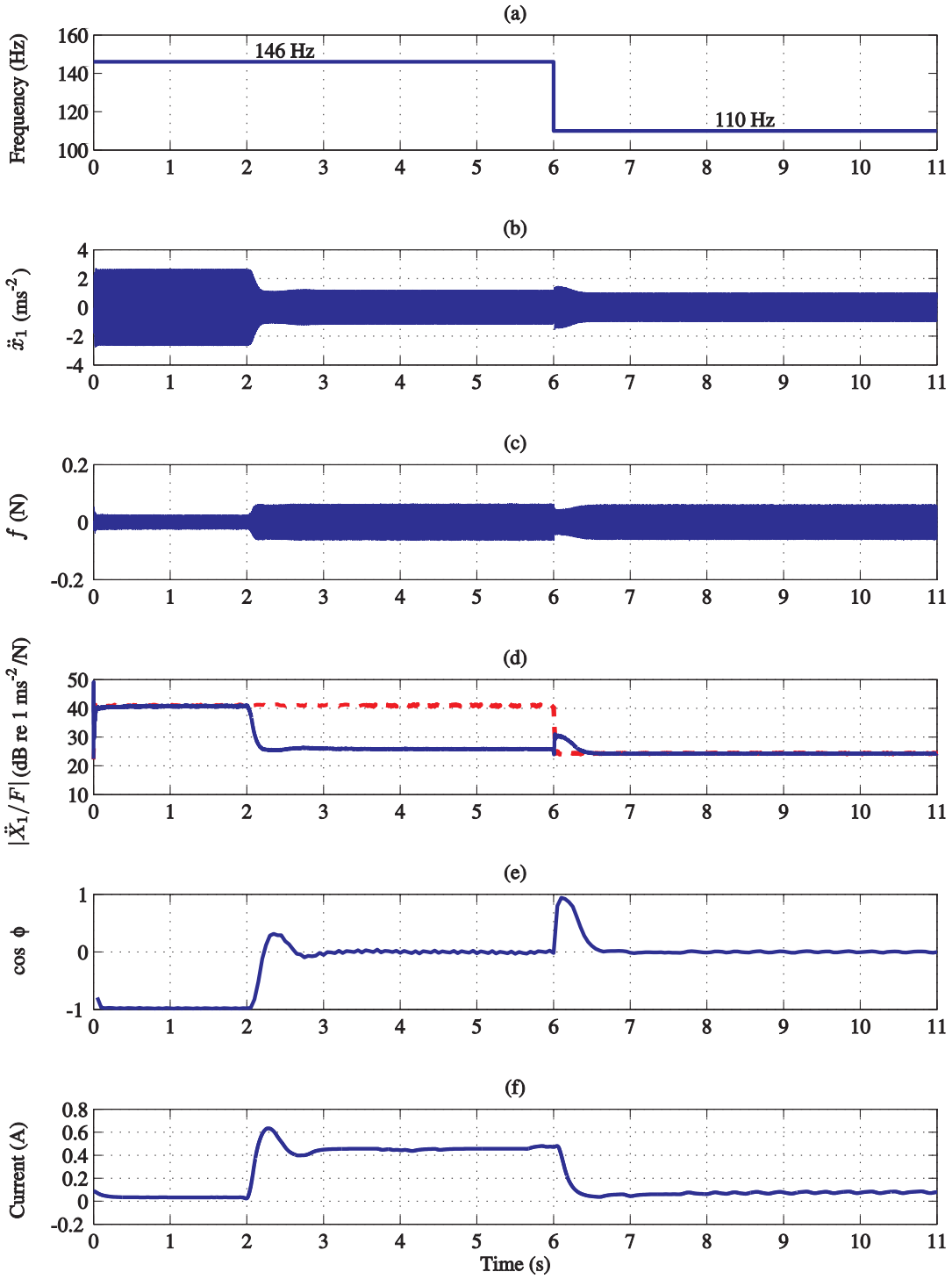

Fig. 7.21: Experimental results of ATVA with the control system for step excitation from 146 to 110 Hz at $t = 6$ s: (a) excitation frequency; (b) host structure acceleration; (c) force; (d) host structure accelerance; (e) $\cos\phi$; (f) current I. $P = 0.13, D = 0.005, T_c = 0.05$; — with and --- without control.

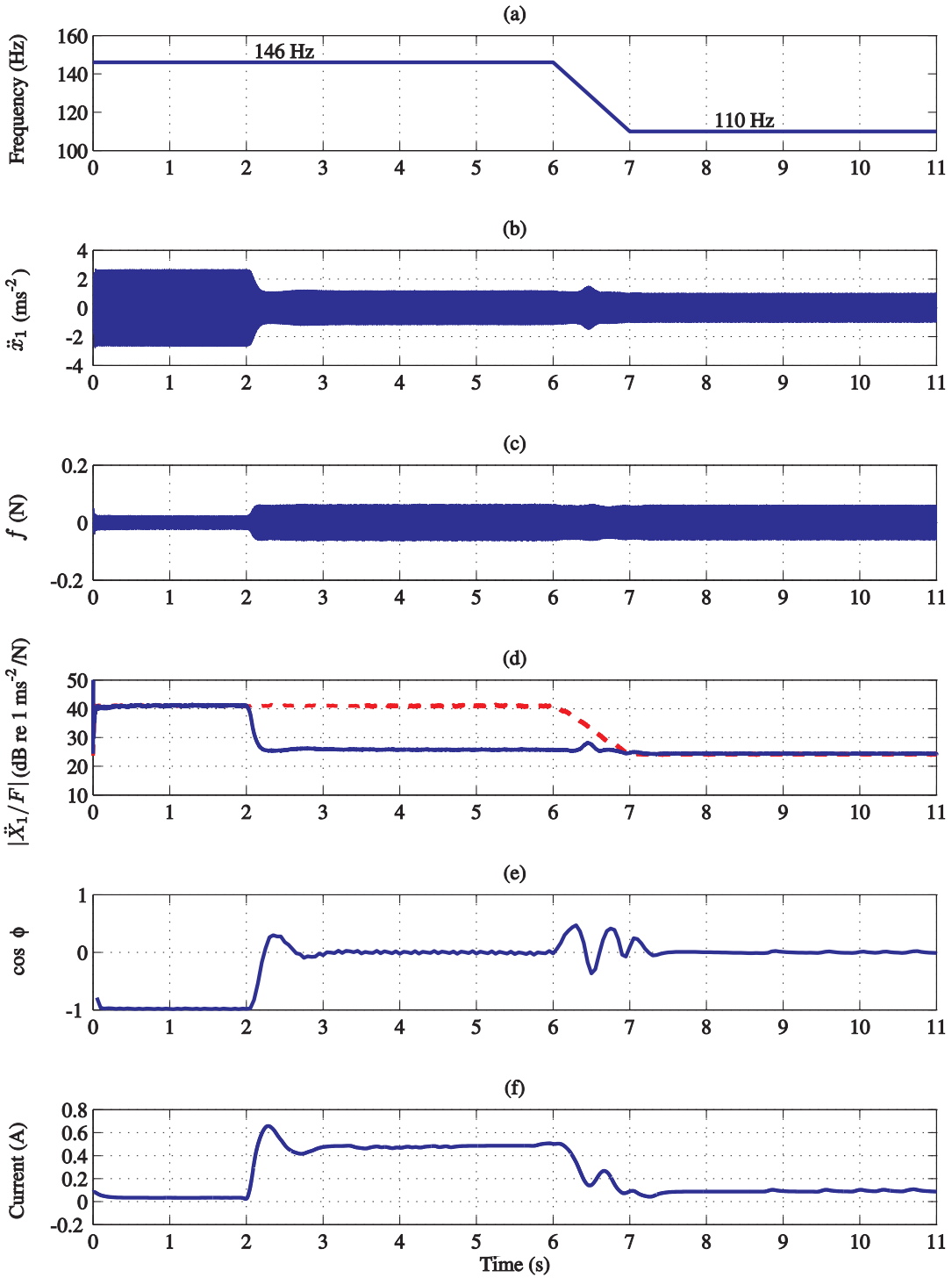

Fig. 7.22: Experimental response of ATVA with the control system for tracking a frequency change of 38 Hz/s (146 Hz to 110 Hz in 1 s starting at $t = 6$ s): (a) excitation frequency; (b) host structure acceleration; (c) force; (d) host structure accelerance; (e) $\cos\phi$; (f) current I. $P = 0.13, D = 0.005, T_c = 0.05$; — with and --- without control.

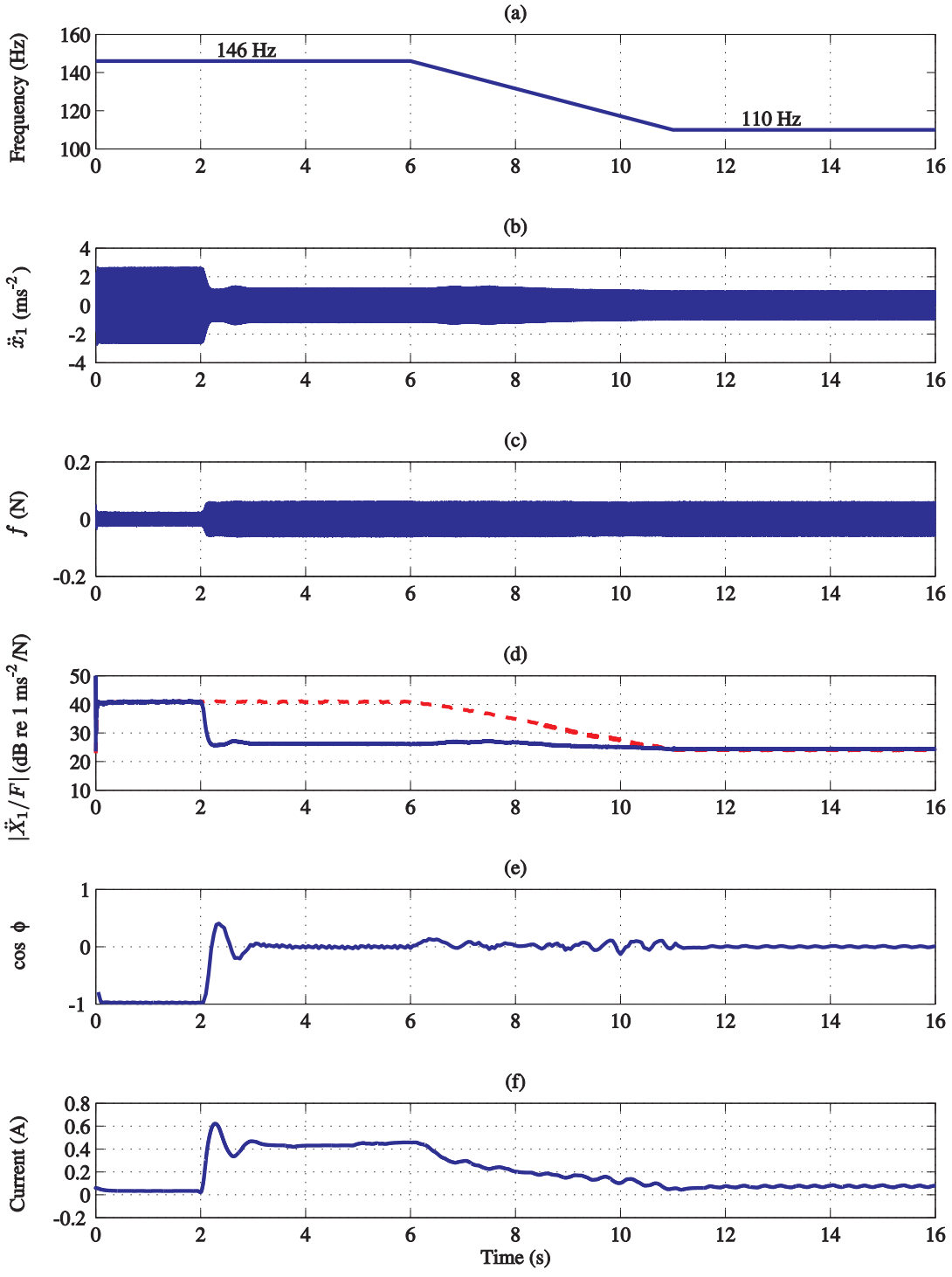

Fig. 7.23: Experimental response of ATVA with the control system for tracking a frequency change of 7.6 Hz/s (146 Hz to 110 Hz in 5 s starting at $t = 6$ s): (a) excitation frequency; (b) host structure acceleration; (c) force; (d) host structure accelerance; (e) $\cos\phi$; (f) current I. $P = 0.13, D = 0.005, T_c = 0.05$; — with and --- without control.

Chapter 8

Concluding Remarks and Suggestions for Further Work

8.1 Summary

This thesis was concerned with an adaptive tuned vibration absorber (ATVA) exploiting the pre-yield properties of magneto-rheological (MR) fluid. The MR fluid-filled ATVA is a narrow-band device aimed to suppress vibration at a specific forcing frequency. This can be done by tuning its natural frequency to the disturbance frequency as presented in Chapter 2. However, the device is capable of being tuned over a particular range of frequencies to increase its effective bandwidth. The key to make the MR fluid-filled ATVA tunable is the changeable properties of MR fluid with a magnetic field. The self-tuning of the ATVA can be achieved by integrating it with the control system.

The complex shear modulus of the MR fluid, which is dependent on a magnetic field, was investigated in Chapter 3. An empirical model was proposed by fitting an exponential function to the experimental data. It was found from the experiment that the storage modulus of the MR fluid increased with the increase in magnetic field, but the loss factor showed the opposite trend. However, both storage modulus and loss factor were independent of magnetic field for very high magnetic fields because of saturation. The maximum applied magnetic field of 347 mT produced a change in storage modulus up to approximately 4.28 MPa.

The design of the MR fluid-filled ATVA and theoretical predictions of its response have been presented in Chapters 4 and 5. The MR fluid-filled ATVA is a three-layer beam comprising two elastic layers with MR fluid in the central core. Electromagnets, which are coils wound around U-shape pieces of mild steel, are attached to the outer layers of the ATVA to generate magnetic field. The MR fluid-filled ATVA behaves as a beam-like ATVA whose centre is attached to the host structure. Its shear stiffness is changed by varying the magnetic field across the core, which changes the shear modulus of the MR fluid in the core, and hence the tuned frequency of the device. The magnetic field can be changed by altering the current applied to electromagnets attached to the beam.

In Chapter 4, the finite element (FE) model for the MR fluid-filled ATVA was developed based on the sandwich beam theory of Mead and Markus [53, 78, 79] which assumes that the elastic outer layers behave as Euler-Bernoulli beams, the core carries shear and all the three-layers undergo the same transverse displacement. The one-dimensional element has three degrees-of-freedom at each node, i.e. axial displacement of the mid-surface of the top layer, transverse displacement, and its first derivative.

The influence of geometric parameters on the tuned frequency of the MR fluid-filled ATVA was investigated numerically in Chapter 5. Parametric studies were conducted using the FE model on the vibration characteristics of the ATVA together with the simple model for the magnetic field, and the empirical model for the shear modulus of MR fluid. Five parameters, i.e the thicknesses of the outer layers and the middle layer, the width and the length of the ATVA beam, and the number of electromagnets attached to the beam, were examined. It was found that the wider beam and the thicker outer layers showed lower changes in tuned frequency, but the beam with more electromagnets provided a higher change. The shorter beam was able be tuned over a wider range. However, too short a beam reduced the effective bandwidth. The thickness of the middle layer showed the same effect as the length of the ATVA beam.

The models developed were verified through experiments on the MR fluid-filled ATVA subjected to various magnetic field in Chapter 6. Parameters, i.e. Young's

modulus of perspex, stiffness of the tape, and the loss factor of MR fluid, used in the FE model were estimated using model updating and sensitivity analysis. The experimental results agreed with the predictions and showed that the MR fluid-filled ATVA exhibited a significant change in the tuned frequency, which was about 40.6%, when the applied current was increased to 646 mA.

In Chapter 7, adaptive-passive control was implemented and the self-tuning of the MR fluid-filled ATVA was investigated numerically and experimentally. Instead of using the FE model for the vibration of the MR fluid-filled ATVA, the two degree-of-freedom model was used in the self-tuning simulations. Three controllers, i.e. non-linear proportional (P) control, derivative (D) control, and proportional-plus-derivative (PD) control, were employed to tune the stiffness of the MR fluid-filled ATVA in real-time. This was done by driving the cosine of the phase between the velocities of the host structure and the ATVA mass to zero, by changing the current input to the electromagnets of the ATVA.

Numerical simulations and experiments on the real-time control of the ATVA subjected to a step change in excitation frequency were conducted to investigate the performance of the three controllers. It was shown that the non-linear P and PD controls worked effectively, however the pure derivative control could not tune the ATVA and hence drive the response of the host structure to its minimum level. The effects of the time increment T_c and the controller constants P and D on the settling time were also illustrated. It was shown in the non-linear P control that larger values of P led to shorter settling times. However, too large a value for P caused oscillations in the system. The control constant D in the PD control showed the same effect as the constant P. However the time constant T_c showed the opposite trend, i.e. the settling time increased as T_c increased. The non-linear PD control with $P = 0.13, D = 0.005$, and $T_c = 0.05$ exhibited the shortest settling time of 0.06 s in the simulation, while the settling time of 0.16 s was found in the experiment. The difference of convergence speed between the simulation and experiment was because of dynamic delays which are not considered in the simulation. However they exist in the real system. These delays are due to the MR fluid response time, the electric circuit response, and the time for transient vibration to decay.

The tracking ability of the MR fluid-filled ATVA was also investigated. It was shown that the ATVA was able to retune itself to track changes in frequency of 38 and 7.6 Hz/s. Also the slower rate of change in forcing frequency showed better tracking ability of the ATVA. The MR fluid-filled ATVA had potential to reduce vibration of the host structure up to 18 dB numerically, while 16 dB reduction was achieved experimentally.

8.2 Conclusions

In summary, the following conclusions can be drawn from this thesis:

- A three-layer beam with MR fluid as a shear core can be used as an ATVA.
- For the fluid used in this thesis the measured storage modulus and loss factor can be modelled empirically as

$$G' = 2470 + (4.33 \times 10^6 - 2470)(1 - e^{-47.3B^2}) \tag{8.1}$$

$$\eta = -2.51B + 0.8. \tag{8.2}$$

- The stiffness of the ATVA increases approximately with increase in the storage modulus of MR fluid, and can be modelled empirically as

$$k_a = 0.0017G' + 6344. \tag{8.3}$$

- A one-dimensional three DOF per node finite element can model the vibrations of the TVA with acceptable accuracy. This can be used to model the uniform three-layer beam and compare its behaviour to the Mead and Markus model, and the non-uniform three-layer ATVA for various currents.
- Sets of small U-shape electromagnets consisting of a mild steel core and a coil of wire is able to provide sufficient magnetic field to change the properties of MR fluid in the shear core.

- A simple model for the magnetic field can be used to estimate the magnetic field generated by the electromagnets to an acceptable accuracy.
- The ATVA with the adaptive-passive control is able to retune itself and can maintain the tuned condition within a reasonably wide frequency range. This ATVA can achieve the change in natural frequency of 40.6%
- Tuning condition $\cos\phi = 0$ is ok even with damping in the ATVA.
- PD control shows better performance than P or D control alone. Nonlinear P is able to tune the ATVA effectively, but the inclusion of the D term increases the tuning speed.
- The values of the controller constants P and D and the control period T_c should be carefully chosen as too large values for P, D and T_c can lead to the instability in the control system.
- The controller with $P = 0.13, D = 0.005$ and $T_c = 0.05$ shows the shortest setting time, which is in the order of 0.2 s. Also the ATVA with this controller is able to track frequency change of 38 Hz/sec from 110 to 146 Hz.

8.3 Suggestions for Future Work

The FE model in the thesis used a one-dimensional finite element. This model is suitable for the structure which is uniform along the width. However for the MR fluid-filled ATVA this is not the case due to the existence of electromagnets. It also assumed the physical construction was symmetric, i.e. the outer layers are identical. A three-dimensional FE model is then proposed for the future work to increase the accuracy of the model.

One factor that affects the effective bandwidth or the tunable range of the MR fluid-filled ATVA is the magnetic field generated by electromagnets. The limitation of the electromagnets designed in the thesis is that they are not able to provide a magnetic field to a larger area of MR fluid in the middle layer of the ATVA due to their weight constraint. Also the limited current of 0.8 A to avoid overheating

is a drawback of the electromagnet design. The challenge for the future work is to improve the design of the electromagnets so that they can provide higher magnetic field strengths, and can thus be applied to a larger area of the fluid resulting in a wider tunable range of the ATVA. This can be done by, for example, increasing the number of turns of wire and using a lighter magnetic material than mild steel. However, the permeability of the new material should be higher or about the same as that of mild steel.

The fastest settling time of the MR fluid-filled ATVA is much greater than the MR fluid response time suggested in many studies. Investigations into the delay time of the ATVA due to, for example the time to reach steady-state vibrations or the electrical circuit, would be beneficial to improve the speed of the ATVA. The delay associated with the electrical circuit might be caused by the power supply, and can be simply determined by measuring a step rise in current generated by the power supply.

It is not necessary to limit the configurations of the ATVA exploiting MR fluid to the design proposed in the thesis. However the design of the ATVA often depends on its application. For example the size of the ATVA could be larger so that it could be used for the heavy load application. Also it would be worthwhile to apply the MR fluid-filled ATVA to suppress vibration of a real structure. However, the mass of the host structure and the location of the ATVA on the structure should be taken into consideration as they affect the effectiveness of the ATVA. Also an additional theory might be required to locate the ATVA in the right place.

References

[1] F.J. Fahy and J.G. Walker. *Fundamentals of Noise and Vibration*. E & FN SPON, 1998.

[2] S-T. Wu, J-Y. Chen, Y-C. Yeh, and Y-Y. Chiu. An active vibration absorber for a flexible plate boundary-controlled by a linear motor. *Journal of Sound and Vibration*, 300(1–2):250–264, 2007.

[3] T.P.C. Bramer. *Basic vibration control*. McGraw-Hill, 1977.

[4] C.M. Harris and C.E. Crede. *Shock and Vibration Handbook*. Sound Research Laboratories Limited, 1961.

[5] *Handbook of Noise and Vibration Control 3rd Edition*. Trade & Technical Press, 1975.

[6] D.J. Mead. *Passive Vibration Control*. John Wiley & Sons, 2000.

[7] R.G. White and J.G. Walker. *Noise and Vibration*. Wllis Horwood, 1982.

[8] C. Park and D. Jeon. Semiactive vibration control of a smart seat with an mr fluid damper considering its time delay. *Journal of Intelligent Material Systems and Structures*, 13(7–8):521–524, 2002.

[9] B.N. Sun, S.S. Chen, and W.J. Lou. Maximum modal damping of cable space vibration control with viscous damper in cable-stayed bridge. *Proceedings of the SPIE - The International Society for Optical Engineering*, 5046:611–621, 2003.

[10] R.S. Jones. *Noise and Vibration Control in Buildings*. McGraw-Hill, 1984.

[11] J. P. Den Hartog. *Mechanical Vibrations*. Dover Publications, 1985.

[12] M. J. Brennan. Vibration control using a tunable vibration neutralizer. *Proceedings of the Institution of Mechanical Engineers, Part C (Journal of Mechanical Engineering Science)*, 211:91–108, 1997.

[13] B.O. Al-Bedoor, K.A. Moustafa, and K.M. Al-Hussain. Dual dynamic absorber for the torsional vibrations of synchronous motor-driven compressors. *Journal of Sound and Vibration*, 220(4):729–748, 1999.

[14] T.H. Yan and R.M. Lin. Dual-mass dynamic absorber for the head actuator assembly in hard disk drives. *Mechanics Based Design of Structures and Machines*, 32(2):119–132, 2004.

[15] M. Jorkama and R. von Hertzen. Optimal dynamic absorber for a rotating reyleigh beam. *Journal of Sound and Vibration*, 217(4):653–664, 1998.

[16] G.J. Lee-Glauser, G. Ahmadi, and L.G. Horta. Integrated passive/active vibration absorber for multistory buildings. *Journal of Structural Engineering*, 123(4):499–504, 1997.

[17] T. Fujinami and S. Yamamoto. Dynamic absorber using lever and pendulum mechanism installed to top of structure. *American Society of Mechanical Engineers, Pressure Vessels and Piping Division (Publication) PVP*, 197:143–148, 1990.

[18] D.J Thompson and P.-E. Gautier. Review of research into wheel/rail rolling noise reduction. *Proceedings of the Institution of Mechanical Engineers, Part F: Journal of Rail and Rapid Transit*, 220(4):385–408, 2006.

[19] D.J Thompson, C.J.C. Jones, T.P. Waters, and D. Farrington. A tuned damping device for reducing noise from railway track. *Applied Acoustics*, 68(1):43–57, 2007.

[20] S. La Malfa, P.A.A. Laura, C.A. Rossit, and O. Alvarez. Use of a dynamic absorber in the case of a vibrating printed circuit board of complicated boundary shape. *Journal of Sound and Vibration*, 230(3):721–724, 2000.

[21] A.H. von Flotow, A. Beard, and D. Bailey. Adaptive tuned vibration absorbers: Tuning laws, tracking ability, sizing, and physical implementations. *Proceedings of Noise-Con 94*, 94:437–454, 1994.

[22] H.M. EI-Khatib, B.R. Mace, and M.J. Brennan. Suppression of bending waves in a beam using a tuned vibration absorber. *Journal of Sound and Vibration*, 288(4–5):1157–1175, 2005.

[23] N.D. Anh, H Matsuhisa, L.D. Viet, and M. Yasuda. Vibration control of an inverted pendulum type structure by passive mass-spring-pendulum dynamic vibration absorber. *Journal of Sound and Vibration*, 307(1–2):187–201, 2007.

[24] R.J. Nagem, S.I. Madanshetty, and G. Medhi. An electromechanical vibration absorber. *Journal of Sound and Vibration*, 200(4):551–556, 1997.

[25] T.D. Truong and S.E. Semerciqil. A variable damping tuned absorber with electro-rheological fluid for transient resonance of light structures. *Journal of Sound and Vibration*, 239(5):891–905, 2001.

[26] N.M. Sakamota, N. Oshima, and T. Fukuda. Tuned sloshing damper using electro-rheological fluid. *Smart Materials and Structures*, 10(5):963–969, 2001.

[27] M.W. Ryan, M.A. Franchek, and R. Bernhard. Adaptive-passive vibration control of single frequency excitations applied to noise control. *Proceedings of Noise-Con 94*, 94:461–466, 1994.

[28] C.A. Buhr, M.A. Franchek, and R.J. Bernhard. Noncollocated adaptive-passive vibration control using self-tuning vibration absorbers. *Proceedings of the 1998 American Control Conference*, 6:3460–3464, 1998.

[29] T. Long, M. J. Brennan, and S. J. Elliott. Design of smart machinery installations to reduce transmitted vibrations by adaptive modification of internal forces. *Proceedings of the Institution of Mechanical Engineering, Journal of Systems and Control Engineering*, 212(13):215–228, 1998.

[30] K. Nagaya, A. Kurusu, S. Ikai, and Y. Shitani. Vibration control of a structure by using a tunable absorber and an optimal vibration absorber under auto-tuning control. *Journal of Sound and Vibration*, 228(4):773–792, 1999.

[31] P.L. Walsh and J.S. Lamancusa. A variable stiffness vibration absorber for minimization of transient vibrations. *Journal of Sound and Vibration*, 158(2):195–211, 1992.

[32] M.R.F. Kidner and M.J. Brennan. Varying the stiffness of a beam-like neutralizer under fuzzy logic control. *Journal of Vibration and Acoustics, Transactions of the ASME*, 124(1):90–99, 2002.

[33] P. Bonello, M. J. Brennan, and S. J. Elliott. Vibration control using an adaptive tuned vibration absorber with a variable curvature stiffness element. *Smart Material and Structures*, 14:1055–1065, 2005.

[34] A. Baz, K. Imam, and J. McCoy. Active vibration control of flexible beams using shape memory actuators. *Journal of Sound and Vibration*, 140(3):437–456, 1990.

[35] K. Williams, G. Chiu, and R. Bernhard. Adaptive-passive absorbers using shape-memory alloys. *Journal of Sound and Vibration*, 249(5):835–848, 2002.

[36] E. Rustighi, M. J. Brennan, and B. R. Mace. Real-time control of a shape memory alloy adaptive tuned vibration absorber. *Smart Material and Structures*, 14:1184–1195, 2005.

[37] A. V. Srinivasan and D. Michael. McFarland. *Smart Structures: Analysis and Design*. Cambridge University Press, 2001.

[38] W. Min and F. Renyuan. Improvement of machining stability using a tunable-stiffness boring bar containing an electrorheological fluid. *Smart Materials and Structures*, 8(4):511–514, 1999.

[39] J. M. Ginder, W. F. Schlotter, and M. E. Nichols. Magnetorheological elastomers in tunable vibration absorbers. *Proceedings of the SPIE - The International Society for Optical Engineering*, 4331:103–110, 2001.

[40] H-X. Deng, X-L. Gong, and Wang L-H. Development of an adaptive tuned vibration absorber with magnetorheological elastomer. *Smart Materials and Structures*, 15:N111–N116, 2006.

[41] A.M. Albanese and K.A. Cunefare. Properties of a magnetorheological semi-active vibration absorber. *Proceedings of SPIE - The International Society for Optical Engineering*, 5052:36–43, 2003.

[42] M. Yalcintas and H. Dai. Magnetorheological and electrorheological materials in adaptive structures and their performance comparison. *Smart Materials and Structures*, 8:560–573, 1999.

[43] E. Rustighi, M.J. Brennan, and B.R. Mace. Real-time control of a shape memory alloy adaptive tuned vibration absorber. *Smart Materials and Structures*, 14(6):1184–1195, 2005.

[44] Y.M. Han, M.H. Nam, S.S Han, H.G. Lee, and S.B. Choi. Vibration control evaluation of a commercial vehicle featuring mr seat damper. *Journal of Intelligent Material Systems and Structures*, 13(9):575–579, 2002.

[45] H. Sahin, Y. Liu, X. Wang, F. Gordaninejad, C. Evrensel, and A. Fuchs. Full-scale magnetorheological fluid dampers for heavy vehicle rollover. *Journal of Intelligent Material Systems and Structures*, 18(12):1161–1167, 2007.

[46] Z.Q. Gu and Oyadiji S.O. Application of mr damper in structural control using anfis method. *Computers and Structures*, 86(3–5):427–436, 2008.

[47] B. Liu, W.H. Li, P.B Kosasih, and X.Z. Zhang. Development of an mr-brake-based haptic device. *Smart Materials and Structures*, 15(6):1960–1966, 2006.

[48] K. Karakoc, E.J. Park, and A. Suleman. Design considerations for an automotive magnetorheological brake. *Mechatronics*, 18(8):434–447, 2008.

[49] V. A. Neelakantan and G. N. Washington. Modeling and reduction of centrifuging in magnetorheological (MR) transmission clutches for automotive applications. *Journal of Intelligent Material Systems and Structures*, 16:703–711, 2005.

[50] B.M. Kavlicoqlu, F. Gordaninejad, C.A. Evrensel, Y Li, N. Kavlicoqlu, and A. Fuchs. Heating of a high-torque magnetorheological fluid limited slip differential clutch. *Journal of Intelligent Material Systems and Structures*, 19(2):235–241, 2008.

[51] H-U. Oh. Characteristics of a magneto-rheological fluid isolator obtained by permanent magnet arrangements. *Smart Materials and Structures*, 13(3):N29–N35, 2004.

[52] D. York, X. Wang, and F. Gordaninejad. A new mr fluid-elastomer vibration isolator. *Journal of Intelligent Material Systems and Structures*, 18(12):1221–1225, 2007.

[53] D. J. Mead and S. Markus. The forced vibration of a three-layer, damped sandwich beam with arbitrary boundary conditions. *Journal of Sound and Vibration*, 10(2):163–175, 1969.

[54] K. A. Stroud. *Engineering Mathematics*. Macmillan Press, 1995.

[55] P. P. Phulé. Magnetorheological (MR) fluids: Principles and applications. *Smart Materials Bulletin*, 2:7–10, February 2001.

[56] J. Rabinow. The magnetic fluid clutch. *Transactions of the AIEE*, 67:1308–1315, 2001.

[57] K. D. Weiss, J. D. Carlson, and D. A. Nixon. Viscoelastic properties of magneto- and electro-rheological fluids. *Journal of Intelligent Material Systems and Structures*, 5:772–775, November 1994.

[58] W. H. Li, G. Chen, and S. H. Yeo. Viscoelastic properties of MR fluids. *Smart Materials and Structures*, 8:460–468, 1999.

[59] W. H. Li, H. Du, G. Chen, S. H. Yeo, and N. Q. Guo. Nonlinear viscoelastic properties of MR fluids under large-amplitude-oscillatory shear. *Rheologica Acta*, 42:280–286, 2003.

[60] W. H. Li, H. Du, and N. Q. Guo. Dynamic behavior of MR suspensions at moderate flux densities. *Materials Science and Engineering A*, 371:9–15, 2004.

[61] A. J. Marqida, K. D. Weiss, and J. D. Carlson. Magnetorheological materials based on iron alloy particles. *Proceedings of the 5th International Conference on Electro-Rheological Fluids, Magneto-Rheological Suspensions and Associated Technology*, pages 544–550, 1996.

[62] V. K. Sukhwani and H. Hirani. Synthesis and characterization of low cost magnetorheological (MR) fluids. *Proceedings of SPIE - The International Society for Optical Engineering*, 6526:65262R, 2007.

[63] R. Tao. Super-strong magnetorheological fluids. *Journal of Physics: Condensed Matter*, 13:R979–R999, 2001.

[64] G. L. Gulley and R. Tao. Structures of a magnetorheological fluid. *International Journal of Modern Physics B*, 15:851–858, 2001.

[65] T. G. Mezger. *The rheology handbook: For users of rotational and oscillatory rheometers*. Vincentz Verlag, 2002.

[66] J. M. Ginder, L. C. Davis, and L. D. Elie. Rheology of magnetorheological fluids: models and measurements. *International Journal of Modern Physics B*, 10(23–24):3293–3303, 1996.

[67] M. R. Jolly, J. W. Bender, and J. D. Carlson. Properties and applications of commercial magnetorheological fluids. *Journal of Intelligent Material Systems and Structures*, 10:5–13, January 1999.

[68] W. H. Li, P. Q. Zhang, X. L. Gong, and P. B. Kosasih. Linear viscoelasticity of mr fluids: dependence on magnetic fields. *International Journal of Modern Physics B*, 19:1198–1204, 2005.

[69] N. R. Harland. *Control of vibration transmission using tunable fluid filled beam inserts*. PhD thesis, Department of Mechanical Engineering, University of Auckland, 1999.

[70] K. D. Weiss, T. G. Duclos, M. J. Chrzan, and L. C. Yanyo. Magnetorheological fluids composite structures. *US Patent*, 5, 1996.

[71] C. Hirunyapruk, B.R. Mace, M.J. Brennan, and W.H. Li. Modelling and experimental characterization of a tunable magneto-rheological fluid vibration absorber. *The 7th European Conference on Structural Dynamics (EURODYN 2008)*, page E31, 2008.

[72] Anton Paar GmbH. Brochure-physica MCR rheometer series. http://www.anton-paar.com.

[73] W. H. Li. *Rheology of MR fluids and MR damper dynamic response: experimental and modelling approaches*. PhD thesis, School of Mechanical and Production Engineering, Nanyang Technology University, 2001.

[74] Lord Corporation. http://www.lord.com/.

[75] K. Wollny, J. Lauger, and S. Huck. Magneto sweep - a new method for characterizing the viscoelastic properties of magneto-rheological fluids. *Applied Rheology*, 12:25–31, 2002.

[76] R. A. DiTaranto. Theory of vibration bending for elastic and viscoelastic layered finite-length beams. *Transactions of the ASME Journal of Applied Mechanics*, 87:881–886, 1965.

[77] R. A. DiTaranto and W. Blasingame. Composite damping of vibrating sandwich beams. *Transactions of the ASME Journal of Engineering for Industry*, 89:633–638, 1967.

[78] D. J. Mead and S. Markus. Loss factors and resonant frequencies of encastré damped sandwich beams. *Journal of Sound and Vibration*, 12(1):99–112, 1970.

[79] D. J. Mead. A comparison of some equations for the flexural vibration of damped sandwich beams. *Journal of Sound and Vibration*, 83(3):363–377, 1982.

[80] S. He and M. D. Rao. Vibration of damping analysis of multi-span sandwich beams with arbitrary boundary conditions. *Journal of Sound and Vibration*, 164(1):125–142, 1993.

[81] T. Sakiyama, H. Matsuda, and C. Morita. Free vibration analysis of sandwich beam with elastic or viscoelastic core by applying the discrete green function. *Journal of Sound and Vibration*, 191(2):189–206, 1996.

[82] M. R. Maheri and R. D. Adams. On the flexural vibration of Timoshenko beams, and the applicability of the analysis to a sandwich configuration. *Journal of Sound and Vibration*, 209(3):419–442, 1998.

[83] A. Fasana and S. Marchesiello. Rayleigh-ritz analysis of sandwich beams. *Journal of Sound and Vibration*, 241(4):643–652, 2001.

[84] R. D. Cook. *Concepts and applications of finite element analysis*. John Wiley & Sons, 1974.

[85] K. M. Ahmed. Free vibration of curved sandwich beams by the method of finite elements. *Journal of Sound and Vibration*, 18(1):61–74, 1971.

[86] K. M. Ahmed. Dynamic analysis of sandwich beams. *Journal of Sound and Vibration*, 21(3):263–276, 1972.

[87] T. T. Baber, R. A. Maddox, and C. E. Orozco. A finite element model for harmonically excited viscoelastic sandwich beams. *Computers and Structures*, 66(1):105–113, 1998.

[88] M. G. Sainsbury and Q. J Zhang. The Galerkin element method applied to the vibration of damped sandwich beams. *Computers and Structures*, 71:239–256, 1999.

[89] M. Petyt. *Introduction to finite element vibration analysis*. Cambridge University Press, 1998.

[90] S. S. Rao. *Mechanical Vibration*. Pearson Prentice Hall, 2004.

[91] R. L. Boylestad. *Introductory Circuit Analysis*. Prentice Hall, 1997.

[92] J. D. Kraus. *Electromagnetics*. McGraw-Hill, 1991.

[93] D. J. Ewins. *Modal Testing: Theory, Practice and Application*. Research Studies Press, 2000.

[94] R. M. Bozorth. *Ferromagnetism*. Van Nostrand; Macmillan, 1951.

[95] F. Fahy. *Foundations of Engineering Acoustics*. AcademicPress, 2001.

[96] M. I. Friswell and J. E. Mottershed. *Finite Element Model Updating in Structural Dynamics*. Kluwer Academic Publishers, 1995.

[97] G. F. Franklin, J. D. Powell, and A. Emami-Naeini. *Feedback Control of Dynamic System*. Addison-Wesley Publishing Company, 1994.

[98] M. J. Brennan. Some recent developments in adaptive tuned vibration absorbers / neutralisers. *Shock and Vibration*, 13:531–543, 2006.

Appendix A

Mead and Markus Model for Three-Layer Beam

A.1 Introduction

The purpose of this appendix is to provide an analytical model to which the results from the FE model presented in Chapter 4 can be compared. The Mead and Markus model is a well-known analytical model for the three-layer beam. This model involves a sixth-order differential equation of motion, which is presented in terms of transverse displacement. By assuming harmonic motion, the solutions are expressed as a function of wavenumbers. Applying six boundary conditions and solving the equation of motion numerically gives the natural frequencies of the beam. This appendix presents the equation of motion for three-layer beam derived in [53] and gives the solution for free-free boundary conditions.

A.2 Equation of Motion for Three-Layer Beam

The sixth-order differential equation of motion is derived based on the assumptions that shear strains in the outer layers and longitudinal direct stresses in the middle layer are negligible. The outer layers are purely elastic with Young's moduli E_1 and E_3. The middle layer is linearly viscoelastic with shear modulus G. All three layers experience the same transverse displacement w and the effects of rotary inertia in all of the layers are ignored. The thicknesses of each layers are h_1, h_2, and h_3 and the

densities of each layers are given by ρ_1, ρ_2, and ρ_3. The subscripts $_{1,2,3}$ represent the top layer, the middle layer, and the bottom layer respectively.

Consider the sandwich beam having width b shown in Fig. A.1(a). The beam is assumed to deform transversely under the external force per unit length $q(x,t)$. The free-body diagram of an element is shown in Fig. A.1(b) where M is the total bending moment and S is the total shear force. As the inertia loading is included, the total transverse loading is given by [53]

$$p_0(x,t) = -bm\frac{\partial^2 w}{\partial t^2} + q(x,t) \tag{A.1}$$

where m is

$$m = \rho_1 h_1 + \rho_2 h_2 + \rho_3 h_3. \tag{A.2}$$

The force equation of motion in the z direction is given by

$$-\left(S + \frac{\partial S}{\partial x}\mathrm{d}x\right) + S + p_0(x,t)\mathrm{d}x = 0 \tag{A.3}$$

which reduces to

$$\frac{\partial S}{\partial x} = p_0(x,t). \tag{A.4}$$

The total moment acting on element $\mathrm{d}x$ at its centre point is given by

$$-M + \left(M + \frac{\partial M}{\partial x}\mathrm{d}x\right) - S\frac{\mathrm{d}x}{2} - \left(S + \frac{\partial S}{\partial x}\mathrm{dx}\right)\frac{\mathrm{d}x}{2} = 0. \tag{A.5}$$

Neglecting the term involving $(\mathrm{d}x)^2$ gives

$$S = \frac{\partial M}{\partial x}. \tag{A.6}$$

The shear force S can be expressed by the shear forces S_1, S_2 and S_3 of each layers as [53]

$$S = S_1 + S_2 + S_3 \tag{A.7}$$

where S_1 and S_3 are given by

$$S_1 = \frac{E_1 b h_1^3}{12} \frac{\partial^3 w}{\partial x^3} \tag{A.8}$$

$$S_3 = \frac{E_3 b h_3^3}{12} \frac{\partial^3 w}{\partial x^3}. \tag{A.9}$$

The shear force S_2 is derived based on the assumption that the shear stress τ acts uniformly between the mid-planes of the outer layers. Hence, the shear force S_2 is related to the core shear stress by [53]

$$S_2 = -\tau b H \tag{A.10}$$

where the thickness H is given by

$$H = h_2 + \frac{1}{2}(h_1 + h_3). \tag{A.11}$$

The shear strain in the core is assumed to be [53]

$$\gamma_2 = \frac{H}{h_2} \frac{\partial w}{\partial x} + \frac{u_1 - u_3}{h_2}. \tag{A.12}$$

Hence, the shear stress τ can be expressed as

$$\tau = G\gamma_2 = G\left[\frac{H}{h_2} \frac{\partial w}{\partial x} + \frac{u_1 - u_3}{h_2}\right]. \tag{A.13}$$

Substituting Eqs. (A.7)-(A.13) into Eq. (A.4) gives

$$b\left\{ D_t \frac{\partial^4 w}{\partial x^4} - \frac{GH^2}{h_2} \frac{\partial^2 w}{\partial x^2} - \frac{GH}{h_2}\left(\frac{\partial u_1}{\partial x} - \frac{\partial u_3}{\partial x}\right)\right\} = p_0(x,t) \tag{A.14}$$

where D_t is given by

$$D_t = \frac{E_1 h_1^3}{12} + \frac{E_3 h_3^3}{12}. \tag{A.15}$$

The longitudinal force in the top layer P_1 and that in the bottom layer P_3 are given by [53]

$$P_1 = E_1 b h_1 \frac{\partial u_1}{\partial x} \tag{A.16}$$

$$P_3 = E_3 b h_3 \frac{\partial u_3}{\partial x}. \tag{A.17}$$

According to the equilibrium equation of motion in the x direction, i.e. $P_1 = -P_3$, the displacement u_1 is related to u_3 by [53]

$$u_1 = -\frac{E_3 h_3}{E_1 h_1} u_3. \tag{A.18}$$

By Eqs. (A.12) and (A.18), the shear strain in the core is given by

$$\gamma_2 = \frac{H}{h_2}\frac{\partial w}{\partial x} - \left(\frac{E_1 h_1 + E_3 h_3}{E_1 h_1 h_2}\right) u_3. \tag{A.19}$$

Substituting Eq. (A.18) into Eq. (A.14) gives

$$\frac{\partial^4 w}{\partial x^4} - gY\frac{\partial^2 w}{\partial x^2} + g\frac{E_3 h_3 H}{D_t}\frac{\partial u_3}{\partial x} = \frac{p_0(x,t)}{bD_t} \tag{A.20}$$

where the shear parameter g is given by

$$g = \frac{G}{h_2}\left(\frac{E_1 h_1 + E_3 h_3}{E_1 h_1 E_3 h_3}\right) \tag{A.21}$$

and the geometric parameter Y is

$$Y = \frac{H^2}{D_t}\left(\frac{E_1 h_1 E_3 h_3}{E_1 h_1 + E_3 h_3}\right). \tag{A.22}$$

The bending moment can be expressed by [53]

$$M = M_1 + M_2 + M_3 \tag{A.23}$$

where the bending moments of the outer layers M_1 and M_3 are

$$M_1 = \frac{E_1 b h_1^3}{12}\frac{\partial^2 w}{\partial x^2} \tag{A.24}$$

$$M_3 = \frac{E_3 b h_3^3}{12}\frac{\partial^2 w}{\partial x^2}. \tag{A.25}$$

The bending moment of the middle layer M_2 is related to the axial force by [53]

$$M_2 = HP_3 \tag{A.26}$$

where the longitudinal force P_3 can be derived by re-arranging Eq. (A.20) to give

$$\frac{\partial u_3}{\partial x} = \left(\frac{D_t}{gE_3h_3H}\right)\left[- \frac{\partial^4 w}{\partial x^4} + gY\frac{\partial^2 w}{\partial x^2} + \frac{p_0(x,t)}{bD_t}\right]. \tag{A.27}$$

Substituting Eq. (A.27) into Eq. (A.17) gives P_3 as

$$P_3 = \left(\frac{bD_t}{gH}\right)\left[- \frac{\partial^4 w}{\partial x^4} + gY\frac{\partial^2 w}{\partial x^2} + \frac{p_0(x,t)}{bD_t}\right]. \tag{A.28}$$

Hence, the total bending moment is given by

$$M = \frac{bD_t}{g}\left(- \frac{\partial^4 w}{\partial x^4} + g(1+Y)\frac{\partial^2 w}{\partial x^2} + \frac{p_0(x,t)}{bD_t}\right) \tag{A.29}$$

and the total shear force is

$$S = \frac{\partial M}{\partial x} = \frac{bD_t}{g}\left(- \frac{\partial^5 w}{\partial x^5} + g(1+Y)\frac{\partial^3 w}{\partial x^3} + \frac{1}{bD_t}\frac{\partial p_0(x,t)}{\partial x}\right). \tag{A.30}$$

The displacement u_3 in Eq. (A.20) can be derived by considering the longitudinal equilibrium of the bottom layer of element $\mathrm{d}x$, which is [53]

$$\frac{\partial P_3}{\partial x}\mathrm{d}x = -b\tau\mathrm{d}x. \tag{A.31}$$

Substituting τ from Eq. (A.13), P_3 from Eq. (A.17) and u_1 from Eq. (A.18) into Eq. (A.31) gives

$$\frac{\partial^2 u_3}{\partial x^2} = gu_3 - gY\frac{D_t}{E_3h_3H}\frac{\partial w}{\partial x}. \tag{A.32}$$

Differentiating Eq. (A.20) with respect to x and re-arranging it gives

$$\frac{\partial^2 u_3}{\partial x^2} = \left(\frac{D_t}{gE_3h_3H}\right)\left[- \frac{\partial^5 w}{\partial x^5} + gY\frac{\partial^3 w}{\partial x^3} + \frac{1}{bD_t}\frac{\partial p_0(x,t)}{\partial x}\right]. \tag{A.33}$$

Equating Eqs. (A.32) and (A.33) gives the displacement u_3 as

$$u_3 = \left(\frac{D_t}{g^2 E_3 h_3 H}\right)\left[- \frac{\partial^5 w}{\partial x^5} + gY\frac{\partial^3 w}{\partial x^3} + g^2 Y\frac{\partial w}{\partial x} + \frac{1}{bD_t}\frac{\partial p_0(x,t)}{\partial x}\right]. \tag{A.34}$$

Differentiating Eq. (A.34) with respect to x and substituting it into Eq. (A.20) gives the sixth-order equation of motion as [53]

$$\frac{\partial^6 w}{\partial x^6} - g(1+Y)\frac{\partial^4 w}{\partial x^4} = \frac{1}{bD_t}\left(\frac{\partial^2 p_0(x,t)}{\partial x^2} - gp(x,t)\right). \tag{A.35}$$

Using Eq. (A.1), the sixth-order equation of motion can be written as

$$\frac{\partial^6 w}{\partial x^6} - g(1+Y)\frac{\partial^4 w}{\partial x^4} + \frac{m}{D_t}\left(\frac{\partial^4 w}{\partial x^2 \partial t^2} - g\frac{\partial^2 w}{\partial t^2}\right) = \frac{1}{bD_t}\left(\frac{\partial^2 q}{\partial x^2} - gq\right). \tag{A.36}$$

A.3 Boundary Conditions for Three-Layer Beam

Two boundary conditions are considered in this thesis. The boundary conditions for the free-end are as follows [53]

1. The bending moment at an end is equal to zero.
2. The shear force at an end is equal to zero.
3. The axial forces of the outer layers are equal to zero, i.e. $P_1 = P_3 = 0$.

Considering free vibration and assuming harmonic motion, i.e. $w = We^{\mathrm{i}\omega t}$, the bending moment from Eq. (A.29), the shear force from Eq. (A.30) and the longitudinal force from Eq. (A.28) can be written respectively as

$$M = \frac{bD_t}{g}\left[- \frac{\mathrm{d}^4 W}{\mathrm{d}x^4} + g(1+Y)\frac{\mathrm{d}^2 W}{\mathrm{d}x^2}\right]e^{\mathrm{i}\omega t} \tag{A.37}$$

$$S = \frac{bD_t}{g}\left[- \frac{\mathrm{d}^5 W}{\mathrm{d}x^5} + g(1+Y)\frac{\mathrm{d}^3 W}{\mathrm{d}x^3}\right]e^{\mathrm{i}\omega t} \tag{A.38}$$

$$P_3 = \frac{bD_t}{gH}\left[- \frac{\mathrm{d}^4 W}{\mathrm{d}x^4} + gY\frac{\mathrm{d}^2 W}{\mathrm{d}x^2}\right]e^{\mathrm{i}\omega t}. \tag{A.39}$$

Hence, the above boundary conditions become

$$\frac{\mathrm{d}^4 W}{\mathrm{d}x^4} - g(1+Y)\frac{\mathrm{d}^2 W}{\mathrm{d}x^2} = 0. \tag{A.40}$$

$$\frac{\mathrm{d}^5 W}{\mathrm{d}x^5} - g(1+Y)\frac{\mathrm{d}^3 W}{\mathrm{d}x^3} = 0. \tag{A.41}$$

$$\frac{\mathrm{d}^4 W}{\mathrm{d}x^4} - gY\frac{\mathrm{d}^2 W}{\mathrm{d}x^2} = 0. \tag{A.42}$$

The boundary conditions for the fixed-end are given by [53]

1. The transverse displacement is equal to zero.

2. The rotation is equal to zero.

3. The outer layer displacements u_1 and u_3 are equal to zero. This leads to zero shear strain in the core, and hence $S_2 = 0$.

By Eqs. (A.10, A.13, A.18, A.34), the shear force in the core can be written as

$$S_2 = \frac{bD_t}{g}\left[-\frac{\partial^5 w}{\partial x^5} + gY\frac{\partial^3 w}{\partial x^3} + \frac{1}{bD_t}\frac{\partial p_0(x,t)}{\partial x}\right]. \tag{A.43}$$

Considering free vibration and assuming harmonic motion, Eq. (A.43) becomes

$$S_2 = \frac{bD_t}{g}\left[-\frac{d^5 W}{dx^5} + gY\frac{d^3 W}{dx^3}\right] e^{\mathrm{i}\omega t}. \tag{A.44}$$

Hence three boundary conditions for the fixed end are

$$W = 0 \tag{A.45}$$

$$\frac{dW}{dx} = 0 \tag{A.46}$$

$$\frac{d^5 W}{dx^5} - gY\frac{d^3 W}{dx^3} = 0. \tag{A.47}$$

A.4 Solutions for Free-Free Three-Layer Beam

Consider the free vibration of the free-free sandwich beam, the equation of motion of Eq. (A.36) is replaced by

$$\frac{\partial^6 w}{\partial x^6} - g(1+Y)\frac{\partial^4 w}{\partial x^4} + \frac{m}{D_t}\left(\frac{\partial^4 w}{\partial x^2 \partial t^2} - g\frac{\partial^2 w}{\partial t^2}\right) = 0. \tag{A.48}$$

Assuming a harmonic solution, $w = We^{\mathrm{i}\omega t}$, gives

$$\frac{\mathrm{d}^6 W}{\mathrm{d}x^6} - g(1+Y)\frac{\mathrm{d}^4 W}{\mathrm{d}x^4} + \frac{m}{D_t}\left(-\omega^2 \frac{\mathrm{d}^2 W}{\mathrm{d}x^2} + g\omega^2 W \right) = 0. \tag{A.49}$$

The solution of Eq.(A.49) can be written in the form of

$$W = A^* e^{kx} \tag{A.50}$$

where A^* is constant and k is the wavenumber. Substituting Eq. (A.50) into Eq. (A.49) gives the dispersion equation

$$k^6 - g(1+Y)k^4 - \Omega^2 k^2 + \Omega^2 g = 0 \tag{A.51}$$

where $\Omega^2 = \frac{m}{D_t}\omega^2$. The roots of Eq. (A.51) can be calculated by solving the dispersion equation, which is a cubic in k^2. The solutions of the cubic equation are given by

$$k_1^2 = \frac{1}{3}g(1+Y) + (O+V) \tag{A.52}$$

$$k_2^2 = \frac{1}{3}g(1+Y) - \frac{1}{2}(O+V) + \mathrm{i}\frac{\sqrt{3}}{2}(O-V) \tag{A.53}$$

$$k_3^2 = \frac{1}{3}g(1+Y) - \frac{1}{2}(O+V) - \mathrm{i}\frac{\sqrt{3}}{2}(O-V) \tag{A.54}$$

where

$$O = \sqrt[3]{R + \sqrt{D}} \tag{A.55}$$

$$V = \sqrt[3]{R - \sqrt{D}} \tag{A.56}$$

and

$$D = Q^3 + R^2 \tag{A.57}$$

$$R = \frac{1}{54}\left(9\Omega^2 g(1+Y) - 27g\Omega^2 + 2g^3(1+Y)^3 \right) \tag{A.58}$$

$$Q = -\frac{1}{9}\left(3\Omega^2 + g^2(1+Y)^2 \right). \tag{A.59}$$

The general solution of Eq.(A.49) is assumed to be

$$W = A_1 e^{-k_1(L-x)} + A_2 e^{-k_1 x} + A_3 e^{-k_2(L-x)} + A_4 e^{-k_2 x} + A_5 e^{-k_3(L-x)} + A_6 e^{-k_3 x} \quad \text{(A.60)}$$

where $\pm k_1, \pm k_2$, and $\pm k_3$ are the six roots of Eq. (A.51) and $A_1 - A_6$ are constants which can be found from the boundary conditions. Applying the boundary conditions from Eqs. (A.40-A.42) at both ends produces six equations with six unknowns, $A_1 - A_6$, which can be written as

$$\begin{bmatrix} b_{11} & b_{12} & b_{13} & b_{14} & b_{15} & b_{16} \\ b_{21} & b_{22} & b_{23} & b_{24} & b_{25} & b_{26} \\ b_{31} & b_{32} & b_{33} & b_{34} & b_{35} & b_{36} \\ b_{41} & b_{42} & b_{43} & b_{44} & b_{45} & b_{46} \\ b_{51} & b_{52} & b_{53} & b_{54} & b_{55} & b_{56} \\ b_{61} & b_{62} & b_{63} & b_{64} & b_{65} & b_{66} \end{bmatrix} \begin{bmatrix} A_1 \\ A_2 \\ A_3 \\ A_4 \\ A_5 \\ A_6 \end{bmatrix} = \begin{bmatrix} 0 \\ 0 \\ 0 \\ 0 \\ 0 \\ 0 \end{bmatrix} \quad \text{(A.61)}$$

where

$$b_{11} = b_{42} = \left(k_1^4 - g(1+Y)k_1^2\right)e^{-k_1 L} \quad \text{(A.62)}$$

$$b_{12} = b_{41} = \left(k_1^4 - g(1+Y)k_1^2\right) \quad \text{(A.63)}$$

$$b_{13} = b_{44} = \left(k_2^4 - g(1+Y)k_2^2\right)e^{-k_2 L} \quad \text{(A.64)}$$

$$b_{14} = b_{43} = \left(k_2^4 - g(1+Y)k_2^2\right) \quad \text{(A.65)}$$

$$b_{15} = b_{46} = \left(k_3^4 - g(1+Y)k_3^2\right)e^{-k_3 L} \quad \text{(A.66)}$$

$$b_{16} = b_{45} = \left(k_3^4 - g(1+Y)k_3^2\right) \quad \text{(A.67)}$$

$$b_{21} = -b_{52} = \left(k_1^5 - g(1+Y)k_1^3\right)e^{-k_1 L} \quad \text{(A.68)}$$

$$b_{22} = -b_{51} = -\left(k_1^5 - g(1+Y)k_1^3\right) \quad \text{(A.69)}$$

$$b_{23} = -b_{54} = \left(k_2^5 - g(1+Y)k_2^3\right)e^{-k_2 L} \quad \text{(A.70)}$$

$$b_{24} = -b_{53} = -\left(k_2^5 - g(1+Y)k_2^3\right) \quad \text{(A.71)}$$

$$b_{25} = -b_{56} = \left(k_3^5 - g(1+Y)k_3^3\right)e^{-k_3 L} \quad \text{(A.72)}$$

$$b_{26} = -b_{55} = -\left(k_3^5 - g(1+Y)k_3^3\right) \tag{A.73}$$

$$b_{31} = b_{62} = \left(k_1^4 - gYk_1^2\right)e^{-k_1 L} \tag{A.74}$$

$$b_{32} = b_{61} = \left(k_1^4 - gYk_1^2\right) \tag{A.75}$$

$$b_{33} = b_{64} = \left(k_2^4 - gYk_2^2\right)e^{-k_2 L} \tag{A.76}$$

$$b_{34} = b_{63} = \left(k_2^4 - gYk_2^2\right) \tag{A.77}$$

$$b_{35} = b_{66} = \left(k_3^4 - gYk_3^2\right)e^{-k_3 L} \tag{A.78}$$

$$b_{36} = b_{65} = \left(k_3^4 - gYk_3^2\right). \tag{A.79}$$

Eq. (A.61) can be expressed in matrix notation as

$$\mathbf{BA_1} = \mathbf{0}. \tag{A.80}$$

It can be seen from equation (A.80) that non-trivial solutions can be obtained if the determinant of the matrix $\mathbf{B} = 0$. Matrix $\mathbf{B}$ is a function of the six wavenumbers which are frequency dependent. Hence, the natural frequencies are the frequencies that cause the determinant of matrix $\mathbf{B}$ to be zero.

Figures

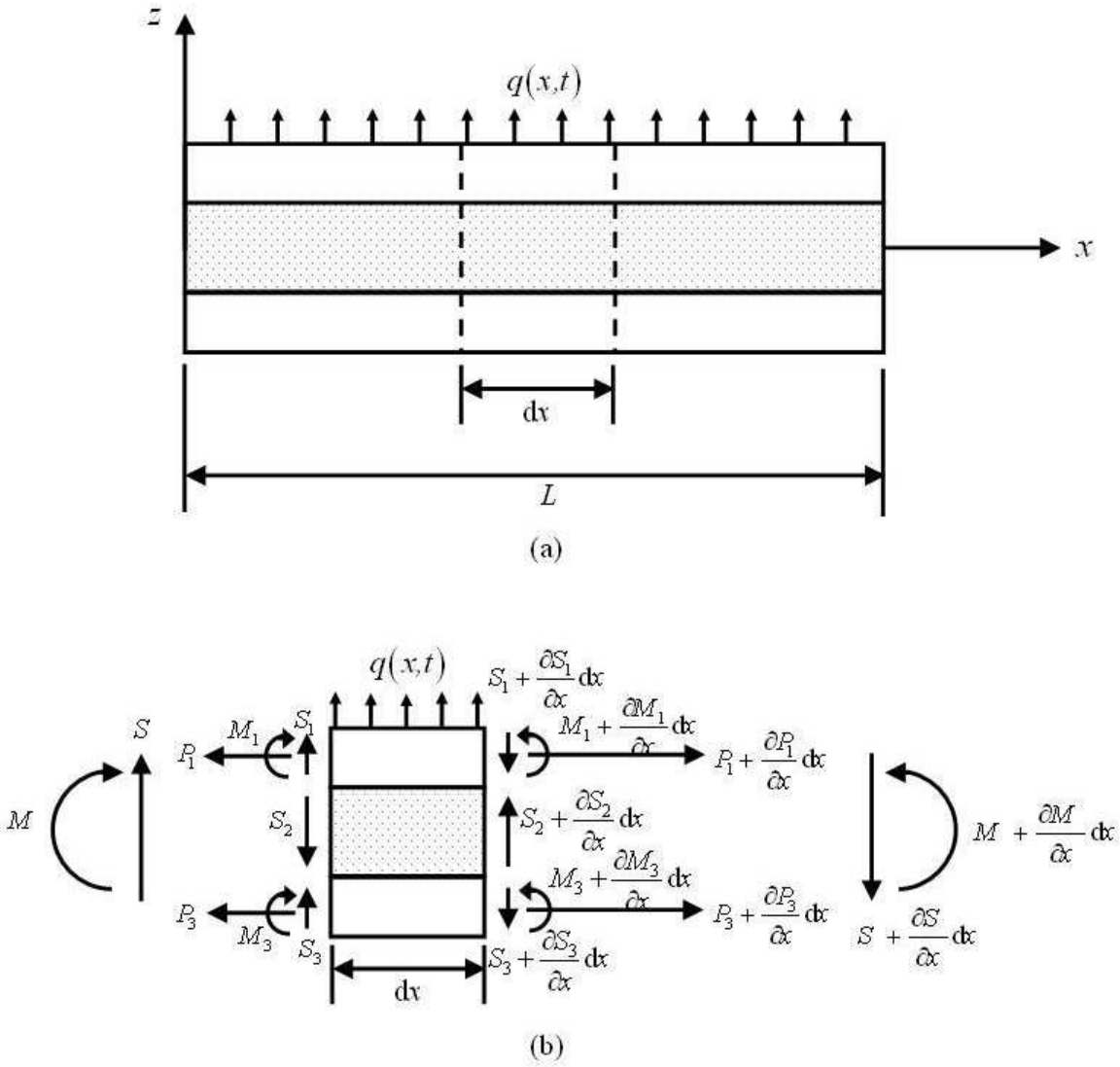

Fig. A.1: A three-layer beam. (a) A beam with length L is subjected to an external force $q(x,t)$. (b) Free-body diagram of an element dx.

Appendix B

Mass and Stiffness Matrices of three-layer elements

B.1 Introduction

In chapter 4, the finite element (FE) method was described. The FE method utilises mass and stiffness matrices to approximate the solutions for the continuous system. Matrix algebra is employed to simplify the derivations of these matrices. In this appendix the displacement functions and the element energy functions are written in matrix forms so that the element mass and stiffness matrices can be obtained. This appendix also introduces some notation used in Chapter 4.

B.2 Displacement Function Matrix

The FE model developed in Chapter 4 employed three displacement functions, which are

$$u_{10} = a_0 + xa_1 \tag{B.1}$$

$$w = b_0 + xb_1 + x^2b_2 + x^3b_3 \tag{B.2}$$

$$w' = \frac{\partial w}{\partial x} = b_1 + 2xb_2 + 3x^2b_3. \tag{B.3}$$

The expressions (B.1)-(B.3) can be written in the alternative form

$$\begin{Bmatrix} u_{10} \\ w \\ w' \end{Bmatrix} = \begin{bmatrix} 1 & x & 0 & 0 & 0 & 0 \\ 0 & 0 & 1 & x & x^2 & x^3 \\ 0 & 0 & 0 & 1 & 2x & 3x^2 \end{bmatrix} \begin{Bmatrix} a_0 \\ a_1 \\ b_0 \\ b_1 \\ b_2 \\ b_3 \end{Bmatrix} = \mathbf{Xa}. \tag{B.4}$$

As described in Chapter 4, a three-layer element consists of two nodes and three degrees-of-freedom (DOFs) are considered at each node. The nodal displacement vector for one element is

$$\mathbf{q_i} = \begin{Bmatrix} u_{10}^{(1)} & w^{(1)} & w'^{(1)} & u_{10}^{(2)} & w^{(2)} & w'^{(2)} \end{Bmatrix}^{\mathrm{T}} \tag{B.5}$$

where $^{(1)}$ and $^{(2)}$ denotes node 1 and node 2 respectively. At node 1 it is defined that $x = 0$ and at node 2 $x = l$, where l is the length of element. Using these definitions, Eqs. (B.1)-(B.3) gives the nodal displacements $\mathbf{q_i}$ as

$$\begin{Bmatrix} u_{10}^{(1)} \\ w^{(1)} \\ w'^{(1)} \\ u_{10}^{(2)} \\ w^{(2)} \\ w'^{(2)} \end{Bmatrix} = \begin{bmatrix} 1 & 0 & 0 & 0 & 0 & 0 \\ 0 & 0 & 1 & 0 & 0 & 0 \\ 0 & 0 & 0 & 1 & 0 & 0 \\ 1 & l & 0 & 0 & 0 & 0 \\ 0 & 0 & 1 & l & l^2 & l^3 \\ 0 & 0 & 0 & 1 & 2l & 3l^2 \end{bmatrix} \begin{Bmatrix} a_0 \\ a_1 \\ b_0 \\ b_1 \\ b_2 \\ b_3 \end{Bmatrix} = \mathbf{Ca}. \tag{B.6}$$

Solving for the vector $\mathbf{a}$ gives

$$\mathbf{a} = \mathbf{C}^{-1}\mathbf{q_i}. \tag{B.7}$$

By Eq. (B.4), the DOF vector $\mathbf{q}$ is

$$\mathbf{q} = \begin{Bmatrix} u_{10} \\ w \\ w' \end{Bmatrix} = \mathbf{Xa}. \tag{B.8}$$

The nodal DOFs $\mathbf{q_i}$ and the DOF vector $\mathbf{q}$ are related by a matrix $\mathbf{N}$, such that

$$\mathbf{q} = \mathbf{X}\mathbf{C}^{-1}\mathbf{q_i} = \mathbf{N}\mathbf{q_i} \tag{B.9}$$

where the matrix $\mathbf{N}$ is

$$\mathbf{N} = \begin{bmatrix} 1-\frac{x}{l} & 0 & 0 & \frac{x}{l} & 0 & 0 \\ 0 & 1-3\frac{x^2}{l^2}+2\frac{x^3}{l^3} & x-2\frac{x^2}{l}+\frac{x^3}{l^2} & 0 & 3\frac{x^2}{l^2}-2\frac{x^3}{l^3} & -\frac{x^2}{l}+\frac{x^3}{l^2} \\ 0 & -6\frac{x}{l^2}+6\frac{x^2}{l^3} & 1-4\frac{x}{l}+3\frac{x^2}{l^2} & 0 & 6\frac{x}{l^2}-6\frac{x^2}{l^3} & -2\frac{x}{l}+3\frac{x^2}{l^2} \end{bmatrix}. \tag{B.10}$$

B.3 Element Strain Energy

The total element strain energy consists of energies of layers 1, 2 and 3, and is given by

$$U_e = U_1 + U_2 + U_3 \tag{B.11}$$

where U_1, U_2 and U_3 are given by

$$U_1 = \frac{1}{2}E\int_v \left(\frac{\partial u_{10}}{\partial x} - z_1\frac{\partial^2 w}{\partial x^2}\right)^2 \mathrm{d}v \tag{B.12}$$

$$U_2 = \frac{1}{2}GbH\int_x \left(\frac{2u_{10}}{h_2} + \frac{H}{h_2}\frac{\partial w}{\partial x}\right)^2 \mathrm{d}x \tag{B.13}$$

$$U_3 = \frac{1}{2}E\int_v \left(-\frac{\partial u_{10}}{\partial x} - z_3\frac{\partial^2 w}{\partial x^2}\right)^2 \mathrm{d}v. \tag{B.14}$$

These are derived based on the assumptions that the outer layers have the same dimensions and $u_{30} = -u_{10}$. The strain energy for each layer in Eqs. (B.12-B.14) can be written in the alterative forms

$$U_1 = \frac{1}{2}E\int_v \left(\mathbf{C_1}\mathbf{q}'\right)^2 \mathrm{d}v; \qquad \mathbf{C_1} = \begin{bmatrix} 1 & 0 & -z_1 \end{bmatrix} \tag{B.15}$$

$$U_2 = \frac{1}{2}GbH\int_x \left(\mathbf{C_2}\mathbf{q}\right)^2 \mathrm{d}x; \qquad \mathbf{C_2} = \begin{bmatrix} \frac{2}{h_2} & 0 & \frac{H}{h_2} \end{bmatrix} \tag{B.16}$$

$$U_3 = \frac{1}{2}E\int_v \left(\mathbf{C_3 q'}\right)^2 \mathrm{d}v; \qquad \mathbf{C_3} = \begin{bmatrix} -1 & 0 & -z_3 \end{bmatrix} \tag{B.17}$$

where $\mathbf{q'}$ is $\frac{\partial \mathbf{q}}{\partial x}$. Hence, the strain energy functions in terms of the nodal displacements can be obtained by substituting $\mathbf{q} = \mathbf{N q_i}$ from Eq. (B.9) into Eqs. (B.15-B.17) to give

$$U_1 = \frac{1}{2}E\int_v \left(\mathbf{C_1 N' q_i}\right)^2 \mathrm{d}v = \frac{1}{2}E\mathbf{q_i}^{\mathrm{T}}\int_v \left(\mathbf{N'}^{\mathrm{T}}\mathbf{C_1}^{\mathrm{T}}\mathbf{C_1 N'}\right)\mathrm{d}v\ \mathbf{q_i} \tag{B.18}$$

$$U_2 = \frac{1}{2}GbH\int_x \left(\mathbf{C_2 N q_i}\right)^2 \mathrm{d}x = \frac{1}{2}GbH\mathbf{q_i}^{\mathrm{T}}\int_x \left(\mathbf{N}^{\mathrm{T}}\mathbf{C_2}^{\mathrm{T}}\mathbf{C_2 N}\right)\mathrm{d}x\ \mathbf{q_i} \tag{B.19}$$

$$U_3 = \frac{1}{2}E\int_v \left(\mathbf{C_3 N' q_i}\right)^2 \mathrm{d}v = \frac{1}{2}E\mathbf{q_i}^{\mathrm{T}}\int_v \left(\mathbf{N'}^{\mathrm{T}}\mathbf{C_3}^{\mathrm{T}}\mathbf{C_3 N'}\right)\mathrm{d}v\ \mathbf{q_i} \tag{B.20}$$

where $\mathbf{N'}$ denotes $\frac{\partial \mathbf{N}}{\partial x}$.

B.4 Element Kinetic Energy

The element kinetic energy is also a sum of the energies of layers 1, 2 and 3

$$T_e = T_1 + T_2 + T_3 \tag{B.21}$$

where the kinetic energy functions for each layer derived in Chapter 4 are expressed as

$$T_1 = \frac{1}{2}\rho_p \int_v \left[\left(\frac{\partial u_{10}}{\partial t}\right)^2 + \left(\frac{\partial w}{\partial t}\right)^2\right]\mathrm{d}v \tag{B.22}$$

$$T_2 = \frac{1}{2}\rho_m \int_v \left[\left(\frac{2z_2}{h_2}\frac{\partial u_{10}}{\partial t} + \frac{z_2 h_1}{h_2}\frac{\partial^2 w}{\partial x \partial t}\right)^2 + \left(\frac{\partial w}{\partial t}\right)^2\right]\mathrm{d}v \tag{B.23}$$

$$T_3 = \frac{1}{2}\rho_p \int_v \left[\left(-\frac{\partial u_{10}}{\partial t}\right)^2 + \left(\frac{\partial w}{\partial t}\right)^2\right]\mathrm{d}v. \tag{B.24}$$

Eqs. (B.22-B.24) can be written in alternative forms

$$T_1 = \frac{1}{2}\rho_p \int_v \left[\left(\mathbf{D_1}\dot{\mathbf{q}}\right)^2 + \left(\mathbf{D_0}\dot{\mathbf{q}}\right)^2\right]\mathrm{d}v; \quad \mathbf{D_1} = \begin{bmatrix} 1 & 0 & 0 \end{bmatrix}; \quad \mathbf{D_0} = \begin{bmatrix} 0 & 1 & 0 \end{bmatrix} \tag{B.25}$$

$$T_2 = \frac{1}{2}\rho_m \int_v \left[\left(\mathbf{D_2}\dot{\mathbf{q}}\right)^2 + \left(\mathbf{D_0}\dot{\mathbf{q}}\right)^2 \right] \mathrm{d}v; \qquad \mathbf{D_2} = \begin{bmatrix} \frac{2z_2}{h_2} & 0 & \frac{z_2 h_1}{h_2} \end{bmatrix} \tag{B.26}$$

$$T_3 = \frac{1}{2}\rho_p \int_v \left[\left(\mathbf{D_3}\dot{\mathbf{q}}\right)^2 + \left(\mathbf{D_0}\dot{\mathbf{q}}\right)^2 \right] \mathrm{d}v; \qquad \mathbf{D_3} = \begin{bmatrix} -1 & 0 & 0 \end{bmatrix}. \tag{B.27}$$

Substituting $\mathbf{q} = \mathbf{N}\mathbf{q_i}$ from (B.9) into (B.25-B.27) gives the kinetic energies in terms of the nodal DOFs vector $\mathbf{q_i}$ as

$$T_1 = \frac{1}{2}\rho_p \dot{\mathbf{q}_\mathbf{i}}^{\mathrm{T}} \int_v \left[\left(\mathbf{N}^{\mathrm{T}} \mathbf{D_1}^{\mathrm{T}} \mathbf{D_1} \mathbf{N}\right) + \left(\mathbf{N}^{\mathrm{T}} \mathbf{D_0}^{\mathrm{T}} \mathbf{D_0} \mathbf{N}\right) \right] \mathrm{d}v \dot{\mathbf{q}_\mathbf{i}} \tag{B.28}$$

$$T_2 = \frac{1}{2}\rho_m \dot{\mathbf{q}_\mathbf{i}}^{\mathrm{T}} \int_v \left[\left(\mathbf{N}^{\mathrm{T}} \mathbf{D_2}^{\mathrm{T}} \mathbf{D_2} \mathbf{N}\right) + \left(\mathbf{N}^{\mathrm{T}} \mathbf{D_0}^{\mathrm{T}} \mathbf{D_0} \mathbf{N}\right) \right] \mathrm{d}v \dot{\mathbf{q}_\mathbf{i}} \tag{B.29}$$

$$T_3 = \frac{1}{2}\rho_p \dot{\mathbf{q}_\mathbf{i}}^{\mathrm{T}} \int_v \left[\left(\mathbf{N}^{\mathrm{T}} \mathbf{D_3}^{\mathrm{T}} \mathbf{D_3} \mathbf{N}\right) + \left(\mathbf{N}^{\mathrm{T}} \mathbf{D_0}^{\mathrm{T}} \mathbf{D_0} \mathbf{N}\right) \right] \mathrm{d}v \dot{\mathbf{q}_\mathbf{i}}. \tag{B.30}$$

B.5 Element Stiffness Matrix

The element stiffness matrix $\mathbf{K_e}$ consists of the stiffness due to the outer layers $\mathbf{K_f}$ and that of the centre layer $\mathbf{K_c}$, i.e.

$$\mathbf{K_e} = \mathbf{K_f} + \mathbf{K_c}. \tag{B.31}$$

The element stiffness matrix can be derived from strain energy, which is given by

$$U = \frac{1}{2}\mathbf{q_i}^{\mathrm{T}} \mathbf{K} \mathbf{q_i}. \tag{B.32}$$

By Eqs. (B.19) and (B.32), the element stiffness matrix for the middle layer is due to the shear deformation, and is expressed as

$$\mathbf{K_c} = GbH \int_{x=0}^{l} \left(\mathbf{N}^{\mathrm{T}} \mathbf{C_2}^{\mathrm{T}} \mathbf{C_2} \mathbf{N}\right) \mathrm{d}x. \tag{B.33}$$

Integrating Eq. (B.33) gives

$$\mathbf{K_c} = \frac{GbH}{h_2^2}\begin{bmatrix} \frac{4}{3}l & & & & & \\ -H & \frac{6}{5}\frac{H^2}{l} & & & sym. & \\ \frac{1}{6}Hl & \frac{1}{10}H^2 & \frac{2}{15}H^2l & & & \\ \frac{2}{3}l & -H & -\frac{1}{12}h_2^2Hl & \frac{4}{3}l & & \\ H & -\frac{6}{5}\frac{H^2}{l} & -\frac{1}{10}H^2 & H & \frac{6}{5}\frac{H^2}{l} & \\ -\frac{1}{12}h_2^2Hl & \frac{1}{10}H^2 & -\frac{1}{30}H^2l & \frac{1}{6}Hl & -\frac{1}{10}H^2 & \frac{2}{15}H^2l \end{bmatrix}. \tag{B.34}$$

The element stiffness matrix for the outer layers concerns stretching and bending of layers 1 and 3 so that

$$\mathbf{K_f} = \mathbf{K_1} + \mathbf{K_3}. \tag{B.35}$$

The element stiffness matrix of layer 1 is obtained from Eqs (B.18) and (B.32) as

$$\mathbf{K_1} = E\int_{z=-\frac{h_1}{2}}^{\frac{h_1}{2}}\int_{y=0}^{b}\int_{x=0}^{l}\left(\mathbf{N'}^{\mathrm{T}}\mathbf{C_1}^{\mathrm{T}}\mathbf{C_1}\mathbf{N'}\right)\mathrm{d}x\mathrm{d}y\mathrm{d}z \tag{B.36}$$

and the element stiffness matrix of layer 3 is from Eqs (B.20) and (B.32)

$$\mathbf{K_3} = E\int_{z=-\frac{h_3}{2}}^{\frac{h_3}{2}}\int_{y=0}^{b}\int_{x=0}^{l}\left(\mathbf{N'}^{\mathrm{T}}\mathbf{C_3}^{\mathrm{T}}\mathbf{C_3}\mathbf{N'}\right)\mathrm{d}x\mathrm{d}y\mathrm{d}z. \tag{B.37}$$

Hence, the resulting element stiffness matrix of the outer layers is

$$\mathbf{K_f} = \begin{bmatrix} 2\frac{EA_p}{l} & & & & & \\ 0 & 24\frac{EI_p}{l^3} & & & Sym. & \\ 0 & 12\frac{EI_p}{l^2} & 8\frac{EI_p}{l} & & & \\ -2\frac{EA_p}{l} & 0 & 0 & 2\frac{EA_p}{l} & & \\ 0 & -24\frac{EI_p}{l^3} & -12\frac{EI_p}{l^2} & 0 & 24\frac{EI_p}{l^3} & \\ 0 & 12\frac{EI_p}{l^2} & 4\frac{EI_p}{l} & 0 & -12\frac{EI_p}{l^2} & 8\frac{EI_p}{l} \end{bmatrix} \tag{B.38}$$

where A_p and I_p are the cross-sectional area and the area moment of inertia of the outer layers respectively. Hence, the total element stiffness matrix $\mathbf{K_e}$ is obtained by summing Eqs. (B.34) and (B.38).

B.6 Element Mass Matrix

By following the same procedure as for the element stiffness matrix, the element mass matrix $\mathbf{M_e}$ is given in terms of the kinetic energy by

$$T = \frac{1}{2}\dot{\mathbf{q}}_\mathbf{i}^{\mathrm{T}}\mathbf{M}\dot{\mathbf{q}}_\mathbf{i}. \tag{B.39}$$

The element mass matrix $\mathbf{M_e}$ is expressed in terms of mass matrix of the outer layers $\mathbf{M_f}$ and that of the core $\mathbf{M_c}$ by

$$\mathbf{M_e} = \mathbf{M_f} + \mathbf{M_c}. \tag{B.40}$$

The mass matrix $\mathbf{M_f}$ is a combination of the mass matrix of layer 1, $\mathbf{M_1}$, and that of layer 3 , $\mathbf{M_3}$, i.e.

$$\mathbf{M_f} = \mathbf{M_1} + \mathbf{M_3}. \tag{B.41}$$

$\mathbf{M_1}$ and $\mathbf{M_3}$ can be obtained using T_1 from Eq. (B.28), T_3 from Eq. (B.30) and T from Eq. (B.39), i.e.

$$\mathbf{M_1} = \rho_p \int_{z=-\frac{h_1}{2}}^{\frac{h_1}{2}} \int_{y=0}^{b} \int_{x=0}^{l} \left[\left(\mathbf{N}^{\mathrm{T}}\mathbf{D_1}^{\mathrm{T}}\mathbf{D_1}\mathbf{N} \right) + \left(\mathbf{N}^{\mathrm{T}}\mathbf{D_0}^{\mathrm{T}}\mathbf{D_0}\mathbf{N} \right) \right] \mathrm{d}x\mathrm{d}y\mathrm{d}z \tag{B.42}$$

$$\mathbf{M_3} = \rho_p \int_{z=-\frac{h_3}{2}}^{\frac{h_3}{2}} \int_{y=0}^{b} \int_{x=0}^{l} \left[\left(\mathbf{N}^{\mathrm{T}}\mathbf{D_3}^{\mathrm{T}}\mathbf{D_3}\mathbf{N} \right) + \left(\mathbf{N}^{\mathrm{T}}\mathbf{D_0}^{\mathrm{T}}\mathbf{D_0}\mathbf{N} \right) \right] \mathrm{d}x\mathrm{d}y\mathrm{d}z. \tag{B.43}$$

Integrating Eqs. (B.42) and (B.43) gives

$$\mathbf{M_f} = \frac{\rho_p A_p l}{210} \begin{bmatrix} 140 & & & & & \\ 0 & 156 & & & Sym. & \\ 0 & 22l & 4l^2 & & & \\ 70 & 0 & 0 & 140 & & \\ 0 & 54 & 13l & 0 & 156 & \\ 0 & -13l & -3l^2 & 0 & -22l & 4l^2 \end{bmatrix}. \tag{B.44}$$

By Eqs. (B.29) and (B.39), the mass matrix of the core is

$$\mathbf{M_c} = \mathbf{M_{c1}} + \mathbf{M_{c2}} = \rho_m \int_{z=0}^{H}\int_{y=0}^{b}\int_{x=0}^{l}\left[\left(\mathbf{N}^{\mathrm{T}}\mathbf{D_2}^{\mathrm{T}}\mathbf{D_2}\mathbf{N}\right) + \left(\mathbf{N}^{\mathrm{T}}\mathbf{D_0}^{\mathrm{T}}\mathbf{D_0}\mathbf{N}\right)\right]\mathrm{d}x\mathrm{d}y\mathrm{d}z \tag{B.45}$$

where the resulting matrices $\mathbf{M_{c1}}$ and $\mathbf{M_{c2}}$ are

$$\mathbf{M_{c2}} = \frac{\rho_m A_m l}{420}\begin{bmatrix} 140 & & & & & \\ 0 & 156 & & & Sym. & \\ 0 & 22l & 4l^2 & & & \\ 70 & 0 & 0 & 140 & & \\ 0 & 54 & 13l & 0 & 156 & \\ 0 & -13l & -3l^2 & 0 & -22l & 4l^2 \end{bmatrix} \tag{B.46}$$

$$\mathbf{M_{c1}} = \frac{\rho_m A_m}{360l}\begin{bmatrix} -80l^2 & & & & & \\ -30h_1 l & 36h_1^2 & & & Sym. & \\ 5h_1 l^2 & 3h_1^2 l & 4h_1^2 l^2 & & & \\ -40l^2 & 30h_1 l & -5h_1 l^2 & -80l^2 & & \\ 30h_1 l & -36h_1^2 & -3h_1^2 l & 30h_1 l & 36h_1^2 & \\ -5h_1 l^2 & 3h_1^2 l & -h_1^2 l^2 & 5h_1 l^2 & -3h_1^2 l & 4h_1^2 l^2 \end{bmatrix}. \tag{B.47}$$

Here A_m is the cross-sectional area of the middle layer. Summing Eqs. (B.44), (B.46), and (B.47) gives the element mass matrix $\mathbf{M_e}$.

Appendix C

Manufacture, Relative Calibration and Experimental Results of the MR Fluid-Filled ATVA

C.1 Introduction

Chapter 6 provides the experimental set-up and measurements of the MR adaptive tuned vibration absorber (ATVA), however, more details are given in this appendix. In this appendix the manufacture of the MR fluid-filled ATVA is described and the calibration of an impedance head used to measure the point accelerance of the test beam is presented. Finally, the experimental results of MR ATVA for various currents are reported.

C.2 Manufacture the MR Fluid-Filled ATVA

The MR ATVA is a three-layer beam consisting of two outer layers and a square piece of perspex and MR fluid in the middle layer. It was manufactured from the drawings shown in Figs. C.1-C.3. The top and bottom layers were the thin outer layer beams, which were made of perspex as shown in Figs. C.1 and C.2 respectively. There were eight holes for electromagnets towards the ends of these layers. Two

holes across the width of the beam were used for one electromagnet, and hence four electromagnets could be attached to each layer using a glue. The square piece of perspex has dimensions shown in Fig C.3. Its centre had a small threaded hole for a 10-32-UNF-2B stud that was used to fasten the beam to the host structure. Another hole was made at the middle of the bottom layer shown in Fig. C.2 for the same purpose. Each layer was separately manufactured and then the top and bottom layers and the square piece of perspex between them were glued.

The procedure by which the core was filled by MR fluid was as follows. Some parts of the sides of the beam were covered by a tape and were sealed by a thin layer of adhesive as shown in Fig. 6.2. Two parts of the tape covered the front sides of the beam, one of which was on the left side and the other on the right side, were opened to be ports for filling the MR fluid. The MR fluid was poured in through the open port. The port was sealed by tape and adhesive. The process was repeated for the other side of the beam.

C.3 Calibration of Impedance Head

The calibration of impedance head was made before the measurements of the test beam were conducted. The impedance head alone was excited by the shaker, and then its response was measured using the equipment and method described in section 6.2. The measured point FRF is shown in Fig. C.4. It can be seen that the magnitude of the measured point accelerance is not zero but more or less constant over the frequency range, though the test beam was not attached to the impedance head. The impedance head on the shaker is assumed to be a mass-like structure, whose mass, m_1, is one over the measured constant value, i.e. $m_1 = \frac{1}{158} = 6.3$ g. As the mass of the mass-like structure has the contribution to the measured response of the test beam, mass m_1 needs to be considered in the FE model for the test beam.

C.4 Experimental Results of the MR ATVA for various supply current

A number of the measurements of the point accelerance of the MR ATVA were conducted. The experimental set-up and method were described in section 6.2. However, the parameter settings of the HP analyser are shown in Tab. C.1 and the sensitivity of the impedance head is shown in Tab. C.2. A photograph of the experimental set-up is shown in Fig. C.5. The measured accelerance of the MR ATVA for various currents were compared to the predictions in Figs. C.6-C.12. However, two measurements, i.e. $I = 0$ A and $I = 646$ mA were reported in Chapter 6. The measured and predicted natural frequencies and total loss factors for various currents are shown in Tab. C.3. The measured stiffness and viscous damping are shown in Tab. C.4.

Tables

Hardware setup	Global	Active channels:	2
		Trigger mode:	Free run
		Trigger source:	Input
	Source	Sine Freq:	1 kHz
		DC offset:	0
		Output level:	10 V
		Output type:	Continuous random
	Front end	Channel 1 Force transducer:	-24 dB V_p
		Channel 2 Accelerometer:	6 dB V_p
Measurement parameter	Frequency response	Start frequency:	0 Hz
		Span frequency:	400 kHz
		Frequency lines:	800
		Averages type:	Stable
		Number of averages:	30
		Exponential time constant:	1000 sec
		Force width:	1000 sec
		Reference mode:	Single channel
		Ref. channel:	1
		Overload reject:	■
		Manual preview:	□
		Manual arm:	□
		Overlap:	0%

Tab. C.1: Parameter settings of HP analyser.

Force transducer	Sensitivity:	21.99 mV/N
	Gain on the signal conditioner:	×100
Accelerometer	Sensitivity:	10.34 mV/ms^{-2}
	Gain on the signal conditioner:	×100

Tab. C.2: Impedance head ICP® PCB 288D01 characteristics and conditioner gains.

Current (mA), I	Magnetic flux density (mT), B	Anti-resonance frequency (Hz)		Total loss factor	
		Measurement $\omega_a^m/(2\pi)$	FE model $\omega_a^F/(2\pi)$	Measurement	FE model
0	0	105.8551	105.6051	0.1545	0.1702
46	14.6	107.1563	107.0501	0.1550	0.1809
109	34.7	108.2212	112.9588	0.2256	0.2105
182	57.9	115.2866	122.2296	0.2214	0.2281
280	89.1	130.6646	133.4630	0.1951	0.2165
327	104.0	134.9809	137.6185	0.1981	0.2056
446	141.9	142.8051	144.8102	0.1688	0.1754
534	169.8	146.4157	147.8876	0.1601	0.1551
646	205.5	149.0324	150.0456	0.1404	0.1310

Tab. C.3: Measured and predicted tuned frequencies and total loss factors of the MR fluid-filled ATVA for various current. G' of Eq. (3.19) and η of Eq. (6.6).

Current (mA) I	Magnetic flux density (mT) B	Stiffness (kN/m) $k_a^m = (\omega_a^m)^2 m_a$	Viscous damping $c_a^m = \eta_T^m m_a \omega_a^m$
0	0	6.3259	1.4073
46	14.6	6.4823	1.4721
109	34.7	6.6118	2.1664
182	57.9	7.5033	2.2575
280	89.1	9.6385	2.2579
327	104.0	10.2859	2.3681
446	141.9	11.5129	2.1380
534	169.8	12.1024	2.0752
646	205.5	12.5388	1.8480

Tab. C.4: Measured stiffness and viscous damping of the MR fluid-filled ATVA.

Figures

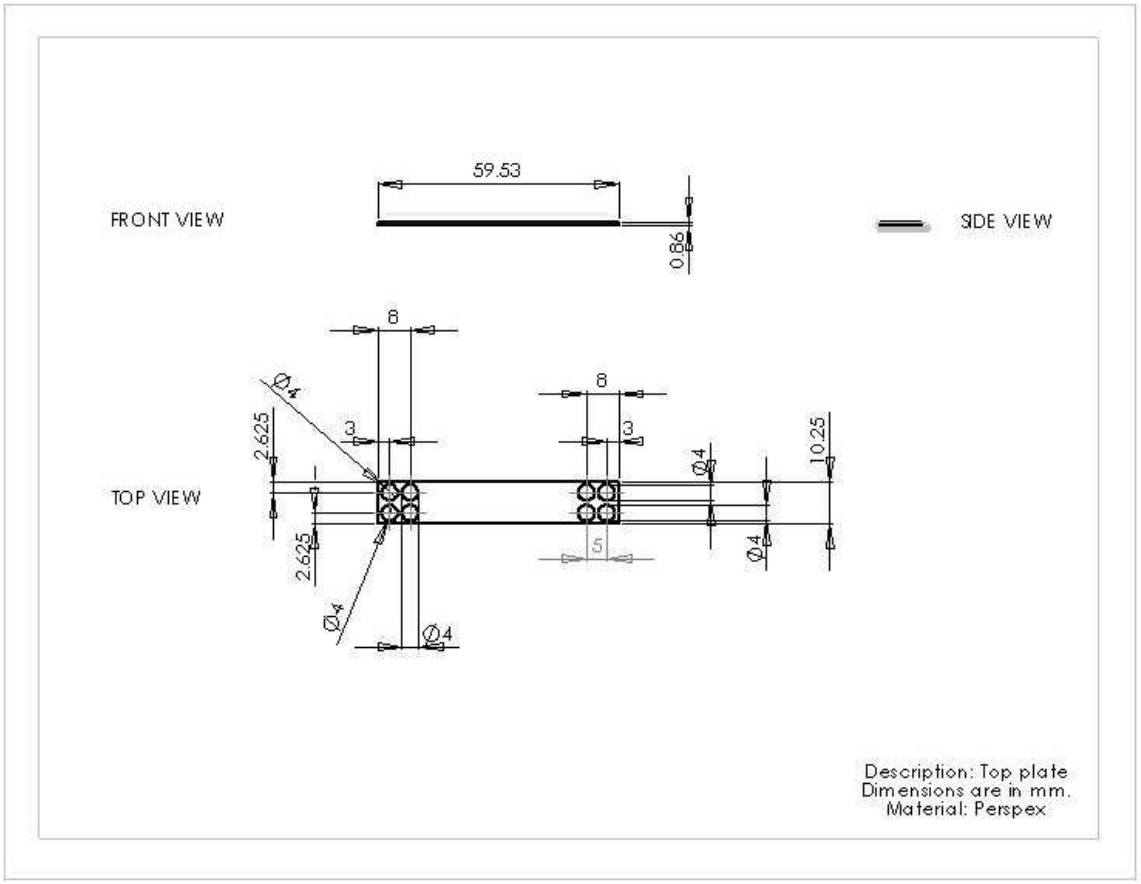

Fig. C.1: Drawing of the top layer of the MR ATVA.

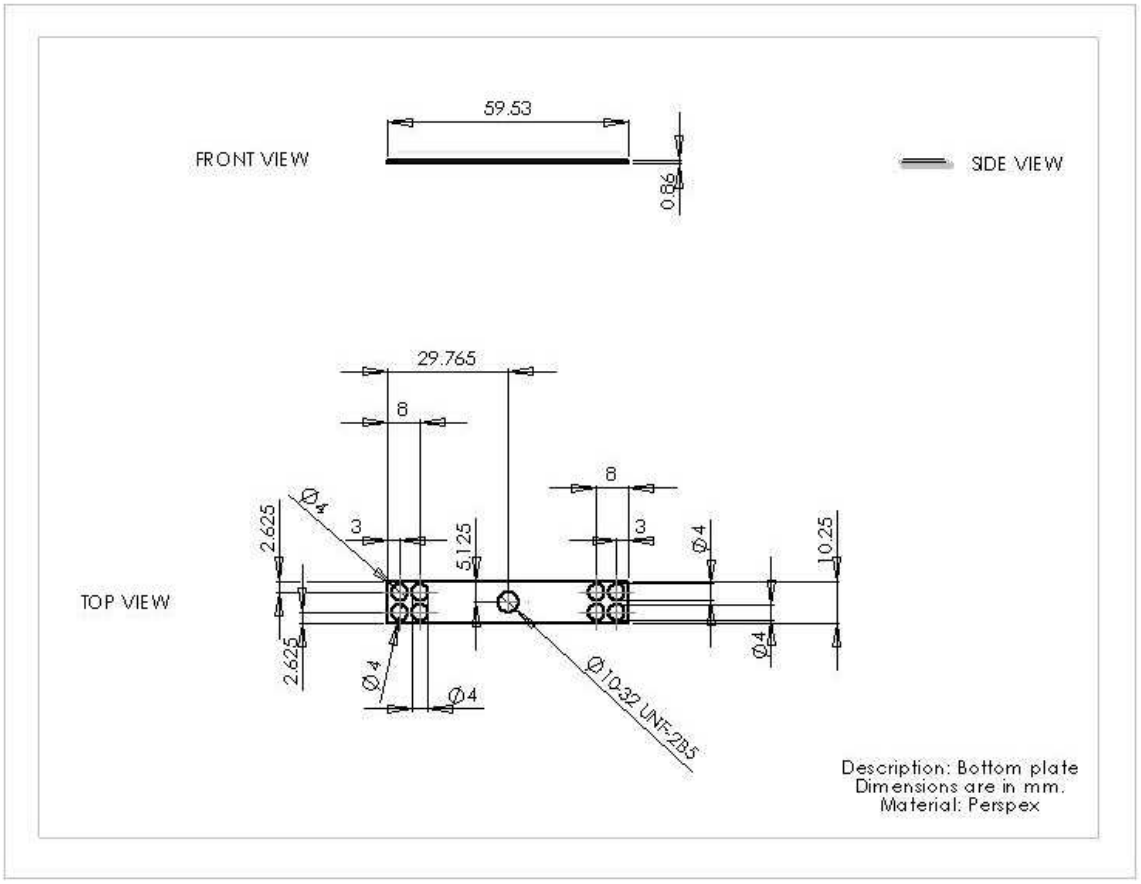

Fig. C.2: Drawing of the bottom layer of the MR ATVA.

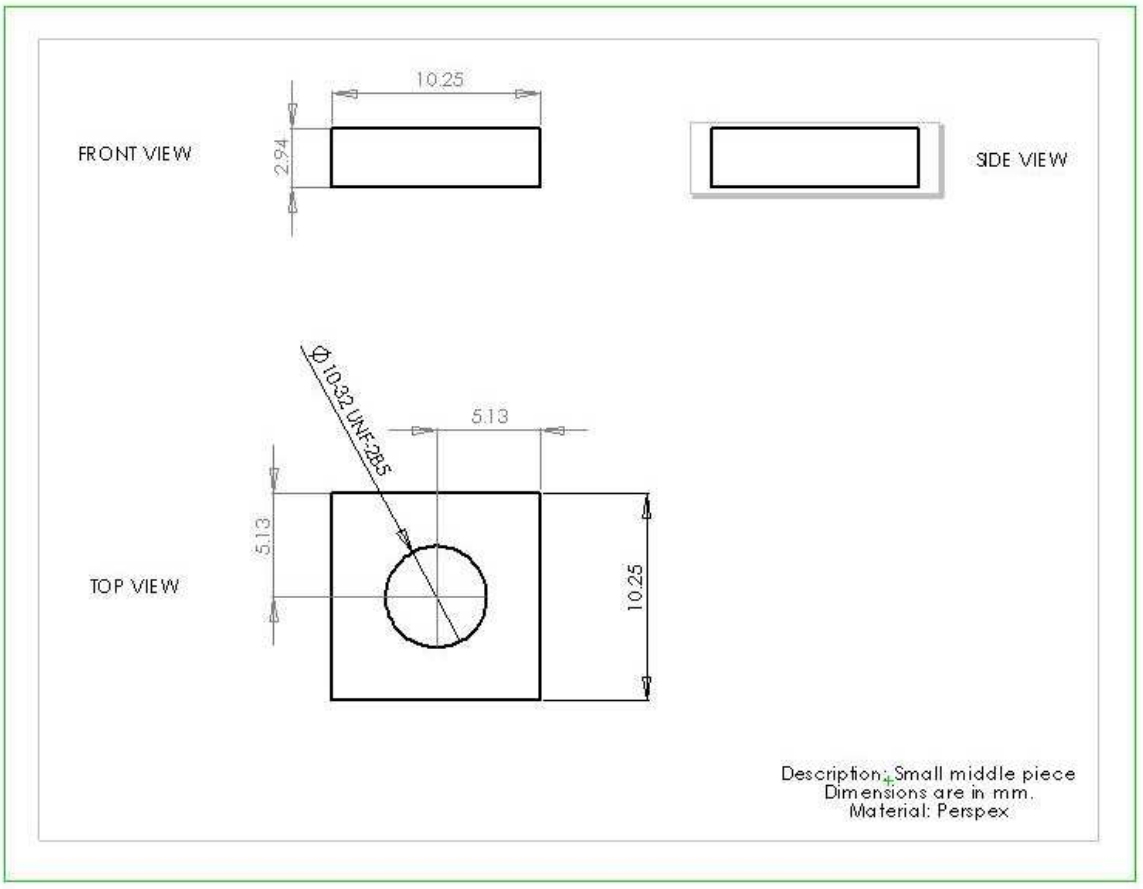

Fig. C.3: Drawing of a centre piece of perspex in the middle layer of the MR ATVA.

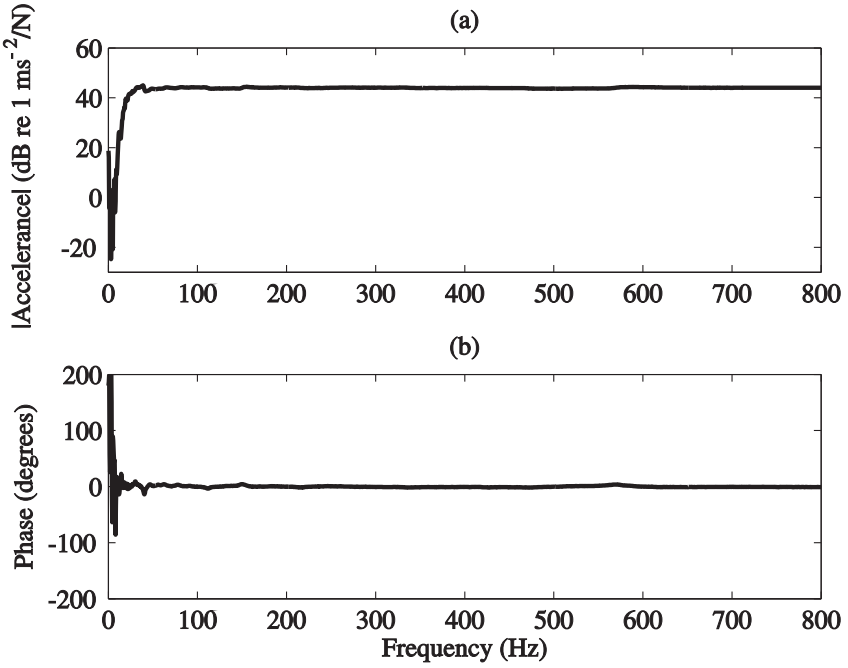

Fig. C.4: Measured input accelerance of the impedance head. (a) Magnitude of accelerance. (b) Phase of accelerance.

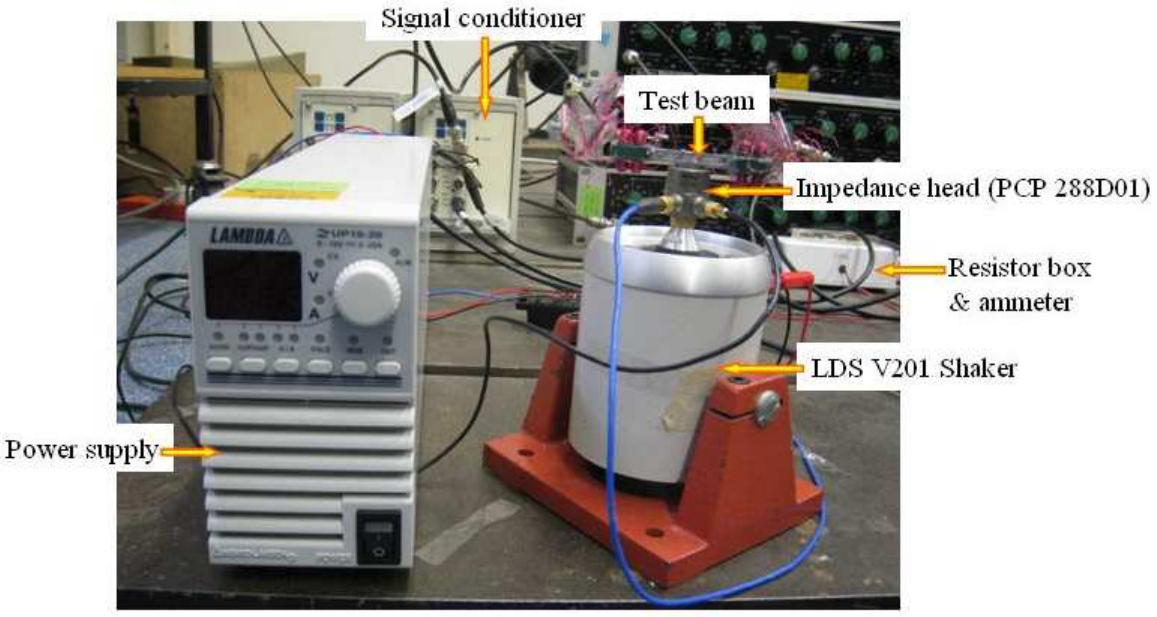

Fig. C.5: Photograph of experimental set-up to test the MR ATVA.

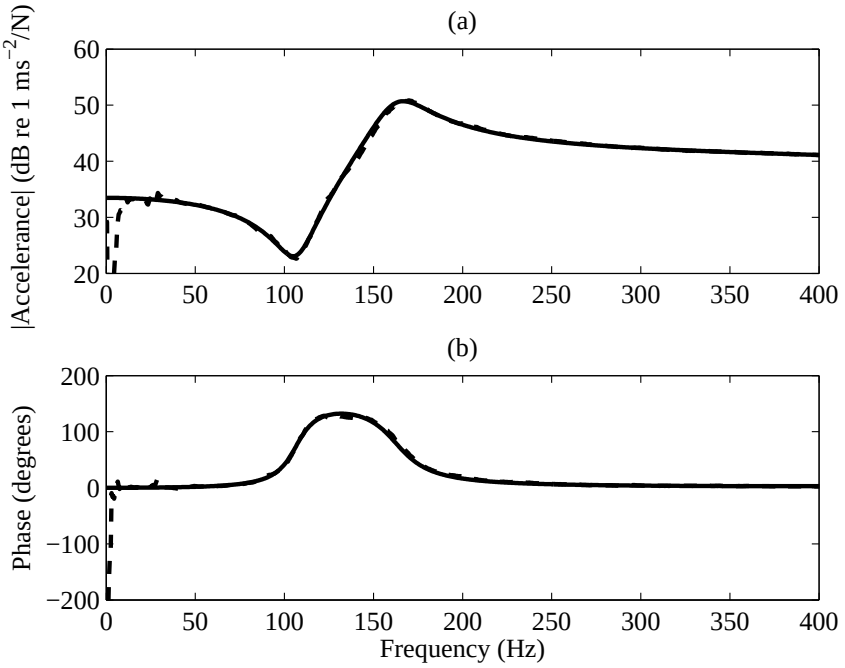

Fig. C.6: Input accelerance of the MR ATVA with $I = 46$ mA:--- measured; — predicted.

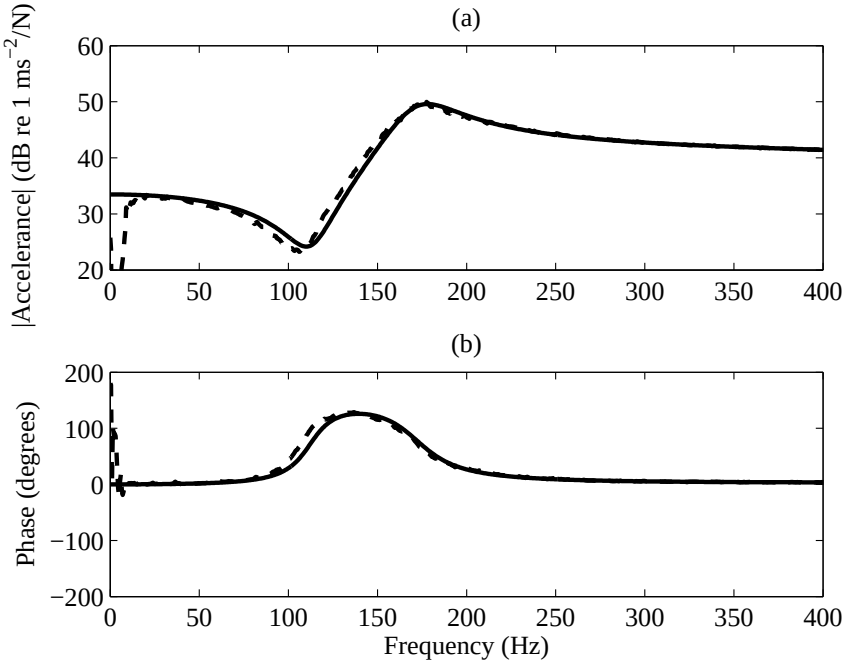

Fig. C.7: Input accelerance of the MR ATVA with $I = 109$ mA:--- measured; — predicted.

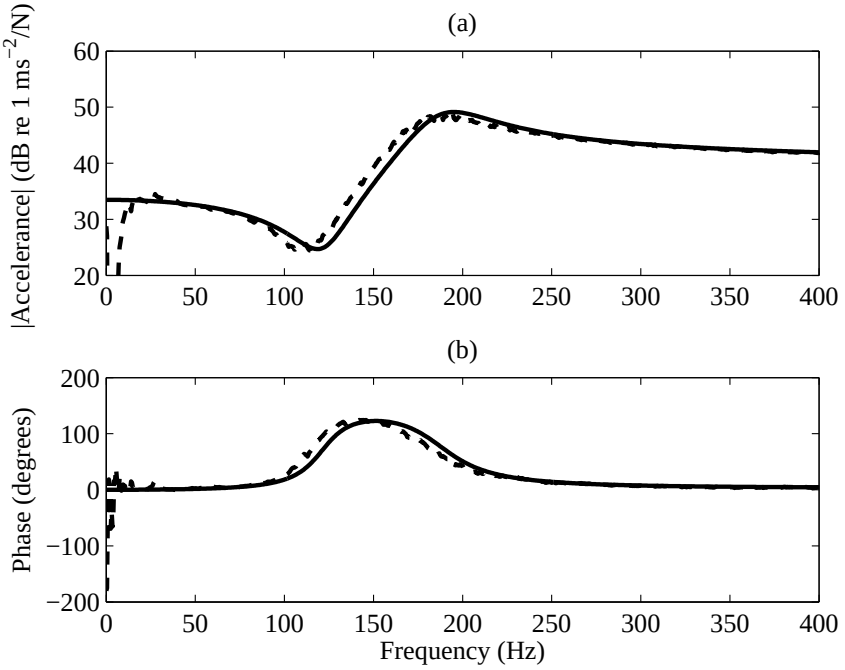

Fig. C.8: Input accelerance of the MR ATVA with $I = 182$ mA:--- measured; — predicted.

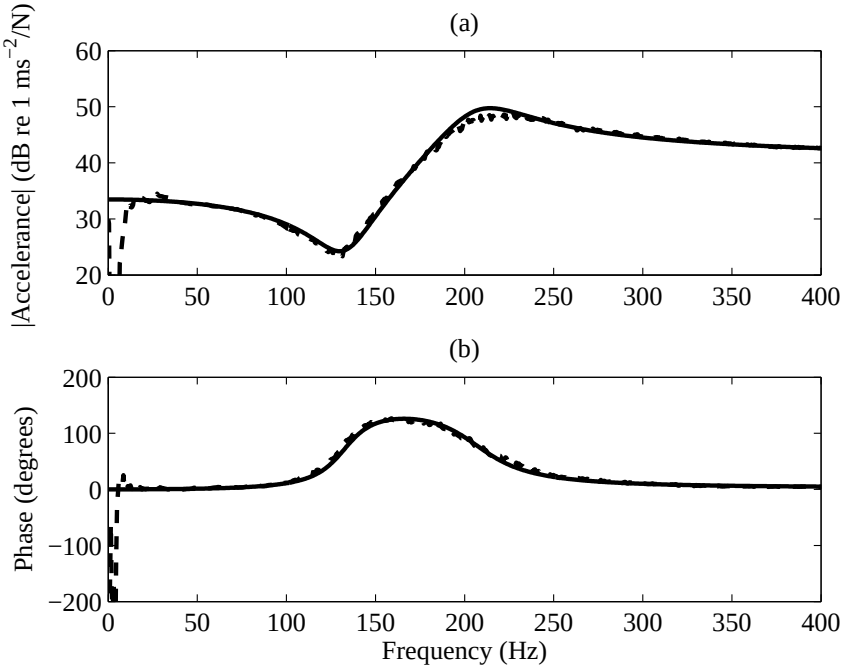

Fig. C.9: Input accelerance of the MR ATVA with $I = 280$ mA:--- measured; — predicted.

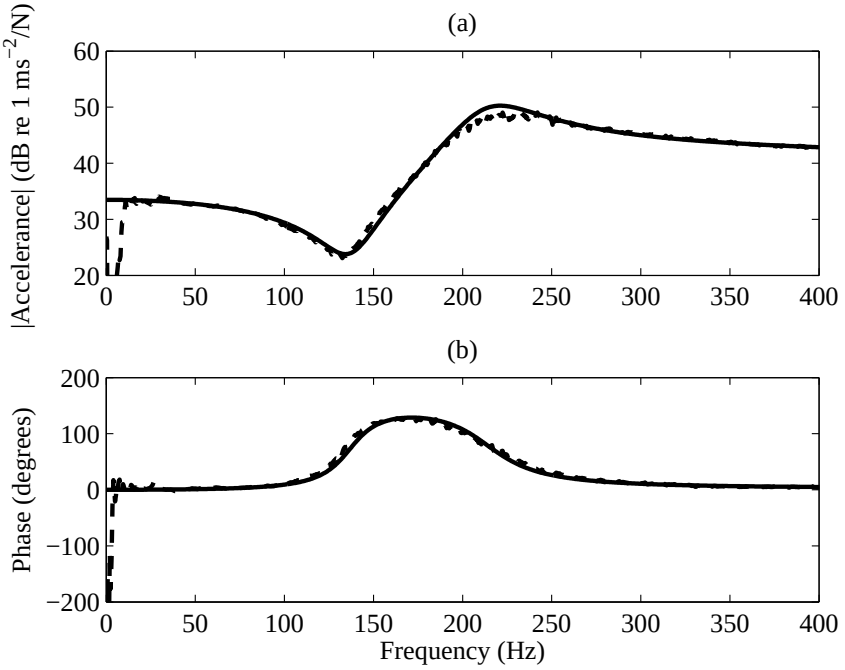

Fig. C.10: Input accelerance of the MR ATVA with $I = 327$ mA:--- measured; — predicted.

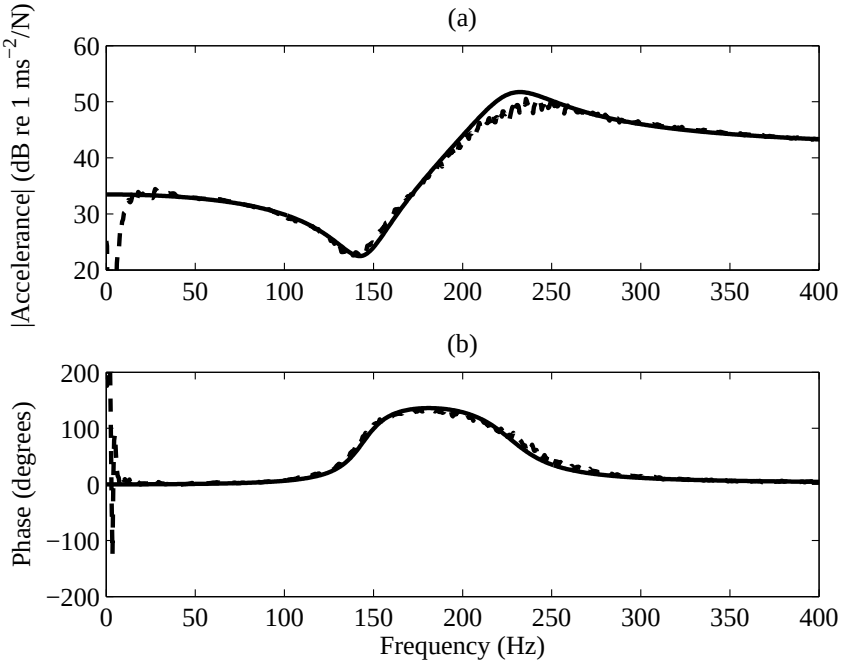

Fig. C.11: Input accelerance of the MR ATVA with $I = 446$ mA:--- measured; — predicted.

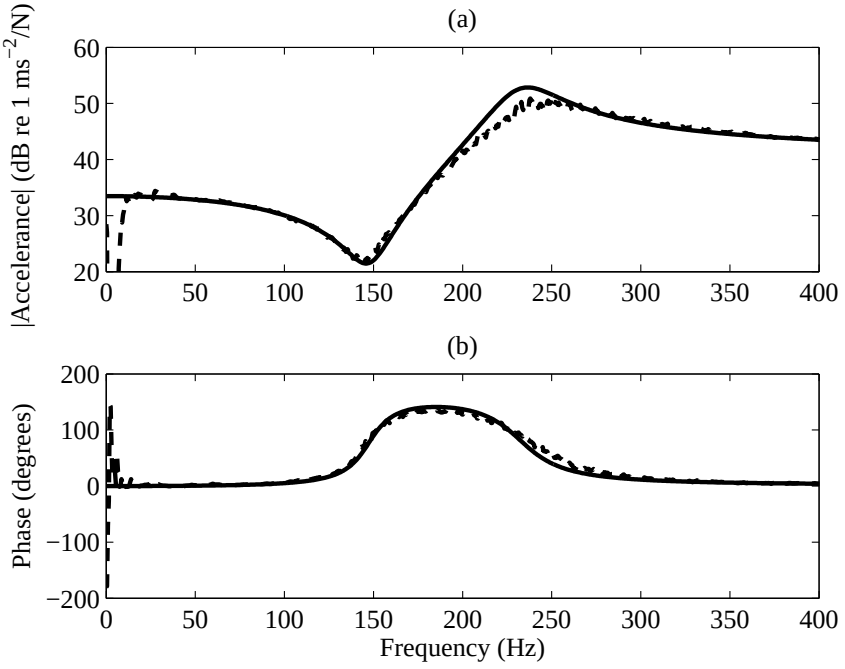

Fig. C.12: Input accelerance of the MR ATVA with $I = 534$ mA:--- measured; — predicted.

Appendix D

SIMULINK® Models

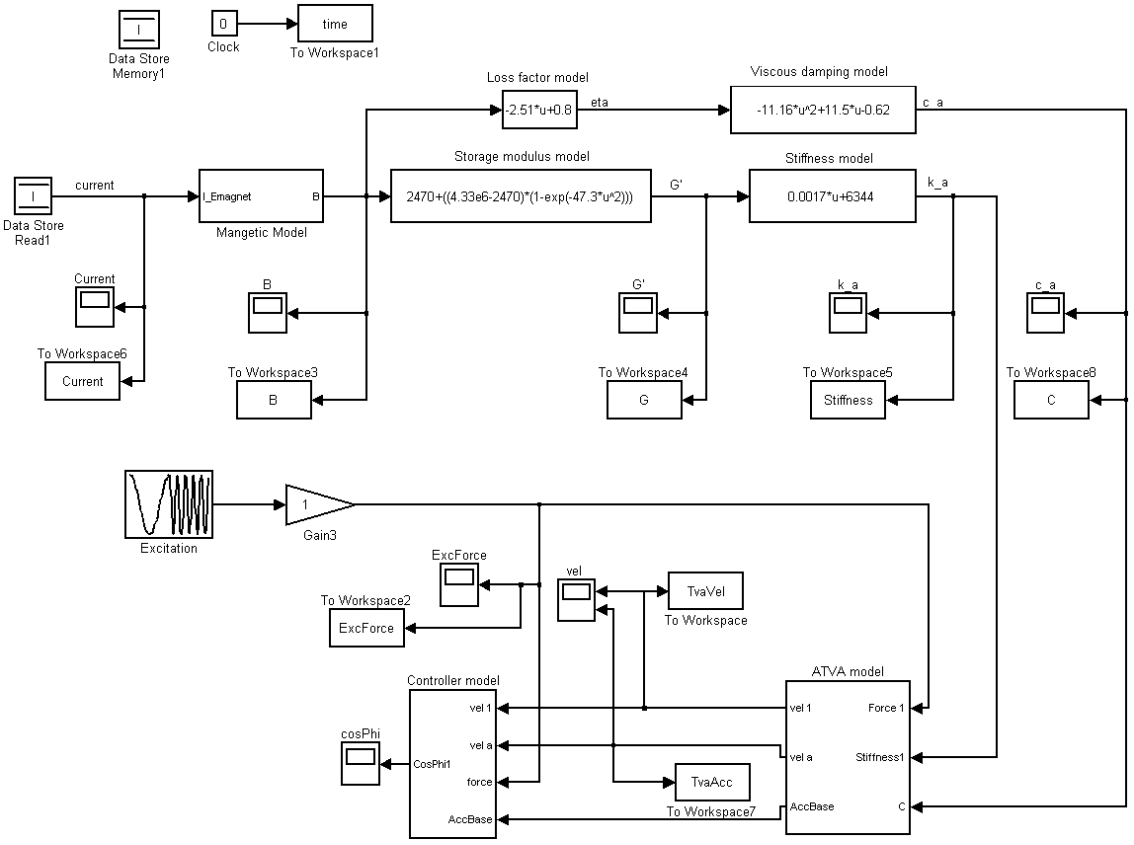

Fig. D.1: SIMULINK® model for MR ATVA and its controller corresponding to the block diagram shown in Fig. 7.2.

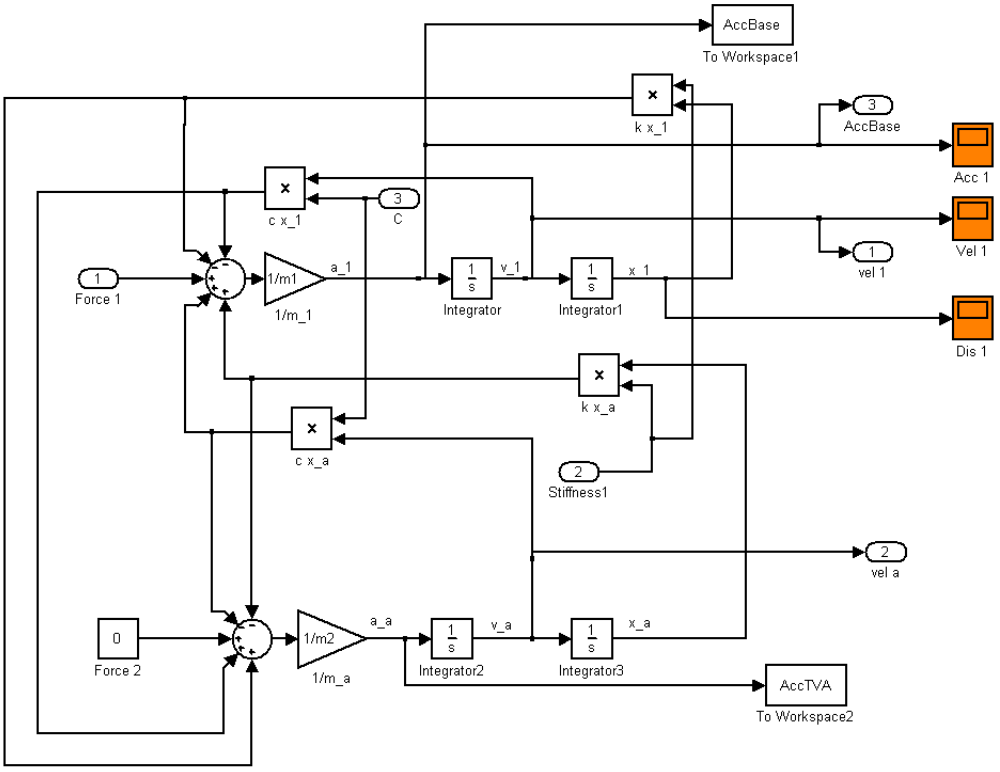

Fig. D.2: SIMULINK® sub-model for MR ATVA.

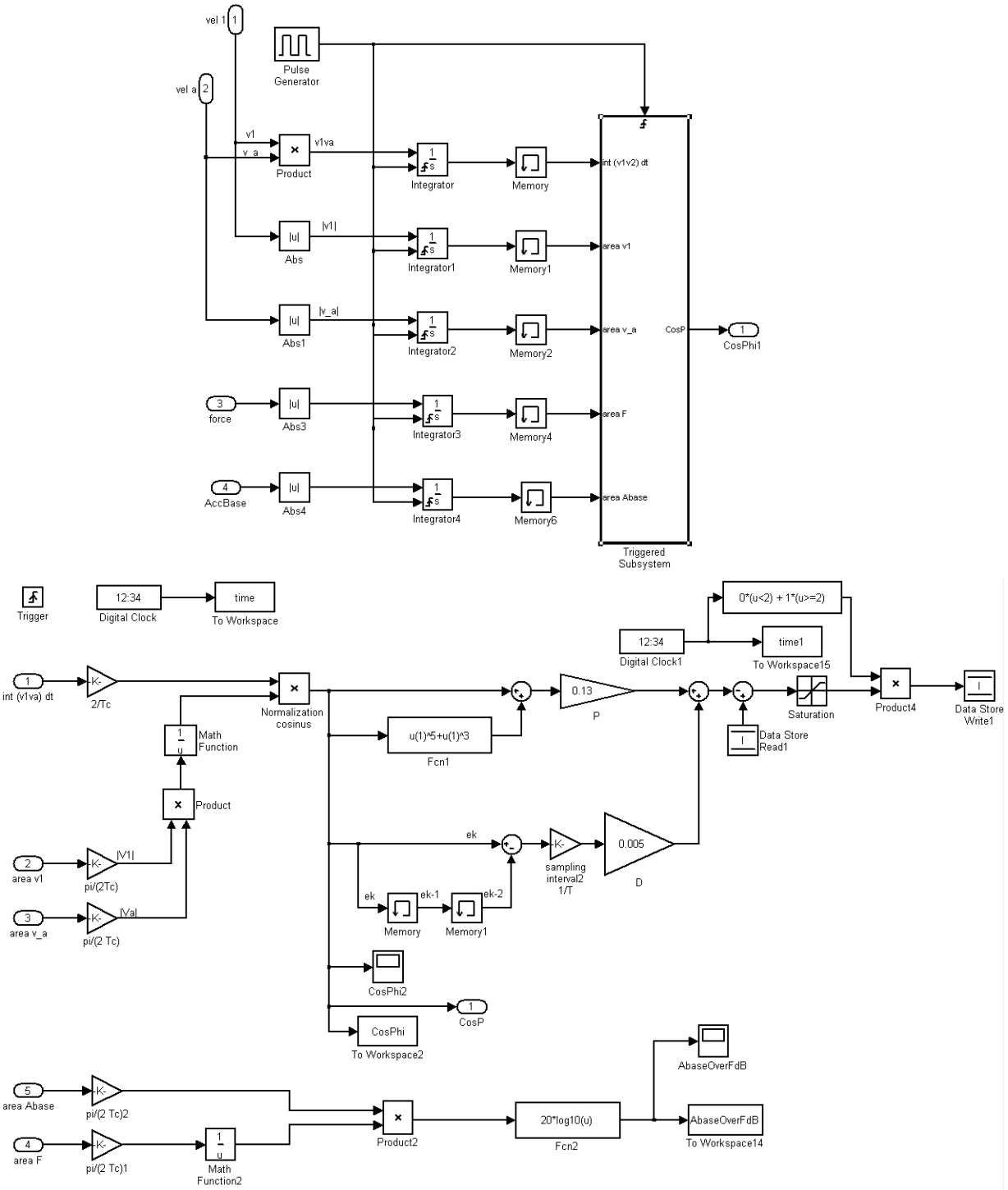

Fig. D.3: SIMULINK® sub-model for controller.

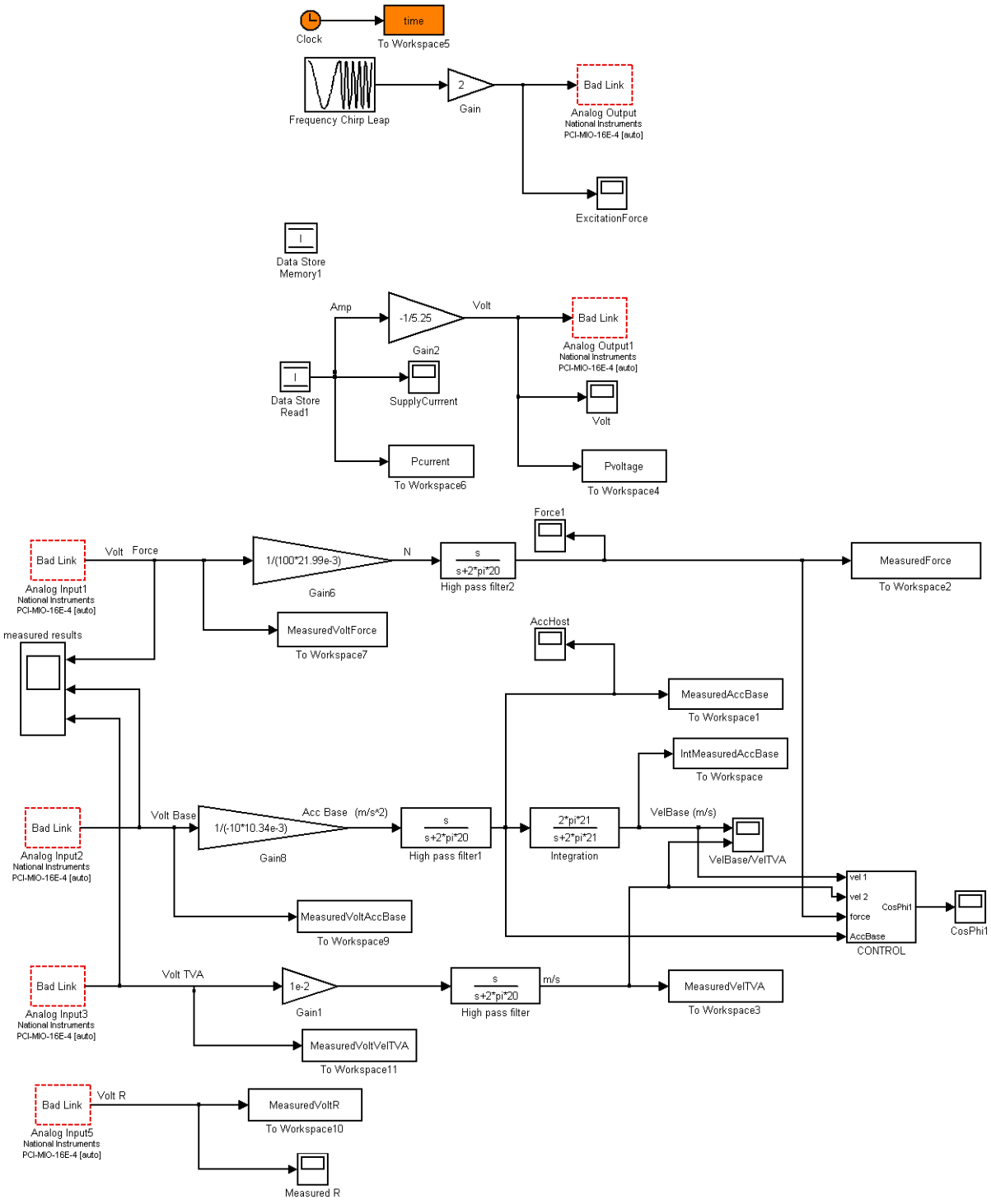

Fig. D.4: SIMULINK® model for connecting the controller to the experimental rig.